

**Three-dimensionality and  
secondary vortex street  
in the wake of  
cylindrical bluff bodies**

by

**Alexander Radi (M. Sc.)**

---

---

A Thesis submitted in fulfilment  
of the requirements for the degree of  
Doctor of Philosophy

---

---

September 2013

Department of Mechanical and Aerospace Engineering  
Monash University



# Notices

1. Under the Copyright Act 1968, this thesis must be used only under the normal conditions of scholarly fair dealing. In particular no results or conclusions should be extracted from it, nor should it be copied or closely paraphrased in whole or in part without the written consent of the author. Proper written acknowledgement should be made for any assistance obtained from this thesis.
2. I certify that I have made all reasonable efforts to secure copyright permissions for third-party content included in this thesis and have not knowingly added copyright content to my work without the owners permission.

---



# Contents

|          |   |           |
|----------|---|-----------|
| <b>1</b> | <b>Introduction</b>   | <b>1</b>  |
| <b>2</b> | <b>Literature Review</b>                                      | <b>7</b>  |
| 2.1      | Stationary circular cylinders . . . . .                       | 7         |
| 2.1.1    | Wake regimes and three-dimensional instabilities . . . . .    | 8         |
| 2.1.2    | Vortex street breakdown and secondary street . . . . .        | 14        |
| 2.1.3    | Experimental considerations . . . . .                         | 18        |
| 2.1.3.1  | Control of end effects . . . . .                              | 18        |
| 2.1.3.2  | Blockage effects . . . . .                                    | 20        |
| 2.1.3.3  | Wire disturbances . . . . .                                   | 21        |
| 2.1.3.4  | Streakline effect . . . . .                                   | 22        |
| 2.1.3.5  | Freestream turbulence . . . . .                               | 23        |
| 2.2      | Elliptical cylinders and normal flat plates . . . . .         | 24        |
| 2.2.1    | Elliptical cylinders . . . . .                                | 24        |
| 2.2.2    | Normal flat plates . . . . .                                  | 25        |
| 2.3      | Rotating circular cylinder . . . . .                          | 29        |
| <b>3</b> | <b>Experimental setup &amp; numerical tools</b>               | <b>35</b> |
| 3.1      | The tunnel facility . . . . .                                 | 35        |
| 3.2      | Rotating cylinder . . . . .                                   | 37        |
| 3.3      | Elliptical cylinders . . . . .                                | 40        |
| 3.4      | Instrumentation . . . . .                                     | 43        |
| 3.4.1    | Flow visualization . . . . .                                  | 43        |
| 3.4.2    | Particle image velocimetry (PIV) . . . . .                    | 44        |
| 3.4.3    | Laser Doppler velocimetry (LDV) . . . . .                     | 46        |
| 3.4.4    | Hot film probes . . . . .                                     | 47        |
| 3.5      | Numerical tools . . . . .                                     | 49        |
| 3.5.1    | Space-time diagrams (rotating cylinder experiments) . . . . . | 49        |
| 3.5.2    | Proper orthogonal decomposition (POD) . . . . .               | 50        |
| <b>4</b> | <b>Reynolds number reduction</b>                              | <b>53</b> |
| 4.1      | Introduction . . . . .  | 53        |

---

|          |   |            |
|----------|---|------------|
| 4.2      | Construction . . . . .  | 54         |
| 4.2.1    | Main Structure . . . . .  | 54         |
| 4.2.2    | Perforated Screen . . . . .   | 55         |
| 4.3      | Validation tests . . . . .  | 56         |
| 4.3.1    | Velocity reduction . . . . .  | 56         |
| 4.3.2    | Dependence on gap size $g$ . . . . .  | 57         |
| 4.3.3    | Dependence on freestream velocity . . . . .   | 59         |
| 4.3.4    | Flow development along the streamwise direction . . . . .                                 | 61         |
| 4.3.5    | Dependence on screen porosity . . . . .   | 62         |
| 4.3.6    | Side walls leading edges . . . . .  | 62         |
| 4.4      | Conclusions . . . . .   | 64         |
| <b>5</b> | <b>Rotating cylinder</b>  | <b>65</b>  |
| 5.1      | Introduction . . . . .  | 65         |
| 5.2      | Setup validation . . . . .  | 66         |
| 5.2.1    | Non-rotating cylinder . . . . .   | 66         |
| 5.2.2    | Rotating cylinder . . . . .   | 67         |
| 5.3      | Results & discussion . . . . .  | 69         |
| 5.3.1    | Mode C . . . . .  | 69         |
| 5.3.2    | Co-existence of modes B and C . . . . .   | 72         |
| 5.3.3    | Modes D & E . . . . .   | 75         |
| 5.3.4    | Mode F . . . . .  | 81         |
| 5.3.5    | Second shedding . . . . .   | 84         |
| 5.4      | Summary . . . . .   | 86         |
| <b>6</b> | <b>Elliptical cylinders: <math>St-Re</math> relationship</b>                              | <b>89</b>  |
| 6.1      | $St-Re$ curves . . . . .  | 89         |
| 6.1.1    | Introduction . . . . .  | 89         |
| 6.1.2    | Method . . . . .  | 90         |
| 6.1.3    | Results . . . . .   | 91         |
| 6.2      | Spectral energy of the primary frequency . . . . .  | 99         |
| 6.3      | Low frequency oscillation in the wake of the $Ar = 0.26$ cylinder: a case study . . . . . | 102        |
| 6.3.1    | Comparison to Johnson <i>et al.</i> (2004) . . . . .                                      | 102        |
| 6.3.2    | Instantaneous flow field . . . . .  | 104        |
| 6.4      | Chapter summary . . . . .   | 106        |
| <b>7</b> | <b>Elliptical cylinders: Secondary wake</b>   | <b>109</b> |
| 7.1      | Wake centreline velocity profiles . . . . .   | 110        |
| 7.2      | Vortex street geometry . . . . .  | 114        |
| 7.2.1    | Method . . . . .  | 114        |

---

---

|          |  |            |
|----------|--|------------|
| 7.2.2    | Results . . . . .  | 115        |
| 7.2.3    | Conclusions . . . . .  | 118        |
| 7.3      | Proper orthogonal decomposition of velocity fields . . . . .                                 | 120        |
| 7.3.1    | Circular cylinder . . . . .  | 120        |
| 7.3.2    | $Ar = 0.72$ and $Ar = 0.64$ cylinders . . . . .  | 123        |
| 7.3.3    | $Ar = 0.39$ cylinder . . . . .   | 125        |
| 7.3.4    | Flat plate . . . . .   | 126        |
| 7.3.5    | Discussion . . . . .   | 130        |
| 7.4      | Chapter summary . . . . .  | 132        |
| <b>8</b> | <b>Conclusions</b>   | <b>133</b> |
| 8.1      | Rotating cylinder . . . . .  | 133        |
| 8.2      | Elliptical cylinders . . . . .   | 134        |
| 8.3      | Recommended future work . . . . .  | 136        |
| 8.3.1    | Rotating cylinder . . . . .  | 136        |
| 8.3.2    | Elliptical cylinders . . . . .   | 136        |
|          | <b>Appendices</b>  | <b>139</b> |
|          | <b>Appendix A Uncertainty analysis</b>   | <b>139</b> |
| A.1      | Estimation of error . . . . .  | 139        |
| A.1.1    | Reynolds number uncertainty . . . . .  | 140        |
| A.1.2    | Strouhal number uncertainty . . . . .  | 142        |
| A.1.3    | Non-dimensional rotation rate uncertainty . . . . .  | 143        |
|          | <b>Appendix B FFT code testing</b>   | <b>145</b> |
|          | <b>Appendix C POD modes of elliptical cylinders at <math>Re = 100, 150, 200</math> &amp;</b> |            |
|          | <b>250</b>   | <b>149</b> |

---

# Abstract

In the research of bluff body aerodynamics, the natural flow complexity has to be reduced to understand fundamental principles of fluid dynamics involved. Often, cylinders with simple cross-sectional geometries such as circle, rectangle or plates with zero thickness are used. This thesis presents results of water channel experiments on selected cylindrical shapes, studying three-dimensionality and vortex dynamics of incompressible bluff body wakes. Results of two distinct but related studies are reported:

A circular cylinder of diameter  $d$ , spinning about its main axis in cross flow, was observed to generate new three-dimensional modes C–F for Reynolds numbers  $175 \leq Re \leq 275$  and non-dimensional rotation rates  $0 \leq \alpha \leq 4$ . Using particle image velocimetry and digitally post-processed hydrogen bubble flow visualizations our experiments confirmed for the first time the linear stability analysis of Rao *et al.* (2013). For  $Re = 275$  and  $\alpha = 1.7$ , we observed the sub-harmonic mode C with a spanwise wavelength of  $1.1d$ . On increasing the rotation rate, two modes with a wavelength of  $\approx 2d$  became unstable in rapid succession, termed modes D and E. Mode D grew on a shedding wake, whereas mode E consisted of streamwise vortices on an otherwise steady wake. For  $\alpha > 2.2$ , a short-wavelength mode F appeared in the wall-bounded shear layer of the cylinder with a wavelength of  $0.5d$ , which is presumably a manifestation of centrifugal instability. Unlike the other modes, mode F was a travelling wave with a spanwise frequency of  $St_{3D} \approx 0.1$ . In addition to these new modes, observations on the one-sided shedding process, known as the ‘second shedding’, are reported for  $\alpha = 5.1$ . Despite suggestions from the literature, this process seems to be intrinsically three-dimensional.

In the second study, we investigated the wake characteristics shared by a circular cylinder and a flat plate aligned normal to the flow. The link between these two models was formed by cylinders of elliptical cross sections of varying axes aspect ratios  $Ar$ . When ‘flattening’ the cross-section into ellipses perpendicular to the flow, the critical Reynolds number of wake transitions decreased. Whilst modified versions of the mode A and B transitions of a circular cylinder wake occurred at aspect ratios above  $Ar \approx 0.4$ , the two-dimensional base flow of the wake changed considerably for lower  $Ar$ . In particular, the wake appeared to re-laminarize after it had already undergone three-dimensional transition. This strictly periodic shedding regime was characterized by an extended wake deficit, where the time-averaged velocities decreased to 5–20% of the

---

freestream velocity. In some cases, a small second recirculation bubble was observed downstream of the wake formation region. Proper orthogonal decomposition of PIV data confirmed the presence of a secondary vortex street of double the wavelength, with a rather abrupt transition between the wake types. It is speculated that the close proximity of the secondary street at very low  $Ar$  stabilised the primary shedding process. The reason for the increased periodicity of the primary shedding, and the exact mechanism leading to suppression of three-dimensional modes in the re-laminarized regime, are subjects for future studies.

# Statement of Originality

This thesis contains no material that has been accepted for the award of a degree or diploma in this or any other university. To the best of the candidate's knowledge and belief, this thesis contains no material previously published or written by another person except where due reference is made in the text of this thesis."

---

Alexander Radi

September 2013

---



# Acknowledgments

In the first place, I would like to thank my supervisors Prof. John Sheridan, Prof. Mark Thompson and Prof. Kerry Hourigan for their support and supervision during my stay at Monash University. I am particularly indebted to Prof. John Sheridan for trusting “some German student writing from the US” and supporting him during the scholarship application process and relocation to Australia.

I will always remember the FLAIR group, united in the shared struggle against laboratory equipment issues and water channel sloshing: Andras ‘Mr. IT’ Nemes, Jisheng Zhao, James Venning and Michael Sherry. Thank you for action-packed late-night ping-pong matches. I would like to express my gratitude to Dr. Justing Leontini, for fruitful discussions of the experimental results and moral support during research lows. Thanks goes to Anirudh Rao for discussions of the rotating cylinder experiments and support in the drafting of the first publication.

Without the guidance of Helen Frost, I would have gotten lost in the administrative jungle. And without the team from the mechanical workshop none of the experiments would have taken place.

I acknowledge personal financial support provided by the Monash International Postgraduate Research Scholarship and the Monash Graduate Scholarship.

Although some periods of the past 3.5 years I can easily count to the most depressing and draining times of my life, I would not want to miss the overall Ph.D. experience. The difficult days were balanced with the help of some special people. On this side of the world, Cain Doherty kept up my spirits by accompanying me on his surfboard through the Victorian waves. I will also miss Benji and his merry world view. On the other side of the globe, I could always be sure of the support and encouragement from my whole (extended) family.



*This Thesis is dedicated to my parents  
Olga and Jakob.*



# Nomenclature

## Miscellaneous & mathematical symbols

| Symbol         | Description  |
|----------------|--|
| $\S$           | Thesis section   |
| $\int$         | Integration  |
| $\nabla$       | Vector gradient operator (grad)                        |
| $\nabla^2$     | Del squared (or div grad) operator                     |
| $\sum_{i=a}^b$ | Sum of arguments with $i$ incrementing from $a$ to $b$ |

## Roman symbols

| Symbol             | Description   |
|--------------------|---|
| $a$                | Streamwise vortex separation of the vortex street                       |
| $a_K$              | Streamwise vortex separation of the primary (von Kármán ) vortex street |
| $a_{\text{sec}}$   | Streamwise vortex separation of the secondary vortex street             |
| $a^{(n)}(t_k)$     | Projection coefficient of the $n$ th POD mode at time instant $t_k$     |
| $A_{\text{open}}$  | Open area of the sub-channel screen                                     |
| $A_{\text{total}}$ | Total area of the sub-channel screen                                    |
| $b$                | Minor axis of the elliptical cross-section                              |
| $B$                | Model blockage ratio  |
| $B$                | Bias limit of measurement uncertainty                                   |
| $d$                | Cylinder model diameter (or major axis of the elliptical cross-section) |
| $d_w$              | Wire diameter   |
| $D$                | Hole diameter of the perforated screen                                  |
| $e$                | Ellipse eccentricity  |

*Continued on the next page.*

---

*Continued from previous page.*

| <b>Symbol</b>     | <b>Description</b>  |
|-------------------|---|
| $e_{\text{def}}$  | Kinetic energy deficit ratio of the wake centre line velocity profile   |
| $f_s$             | Sampling frequency  |
| $f_K$             | von Kármán shedding frequency   |
| $f_{\text{sec}}$  | Shedding frequency of the secondary vortex street                       |
| $\Delta f^*$      | Spectral width of the von Kármán frequency peak                         |
| $h$               | Cross-stream vortex separation of the vortex street                     |
| $h$               | Water depth   |
| $h/a$             | Vortex spacing ratio of the vortex street                               |
| $I$               | Electrical current  |
| $Nu$              | Nusselt number  |
| px                | Pixel   |
| $P$               | Precision limit of measurement uncertainty                              |
| $R_w$             | Electrical resistance   |
| $Re$              | Reynolds number   |
| $Re_{c_0}$        | Critical Reynolds number at onset of vortex shedding                    |
| $Re_{c_1}$        | Critical Reynolds number of mode L                                      |
| $Re_{c_2}$        | Critical Reynolds number of mode S                                      |
| $St$              | Strouhal number   |
| $St_C$            | Strouhal number at onset of vortex shedding at $Re_{c_0}$               |
| $St_{300}$        | Strouhal number of elliptical cylinders sampled at $Re = 300$           |
| $St_{3D}$         | Non-dimensional frequency of mode F on a rotating cylinder              |
| $t$               | Time  |
| $T$               | Shedding period   |
| $T_w$             | Water temperature   |
| $Tu$              | Turbulence intensity [%] ( $Tu_i$ is the component in $i$ th direction) |
| $U$               | Uncertainty of measurements   |
| $U_{\text{diff}}$ | Velocity difference relative to local mean                              |
| $U_0$             | Velocity inside the sub-channel at model location                       |
| $U_\infty$        | Velocity in the main channel test section (sub-channel removed)         |

*Continued on the next page.*

---

*Continued from previous page.*

| <b>Symbol</b>                                 | <b>Description</b>  |
|---|---|
| $U, V, W$                                     | Time-averaged velocity components in streamwise, cross-stream and vertical flow direction, respectively |
| $\overline{u'}, \overline{v'}, \overline{w'}$ | Root-mean-squared velocity components in streamwise, cross-stream and vertical direction, respectively  |

---

## Abbreviations

| <b>Symbol</b> | <b>Description</b>   |
|---------------|--|
| 2D            | Two-dimensional  |
| 3D            | Three-dimensional  |
| <i>A.U.</i>   | Arbitrary unit   |
| CTA           | Constant temperature anemometer                            |
| FFT           | Fast Fourier transform                                     |
| FLAIR         | Fluids Laboratory for Aeronautical and Industrial Research |
| LDV           | Laser Doppler velocimetry                                  |
| <i>LE</i>     | Sub-channel leading edges                                  |
| PIV           | Particle image velocimetry                                 |
| PMT           | Photo multiplier tube                                      |
| POD           | Proper orthogonal decomposition                            |
| PSD           | Power spectral density                                     |

---

## Greek symbols

| <b>Symbol</b>   | <b>Description</b>                             |
|-----------------|--|
| $\alpha$        | Non-dimensional cylinder rotation rate         |
| $\alpha$        | Sub-channel screen porosity                    |
| $\theta_i$      | Sensitivity coefficient of the $i$ th variable |
| $\kappa$        | Diffusion coefficient of the passive scalar    |
| $\lambda$       | POD eigenvalue                                 |
| $\lambda^{(n)}$ | POD eigenvalue of the $n$ th mode              |
| $\lambda$       | Wavelength                                     |
| $\lambda_z$     | Spanwise wavelength                            |
| $\lambda_L$     | Spanwise wavelength of mode L                  |

---

*Continued on the next page.*

---

*Continued from previous page.*

**Symbol Description**

|             |                                       |
|-------------|---------------------------------------|
| $\lambda_S$ | Spanwise wavelength of mode S         |
| $\mu$       | Dynamic fluid viscosity               |
| $\nu$       | Kinematic fluid viscosity             |
| $\psi$      | Streamfunction                        |
| $\Omega$    | Spinning cylinder rotation rate [rad] |

---

**Superscript**

**Symbol Description**

|   |                   |
|---|-------------------|
| ' | fluctuating value |
|---|-------------------|

---



# Chapter 1

## Introduction

A body is designated as ‘bluff’ when its drag force is dominated by pressure drag. Above a certain Reynolds number, the flow field contains large regions of separated flow as a consequence of boundary layer separation caused by adverse pressure gradients. The separated vorticity in the free shear layers rolls up into coherent regions, known as wake vortices. It is the low pressure in the cores of these vortices that causes large fluctuating forces on the rear of the body.

This process has direct engineering significance. The alternate shedding of vortices in the near wake and the associated pressure forces may cause structural vibrations, acoustic noise, or resonance, which in some cases can trigger failure (Tropea *et al.* 2007). Road vehicles such as cars, trucks and trains can be considered as bluff, in which case the issues of surface flutter, noise generation and overall drag reduction need to be addressed by engineers (Hucho & Sovran 1993). Furthermore, high chimneys, bridges, free swinging cables and oil rig pillars are in direct danger of structural failure due to vortex induced vibrations.

But not only from the perspective of drag and flow induced vibrations are wakes interesting study objects. Nature creates wakes in various sizes and shapes (see figure I). Many of the fluid dynamics phenomena associated with such flows are not fully understood. Three-dimensional instabilities, vortex interactions and parameter discontinuities have posed significant challenges to researchers for many years.

The question of how the body-shape determines its wake dynamics has been the subject of numerous studies. A minor change of body shape, even the orientation to the incoming flow, can lead to significant changes in drag and wake structure. Table I exemplifies these changes in terms of the drag coefficient and shedding frequencies for a range of two-dimensional bodies. A semicircular cylinder, for example, will experience

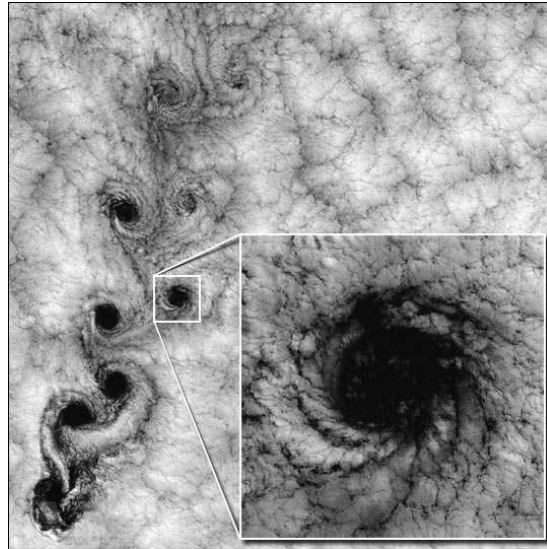


FIGURE I: Landsat 7 image of clouds off the Chilean coast. This ‘wake’ forms behind the Alejandro Selkirk Island on the bottom left and develops into the well known von Kármán vortex street (reproduced with permission from Robert Cahalan, NASA Goddard Space Flight Center; <http://earthobservatory.nasa.gov/IOTD/view.php?id=625>).







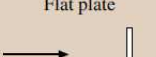

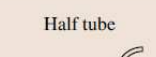
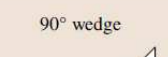


a 42% drag increase if facing the stream with the flat side, compared to the curved side facing upstream. Clearly, the fluid dynamics of such simple geometries need to be understood first, before the flow around more complex (three-dimensional) objects can be apprehended and predicted reliably.

When studying fundamental fluid dynamics, it is customary to reduce the natural flow complexity by the use of simple geometric shapes, such as the ones shown in table I, and by considering only two-dimensional flows. In how far truly two-dimensional flows can be achieved experimentally using finite model lengths, and which role three-dimensional effects play, will be discussed in section 2.1. All models considered in this thesis are (nominally) two-dimensional, meaning that we are dealing with cylinders which main axis is several orders bigger than the characteristic length of the cross-sectional shape.

The choice of the cross-sectional shape determines the number of control parameters, which impact the flow symmetry, complexity and richness of flow phenomena. Among the most commonly studied shapes are the canonical circular cylinder and the flat plate normal to the stream. The circular cylinder is the simplest model, with diameter  $d$  as the only geometrical parameter. This body type has been studied for over 100 years (Bénard 1908; Kármán 1911), and it still challenges researchers with a richness of two- and three-dimensional flow phenomena, which is truly astonishing for such a

‘plain’ geometry. Similarly, the normal flat plate is uniquely defined by its width, as the thickness is assumed to be ideally zero and the plate to be infinitely long. Again, the last two assumptions are a matter of debate.

TABLE I: Drag coefficients ( $C_D$ ) and Strouhal numbers (S) for common two-dimensional shapes. Note how the body shape and orientation impact the overall drag coefficient. The drag tends to increase when the flat side of the body is pointing into the stream. Note, that the shown values are valid only above some specific Reynolds number (reproduced with kind permission of Springer Science+Business Media from Tropea *et al.* 2007).

| 2-D BODY  | $C_D$ | S    | 2-D BODY   | $C_D$ | S    |
|---|-------|------|--|-------|------|
| Circular cylinder<br>      | 1.2   | 0.21 | Square cylinder<br>              | 2.1   | 0.13 |
| Semi-circular cylinder<br> | 1.2   | 0.21 | Square cylinder at 45°<br>       | 1.6   | 0.15 |
|                            | 1.7   | 0.16 | Rectangular cylinder (2:1)<br>   | 1.8   | 0.08 |
| Flat plate<br>           | 2.0   | 0.16 | Rectangular cylinder (1:2)<br> | 2.4   | 0.14 |
| Half tube<br>            | 1.2   | 0.21 | 90° wedge<br>                  | 1.6   | 0.18 |
|                          | 2.3   | 0.13 |                                | 2.0   | 0.13 |

The models do not have to be stationary. The vortex shedding phenomenon can be altered dramatically for cylinders undergoing in-line, transverse or rotational oscillations (Nazarinia 2010). A particularly interesting configuration is the circular cylinder rotating at a constant rate in cross flow. Now, that one side of the cylinder accelerates the adjacent flow and the other side delays it, the flow field loses its mirror symmetry along the wake centreline. One of the consequences of this asymmetry is a lift force in cross-stream direction (‘Magnus effect’: Magnus 1853). In terms of wake dynamics, cylinder rotation can lead to full suppression of the shedding motion for certain rotation rates (Mittal & Kumar 2003).

This thesis attempts to shed more light on how far the shape and motion of a nominally two-dimensional body influences its wake dynamics. As this is a very broad field, we limit the scope of this project to a carefully selected set of models and to one

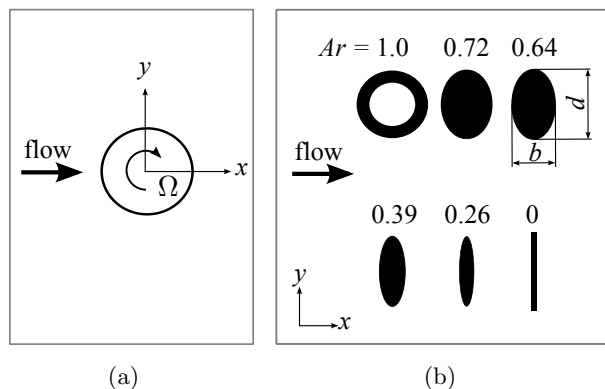


FIGURE II: The two model types studied in this thesis: (a) rotating circular cylinder; (b) elliptical cylinders, with the circular cylinder and normal flat plate as the limiting cases.

motion type. The pivot point of our experiments is the canonical circular cylinder, which offers an abundant amount of literature for validation. From this point, our research moves into two directions by modifying this canonical case twofold:

1. To investigate the role of motion, we spin the cylinder about its main axis at a constant angular velocity  $\Omega$  (figure IIa). In this set of experiments we are primarily interested in three-dimensional instabilities of the wake as a function of the dimensionless rotation rate  $\alpha$  (Rao *et al.* 2013), and the phenomenon of vortex suppression (Mittal & Kumar 2003; Kumar *et al.* 2011). The investigated parameter range is  $175 \leq Re \leq 275$  and  $0 \leq \alpha \leq 4$ .
2. To investigate the role of shape, we change the cross-section in a systematic way, by ‘flattening’ the circle into ellipses of decreasing aspect ratio  $Ar = b/d$ , obtaining a normal flat plate at the end of this process (figure IIb). As a result, the circular cylinder and the flat plate become limiting cases to a spectrum of general body shapes, in this case elliptical cylinders. It is expected that these cylinders will exhibit flow phenomena common to both limiting model types. By varying the ‘mix’ of the wake types (by varying the eccentricity / aspect ratio of the elliptical cylinders), we gain new insight into the wake dynamics of the two limiting cases. The investigated parameter range is  $100 \leq Re \leq 300$  and  $Ar = 1.00, 0.72, 0.64, 0.39, 0.26$  and  $0$ .

---

## Thesis structure

**Chapter 2:** A review of the relevant literature is conducted in order to assess the current state of knowledge and to highlight unanswered questions and gaps in the existing research. Practical issues associated with experimental research of two-dimensional bluff bodies are discussed.

**Chapter 3:** The experimental setups (for rotating and stationary cylinders) are introduced, followed by an outline of the experimental methods.

**Chapter 4:** Due to a modification of the existing water channel, an extensive validation study was carried out, which results are presented in this chapter.

**Chapter 5:** The results of experiments on the rotating circular cylinder are presented. Using PIV and digitally post-processed hydrogen bubble flow visualizations, we study several three-dimensional instability modes, some of which are observed experimentally for the first time.

**Chapter 6:** The elliptical cylinder wakes are studied using the hot film technique. The wake properties are compared to the circular cylinder and the flat plate wakes. The results suggest that, besides expected similarities, several new flow phenomena arise, including the ‘re-laminarized’ flow regime.

**Chapter 7:** An explanation is offered for the ‘re-laminarized’ regime. Studying the time-averaged flow field, the wake geometry and the dominant POD modes, it was concluded that the re-laminarization is a consequence of the appearance of the secondary vortex street.

**Chapter 8:** The overall conclusions of the thesis are presented.

**Appendix A:** An error analysis of the main parameters is carried out.

**Appendix B:** A short study of the used FFT algorithm is presented.

**Appendix C:** Flow fields of POD modes 0–5 of the elliptic cylinder wakes are included for completeness.



## Chapter 2

# Literature Review

### 2.1 Stationary circular cylinders

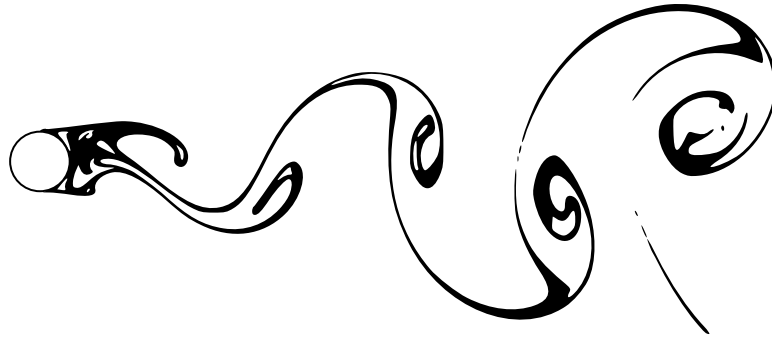


FIGURE 2.1: The von Kármán vortex street behind a circular cylinder. (Artistic representation based on Van Dyke 1982)

The flow about a circular cylinder is a canonical case of incompressible bluff body flows, and has been studied for over 100 years (Strouhal 1878; Bénard 1908; Kármán 1911). This model intrigues with its simple geometry and a straightforward experimental setup. Nevertheless, the flow around this simple object exhibits an astonishing variety of flow phenomena. The most famous flow pattern – partly due to its aesthetic appeal – is the von Kármán vortex street (figure 2.1). With the progress of fluid dynamics research, several flow regimes of the cylinder wake have been identified, which will be introduced in §2.1.1.

The flow regimes are determined by the non-dimensional Reynolds number:

$$Re = \frac{dU_\infty}{\nu}, \quad (2.1)$$

with cylinder diameter  $d$ , flow velocity  $U_\infty$  and kinematic viscosity  $\nu$ . The frequency  $f$  of the periodic velocity fluctuations in the vortex street is expressed by the Strouhal

number:

$$St = \frac{fd}{U_\infty}. \quad (2.2)$$

The dependence of the Strouhal number on the Reynolds number, and especially discontinuities in this relationship, are of great interest, as they are reliable indicators of transitions between wake regimes (Roshko 1993).

The exact transition Reynolds numbers and the appearance of associated wake regimes are very sensitive to experimental conditions. Cylinder roughness, freestream turbulence, aspect ratio of the cylinder, end conditions and blockage ratio can modify these values. Therefore, the Reynolds number ranges discussed hereafter should be treated as approximations of often gradual transitions, unless stated otherwise.

### 2.1.1 Wake regimes and three-dimensional instabilities

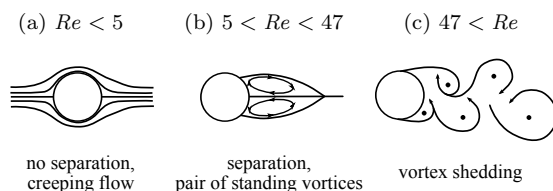


FIGURE 2.2: The wake of a circular cylinder develops several flow regimes for increasing Reynolds number.

$Re < 5$  At very low Reynolds numbers, the flow is dominated by viscosity and stays attached to the cylinder surface (figure 2.2a). This *creeping flow* is steady, and the streamline pattern is nearly symmetrical in the streamwise direction. This flow can be approximated by potential theory by a superposition of a uniform steady flow and a doublet (see for example Panton 2006).

$5 < Re < 47$  An increase of the Reynolds number above 5 leads to a steady and symmetrical flow separation from the cylinder surface (figure 2.2b). The separated shear layer rolls up into two symmetrical standing vortices downstream of the cylinder. The length of the mean recirculation region grows with increasing Reynolds number (Williamson 1996c).

$47 < Re < 180 - 190$  This Reynolds number range is often referred to as the *laminar shedding regime* (Williamson 1996b). Shortly before  $Re \approx 47$  is reached, the recirculation region becomes unstable to flow perturbations (Williamson 1996c; Dusek *et al.* 1994; Le Gal *et al.* 2001). The amplitude of the velocity fluctuations increases, and the point of maximum fluctuation intensity (marking the *formation length*) moves



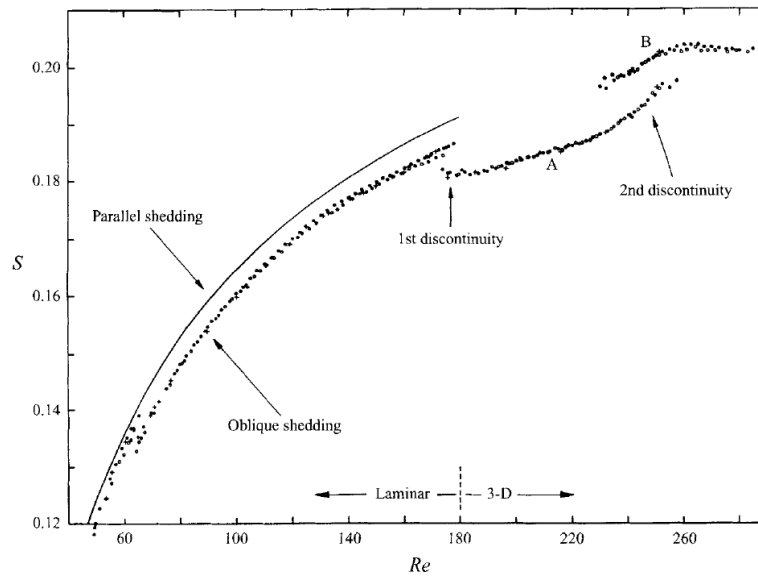


FIGURE 2.3: Strouhal-Reynolds number relationship of the circular cylinder wake in the laminar and transitional regimes. The curve is characterized by two transitions: The first at  $Re \approx 180$  is hysteretic and marks the transition to three-dimensionality and the appearance of the mode A instability. At the second transition, energy is transferred gradually from mode A to mode B instability (reproduced with permission from Williamson 1996b).

upstream towards the cylinder. Laminar two-dimensional vortex shedding sets in, during which spanwise vortices are released from alternate sides of the cylinder into the wake (figure 2.2c).

Roshko (1954) pointed out that the change at  $Re \approx 47$  is not a laminar-turbulent instability, but a transition between two different stable flows. In terms of nonlinear dynamics, the transition to a shedding state is a Hopf bifurcation (Jackson 1987; Dusek *et al.* 1994). It has been shown that a region of absolute instability in the near wake is necessary for vortex shedding to occur (Monkewitz 1988).

The upper Reynolds number limit of the laminar shedding regime shows a wide spread of  $Re$ , from 160 to 190. Numerical studies of the periodic two-dimensional wake, using Floquet analysis, suggest a value of  $Re = 188.5 \pm 1$  (Henderson & Barkley 1996). The reason for this discrepancy is premature transition caused by various ‘real-world’ effects which will be discussed in §2.1.3.

$180 - 190 < Re < 230 - 260$  This *transition regime* is characterised by two gradient changes of the  $St-Re$  curve. As seen in figure 2.3, the first change is an hysteretic discontinuity at  $Re \approx 180$ , which marks the amplification of three-dimensional disturbances. This leads to a periodic spanwise modulation of the primary vortices at a wavelength  $\lambda_z \approx 4d$  (Williamson 1988; Barkley & Henderson 1996). The three-dimensional

flow structures of this *mode A* instability initially consist of vortex loops, which are stretched between consecutive von Kármán vortices into counter-rotating streamwise vortex pairs. The loops possess an out-of-phase symmetry, meaning that consecutively formed vortices have opposite vorticity (see figure 2.4).

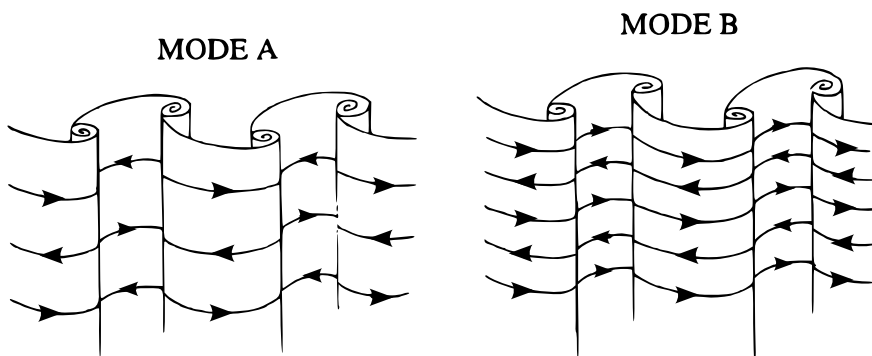


FIGURE 2.4: Symmetry properties of the secondary (streamwise) vortices of mode A and B. The vortices of mode A change their sense of rotation from one shedding cycle to the next, while consecutively formed vortices of mode B have equal vorticity. See figure 2.5 for a flow visualization of both modes (reproduced with permission from Williamson 1996c).

The *elliptic instability* of the von Kármán vortex cores has been suggested as a possible physical mechanism of mode A (Williamson 1996b; Thompson *et al.* 2001). This instability affects flows with elliptically shaped streamline patterns (Kerswell 2002; Leweke & Williamson 1998; Landman & Saffman 1987), which can be created by vortices exposed to strain fields, as happens in the von Kármán vortex street. Such flows can be modelled by a superposition of a two-dimensional base flow, a solid-body rotation and a potential stagnation-point flow (creating the strain field). The emerging instability shifts the vortex core periodically in the radial direction, leading to its wavy deformation. The axial wavelength scales on the size of the vortex core.

In the case of two parallel, counter-rotating vortices, an interaction between the vortices can take place. As has been shown by Leweke & Williamson (1998) and Meunier & Leweke (2005), the vortices influence each other and develop ‘cooperatively’. Unlike the large-scale Crow instability (Crow 1970), this *cooperative elliptic instability* leads to a short-wavelength deformation of the primary vortex cores with an antisymmetric phase relationship. Due to this deformation, each vortex pulls out ‘tongues’ of fluid from the other. These tongues are drawn around the vortices and stretched into counter-rotating secondary vortex pairs. These intensify and lead to the breakdown of the primary vortices.

Based on these experiments, Thompson *et al.* (2001) showed in numerical simula-

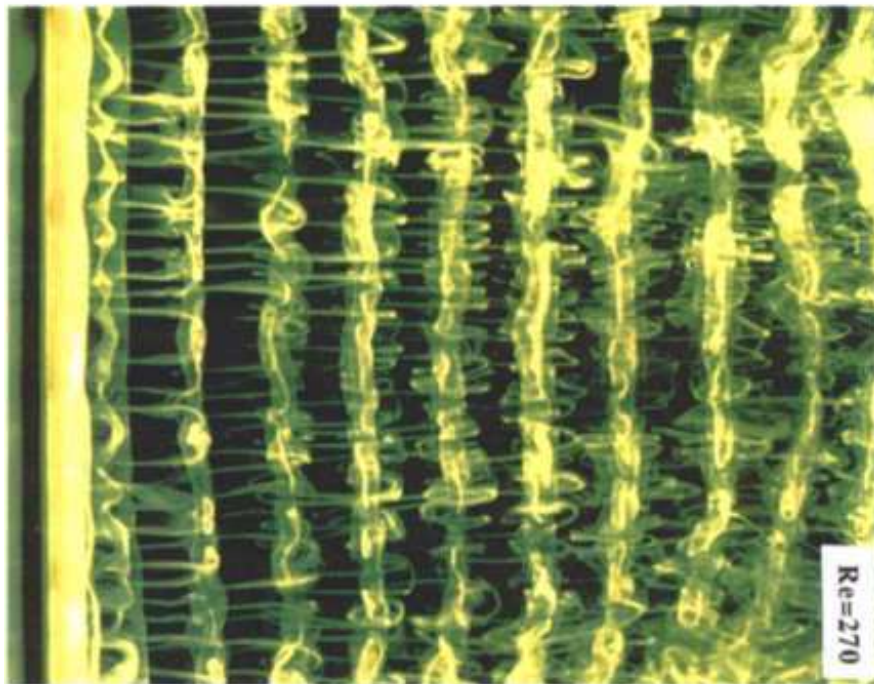
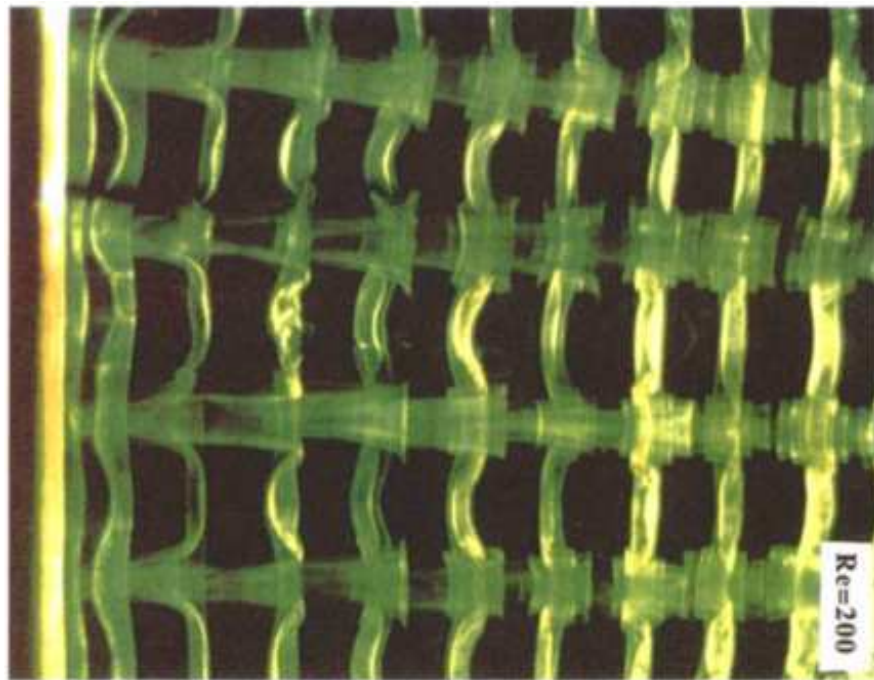


FIGURE 2.5: Flow visualisations of mode A at  $Re = 200$ , and mode B at  $Re = 270$ . The flow is from left to right (reproduced with permission from Williamson 1996c).

tions that a cooperative elliptic instability dominates the flow in the vicinity of cylinder, in the moment the von Kármán vortex cores are formed. Once the formation process is complete and the vortices detach from the cylinder, further amplification of spanwise perturbations takes place in the strained braid regions connecting these vortices. Thus, the elliptical instability determines only initially the spanwise wavelength of the disturbance, and much of the actual amplification takes place outside of the vortex cores.

In experiments, the transition regime is characterized by a phenomenon termed *vortex dislocations* (figure 2.6). First reported by Roshko (1954), large amplitude low-frequency irregularities of the velocity signal have been observed, caused by dislocations of the primary vortices (referred to as the *vortex adhesion mode* by Zhang *et al.* 1995). These dislocations are formed between spanwise cells of different frequency, when the primary vortices move out of phase with each other (Williamson 1992, 1996a; Prasad & Williamson 1997). Dislocations can be generated at the sites of the vortex loops of the mode A instability, and evolve spontaneously and intermittently along the span, independent of the cylinder end conditions. They grow and dominate the velocity fluctuation profiles in the wake and lead to a broadening of the peak in the measured velocity frequency spectrum (Braza *et al.* 2001). These large scale structures are not a consequence of (unfavourable) experimental conditions, but an intrinsic property of the transition regime, as has been confirmed by numerical simulations by Henderson (1997); Braza *et al.* (2001); Behara & Mittal (2010). Braza *et al.* (2001) showed that these structures lead to a drastic fundamental frequency reduction and amplitude modulation.

$Re > 230$  In this Reynolds numbers range, a new three-dimensional mode appears (Williamson 1988; Zhang *et al.* 1995; Barkley & Henderson 1996; Thompson *et al.* 1996; Wu *et al.* 1996; Henderson 1997), whose spanwise wavelength  $\lambda_z \approx 1d$  scales on the size of the braid shear layer between the primary von Kármán vortices. Williamson (1996b) argues that *mode B* is a result of a hyperbolic instability of the braid region (see Kerr & Dold 1994; Leblanc & Godefert 1999, for hyperbolic instability). Barkley (2005) showed that the development of mode B, and similarly of mode A, is confined to the flow just behind the cylinder. It can be concluded that the formation region of these three-dimensional modes spans only a few diameters downstream of the cylinder.

The streamwise vortex pairs of mode B exhibit a different spatio-temporal symmetry compared to mode A, by maintaining their orientation from one shedding half cycle to

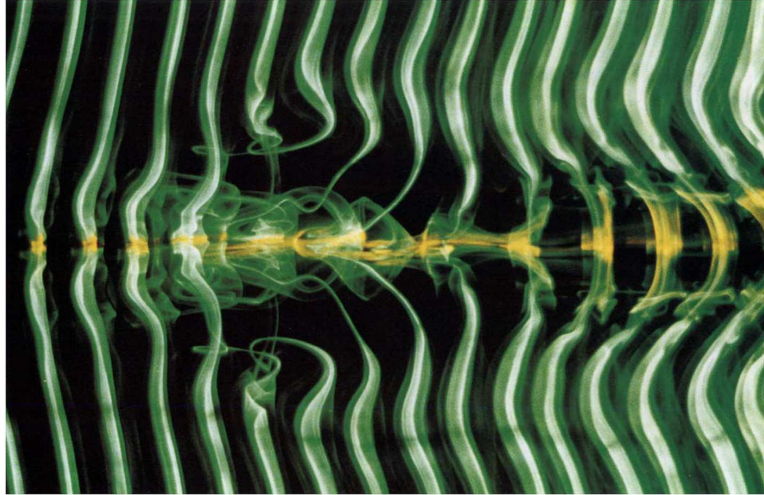


FIGURE 2.6: Flow visualisations of a (forced) vortex dislocation. The flow is from left to right (reproduced with permission from Williamson 1992).

the next (figure 2.4).

The appearance of mode B is noticeable in the  $St-Re$  diagram by the second rapid change of Strouhal numbers (figure 2.3). A gradual energy transfer from mode A to mode B takes place for  $Re = 230-260$  (Williamson 1996b; Thompson *et al.* 1996). It is assumed that these two modes do not exist simultaneously during this transition stage, but an intermittent swapping between the lower frequency and higher frequency mode takes place. This swapping leads to a broadening of the peak in the velocity frequency spectrum. Mode B is devoid of vortex dislocations and, therefore, of low-frequency modulations of the velocity-time signal (Behara & Mittal 2010).

Once the Reynolds number exceeds 260, mode B is the only detectable mode. Although the wake becomes increasingly irregular and disturbed at higher Reynolds numbers, traces of mode B are still detectable up to  $Re = 10,000$  (Wu *et al.* 1996). Poncet (2002) showed that mode B can be almost completely suppressed by a rotational oscillation of the cylinder up to  $Re = 500$ , recovering the laminar two-dimensional shedding regime.

Besides the modes A and B, which grow on the natural wake of a circular cylinder, a third mode has been observed. *Mode C* was reported by Zhang *et al.* (1995) for  $170 < Re < 270$ , when a thin control wire was placed close to the cylinder surface. The wavelength was  $\lambda_z/d = 1.7$  in simulations, and  $\lambda_z/d \approx 2$  in experiments. Sheard *et al.* (2003b, 2005) observed a subharmonic mode ( $\lambda_z = 1.9d$ ) in the wake of a torus aligned normal to the direction of flow (figure 2.7). Depending on the aspect ratio of the torus,

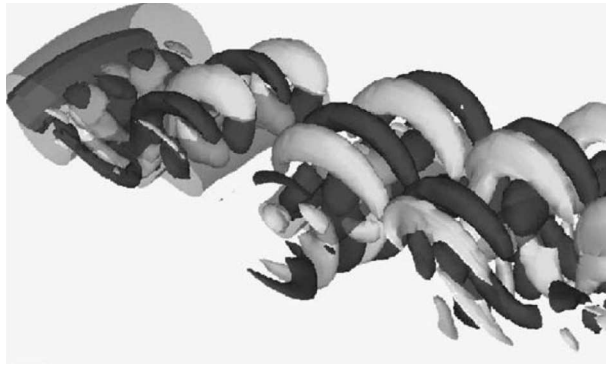


FIGURE 2.7: Perspective view of the subharmonic instability mode C on a large aspect ratio torus. The flow is visualized using iso-surfaces of positive and negative streamwise vorticity. The azimuthal wavelength is approximately  $1.7d$ , with  $d$  being the cross-section diameter of the torus (reproduced with permission from Sheard *et al.* 2004).

this mode became unstable at a Reynolds number lower than modes A and B.

The reason for the subharmonic nature of mode C is the broken spatial symmetry of the base flow. Placing a wire off-centre, close to the cylinder surface, breaks the planar reflective symmetry of the geometry and the spatio-temporal symmetry of the base flow. That latter symmetry corresponds to invariance on evolving the flow for half a period combined with reflection about the centre plane. In the case of flow past a torus, the otherwise infinite cylinder is curved to form a closed ring, which breaks the geometrical reflective symmetry, and this also breaks the spatio-temporal symmetry. Blackburn & Lopez (2003); Blackburn & Sheard (2010) showed that true subharmonic modes should not occur for flows with the half-period shift/reflection symmetry, such as the circular cylinder wake.

Yildirim *et al.* (2013b) reproduced and extended experiments by Zhang *et al.* (1995) by placing a thin control wire close to the circular cylinder. With help of time-resolved PIV and volumetric flow-visualizations it was shown that mode C leads to a period-doubling of the main shedding cycle, such that consecutive mode C structures are out of phase with the previous ones. This period-doubling phenomenon is due to a feedback mechanism between the consecutively shed upper vortices. The spanwise wavelength was confirmed to be approximately 2 cylinder diameters.

### 2.1.2 Vortex street breakdown and secondary street

Kármán (1911) modelled the cylinder wake as a double row of potential vortices infinite in both directions. The distance between the rows  $h$  and the spacing of the vortices in each row  $a$  are kept constant (figure 2.8). The theory shows that the configuration is

stable when the rows are staggered by a half wavelength and the *vortex spacing ratio* is

$$h/a = 0.281. \quad (2.3)$$

The real vortex street differs from the idealized one in the following points:

1. The street is not infinite.
2. The vortex spacing is not constant. In particular, the lateral spacing  $h$  increases downstream.
3. The real vortices have cores of finite radius, which grow in downstream direction.

Approximating the real flow, Saffman & Schatzman (1982) showed in a stability analysis that assigning a final core size to vortices in a von Kármán vortex street configuration, can stabilize the vortex array with respect to two-dimensional disturbances.

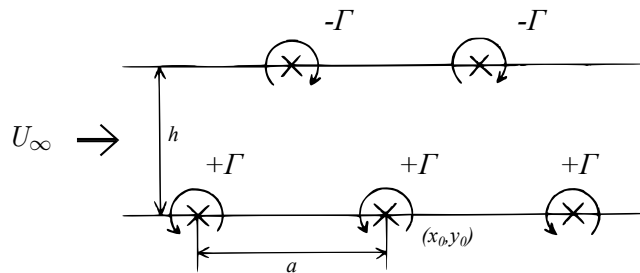


FIGURE 2.8: Schematic of the von Kármán vortex street geometry.

As predicted by theory, in real vortex streets, the vortices arrange themselves with a ratio of  $h/a \approx 0.28$ , at least in the near wake (Roshko 1954). The question arises how the vortex street decays at large downstream distances. The simplest mechanism is viscous diffusion of the vortex cores with cross-annihilation of vorticity (Morton 1984). If three-dimensional effects dominate the vortex evolution, which is the case at higher Reynolds numbers, Reynolds stresses are likely to destroy the vortex street at early stages and create a turbulent wake. Besides these effects, another mechanism has been reported.

Taneda (1959) observed that the primary von Kármán vortex street behind circular cylinders can become unstable as the distance from the obstacle increases, and finally breaks down. The dimensionless distance between the cylinder and the point of breakdown decreases consistently with a  $Re^{-1/2}$  power law (figure 2.9) (Vorobieff & Ecke 1999; Vorobieff *et al.* 2002). Thereafter, the wake tends to rearrange itself again

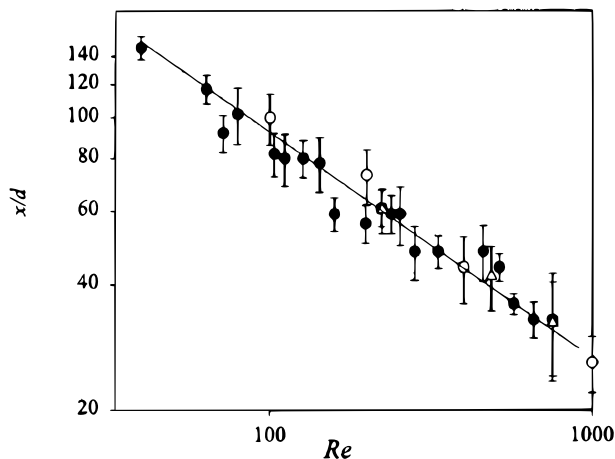


FIGURE 2.9: The streamwise distance between a circular cylinder and the onset of the second wake as function of Reynolds number. The solid line shows the best power-law fit to the data (exponent -0.51). The data were obtained in flowing soap film experiments (reproduced with permission from Vorobieff *et al.* 2002)

into a configuration of the von Kármán vortex street. The dimension of this *secondary vortex street* is much larger than that of the primary one. Two regimes were reported by Taneda (1959): when the Reynolds number was lower than about 150, the ratio of the wavelength of the secondary vortex street to that of the primary one was about 1.8 to 3.6, while it was about 10 when the Reynolds number was higher than about 150. The hydrodynamic stability (of convective type) of the mean wake velocity profiles was named as the reason for the appearance of the larger vortex street.

The amalgamation of shed vortices (vortex pairing) was excluded as a possible mechanism, as porous flat plates normal to the stream develop a similar secondary vortex street, even in the absence of the primary shedding (Castro 1971; Cimbala *et al.* 1988). Cimbala *et al.* (1988) predicted the shedding frequency of this oscillation by means of a locally parallel stability analysis of experimentally obtained mean velocity profiles. He concluded that “hydrodynamic instability in a far wake leads to the growth of downstream structure, the scale of which is determined by local wake properties; the far-wake structure is not dependent on the scale of shed von Kármán vortices – which for the case of a porous plate do not even exist”.

The geometric arrangement of vortices in the street determines its tendency for breakdown; the critical parameter being the ratio of the lateral to streamwise vortex spacing  $h/a$ . A ratio of  $h/a > 0.3-0.5$  is stated as the condition for the decay of the primary vortex street (Durgin & Karlsson 1971; Tsuboi & Oshima 1985; Karasudani & Funakoshi 1994). By artificially changing this ratio (increasing the lateral spacing



between the vortices), the primary vortex street can be annihilated prematurely, which is followed by a stationary wake and a new vortex street of larger scale (Durgin & Karlsson 1971).

The primary vortex street breaks down into a nearly parallel shear flow of Gaussian profile, before the secondary vortex street can develop downstream of this breakdown location (Karasudani & Funakoshi 1994). Durgin & Karlsson (1971) described the resulting shear flow as a region where no significant velocity fluctuations were observed ('calm region'). A model was suggested in which a vortex is strained into an elliptical shape by mutual induction of neighbouring vortices. This distorted vortex then rotates in the proper direction, approaching alignment of its major axis in the downstream direction. A region is reached where all vortices touch, or overlap, to the extent they become shear layers on either side of the wake. These shear layers are then unstable and give rise to the secondary vortex street. Figure 2.10 shows inviscid discrete vortex method simulations that illustrate this process. When  $h/a$  is small (0.31), the initial vortex regions remain isolated from each other. In contrast, when  $h/a$  is large (0.41), the vortex regions amalgamate to form a nearly parallel shear flow.

The question whether there is a more profound connection between far-wake structures and the near-wake dynamics was addressed by Williamson & Prasad (1993), who concluded that this link is formed via the sensitivity of the cylinder wake to the free-stream disturbances. It was found that the far wake is receptive to a combination frequency given by  $f_{FW} = f_K - f_T$ , where  $f_K$  and  $f_T$  are the von Kármán shedding frequency and the freestream frequency, respectively.

Global linear stability analysis of the time-averaged flow by Kumar & Mittal (2012) revealed the presence of convectively unstable modes just downstream of the primary vortex street breakdown. Beyond this region, a broad band of frequencies was selectively amplified, leading to the formation of a secondary vortex street consisting of packets of large-scale vortex structures. As these packets were advected downstream while they were growing, their detection was delayed to much further downstream locations. For  $Re = 150$ , the convective modes were most unstable at  $x = 30 - 60d$ , while the packets grew to detectable amplitudes only at  $x = 110 - 125d$ . When forcing with the frequency  $f_T$ , the secondary wake responded with the resonance frequency  $f_{FW} = f_K - f_T$ , which confirms the experimental findings of Williamson & Prasad (1993). Interestingly, a shallow trough was observed in the time averaged centreline velocity (at  $x = 46d$  for

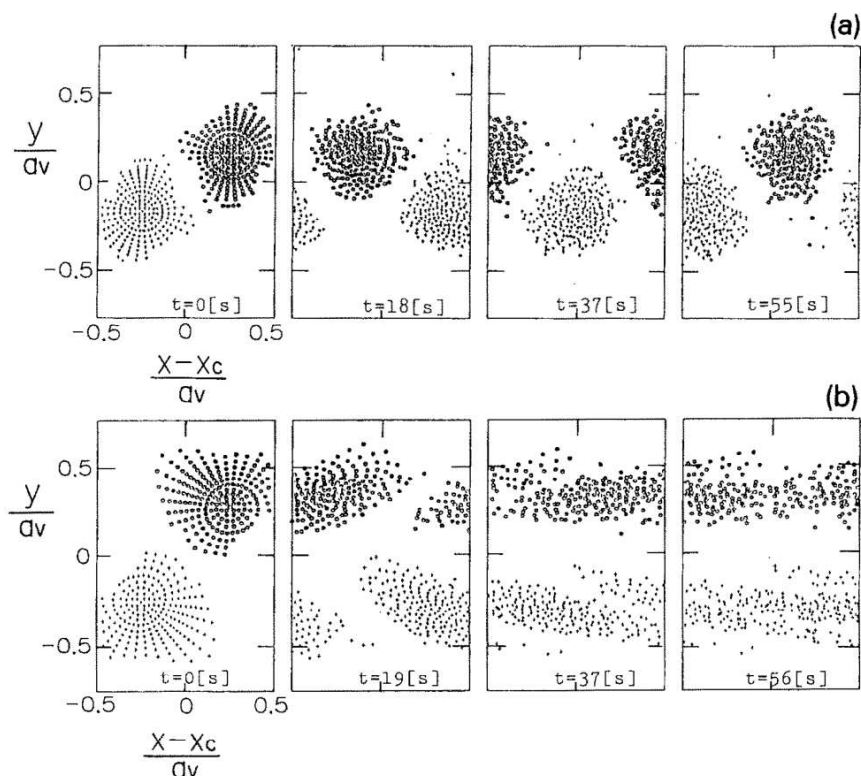


FIGURE 2.10: Evolution of vortex street composed of vortex regions each approximated by point vortices of the same strength. (a):  $h/a=0.31$ ; (a):  $h/a=0.41$ . +, positive vortices. o, negative vortices. (From Karasudani & Funakoshi 1994)

$Re = 150$ ), which might be related to local instabilities. Similar troughs have been observed in the present study in the wake of elliptical cylinders (§7.1). These were located considerably further upstream than in the circular cylinder case, which is a consequence of the smaller aspect ratio.

For cylinders with elliptical cross-sections, Johnson *et al.* (2004) showed that by reducing the ellipse aspect ratio  $Ar$  the onset of the secondary wake can be moved upstream. For  $Ar = 0.25$  and  $Re = 150$ , the fluctuation energy of the secondary wake oscillations exceeded the energy of the primary von Kármán street already at a downstream distance of  $x \approx 18d$ , implying an earlier appearance of the second wake.

Additional results can be found in Qu *et al.* (2013) and Inoue & Yamazaki (1999).

## 2.1.3 Experimental considerations

### 2.1.3.1 Control of end effects

As distinct from the theoretical ‘infinite’ cylinder, the flow in experiments is affected by finite aspect ratio effects (here ‘aspect ratio’ refers to the ratio of the spanwise length of the cylinder to its diameter). The three-dimensionality of the wake induced by end-

effects is referred to as *extrinsic*, whereas phenomena not associated with boundary conditions, such as modes A, B and vortex dislocations, are *intrinsic* three-dimensional effects (Roshko 1993).

The influence of aspect ratio and end effects were studied by Gerich & Eckelmann (1982); Eisenlohr & Eckelmann (1989); Williamson (1989) and Lee & Budwig (1991), who report a region at the cylinder ends ( $\approx 10 - 15d$  long) that is directly influenced by the end effects. The shedding frequency in this *affected region* is 10 – 15% lower than over the remaining cylinder length, which leads to a beat frequency at the junction points. For aspect ratios below  $l/d \approx 15$ , only the lower frequency is observed over the whole cylinder span. When increasing  $l/d$  above 45, the vortex shedding frequency in the central span becomes independent of aspect ratio (Williamson 1989), which implies that experimental results should be consistent for  $l/d > 45$ . In addition, there is evidence that the necessarily required length-to-diameter ratio of a cylinder is actually dependent on the Reynolds number (Norberg 1994). However, even for cylinder lengths of several hundred diameters, considerable spread in the measurement of shedding frequency exists (Lee & Budwig 1991).

This scatter was finally linked to *oblique shedding* (Williamson 1989). Without suitable boundary conditions, the von Kármán vortices are shed under an angle (up to  $20^\circ$ ) relative to the main cylinder axis, which leads to a lower measured Strouhal number. Once parallel shedding is enforced, the Strouhal numbers increase. The proposed formula for the laminar shedding regime

$$St_0 = \frac{St_\theta}{\cos(\theta)} \quad (2.4)$$

corrects the Strouhal number  $St_\theta$ , measured during oblique shedding under the angle  $\theta$ , to the value  $St_0$ , which would have been observed under parallel shedding conditions. Using this formula, the previously measured data collapse onto a single  $St-Re$  curve (this line is shown in figure 2.3).

Unlike the ‘affected region’ at the cylinder ends, oblique shedding is an indirect effect of the boundary conditions. Oblique shedding begins at the cylinder ends and propagates in the spanwise direction by induction, during the process of vortex shedding (Albarede & Monkewitz 1992). This is best seen when the cylinder is moved from rest in a XY towing tank (Williamson 1989). Within a traversing distance of  $100d$ , the vortices are shed parallel to the cylinder axis. Then, two *oblique fronts* propagate from the cylinder ends towards the centre plane. The oblique front is the division line

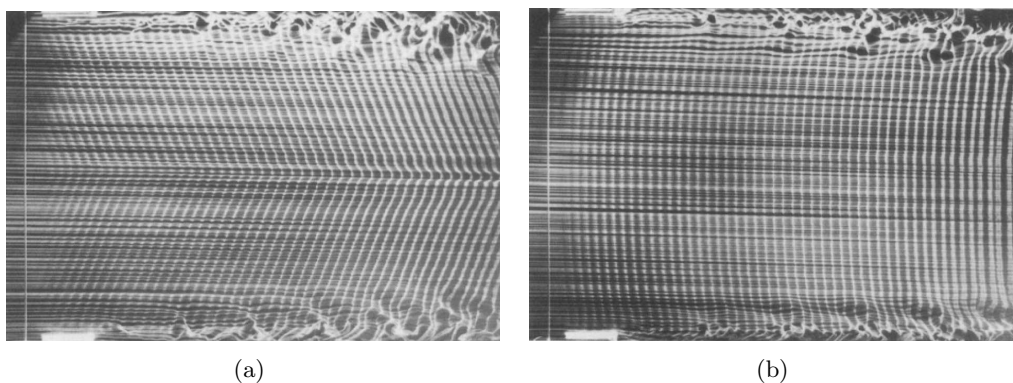


FIGURE 2.11: Control of boundary conditions of a circular cylinder using suction tubes. (a) ‘Chevron pattern’ as extreme form of oblique shedding. (b) Parallel shedding. The cylinder is the vertical line near the left edge, and the suction tubes can be seen at the top and bottom edges of the pictures, causing the bright reflections just behind the cylinder. The flow is from left to right (reproduced with permission from Miller & Williamson 1994).

between the oblique shedding region at the cylinder ends (having a lower frequency) and the parallel shedding region in the centre of the cylinder. After traversing a distance of  $500d$ , the whole cylinder span is contaminated with oblique shedding, which is the asymptotic end state. This end state is the only observable regime in a continuous flow water or wind tunnel. This way, disturbances can propagate through a ‘chain reaction’ along the span, making the end effects felt over the whole span, independent of the aspect-ratio of the cylinder.

There are several techniques that can prevent the decrease of Strouhal number and enforce parallel shedding. These include inwards angled end-plates (‘inclined end-plates’), ending the cylinder with larger coaxial cylinders, or placing larger cylinders upstream and normal to the test cylinder at its ends (Williamson 1996c). A non-mechanical and continuously variable technique by Miller & Williamson (1994) is used in the present study, which employs two suction tubes placed parallel to the flow at a distance of  $10d$  behind the cylinder ends (see figure 3.9 in §3.3). All mentioned techniques involve a speeding up of the incident flow at the cylinder ends, which is equivalent to a local increase of effective Reynolds number in that region (Albarede & Monkewitz 1992).

### 2.1.3.2 Blockage effects

The numerical study by Kumar & Mittal (2006) found that the non-dimensional vortex shedding frequency of a circular cylinder at the onset of the primary instability ( $Re_{c_0} \approx$

47) is very sensitive to blockage. For ratios  $0.005 < d/W < 0.125$  ( $W$  is the lateral width of the domain), the increased blockage damped out the low-frequency modes, giving way to higher frequency modes, effectively increasing the Strouhal number. Using the curve fit in equation 2.5, the Strouhal number at the onset of instability is expected to be increased by only 1% for the biggest blockage ratio  $B = 1/57$  in the present study. Similarly small changes can be expected in the advanced shedding regimes, as shown for  $Re = 100$  by Behr *et al.* (1995), where the variations were below 1% for domain widths larger than 32 diameters:

$$St_c = 0.116311 + 0.0403825B + 1.81145B^2 - 3.97608B^3. \quad (2.5)$$

The impact on the separation angle from the cylinder surface was explored by Ming-Hsun Wu *et al.* (2004), who found that the separation point moves upstream for higher blockage. Yet, this change was less than  $0.5^\circ$  during the shedding regime.

Due to these findings, no blockage correction will be applied to the data of the present study.

### 2.1.3.3 Wire disturbances

A thin platinum wire, aligned parallel to the main cylinder axis, is used in the present study for hydrogen bubble flow visualizations. The equivalent of this technique is the smoke wire in wind tunnels (Cimbala *et al.* 1988; Hammache & Gharib 1991). It is known that the wire can change the wake dynamics and can be used as a means of flow control (Choi *et al.* 2008; Strykowski & Sreenivasan 1990). Possible flow changes will depend on the position of the wire relative to the separating shear layers and the distance to the cylinder surface. Despite the fact that the thin wire does not create its own vortex street, the introduced vorticity can be sufficient to modify the vortex dynamics of the main cylinder.

Yildirim *et al.* (2010) showed that at  $Re = 100$  the primary effect of a wire (acting as a *control cylinder*), positioned in one of the separating shear layers, was the reduction of velocity fluctuations in the vortex formation region of the main cylinder. Additionally, the shedding frequency was reduced. The secondary effect was observed in the kinematics of the vortices, leading to a modified vortex arrangement and strength difference between the upper and lower vortices. The wake was deflected downward or upward, depending on the lateral position of the wire.

A more drastic effect, in form of full vortex suppression, can be achieved for  $Re < 100$ . For this purpose, the control cylinder is typically placed downstream of the main cylinder. The regions of maximum effectiveness are the separated shear layer and the wake centreline. The shape of these regions depends on the Reynolds number of the main cylinder and the diameter ratio of both cylinders (Strykowski & Sreenivasan 1990).

For higher Reynolds numbers, the control cylinder can modify the three-dimensional wake instabilities, as shown by Zhang *et al.* (1995). The transition from the laminar shedding regime to three-dimensional flow was delayed until  $Re = 220$  when a thin wire was placed in the centre plane, one diameter downstream of the cylinder. In addition, the three-dimensional mode C was excited when positioning the wire close to the cylinder surface, but off-centre at  $(x_w/d, y_w/d) = (0.75, 0.75)$ .

It can be concluded, that the hydrogen bubble wire should not be placed close to, and downstream of the cylinder in the present study. For most flow visualization purposes, the wire will be positioned upstream, at a distance of approximately  $5d$  from the model, to prevent wake interaction.

#### 2.1.3.4 Streakline effect

Flow visualisation techniques using tracer particles have inherent pitfalls, which might lead to a misinterpretation of the results. There are three major issues:

First: When a passive scalar (dye, smoke, hydrogen bubbles) is introduced into a flow where strong vortex stretching is present, its time evolution might not be identical to the evolution of vorticity. This is a result of the transport equation of vorticity  $\vec{\omega}$

$$\frac{\partial \vec{\omega}}{\partial t} = -(\vec{V} \cdot \nabla)\vec{\omega} + (\vec{\omega} \cdot \nabla)\vec{V} + \nu \nabla^2 \vec{\omega} \quad (2.6)$$

containing the term  $(\vec{\omega} \cdot \nabla)\vec{V}$ , which describes vortex stretching caused by local strain (Smits & Lim 2000), while this term is absent in the scalar transport equation:

$$\frac{\partial S}{\partial t} = -(\vec{V} \cdot \nabla)S + \kappa \nabla^2 S. \quad (2.7)$$

When a vortex filament is stretched, its vorticity increases, while the concentration of the passive scalar decreases. Under intense vortex stretching, the concentration of marker particles can decrease to such extent, that the still present vortex becomes not visible in flow visualization data. The conclusion is, that the absence of a passive scalar may not necessarily indicate the absence of vorticity.

Second: The diffusion time scales are determined by the diffusion coefficient of vorticity  $\nu$  and the diffusion coefficient of the passive scalar  $\kappa$ , with the ratio being the Schmidt number  $\nu/\kappa$ . If dye or smoke are used as tracer particles in water or air, respectively, this number is in the order of 1000. This means, that the tracer will follow the vorticity exactly only in the initial stages. In later stages of flow development the vorticity might have diffused due to the high viscosity coefficient, while the passive scalar is still present, and visible, giving the wrong impression of vortical flow. An impressive demonstration of this effect is given by Cimbala *et al.* (1988) for the wake of a circular cylinder.

Third: Tracer particles have a ‘memory’. A streakline pattern shows only a spatially integrated view of the flow field. It is the result of an accumulated distortion which the particles have undergone from the point of release. This makes the observed streakline pattern strongly dependent on the location where they have been introduced. To obtain a true representation of the flow structures, the marker particles should be introduced as close as possible to the zone of interest.

Finally, instantaneous streamlines patterns, e.g. as obtained from PIV vector fields, depend on the frame of reference of the observer (Perry & Fairlie 1974; Perry *et al.* 1982). Two observers moving with different velocities will see different patterns, which can make the identification of coherent structures ambiguous.

#### **2.1.3.5 Freestream turbulence**

The effect of freestream turbulence on the flow about a circular cylinder was investigated by Norberg (1987) for Reynolds numbers 50 to 200,000 for grid-generated (approximately homogeneous) turbulence of low intensity ( $Tu \approx 1.4\%$ ). It was found that for  $Re < 1000$ , the main flow properties (Strouhal number, mean and r.m.s. pressure coefficients) are rather insensitive to an increase of turbulence intensity. In this range, which is particularly relevant to the present study, the large relative scales of turbulence result in a quasi-stationary flow. Still, large-scale velocity fluctuations cause a local variation of Reynolds number, which can lead to premature transitions for mean Reynolds numbers close to a critical value. Furthermore, the spanwise coherence of three-dimensional modes will be disrupted by increased turbulence.

## 2.2 Elliptical cylinders and normal flat plates

### 2.2.1 Elliptical cylinders

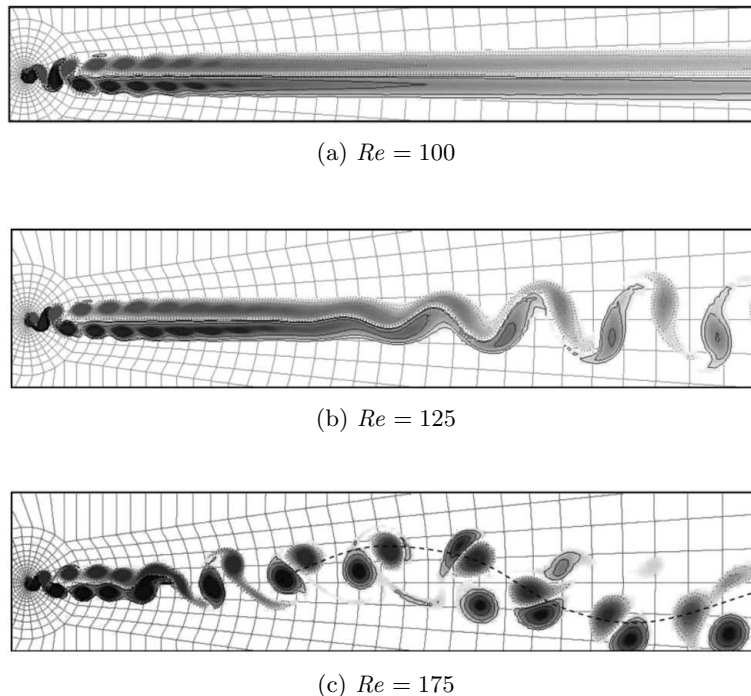


FIGURE 2.12: Decay of the primary von Kármán vortex street and the development of the secondary street of larger scale downstream of the  $Ar = 0.25$  elliptic cylinder. The onset of the secondary street moves upstream for higher Reynolds numbers. The 2D numerical simulations show the presence of a third wake frequency at  $Re = 175$ , which is indicated by the dashed line in (c). The flow is from left to right. (Reproduced with permission from Johnson *et al.* 2004)

There has been significantly less research on elliptical cylinders than on circular cylinders or the flat plate. In most investigations, this body shape has been studied either at very high Reynolds numbers (Modi & Wiland 1970; Modi & Dikshit 1975; Ota *et al.* 1987), or under Stokes flow conditions (Shintani *et al.* 1983). In the majority of cases, the main axis of the ellipse was aligned in the streamwise direction, or at an angle of attack  $\neq 90^\circ$ , such as in Mittal & Balachandar (1995).

For elliptical cylinders normal to the flow, Jackson (1987) showed that the critical Reynolds number for the onset of vortex shedding decreases from  $Re_{c_0} = 45.4$ , for  $Ar = 1$ , to  $Re_{c_0} = 27.7$ , for the flat plate.

Only recently, research work has been extended to the transitional Reynolds number regime. The numerical simulations by Johnson *et al.* (2004) investigated the effect of aspect ratio  $Ar$  variation on the far wake at Reynolds numbers  $75 \leq Re \leq 175$ . A low



frequency modulation of the wake velocity signal was found for certain combinations of  $Ar$  and  $Re$  (figure 2.12). Several flow regimes were defined, depending on the interaction of these secondary flow structures with the primary von Kármán vortices. The low frequency was not a subharmonic of the main shedding frequency, and was attributed to an instability of the mean velocity profile. The saturation point for these structures moved upstream, closer to the cylinder with increasing Reynolds number and decreasing aspect ratio.

A similar observation was made by Alekseyuk *et al.* (2012) in 2D simulations, who showed that an elliptical cylinder ( $Ar = 1/10$ ) normal to the flow undergoes the sequence of von Kármán vortex street formation, vortex street decay and the formation of a secondary vortex street of larger dimensions. Unlike the circular cylinder, the decay of the primary and the formation of the secondary vortex streets take place close to the cylinder, within 40 cylinder diameters at  $Re = 100$ .

Apart from this knowledge, no further literature could be found on the existence of three-dimensional modes for the proposed Reynolds number range and cylinder orientation.

### 2.2.2 Normal flat plates

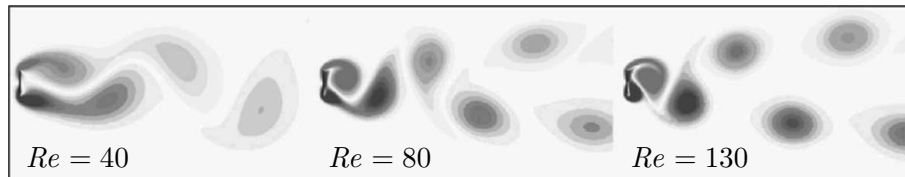


FIGURE 2.13: Two-dimensional grey-scale vorticity contours showing the shedding pattern for flow past a normal flat plate. The characteristic von Kármán wake is replaced by a wake consisting of two rows of vortices offset from the wake centreline as the Reynolds number is increased from  $Re = 40$  to 80 and 130 (reproduced with permission from Thompson *et al.* 2006).

The first extensive study of the normal flat plate wake was undertaken by Fage & Johansen (1927), who used a hot wire to measure mean and fluctuating velocity profiles, and to determine the vortex spacing geometry. Jackson (1987) determined the critical Reynolds number for the onset of vortex shedding as  $Re_{c_0} = 27.7$ , with  $St_C = 0.124$ , whereas Saha (2013) reports a higher value of  $Re_{c_0} = 32.45 \pm 0.1$ . For increasing Reynolds numbers, the characteristic von Kármán wake is displaced by a wake consisting of two sets of vortices offset from the wake centreline, as seen in figure 2.13.

The three-dimensional instabilities of the normal flat plate wake are largely unexplored, although it has been shown in numerical studies that three-dimensional effects are essential for the accurate prediction of aerodynamic coefficients, such as lift and drag (Tafti & Vanka 1991; Najjar & Vanka 1995a,b; Mittal & Balachandar 1995). The consensus is that the flat plate wake remains two-dimensional until  $Re \approx 200$ , after which a short-wavelength mode develops (Saha 2007; Najjar & Vanka 1995b). This mode has a spanwise wavelength  $\lambda_z/d = 1.2$  at  $Re \geq 250$ , which is comparable to mode B of the circular cylinder (Najjar & Balachandar 1998).

Yet, the absence of three-dimensional modes for  $Re < 200$  appears questionable. Thompson *et al.* (2006) report two three-dimensional modes being linearly unstable in the periodic 2D wake: The first mode becomes unstable at  $Re \approx 105 - 110$  with a spanwise wavelength of  $5-6d$  (with  $d$  being the plate height). It has a complex Floquet multiplier (quasi-periodic flow), and the period of this mode is not commensurate with the base flow period. The mode is strong close to the rear of the plate, but decays rapidly with downstream distance.

The second mode has a dominant wavelength of  $2d$  and becomes linearly unstable at  $Re \approx 125$ . This shorter wavelength mode has the same spatio-temporal symmetry as mode A of the circular cylinder. In addition, there is strong evidence of elliptical instability in the vortex cores, consistent with mode A. A mode with this wavelength was observed by Yang *et al.* (2012) in the wake of an inclined ( $25^\circ$ ) plate up to  $Re = 350$ .

The normal flat plate wake exhibits a low-frequency unsteadiness in the drag and lift coefficients for  $Re > 250$ , accompanied by a low-frequency modulation of the shedding frequency with a period of approximately 10 times the primary shedding period (Lisoski 1993). Najjar & Balachandar (1998) propose a physical interpretation, showing that the flow gradually varies between two different regimes: a regime H of high mean drag, and a regime L of low mean drag. The regimes are a result of a phase mismatch / imbalance of 3D and 2D structures. In regime H, the shear layer rolls up closer to the plate to form coherent spanwise vortices, while in regime L the shear layer extends farther downstream, and the rolled-up von Kármán vortices are less coherent.

Similarly to the circular and the elliptic cylinders, the flat plate wake develops a secondary vortex street after the decay of the primary street (Taneda 1959; Saha 2007). This process is shown in figure 2.14 for a flat plate moving at  $Re = 8150$ . Again, the second wake was contributed to a hydrodynamic instability of the mean

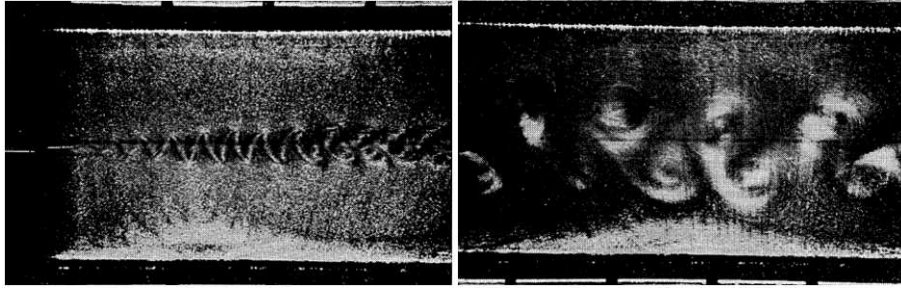
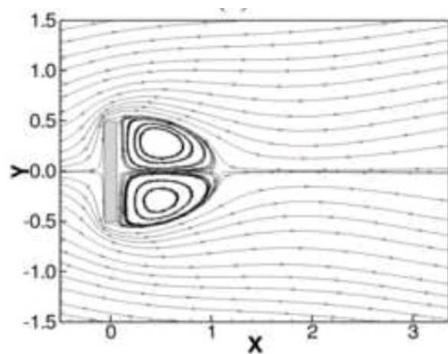


FIGURE 2.14: Formation of the secondary vortex street is shown for a normal flat plate in a towing tank at  $Re = 8150$ . Oscillating wake immediately behind the flat plate (left). Secondary vortex street about 200 cm to 240 cm behind the model (right) (reproduced with permission from Taneda 1959).

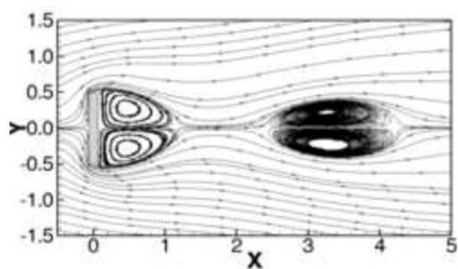
wake profile. This is supported by reports of a low-frequency oscillation of the wake behind perforated flat plates (Castro 1971). Above a certain porosity value, the primary vortex street is suppressed and the flow around the plate itself is essentially steady. Farther downstream, the two shear layers (with the bleed air in between) coalesce, and the turbulent wake is unstable and starts to ‘flap’. This observation excludes vortex pairing as a mechanism for the formation of the larger vortices.

The time-mean flow field of the flat plate shows a feature absent in circular or elliptical cylinder flows. Saha (2013) described an additional pair of recirculating bubbles downstream of the primary recirculation region at  $Re \geq 150$  (figure 2.15). The strength and size of the secondary bubbles were found to increase with increasing Reynolds number; and the bubbles shifted upstream. These bubbles led to an extensive low-velocity region in the time-averaged streamwise velocity profile along the wake centreline, followed by a rapid velocity recovery along the downstream direction. No explanation for this phenomenon was offered, but it was stated that the higher entrainment in the near-wake and slow moving fluid downstream of the primary recirculation region may be responsible for the formation of these bubbles. It should be noted that the flat plate in this 2D simulation had a thickness of 12.5%, which lies between the flat plate model ( $Ar = 0.07$ ) and the  $Ar = 0.26$  elliptic cylinder used in the present study.

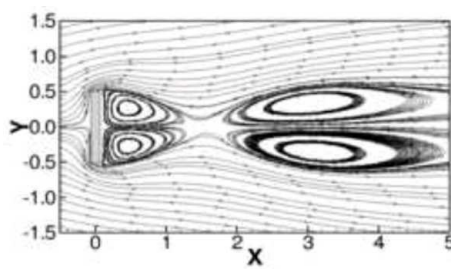
Additional studies on this subject can be found in Narasimhamurthy & Andersson (2009); Khaledi *et al.* (2012); Afgan *et al.* (2013); Han *et al.* (2012).



(a)  $Re = 125$



(b)  $Re = 150$



(c)  $Re = 175$

FIGURE 2.15: Additional pair of recirculating bubbles downstream of the primary recirculation region in the time-averaged flat plate wake. The flow is from left to right (republished with permission of the American Society of Civil Engineers from Saha 2013, permission conveyed through Copyright Clearance Center, Inc.)

## 2.3 Rotating circular cylinder

As mentioned in the introduction, vortex shedding can lead to structural vibrations, which can resonate with the shedding body and lead to structural failure. Due to such critical engineering applications, there have been attempts at controlling the wake of bluff bodies with the explicit aim of vortex shedding suppression.

One active flow control technique is the rotation of a circular cylinder about its main axis at a constant or alternating rate. When mounting rotating cylinders on bluff bodies, drag reduction and suppression of vortex-induced oscillations can be achieved (Modi 1997). In this thesis, the fundamental fluid dynamics of a rotating cylinder in cross-stream are studied.

When rotating the cylinder about its main axis, the non-dimensional rotation rate

$$\alpha = \frac{\Omega d}{2U_\infty} \quad (2.8)$$

becomes the second control parameter besides  $Re$ , where  $\Omega$  is the constant angular velocity,  $d$  is the cylinder diameter and  $U_\infty$  is the freestream velocity. Note the scaling is such that the surface speed of the cylinder matches the freestream flow speed when  $\alpha = 1$ .

The effect of rotation rate on the two-dimensional base flow is well-investigated. It is known that the wake shedding frequency is a function of the rotation rate (Stojković *et al.* 2003), and that shedding can be suppressed altogether if the rotation rate is sufficiently high. This vortex shedding suppression has been demonstrated in two-dimensional computations by Mittal & Kumar (2003) for  $Re = 200$ , and rotation rates  $0 \leq \alpha \leq 5$ . For  $\alpha < 1.91$ , the von Kármán vortex street was observed. For increasing rotation rates, it became narrower, and was deflected in the cross-stream direction. Shedding ceased beyond  $\alpha \approx 1.9$ , and the wake became steady.

When increasing  $\alpha$  further, the wake becomes unstable again for a narrow range of rotation rates. Depending on Reynolds number, the wake resumes shedding at  $\alpha = 4-5$  (Stojković *et al.* 2003; Mittal & Kumar 2003; El Akoury *et al.* 2008; Kumar *et al.* 2011), but at a much lower frequency (referred to as the *second shedding mode* or *mode II*). For these rotation rates, the shed vortices are of same sign, indicating an underlying physical mechanism different to that of the typical von Kármán wake (Pralits *et al.* 2010).

The described behaviour was confirmed experimentally by Kumar *et al.* (2011), who

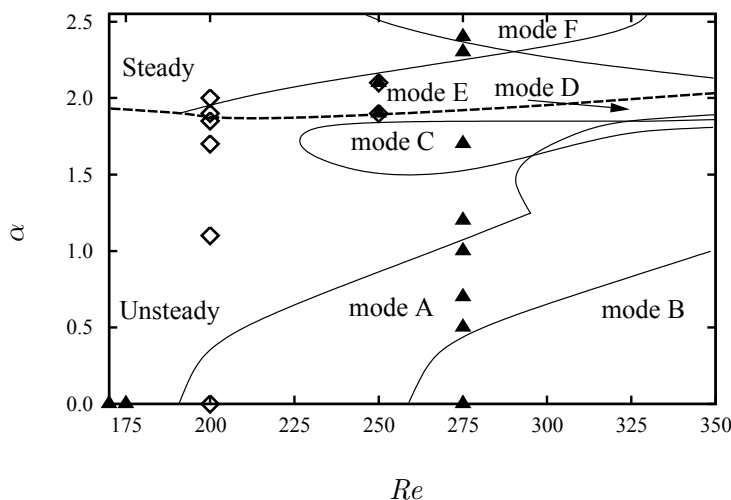


FIGURE 2.16: Diagram showing the lines of marginal stability in the parameter space for  $0 < \alpha < 2.5$  and  $170 < Re < 350$ . The steady-unsteady transition is marked by a dashed line. The solid lines indicate the marginal stability curves for modes A–F. The points in the  $\alpha - Re$  parameter space where experiments were carried out are marked by symbols: diamonds for PIV and triangles for flow visualisation.

observed the decay of vortex shedding at  $\alpha \approx 1.9$ , and its one-sided reappearance at  $\alpha \approx 4.4$ . We will use aspects of that study for comparison and partial validation of our experimental setup in §5.2.2.

Much less knowledge exists on the three-dimensional aspects of wakes of rotating cylinders in free-stream. For high rotation rates, the flow becomes susceptible to the centrifugal instability, as reported by Mittal (2004) for  $Re = 200$  and  $\alpha = 5$ . Centrifugal instability was observed along the entire cylinder span as a row of closed vortex loops, encircling the cylinder surface. Nevertheless, the wake remained steady for the parameter pair investigated.

For a low rotation rate of  $\alpha = 0.5$ , El Akoury *et al.* (2008) describe a three-dimensional instability at  $Re \geq 220$ . The structure and wavelength of this mode suggest that it is essentially mode A. The rotation of the cylinder has a stabilizing effect on the flow, increasing the critical Reynolds number of this mode to 220.

The most extensive study on the three-dimensional stability of spinning cylinder wakes was performed by Rao *et al.* (2013). Using linear (for the steady flows) and Floquet (for the periodic flows) stability analyses several new three-dimensional modes were predicted, which are distinctly different from the well known modes A and B. The findings of this numerical study will be discussed in more detail to explain the motivation behind the experiments of chapter 5. We seek to confirm the existence of

the predicted modes, and to explore their possible interaction in the fully developed nonlinear state. The  $(Re, \alpha)$  parameter map of figure 2.16 will be used as a guide.

Figure 2.16 shows the core results of Rao *et al.* (2013) in form of neutral stability curves in the  $(Re, \alpha)$  parameter map. The map is divided into two regions by the roughly horizontal dashed line through  $\alpha \approx 2$ . For rotation rates of the lower region, the wake resembles the von Kármán vortex street with periodic shedding, whereas it is steady for rotation rates above the dividing line.

The three-dimensional transition scenario is similar to that of the non-rotating cylinder for low rotation rates of  $\alpha < 1$ . The two unstable modes are modes A and B, whose critical Reynolds numbers increase with increasing rotation rates. However, for  $\alpha > 1$  the three-dimensional scenario becomes increasingly complex, with three new modes identified that bifurcate from the unsteady flow, and two modes that bifurcate from the steady flow.

The first new mode, mode C (figure 2.17a), becomes unstable in a closed region of the  $(Re, \alpha)$  plane, centred around  $Re = 260$  and  $\alpha = 1.7$ . The mode grows with a spanwise wavelength of  $\lambda_z/d \approx 1$ , and has a purely real but negative Floquet multiplier. This means that this mode is subharmonic, repeating over two cycles of the base flow. We will confirm this property experimentally, yet show that mode C also exists outside of its linearly unstable region, at rotation rates as low as  $\alpha = 1$ . This surprising observation will be discussed in §5.3.1.

Equivalents of mode C have been reported in the non-rotating cylinder wake when a thin control wire was placed close to the cylinder surface (Zhang *et al.* 1995; Yildirim *et al.* 2013b), and in the wake of a torus aligned normal to the direction of flow (Sheard *et al.* 2003b, 2005). These examples are characterized by the broken spatial symmetry of the base flow, which also applies to the rotating cylinder wake. Blackburn & Lopez (2003); Blackburn & Sheard (2010) showed that broken symmetry is a necessary condition for a subharmonic mode to appear.

In Yildirim *et al.* (2013b) mode C is described as vortex loops that originate from the upper von Kármán vortex. These vortex loops are further stretched in the braid region and roll up to form streamwise vortex pairs from the sides of the loops. They are located between the upper and lower vortices and affect the near-wake vortex shedding process. Besides, it is shown that mode C instability exhibits feedback of streamwise vortices between the upper primary vortices only, which is contrary to the natural

instability modes A and B. In mode C, the vortex loops are generated at the same spanwise position every two cycles.

Mode D (figure 2.17b) becomes unstable in the narrow region between the top boundary of mode C and the steady – unsteady transition of the two-dimensional base flow, at approximately  $\alpha = 1.95$ . The mode grows with a characteristic spanwise wavelength of approximately  $2d$ . When the rotation rate is increased beyond  $\alpha = 2$ , shedding ceases, and the wake becomes steady. Mode D is replaced by mode E (figure 2.17c), with the wavelength remaining unchanged. Perturbation vorticity plots in Rao *et al.* (2013) show that both modes grow in the region between the highly strained standing vortices in the wake, suggesting the hyperbolic instability as a plausible explanation for both modes. Experimental results on modes D and E will be presented in §5.3.3.

Linear stability analysis predicts a second three-dimensional mode on the steady base flow, termed mode F (figure 2.17d). It grows at higher rotation rates ( $\alpha > 2.25$ ), with a wavelength of  $0.45d$ . This mode exists primarily in the wall-bounded shear layer of the spinning cylinder, and in the near wake, pointing to a centrifugal instability as its origin. The Floquet multipliers for this mode occur in complex conjugate pairs. This indicates that, while the two-dimensional base flow is steady, transition to this mode marks a transition to three-dimensional flow and the onset of time dependence. This observation will be confirmed by our experimental results presented in §5.3.4.

This section has presented only a short overview of the modes described in Rao *et al.* (2013), and we refer the reader to the original paper for an in-depth discussion of mode characteristics and proposed physical mechanisms. For easier comparison with numerical predictions, the  $(Re, \alpha)$  map of figure 2.16 has been annotated with symbols showing the parameter pairs investigated experimentally. Figure 2.17 shows modes C–D as reported by (Rao *et al.* 2013).



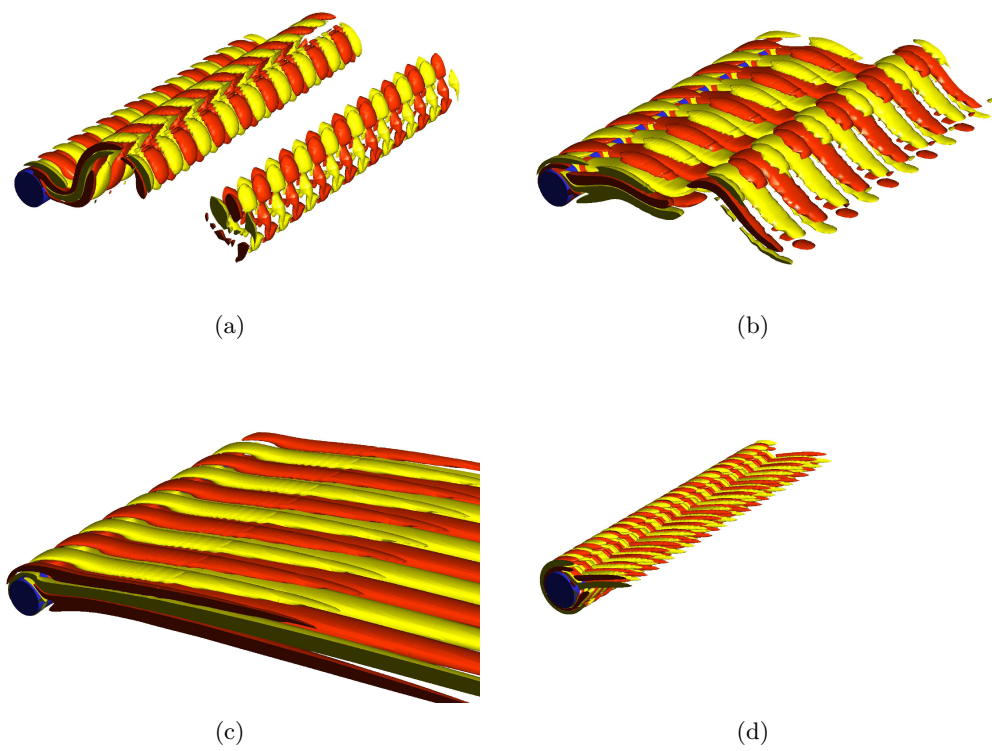


FIGURE 2.17: Modes C, D, E and F (a–d, respectively) from the stability analysis of Rao *et al.* (2013) are shown as iso-surfaces of streamwise vorticity (private communication).



## Chapter 3

# Experimental setup & numerical tools

### 3.1 The tunnel facility

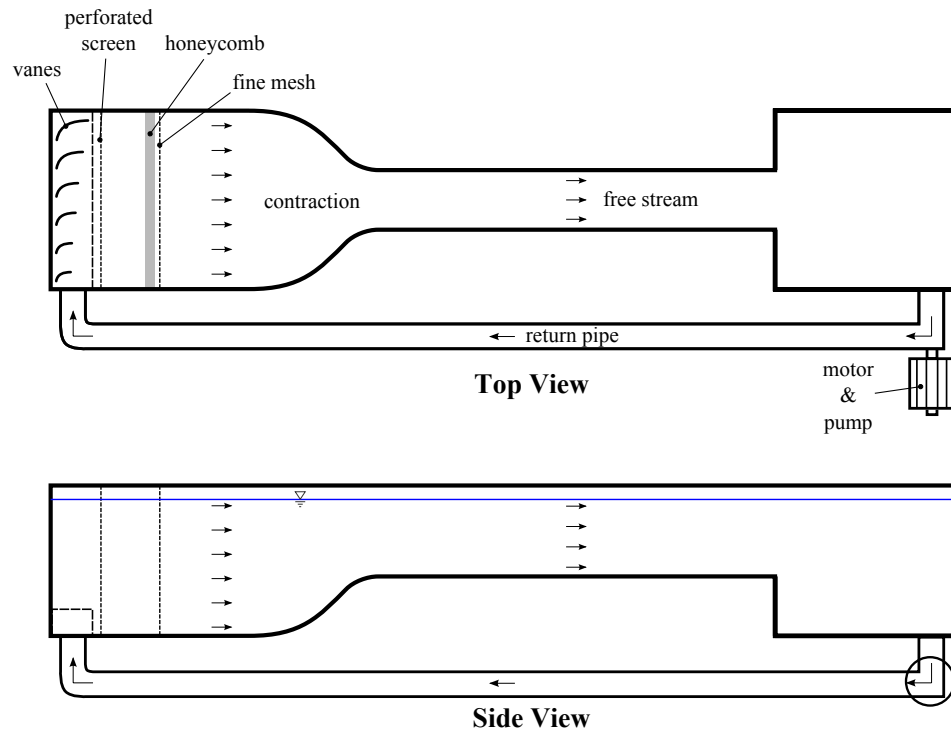


FIGURE 3.1: Schematic views of the water channel. (Figure is courtesy of Dr. Jisheng Zhao)

The experiments were performed in the FLAIR open surface water channel. Its test section is 0.6 m wide and 4 m long, with a water depth of 0.77 m. The velocity range is  $0.05\text{--}0.5\text{ ms}^{-1}$  with a freestream turbulence level below 1.5%, except for very low pump settings, when the fluctuating  $x$ -velocity component increases again (see LDV measurements in figure 3.1). In the present study, a pump setting of 5 Hz translates to a Reynolds number of approximately 100.

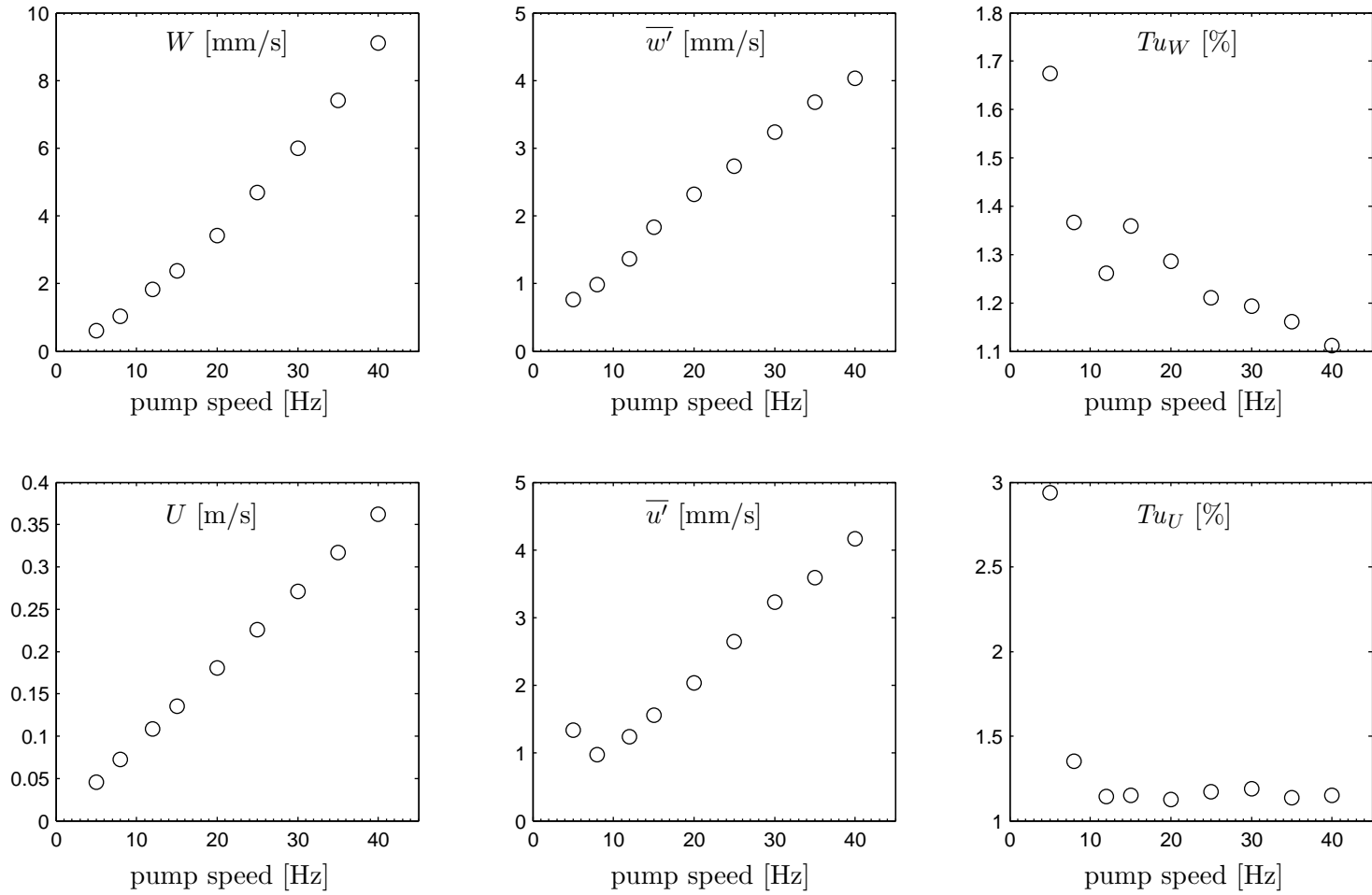


FIGURE 3.2: Average and fluctuating velocities in the centre plane of the empty water channel test section.  $U$  is the streamwise and  $W$  the vertical velocity component.

The turbulence spectrum is dominated by streamwise sloshing of the water with a frequency of 0.1 Hz. This frequency is about five times smaller than the cylinder shedding frequency over the range of tunnel speeds used for all experiments. Filtering out this component results in a background turbulence level of approximately 0.5%.

All coordinates and directions used in the following chapters refer to a right-hand Cartesian system, in which the  $x$ -axis is aligned with the oncoming flow, the  $y$ -axis points in the cross-stream direction, and the  $z$ -axis coincides with the cylinder axis (pointing upwards).

### 3.2 Rotating cylinder

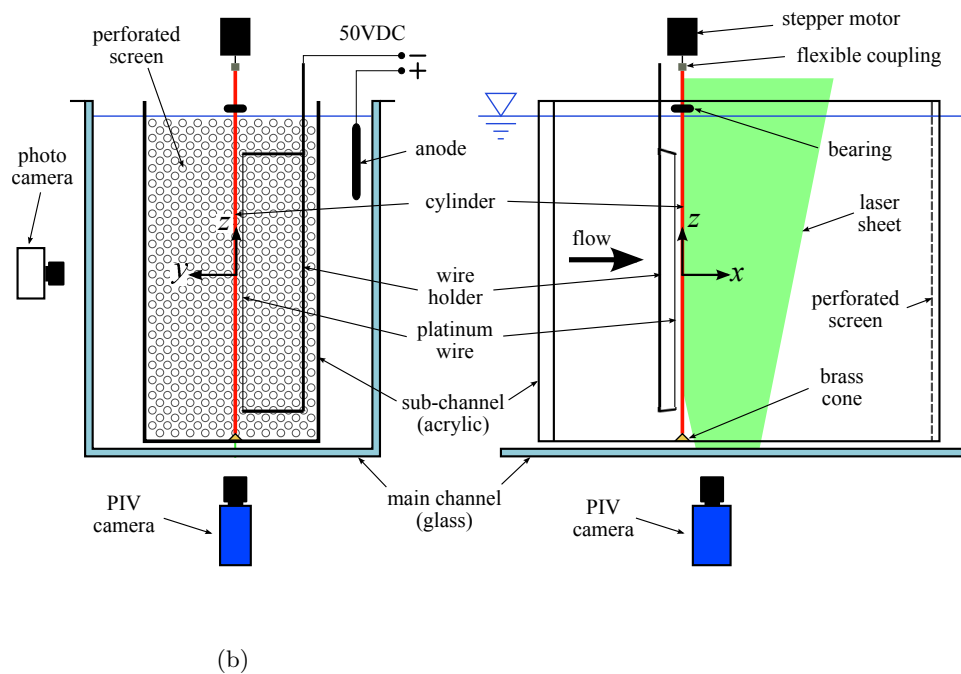


FIGURE 3.3: Schematic of the setup for the flow visualization experiments. (a) View downstream; (b) Side view. Perforated screen holes are not to scale.

The rotating cylinder model was mounted vertically in the centre plane of the sub-channel (see chapter 4 for a description of the sub-channel), positioned one third downstream of its entrance. The hollow shaft of an archery arrow of  $5.82 \pm 0.01$  mm outer diameter, and 800 mm length was used. These arrows are designed for Olympic competition, which effectively guarantees a high degree of straightness and stiffness. The wall material was carbon fibre, with an aluminium mantle and a smooth enamel finish. With a solid blockage of just 1.6%, no velocity correction was performed on the collected data. The cylinder rotation was driven directly by a stepper motor, whose

rotation rate was monitored by an optical encoder, and was typically within 0.5% of the target value.

The end conditions were the channel floor at bottom and the free water surface at top. This resulted in an aspect ratio (wetted length to cylinder diameter) of 130. The cylinder was fixed at two points. The upper fix point was an aluminium sting with two steel bearings, mounted above the water surface (figure 3.4). The cylinder model was electrically insulated from the stepper motor to reduce corrosion of the model's aluminium mantle. The lower end of the cylinder spun on a brass cone, which was fixed to the tunnel floor. The cone proved to be superior to a second (plastic) bearing, as it assured less play at the lower end, which resulted in less wobbling of the cylinder. The stepper motor was attached over a flexible aluminium coupling directly to the model. A Motion Control 6K2 controller was used to drive the stepper motor.

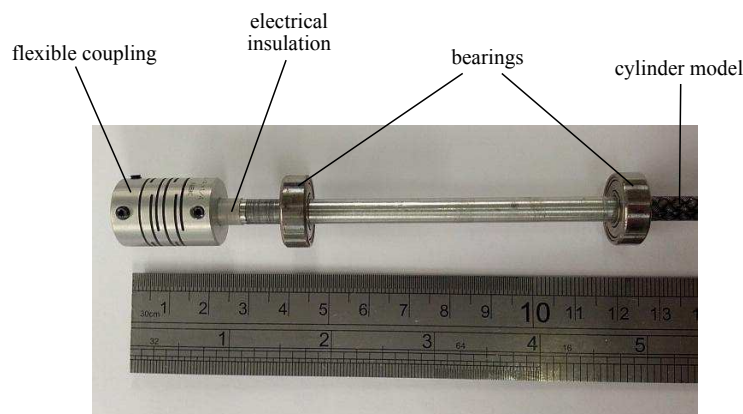


FIGURE 3.4: The upper mounting sting of the rotating cylinder model. The flexible coupling connects to the stepper motor.

To quantify its eccentricity of rotation ('wobbling'), the cylinder was spun in its final configuration outside the water channel, and the deflection was measured with a mechanical deflection gauge at several points along its axis (figure 3.5a). It was found that the deflection distribution is bow-shaped, with minimum deflection amplitudes close to the cylinder's two fixed points, and maximum amplitudes at the mid-length of the cylinder. Here, the largest measured half-amplitude was less than 0.15 mm, equivalent to 2% of the cylinder diameter (figure 3.5b). Moderate amplitudes of up to 5% of cylinder diameter can be assumed acceptable, since according to Mittal (2001), who investigated the eccentric cylinder rotation numerically (for  $\alpha = 5$ ), amplitudes between 0.005 and 0.05 $d$  do not change the mean flow. Thus, the two-dimensional wake flow can be assumed to be relatively insensitive with respect to disturbances caused by

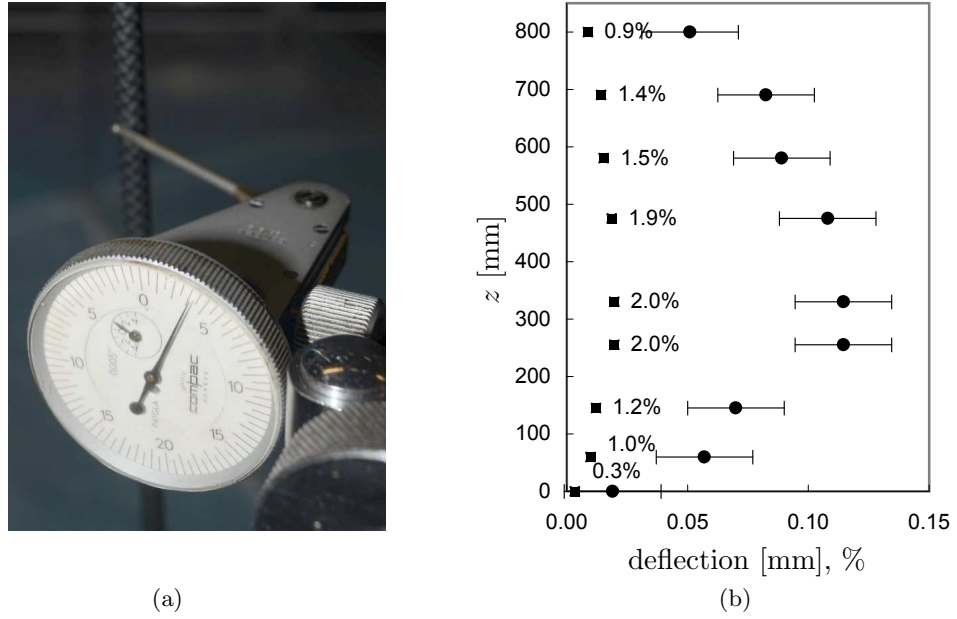


FIGURE 3.5: (a) Measurement of cylinder deflection during rotation (‘wobbling’) with a mechanical deflection gauge. (b) Half-amplitude deflection in mm and in percent of cylinder diameter. The error bars are subjective estimates of the dial read uncertainty.

non-perfect cylinder rotation.

The maximum deflection due to fluid loading was estimated to be 0.15 mm at the mid-span of the cylinder for  $\alpha = 5$  at  $Re = 200$  (using force coefficients from Mittal & Kumar 2003). This deflection is the result of the lift force; the drag force is one order of magnitude smaller. The deflection is highly dependent on rotation rate, and can be expected to be 1/4 of the stated value for  $\alpha = 2$ .

The freestream velocity was measured with LDV during the experiments 15d upstream of the cylinder. At this location, the velocity at  $\alpha = 5$  differs by less than 0.5% from the non-spinning cylinder. Figure 3.6 shows that, up to  $x/d > -15$ , the streamwise velocity component is increased by the spinning motion of the cylinder. For  $x/d < -20$ , the measured velocities are comparable for both rotation rates, but increase slightly due to the velocity gradient in the sub-channel entrance.

The uncertainties of the Reynolds and Strouhal number measurements are less than  $\pm 1.6\%$ ; the rotation rate could be determined with an uncertainty of  $\pm 0.5\%$  at a confidence interval of 95% (at  $Re = 200$ ). The full error analysis is given in appendix A.

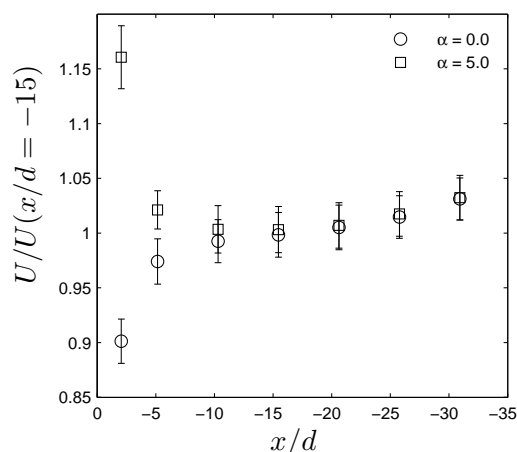


FIGURE 3.6: Dependence of the streamwise velocity on the rotation rate  $\alpha$ . The free-stream velocity  $U_\infty$  was measured at  $x/d = -15$  in the experiments, where the velocity difference between a stationary and a rotating cylinder is less than 0.5%. Error bars denote  $\pm \overline{u'}$  of the LDV measurement.

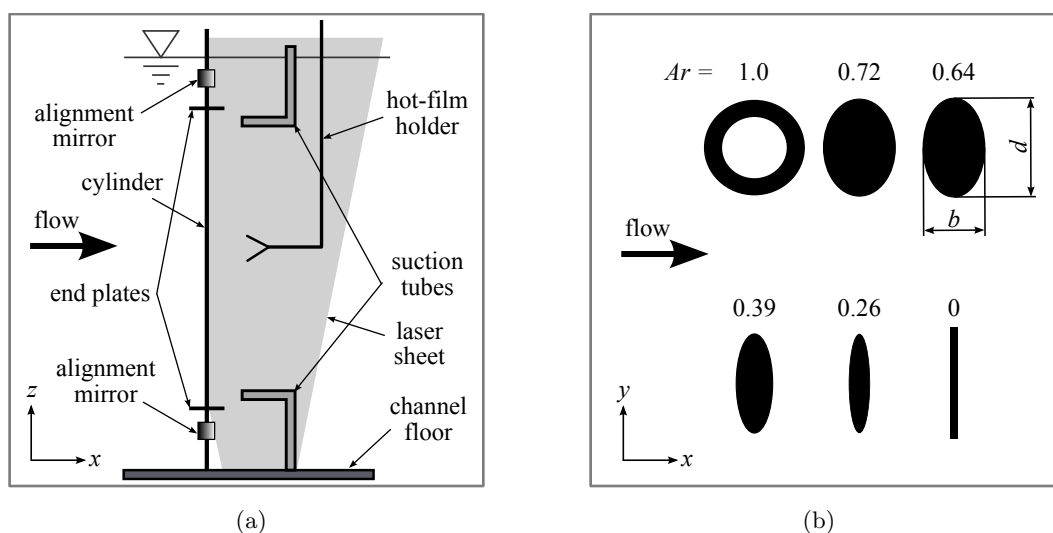


FIGURE 3.7: (a) Schematic of the experimental setup from a side perspective; (b) Cross-sections of the cylinder models and their orientation to the incoming flow.

### 3.3 Elliptical cylinders

Initially, elliptical cylinders models of aspect ratios  $Ar = 0.75$  and  $Ar = 0.5$  were manufactured in-house from epoxy resin, using a machined aluminium mould. Preliminary experiments were performed on these models. However, with the available tools, it was not possible to machine a mould for the  $Ar = 0.25$  cylinder due to its small radii. In the end, a rapid prototyping company was found that printed all elliptical models from plastic. This manufacturing process allowed the implementation of two additional features: Square cross-sections at both ends of each cylinder for precise alignment of the



models in the flow, and a hole through the whole length of the  $Ar = 0.72$ ,  $0.64$  and  $0.39$  cylinders. This feature allowed the structural strengthening of these three cylinders by insertion of a stainless steel rod. This was not possible with the  $Ar = 0.26$  cylinder due to its minimum thickness of just  $b = 1.5$  mm. A carbon fibre tube was used as the circular cylinder; the flat plate model was a thin brass strip with untapered edges (7% plate thickness). The diameters  $d$  of the cylinder models were measured with a micrometer; the results are given in table 3.1. The precision limits were estimated from at least 10 measurements along the span. The micrometer resolution was used as the bias limit.

TABLE 3.1: Dimensions of cylinder models used in the experiments.  $U_d$  is the uncertainty of the diameter measurement;  $U_{Ar}$  is the uncertainty of the aspect ratio  $Ar$ .

| $Ar$ | $d$ [mm] | $U_d$ [ $\pm\%$ ] | $U_{Ar}$ [ $\pm\%$ ] | material      |
|------|----------|-------------------|----------------------|---------------|
| 1.00 | 5.94     | 0.3               | 0.3                  | carbon fibre  |
| 0.72 | 5.78     | 1.6               | 2.6                  | plastic print |
| 0.64 | 5.88     | 1.4               | 1.8                  | plastic print |
| 0.39 | 5.81     | 0.4               | 1.0                  | plastic print |
| 0.26 | 5.82     | 1.5               | 2.3                  | plastic print |
| 0    | 6.32     | 0.4               | 3.4                  | brass         |

The elliptical cylinders were mounted vertically in the centre plane of the sub-channel, with the main ellipse axis oriented perpendicular to the incoming flow. The precise orientation of the cylinder cross section with respect to the flow direction was accomplished by glueing small mirrors on the cylinder square sections, on the side parallel to the flow direction (figure 3.8). A laser beam, aligned perpendicular to the channel wall, was shone onto these mirrors. The cylinder model was rotated about its main axis until the laser beam was reflected back into its source. This was done for the top and bottom ends of the cylinder to prevent twisting of the model. Using this technique, the elliptical cylinder cross-section could be aligned with an uncertainty of  $\pm 0.4^\circ$ .

The usable model length ( $\approx 100d$ ) was defined by circular end plates of  $10d$  diameter, oriented parallel to the flow (figure 3.7). To induce parallel shedding, suction tubes were used (Miller & Williamson 1994; Williamson 1996c). The suction system is shown schematically in figure 3.9. The 10 mm diameter tubes were placed in the symmetry plane downstream, and perpendicular to the cylinder axis, with their intakes positioned close to the end plates, at  $x \approx 10d$ . The tubes were connected to a pump, which removed the water into a buffer container above the water level. An overflow pipe guided the

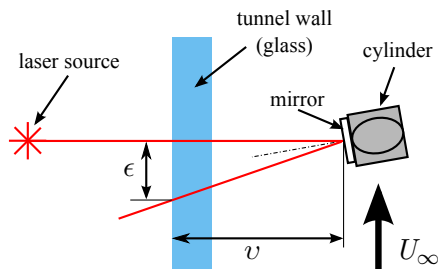


FIGURE 3.8: Precise alignment of the elliptical cylinders using an optical setup. The alignment error is  $\tan^{-1}(\epsilon/v)$

water back into the channel, without causing surface disturbances. The suction tubes proved very effective, and even essential, during the flow visualization experiments and hot film measurements. The tubes had to be removed for PIV recordings, as the lower tube obscured the view for the PIV camera mounted under the channel. As a note, the technique of inclined end-plates (Williamson 1996c) was found to be ineffective in producing parallel shedding in our experiments.

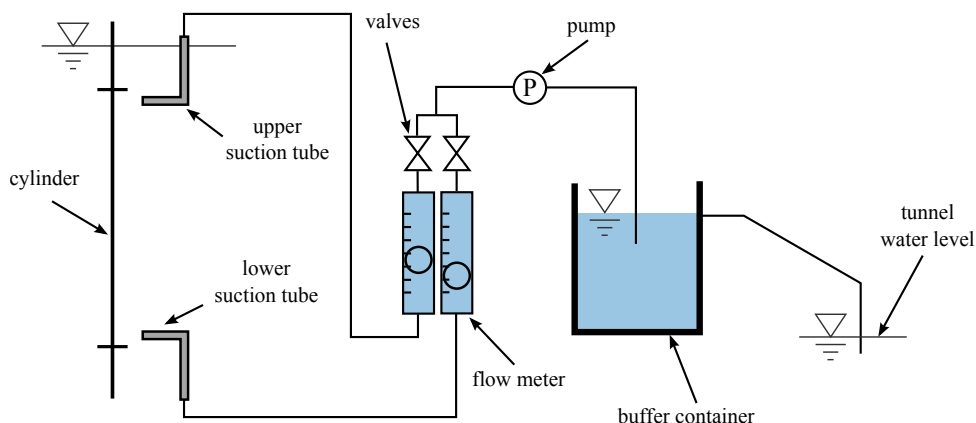


FIGURE 3.9: Schematic of the suction system used to induce parallel shedding.

The volumetric flow rate of each tube was monitored by a flow meter, and adjusted with valves until parallel shedding was confirmed by flow visualizations (typically 300l/h). When switched on, the ends of the von Kármán vortices were bent in the downstream direction, creating a section of parallel vortices at the half-width of the cylinder (see figure 3.10b). This had an impact on the critical Reynolds number, delaying the transition of the circular cylinder wake to three-dimensionality from  $Re = 165$  to 177.

The plastic material used for printing of the models had the undesirable property of expanding from water absorption. The maximum length expansion after one night in the water was 5 mm, which equals to 0.7% of model length. While this makes

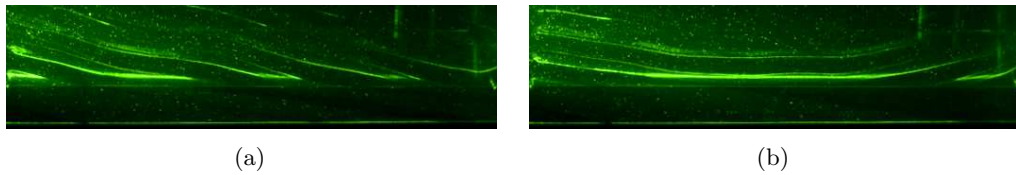


FIGURE 3.10: The effect of suction tubes on vortex shedding of the circular cylinder: (a) tubes off, oblique shedding; (b) tubes on, parallel shedding.

the diameter change negligible, the issue of mounting the cylinder became challenging. The expansion had to be compensated to prevent slackening of the model (the plastic is elastically deformable). This was accomplished by installing a spring loaded linear slide (Del-Tron Precision LMS-200/20) at the top mounting point of the model (figure 3.11). This limited the cylinder movement to only one degree of freedom (vertical direction), which prevented twisting of the model during expansion. The tension could be adjusted with a wing nut, and was kept as high as possible to avoid flow induced vibrations of the model.

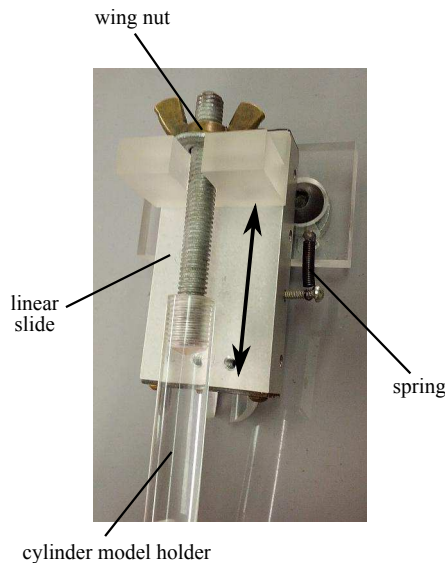


FIGURE 3.11: Linear slide at the upper mounting point. The arrows show the movement direction.

## 3.4 Instrumentation

### 3.4.1 Flow visualization

A  $50\ \mu\text{m}$  platinum wire, 500 mm long, was soldered between the prongs of an F-shaped stainless steel frame and positioned upstream, and parallel to the cylinder axis (fig-

ure 3.12). The frame was attached to a tiltable platform (Melles-Griot<sup>®</sup> kinematic tilt mount 07 MEA 505), which allowed a very accurate alignment of the wire parallel to the cylinder axis. The wire could be moved in the  $x$ - $y$  plane by a two-axes Zaber<sup>®</sup> traverse. A potential of 50 VDC was sufficient to produce a dense sheet of hydrogen bubbles. No additional electrolytes were added to the tunnel water. The maximum Reynolds number based on the platinum wire diameter was 2.5, meaning steady flow around the wire.

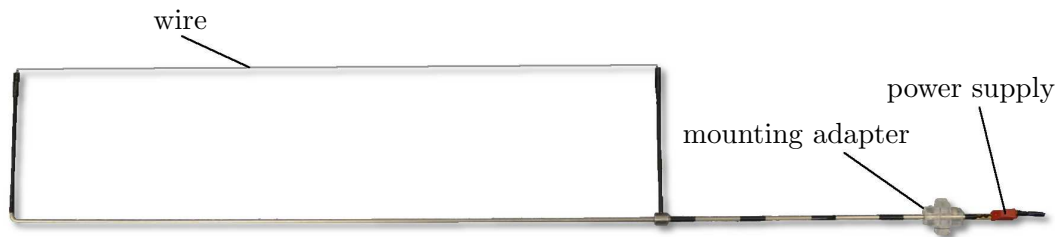


FIGURE 3.12: Frame with the hydrogen bubble wire.

A continuous NdYag laser was used to illuminate the bubble sheet. Shining from below, through the tunnel glass floor, the beam was spread into a sheet of 2–3 mm thickness and aligned parallel to the  $x$ - $z$  plane. A Nikon<sup>®</sup> D7000 camera with 28, 50 or 105 mm lenses was used to record still images or videos from a 90° side perspective.

It was observed during the rotating cylinder experiments that the best visualization results were achieved when the wire was placed at a certain distance from the  $x$ - $z$  symmetry plane. The optimum distance varied with freestream velocity, and rotation rate  $\alpha$ , such that the distance had to be adjusted for each run. The streamwise location was chosen conservatively with  $x/d = -5$ , to reduce the risk of a possible interaction between the wire and cylinder wakes, as discussed in §2.1.3.3.

### 3.4.2 Particle image velocimetry (PIV)

PIV is a member of a broader class of velocity-measuring techniques that measure the motion of small, marked regions of a fluid by observing the locations of the images of some markers at two or more times (Adrian 1991). These techniques exploit the fundamental definition of velocity  $\vec{u}$  as

$$\vec{u}(\vec{x}, t) = \frac{\Delta \vec{x}(\vec{x}, t)}{\Delta t}$$

where  $\Delta \vec{x}$  is the displacement of a marker, located at  $\vec{x}$  at time  $t$ , over a short time interval  $\Delta t$  separating observations of the marker images. It provides non-intrusive

measurements of an instantaneous velocity field of a fluid flow and subsequently derived quantities, e.g. vorticity.

The PIV type used in the present study is the two-dimensional, two velocity component PIV (2D2C-PIV), in conjunction with the normalised spatial cross-correlation analysis. The system consists of a pulsed laser which creates a thin laser sheet, a high-resolution camera with a suitable lens, a timing electronic that triggers the components in a prescribed sequence, and a computer that calculates the velocity vectors from the recorded images. The fluid is seeded with neutrally buoyant seeding particles (Spherical<sup>®</sup> 110P8 by Potters Industries Inc.). The particles scatter light into a photographic lens located at 90° to the sheet, so that its in-focus object plane coincides with the illuminated slice of the fluid. The images are recorded with the multiframe / single pulse method, meaning that two frames are recorded at a time interval  $\Delta t$ , and the laser is fired once per frame. The images were analysed with an in-house PIV software (Fouras & Soria 1998), using  $32 \times 32$  px<sup>2</sup> interrogation windows in a grid layout with 50% window overlap.

The used hardware is described in detail in Sherry (2012). The principle of the PIV method can be found in common literature, such as Adrian & Westerweel (2010) or Raffel *et al.* (2007).

The vorticity field  $\vec{\omega}$  is an important Galilean invariant vector field. Each of the vorticity components can be computed from corresponding in-plane velocity, using its basic definition

$$\vec{\omega} = \nabla \vec{u}$$

The 2D2C-PIV provides the  $x, y$  components of the velocity field,  $u$  and  $v$ , such that one component of the vorticity field can be computed

$$\omega_z = \frac{\partial v}{\partial x} - \frac{\partial u}{\partial y}$$

To calculate  $\omega_z$  from the PIV data, the algorithm uses a second order polynomial  $\chi^2$  fit to the local velocity components, with subsequent analytic differentiation. This method yields an accuracy improvement compared to a finite difference calculation.

The accuracy of the  $\omega_z$  calculation depends on the spatial sampling distance between the velocity data points (i.e. the spatial resolution between the in-plane velocity vector samples) and on the accuracy of the velocity vector field measurements (Fouras & Soria 1998). An increase of the velocity spatial sampling separation (larger interrogation

windows) introduces a larger bias error, resulting in an increasing underestimation of the vorticity in the peak vorticity regions. The effect of the random velocity measurement error is to scatter the vorticity measurements around the corresponding biased vorticity. Unfortunately, the requirements to minimise the random error and to minimise the bias error cannot be satisfied simultaneously, as both effects are coupled and oppose each other. The coupling parameter is the non-dimensional velocity sampling separation. A more detailed discussion of the accuracy of the used code can be found in (Fouras & Soria 1998).

### 3.4.3 Laser Doppler velocimetry (LDV)

When light is reflected from a moving object, the frequency of the scattered light is shifted by an amount proportional to the speed of the object. The LDA system uses this Doppler shift to estimate the speed of the flow by observing the frequency shift caused by moving seeding particles.

The configuration used here is based on an Argon laser that creates a multiple band laser beam. The TSI<sup>®</sup> Colorburst multicolour beam generator extracts two wavelengths (514.5 nm and 488 nm), which are split into two beams of equal intensity. Thus, four laser beams are needed to measure two perpendicular velocity components. One beam of each colour is shifted by a known value (usually 40 MHz) to avoid directional ambiguity of the measured velocity. The four beams are coupled into optical fibres and guided to the optical head.

Once the beams exit the optical head, an interference fringe pattern is generated at the crossing point (figure 3.13a). The fringe pattern consists of alternating zones of brightness and darkness (figure 3.13c). The fringe spacing,  $d_f$ , is the distance between sequential bright (or dark) zones. As a particle crosses the fringe pattern, the intensity of the scattered light varies with the intensity of the fringes (figure 3.13b). Thus, the amplitude of the signal burst varies depending on the velocity component perpendicular to the fringe pattern. The frequency of the amplitude modulation is equal to the Doppler frequency  $f_D$ . The scattered light is detected by a photomultiplier tube (PMT), an instrument that generates a current in proportion to absorbed photon energy, and then amplifies that current. A computer calculates the velocity value.

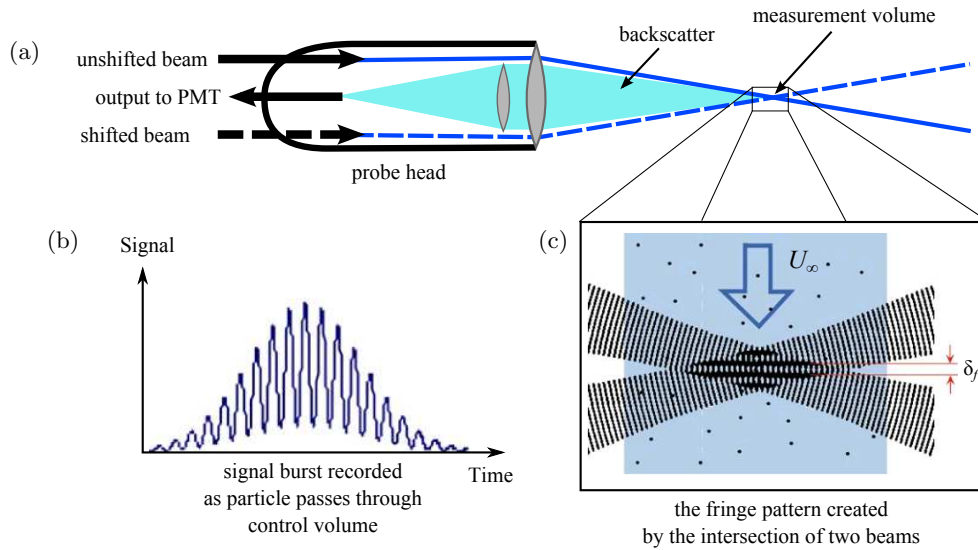


FIGURE 3.13: Principle of operation of the LDV. See text for explanations.

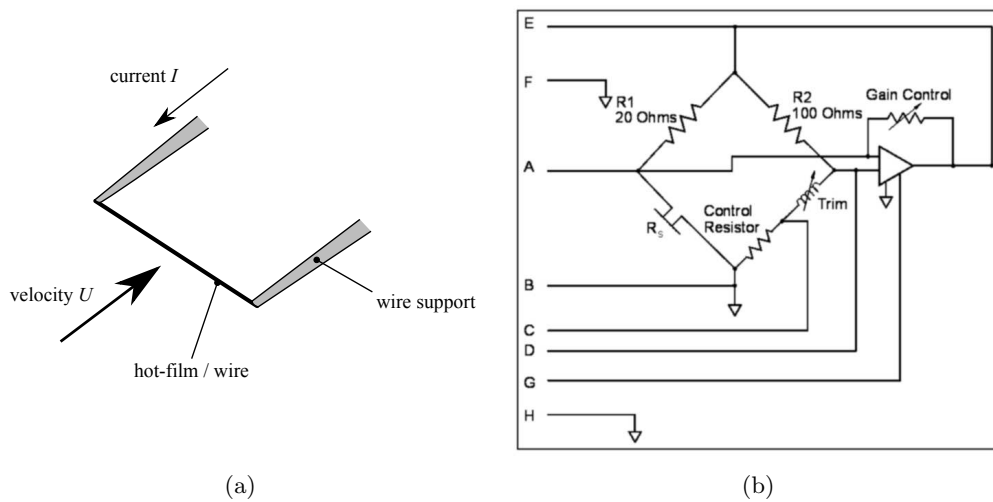


FIGURE 3.14: (a) A hot film / wire sensor in a fluid flow. (b) Electric block diagram of the anemometer. The sensor is represented as  $R_s$  in the Wheatstone bridge (TSI<sup>®</sup> manual).

### 3.4.4 Hot film probes

A hot wire / film makes use of the principle that heat transfer from a heated surface depends upon the flow conditions passing over it (figure 3.14a). The mode of operation used for the present experiments is Constant Temperature Anemometry (CTA). A feedback circuit is used to maintain the wire at a constant temperature (figure 3.14b). The hot wire, shown between A and B, forms part of a Wheatstone bridge, such that the wire resistance is kept constant over the bandwidth of the feedback loop. Since the hot wire voltage is a simple potential division of the output voltage, the output voltage

E–B is normally measured for convenience. The hot wire anemometer remains the only instrument that can deliver as an output a truly analogue representation of the velocity up to high frequencies.

The hot film sensor is essentially a conducting film laid on a ceramic or quartz substrate. The sensor can be a quartz rod coated with a platinum film. Because of their stability, film sensors have been used for many measurements which were otherwise very difficult with the more fragile and less stable hot wires. A downside is that the film sensor is generally less sensitive. The metal film thickness on a typical film sensor is less than  $0.1\ \mu\text{m}$ . Thus, the mechanical strength and the effective thermal conductivity of the sensor are determined almost entirely by the substrate material. Hot film sensors made for water or conducting fluids have an additional coating of quartz on top of the metal film, providing complete electrical insulation. In the present experiments, hot films were used exclusively.

The hot wire sensor itself is very small: typical dimensions of the heated wire are  $5\ \mu\text{m}$  in diameter, and 1 to 3 mm in length. With  $25\ \mu\text{m}$ , the hot film diameter is considerably larger. When a current is passed through the wire, heat is generated according to  $I^2 R_w$ , with  $I$  being the current, and  $R_w$  being the resistance of the wire. In thermal equilibrium, this must be balanced by heat loss to the surroundings. These losses include convection to fluid, conduction to supports, and radiation (usually neglected). In static analysis, the forced convection to fluid is described by the Nusselt number  $Nu$ . Assuming an exponential function for the Nusselt number – velocity dependence, the *King's law* gives a theoretical calibration equation.

In practice, the probe is calibrated against a velocity standard, if quantitative velocity data are desired. The calibration curve is nonlinear, with maximum sensitivity at low velocities (Bruun 1995). As no quantitative velocity data were required from the hot film measurements in the present experiments (only spectral information was of interest), no calibration was performed.

The theoretical treatment of the frequency response of a hot wire / film is not straightforward, and should only be considered when a broadband and/or high frequency velocity fluctuations are present in the flow, e.g. in supersonic or turbulent flows. More conveniently, the frequency response can be optimized by injecting a small voltage square wave of 1 kHz into the Wheatstone bridge at points A and D, and optimizing the output by adjusting the trim and gain shown in figure 3.14b. The output



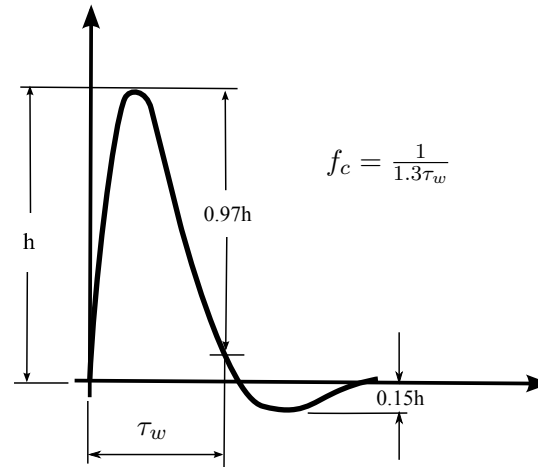


FIGURE 3.15: Optimum square wave response of a hot wire.

voltage curve should have the shape shown in figure 3.15. This was not necessary for the current experiments, as the dominant frequencies in the flow are low (1–10 Hz), but the square wave optimization was still performed, as the bridge output voltage was unstable for some film probes used.

The CTA bridge output was filtered with a low-pass filter set to 10 Hz, before being sampled with a National Instruments<sup>®</sup> BNC-2110 board at 20 Hz.

## 3.5 Numerical tools

### 3.5.1 Space–time diagrams (rotating cylinder experiments)

During the experiments presented in chapter 5, flow visualisation data of the rotating cylinder wake were recorded with an IDT<sup>®</sup> Y4 high-speed camera. Algorithms, which were coded in Matlab<sup>®</sup>, extract information on spatio-temporal symmetry, wavelengths of three-dimensional modes and the von Kármán shedding frequency from these flow visualization sequences.

To gain information on spatio-temporal symmetry, space-time ( $s$ – $t$ ) diagrams were created. In this context, an  $s$ – $t$  diagram shows the temporal evolution of the flow at a fixed location in space, by plotting some chosen quantity as a function of time. To investigate the temporal behaviour of the three-dimensional modes, we used the brightness distribution in our flow visualization images at a fixed downstream location in the wake. For this purpose, a 10 pixels wide band, parallel to the cylinder axis, was selected at the same downstream location in each picture. This location had to be adjusted for each Reynolds number and rotation rate, to adapt to changes of the flow

field. At each point along the span, the band was averaged over its width to form a brightness distribution along the span. The bands of all pictures, plotted as a function of time, formed a space-time-diagram.

A windowed ( $8d$  wide, 50% overlap) Fast Fourier Transform (FFT) was performed on each band of the  $s$ - $t$  diagram to calculate the instantaneous spanwise wavelength spectrum. To decrease finite-length effects, a Hann function was applied to each window. The spectra of all bands were averaged, and the result plotted as a function of wavelength  $\lambda$  (in units of cylinder diameter  $d$ ). The highest peak (besides possible long-wavelength noise) was considered as the mode's spanwise wavelength.

To estimate the Strouhal number  $St$  of the two-dimensional base flow, a (windowed) FFT in time was performed on all averaged bands. The resulting spectra typically showed a clear peak at the von Kármán shedding frequency. A Gaussian normal distribution was fitted to this peak to improve the spectral resolution. The shedding frequency was defined as the mean of the Gaussian fit; the standard deviation could be used as an estimate of the peak width.

### 3.5.2 Proper orthogonal decomposition (POD)

POD is a proven method for identifying dominant features and events in experimental and numerical data (other names for this method are Karhunen–Loève decomposition or singular value decomposition). The POD method identifies fluid motions that contain most of the flow energy. The result is a set of modes that represents an average spatial description of most energetic structures. It should be kept in mind, that these modes may also correspond to events, which are limited in time but contain large amounts of energy. the following limitations of the method should be considered: (Kostas *et al.* 2005):

- The less deterministic a flow is, the less efficiently it will be represented by the POD expansion. For the present study, this means that at higher Reynolds number, when the wake has undergone three-dimensional transition, more modes will be needed to capture a large contribution of the kinetic energy in the flow. During laminar shedding, with its periodicity and limited length scales, most of the energy can be expected to be contained in the first few modes (up to 10).
- The analysis de-emphasizes infrequent events, although they may be dynamically important, such as flow disruptions by vortex dislocations.

- The POD modes represent only time averaged information about the flow structures.

The idea behind POD is to approximate a vector-valued function  $u(\vec{x}, t)$  as a finite sum of  $K$  functions  $\phi(\vec{x})$ :

$$u(\vec{x}, t) \simeq \sum_{k=1}^K a^{(k)}(t) \phi^{(k)}(\vec{x}) \quad (3.1)$$

with  $\vec{x}$  being the spatial and  $t$  the temporal coordinate, and  $a$  a scaling factor. Now, instead of using an priori given basis function for  $\phi^{(k)}(\vec{x})$ , such as Fourier series or Legendre polynomials, the POD method determines the functions  $\phi$  that are naturally intrinsic for the problem at hand. The criterion for determining the sequence of orthonormal functions  $\phi^{(k)}(\vec{x})$  is such that the approximation for each  $K$  is as good as possible in a least-squares sense. This minimization problem is solved by the singular value decomposition of the snapshot data matrix  $A \in \mathbb{R}^{M \times N_t}$ , which contains  $N_t$  realizations at  $M$  spatial locations.

In this thesis, the *snapshot* technique suggested by Sirovich (1987) is used. The snapshot POD drastically reduces the computational effort when the number of spatial points in the snapshots data is much larger than the number of realizations, as is usually the case for PIV data (Tropea *et al.* 2007). Assuming a set of  $N_t$  flow field realizations  $\vec{u}(\vec{x}, t_k)$  at time instances  $t_k$ , we are looking for a set of orthogonal functions  $\vec{\phi}^{(k)}(\vec{x})$ :

$$\vec{\phi}^{(k)}(\vec{x}) = \sum_{k=1}^{N_t} a^{(k)}(t_k) \vec{u}(\vec{x}, t_k) \quad (3.2)$$

where the coefficients  $a(t_k)$ ,  $k = 1, \dots, N_t$  are to be determined such that the reconstruction becomes optimal in the sense that any reconstruction using another basis with the same number of modes contains less energy. This is done by solving an eigenvalue problem over the domain  $\Omega$ , where the kernel is the two-point spatial correlation tensor  $R$ :

$$\int_{\Omega} R(\vec{x}, \vec{x}') \vec{\phi}(\vec{x}') d\vec{x}' = \lambda \vec{\phi}(\vec{x}). \quad (3.3)$$

Substituting (3.2) into (3.3) leads to the eigenvalue problem which determines  $a(t_k)$ , and which is solved numerically<sup>1</sup>:

$$C\vec{V} = \lambda\vec{V}, \quad (3.4)$$

---

<sup>1</sup>The present computations use the open source python library MODRED (<http://pythonhosted.org/modred>).

where

$$C_{ki} = \frac{1}{N_t} \int_{\Omega} \vec{u}(\vec{x}, t_k) \cdot \vec{u}^*(\vec{x}, t_i) d\vec{x} \text{ and } \vec{V} = [a(t_1), a(t_2), \dots, a(t_{N_t})]^T.$$

$\vec{V}^{(k)}$  is set of orthogonal eigenvectors (or orthonormal, depending on the normalization), and  $\lambda$  are the eigenvalues, sorted as  $\lambda^{(1)} \geq \lambda^{(2)} \geq \dots \lambda^{(N_t)} \geq 0$ .

The eigenmodes  $\vec{\phi}$  are computed using (3.2). The corresponding eigenvalues  $\lambda$  represent the energy contained in each mode. A low-order reconstruction of the  $k$ 'th snapshot can be created using (3.1).

There remains the choice of the physical quantity used for the decomposition. 2D2C-PIV provides two velocity components, which makes velocity a natural choice. Equally, vorticity computed from these vector fields can be used for the POD analysis. Indeed, these two variables will lead to slightly different results; after all, two different quantities are being compared: the kinetic energy content in case of velocity, and the enstrophy in case of vorticity. Kostas *et al.* (2005) conclude that the choice of quantity will depend on the aim of the POD analysis. For the identification of coherent structures, vorticity might be the better choice, as it is a Galilean invariant quantity. The flow structures deduced from velocity fields can be misleading, as they depend on the velocity of the observer (Perry *et al.* 1982). On the other hand, POD modes based on velocity tend to have a better energy convergence, requiring fewer modes to describe the flow. Furthermore, the order of the modes might be not the same for the velocity and vorticity decompositions, which can make the modes incomparable between these two quantities.

Relevant for the present study, Kostas *et al.* (2005) report similar energy convergence for velocity and vorticity based decompositions at low Reynolds numbers (backward facing step:  $Re = 580$ ). The limited range of length scales of low Reynolds number flows leads to almost identical decompositions for both variables. For a turbulent flow at a high Reynolds number ( $Re = 4660$ ), vorticity based decomposition was the more efficient technique, identifying coherent structures clearer and with a better energy convergence. The conclusion is, that either variable can be used in the present study, as the Reynolds numbers are very low ( $Re \leq 300$ ), resulting in a very periodic and coherent flow field.

## Declaration for Thesis Chapter 4

### Declaration by candidate

In the case of Chapter 4, the nature and extent of my contribution to the work was the following:

| Nature of contribution  | Extent of contribution (%) |
|---|----------------------------|
| Design & execution of experiments. Design & (partial) construction of experimental models. Data processing & presentation. Interpretation of results. | 80%                        |

The following co-authors contributed to the work. Co-authors who are students at Monash University must also indicate the extent of their contribution in percentage terms:

| Name                | Nature of contribution   | Extent of contribution (%) for student co-authors only |
|---------------------|--|--|
| Dr. David Lo Jacono | Research guidance & interpretation of results. Revisions of manuscript and proof-reading. Assistance with data analysis. | -  |
| Prof. John Sheridan | Manuscript formulation. Research guidance & interpretation of results. Proof-reading.                                    | -  |

Candidate's Signature  Date 30.8.2013

### Declaration by co-authors

The undersigned hereby certify that:

- (1) the above declaration correctly reflects the nature and extent of the candidate's contribution to this work, and the nature of the contribution of each of the co-authors.
- (2) they meet the criteria for authorship in that they have participated in the conception, execution, or interpretation, of at least that part of the publication in their field of expertise;
- (3) they take public responsibility for their part of the publication, except for the responsible author who accepts overall responsibility for the publication;
- (4) there are no other authors of the publication according to these criteria;
- (5) potential conflicts of interest have been disclosed to (a) granting bodies, (b) the editor or publisher of journals or other publications, and (c) the head of the responsible academic unit; and
- (6) the original data are stored at the following location(s) and will be held for at least five years from the date indicated below:

Location(s)

[Please note that the location(s) must be institutional in nature, and should be indicated here as a department, centre or institute, with specific campus identification where relevant.]

Signature 1  Date 30/08/13  
 Signature 2  Date 30/08/2013

.....



# Chapter 4

## Reynolds number reduction

This chapter is based on:

RADI, A., LO JACONO, D. & SHERIDAN, J. 2013a A device to achieve low Reynolds numbers in an open-surface water channel. *Experiments in Fluids* (submitted for publication)

### 4.1 Introduction

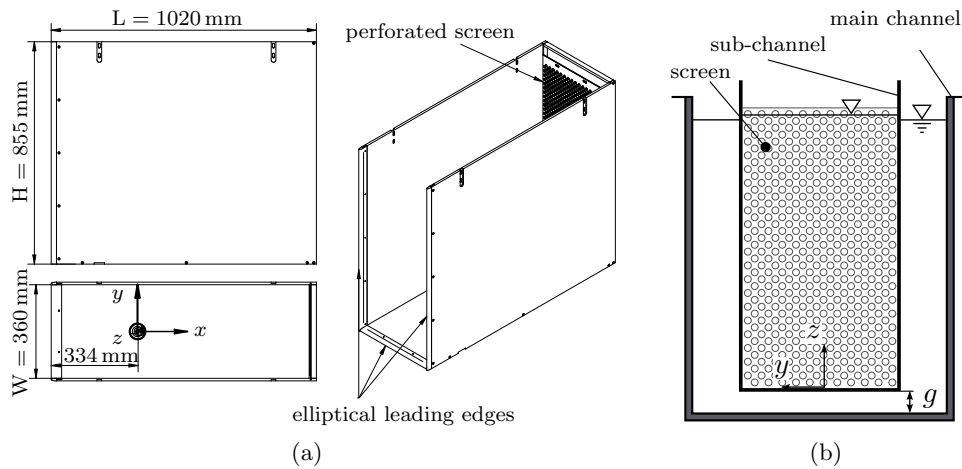


FIGURE 4.1: (a) Layout and dimensions of the sub-channel insert. The model is mounted at 334 mm downstream of the leading edges. (b) View in downstream direction on the sub-channel positioned in the main channel test section. Note the gap  $g$ .

The minimum workable Reynolds number of the FLAIR water channel was too high for the present experiments. A short literature review was undertaken to find means of reducing  $Re$ .

Three parameters determine the minimum Reynolds number  $Re = dU/\nu$ : the fluid viscosity  $\nu$ , model dimension  $d$  and the freestream velocity  $U$ . The minimum model dimension  $d$  is usually prescribed by experimental requirements, such as model stiffness,

manufacturing process or minimum spatial resolution of PIV recordings. The kinematic viscosity  $\nu$  can be adjusted by changing the fluid temperature, or by using a different working fluid. The high viscosity of e.g. mineral oil, is often exploited when a low Reynolds number is required, such as in insect flight or micro-air vehicles research (Bechert *et al.* 1992; Wang *et al.* 2004; Willert *et al.* 2010). A more exotic way of modifying the (effective) viscosity is the use a ‘flowing soap film’, where the viscosity is also a function of the film thickness (Vorobieff & Ecke 1999).

The last parameter, the freestream velocity  $U$ , is limited solely by the specifications of the research facility. But reducing the velocity of an existing recirculating water channel has its limitations. Tunnels are designed for a certain velocity range, with the turbulence management system optimised for that range. Decreasing the channel speed far below specifications can affect the turbulence level and frequency content of the flow, and – more importantly – can have a negative effect on the uniformity of the flow, leading to skewed velocity profiles in the test chamber.

To avoid these adverse effects, it was decided to modify the flow velocity only locally, by splitting the flow inside the main channel test chamber. An U-shaped ‘sub-channel’ insert, with a perforated screen at its downstream end, was built (see figure 4.1). The screen creates a pressure drop, which leads to a pressure increase within this structure. The remaining flow bypasses it at higher velocity, keeping the overall flow rate through the water channel unchanged. The *porosity* of the screen,  $\alpha$ , defined as the ratio of the open area  $A_{\text{open}}$  to the total area of the screen  $A_{\text{total}}$ , determines the degree of velocity reduction.

## 4.2 Construction

### 4.2.1 Main Structure

The sub-channel is designed to occupy 2/3 of the test chamber cross section area. Its (inner) width is  $W = 360$  mm, leaving 110 mm on each side to the main channel walls for the bypass flow. The side walls ( $L \times H = 1000 \times 855$  mm) and bottom plate of the insert are made of 10 mm thick transparent acrylic. The leading edges of the side walls and the bottom plate are elliptical, with a main axes ratio of 4 : 1. The experimental model attaches to the bottom plate, 334 mm downstream of the leading edges. The rear screen consists of two perforated acrylic sheets, with adjustable porosity  $\alpha$ .

The sub-channel can be suspended in the channel test chamber, leaving a gap of



size  $g$  between its bottom plate and the main channel floor, or placed directly onto the floor. It will be shown that this gap width has to be chosen carefully to achieve uniform velocity profiles inside the sub-channel.

#### 4.2.2 Perforated Screen

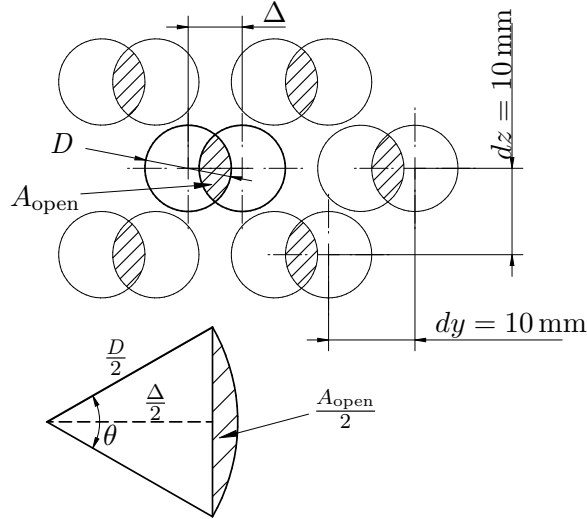


FIGURE 4.2: (top) Holes pattern of the perforated screen, when the two acrylic sheets are shifted with respect to each other by the distance  $\Delta$ ; (bottom) Geometry for calculation of the screen porosity  $\alpha$ .

The adjustable screen consists of two perforated acrylic sheets of 3 mm thickness. A staggered pattern of over 1200 holes of diameter  $D = 10 \text{ mm}$  was drilled into each sheet. By overlaying the two sheets, and shifting them horizontally with respect to each other, as shown in figure 4.2 (top), the ratio of open area  $A_{\text{open}}$  to total screen area  $A_{\text{total}}$  can be varied continuously. For a fully open screen (shift distance  $\Delta = 0$ ), the porosity is  $\alpha = \pi/8 \approx 0.393$ . When decreasing the open area, this ratio varies according to

$$\alpha = \frac{A_{\text{open}}}{A_{\text{total}}} = 0.393 \left( \frac{2 \arccos(\delta)}{\pi} - \frac{2\delta}{\pi} \sqrt{1 - \delta^2} \right) \quad (4.1)$$

where  $\delta = \frac{\Delta}{D}$ ,

which can be derived from geometric considerations shown in figure 4.2 (bottom).

The screen can be removed easily, by sliding it vertically along grooves machined in the side walls. This allows quick adjustment of  $\alpha$  between experiments, without requiring the whole structure being removed from the water channel.

Seven values of  $\alpha$ , between 0.393 and 0.0041, were chosen for the tests. Alignment holes were drilled into both acrylic sheets in such a way that these values could be

reproduced accurately by the insertion of a metal pin.

### 4.3 Validation tests

The following conventions are used for velocity measurements.  $u$ ,  $v$  and  $w$  are the streamwise, cross-stream and vertical velocity components. A velocity time series  $u(t)$  is decomposed into  $u(t) = U + u'(t)$ , where  $U$  is the time-averaged, and  $u'(t)$  is the fluctuating component. The velocity in the empty main channel test section (sub-channel not inserted) is referred to as  $U_\infty$ . Velocity profiles and cross-sectional velocity contours are presented as difference to the average velocity:  $U_{\text{diff}} = (U - U_{AVG})/U_{AVG}$ , where  $U_{AVG}$  is the average of all data points of the profile or contour. The flow velocity at model location ( $x/L \approx 1/3$ ) is referred to as  $U_0$ . The turbulence intensities are based on root-mean-squares of the  $u$  and  $w$  velocity components:

$$Tu = \frac{\sqrt{\frac{1}{2}(\overline{u'^2} + \overline{w'^2})}}{U_{AVG}} \quad (4.2)$$

The tested channel velocities were  $U_\infty = 0.045$ ,  $0.090$  and  $0.135$  m/s (pump speeds: 5, 10 and 15 Hz), which translate to approximately  $Re = 100$ ,  $200$  and  $300$  in the rotating and elliptical cylinder experiments

#### 4.3.1 Velocity reduction

The dependence of freestream velocity inside the sub-channel on porosity  $\alpha$  is shown in figure 4.3. These LDV measurements were taken in the centre plane of the sub-channel, at model location, where the inflow has reached a steady velocity.

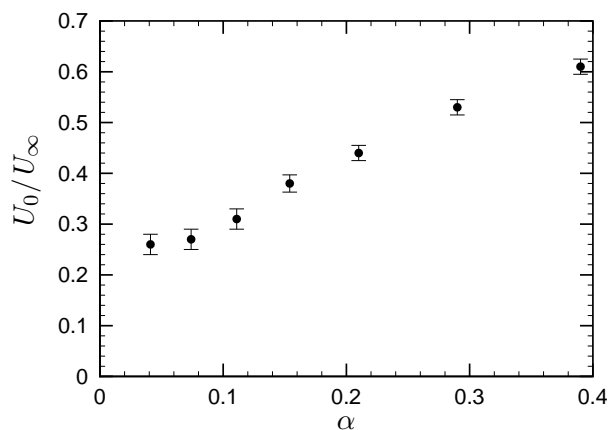


FIGURE 4.3: Freestream velocity reduction inside the sub-channel at model location as a function of screen porosity  $\alpha$  ( $U_\infty = 0.09$  m/s). Error bars show  $\pm\overline{u}$ .

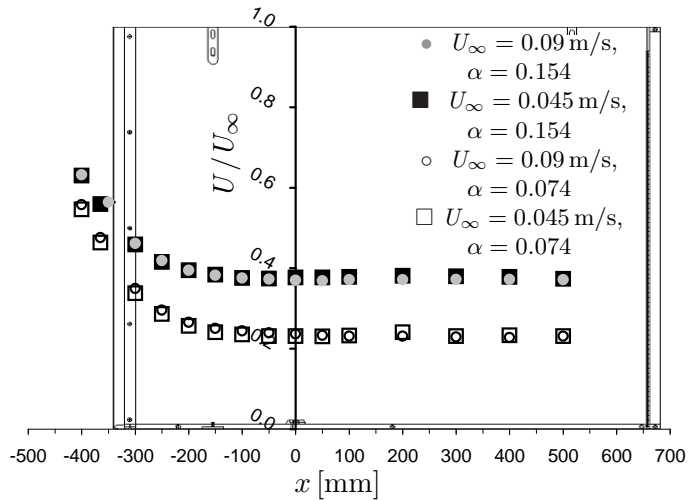


FIGURE 4.4: Change of streamwise velocity  $U$  along the centre-line, as the flow enters the sub-channel. Data for two pump speeds and two values of  $\alpha$  are overlaid on a side view of the sub-channel. The velocity error bars ( $\overline{u'}$ ) are smaller than the shown symbols. Flow is from left to right.

For a fully open screen ( $\alpha = 0.393$ ), the flow velocity is 39% lower than  $U_\infty$ . The velocity decreases approximately linearly up to  $\alpha = 0.074$ ; it then tends to level out for the lowest porosity value. Theoretically, a velocity reduction of more than 70% can be achieved with the screen.

Figure 4.4 shows the streamwise velocity along the centreline (at  $z/H \approx 0.5$ ) for two channel pump settings and two values of  $\alpha$ . Velocity reduction can be seen to have already occurred upstream of the sub-channel entrance. The flow slows down monotonically as it enters the structure and reaches a constant velocity at  $x \approx -100$  mm. For best results, the model should be placed slightly downstream of this location, at  $x = 0$  mm. This means that the rear two thirds ( $0 \text{ mm} < x < 650 \text{ mm}$ ) of the sub-channel can be used for experiments.

### 4.3.2 Dependence on gap size $g$

A particularly interesting observation was made during the first velocity measurements. The first version of the sub-channel did not possess a bottom plate, but was standing on the water channel floor. Placed like this, the whole structure represented an obstacle to the incoming floor boundary layer. For similar configurations, e.g. a vertical cylinder mounted on a flat plate, it is known that a *horse-shoe vortex* is likely to develop in front of the obstacle. For our configuration, flow visualizations revealed a standing vortex of 15–20 cm in diameter at the entrance to the sub-channel. As it was formed not by a

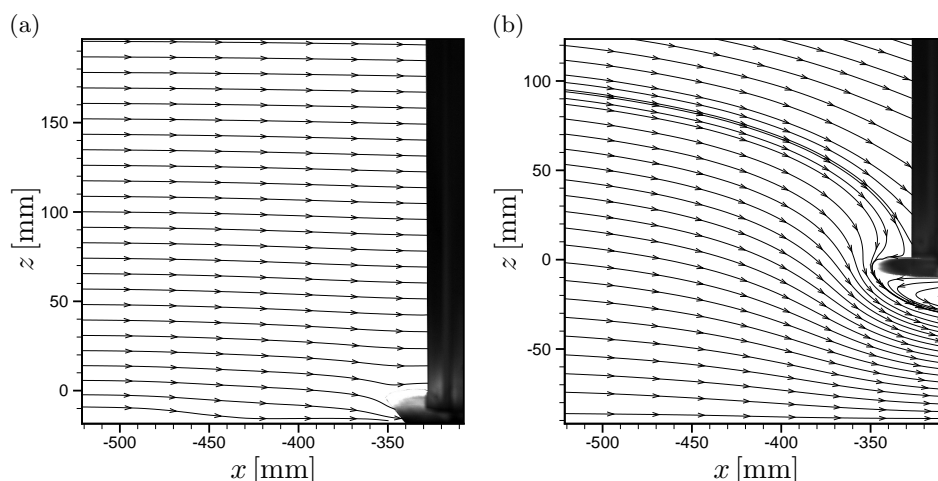


FIGURE 4.5: Time-averaged PIV recordings at the bottom leading-edge of the sub-channel, showing the impact of different gap sizes on the flow field in the centre plane  $y/W = 0$ : (a) gap: 5 mm, (b) 76 mm. ( $U_\infty = 0.075$  m/s,  $\alpha = 0.154$ )

solid object but was pressure-induced (a sudden increase in pressure with subsequent boundary layer separation), its location was not stable. After it reached a maximum size, it periodically detached and was convected through the sub-channel, after which a new standing vortex was slowly formed. The convection of this detached vortex led to unacceptably large velocity fluctuations inside the structure.

To suppress this phenomenon, the sub-channel was suspended in the main test chamber, with its bottom plate above the floor boundary layer (see figure 4.1b). A study was undertaken to determine the effect of the gap size  $g$  between the bottom plate and the channel floor. It was found that large gap sizes (38, 76 and 114 mm) suppressed the standing vortex, but with the adverse effect of strongly skewed vertical  $U$ -velocity profiles at model location. Particularly, a velocity deficit of up to 10% of the local mean was noticed in the lowest 200 mm of the profiles, which persisted throughout the streamwise extent of the structure. Smaller gaps of 2, 5 and 10 mm, on the other hand, achieved the desired effect of suppressing the standing vortex, at the same time leading to more uniform velocity profiles.  $g = 5$  mm was chosen for all subsequent experiments.

The increased skewness resulting from larger gap sizes is explained by the time-averaged PIV data shown in figure 4.5. A small gap below the sub-channel – of the order of 5 mm – results in a suction effect, which removes fluid from the incoming floor boundary layer. As seen in figure 4.5a, this is sufficient to prevent large-scale boundary layer separation and a possible build-up of the horse-shoe vortex. In this case, the

inflow into the sub-channel is parallel to the bottom plate. A large gap, on the other hand, modifies the global inflow, by deflecting a large portion of the incoming stream downward into the gap (figure 4.5b). This downward motion moves the stagnation line on top of the plate leading edge and establishes a low-velocity zone in the vicinity of the stagnation point. This results in a velocity deficit in the lower third of the streamwise velocity profiles, which persists throughout the streamwise extent of the sub-channel.

The boundary layer thickness on the floor of the main test chamber is estimated from PIV measurements to be 30–40 mm. The displacement thickness, which is approximately 1/3 of the boundary layer thickness (Schlichting & Gersten 2000), can be used as a rough estimate for the choice of the gap size  $g$ .

### 4.3.3 Dependence on freestream velocity

The flow uniformity and turbulence intensity of the sub-channel cross-section were compared to the base case of the empty main channel test chamber at three tunnel velocities. The LDV point velocity measurements were made in a plane perpendicular to the flow direction. The focal length of the LDV lens allowed to traverse only half of the channel width. Between 4 and 6 minutes were recorded per sampling point.

Figure 4.6 shows the streamwise velocity contour maps, overlaid with turbulence intensity contour lines (turbulence contour levels: 1, 1.5, 2, 3, 4, 6, 8 %). The vertical direction is measured from the sub-channel bottom plate and is non-dimensionalized by the water depth  $h$ .

Figure 4.6a shows the flow field in the empty test section at  $U_\infty = 0.045$  m/s, 0.090 m/s and 0.135 m/s (from left to right). With the exception of the lowest pump setting, the streamwise velocity variations remain largely within  $\pm 1\%$  of the plane average. The turbulence intensity lies between 1.5 and 2%. At all velocities, the bottom corner of the channel cross-section exhibits a pronounced velocity deficit and increased turbulence intensity. This is likely the result of a secondary flow in form of a corner vortex. The grey arrow heads, showing the time-averaged vertical velocity component  $W$ , indicate counter-clockwise rotation (the largest arrow seen in (a) is equivalent to 7% of  $U_\infty$ ). In addition, it is observed that the flow quality deteriorates at the lowest tunnel velocity, resulting in an increased turbulence level.

The flow quality in the sub-channel at the two highest velocities,  $U_\infty = 0.090$  m/s and 0.135 m/s (figure 4.6b), is comparable to the empty test section. A mild velocity

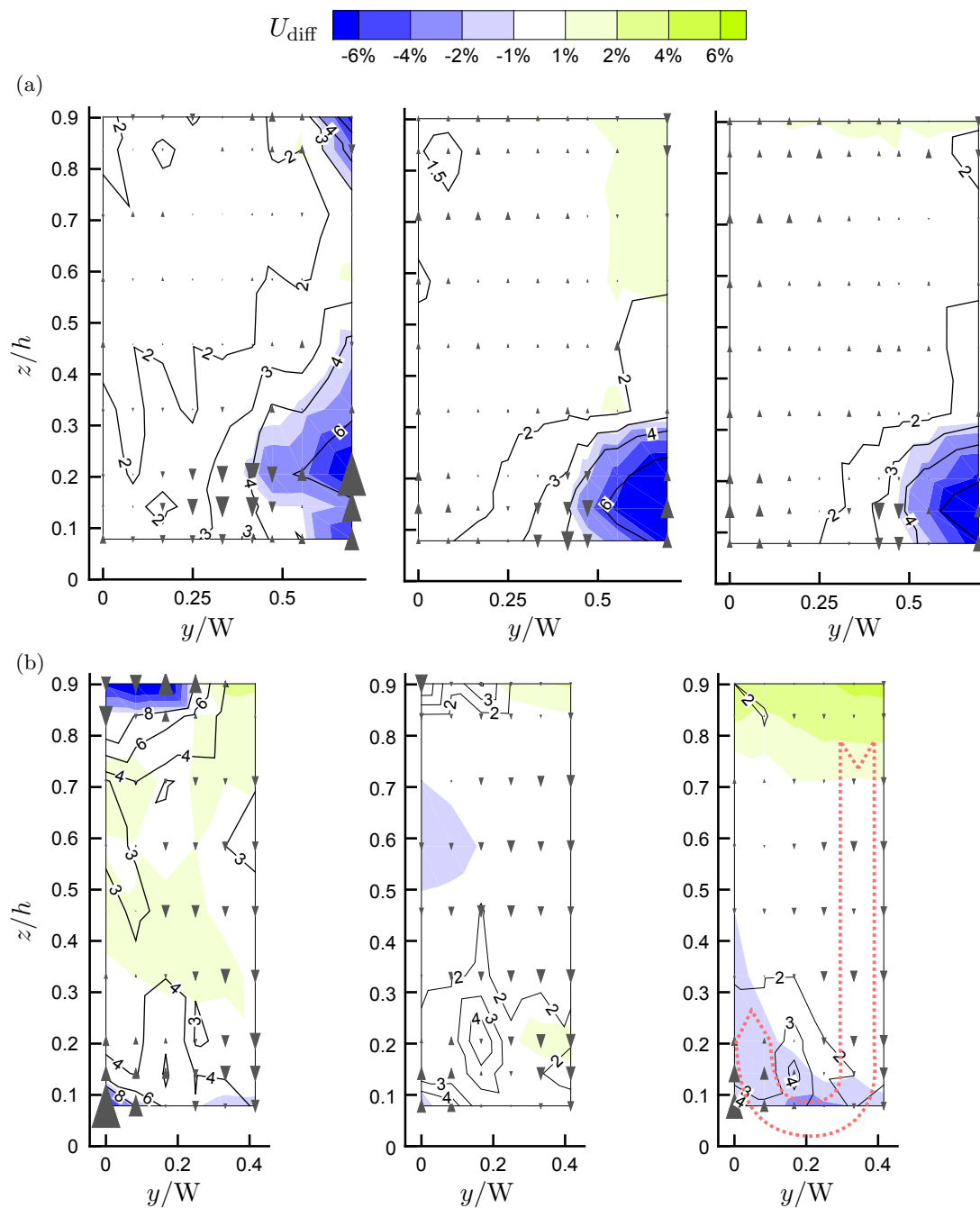


FIGURE 4.6: Flow uniformity in the empty test section (a) and in the sub-channel at model location (b) at three tunnel velocities. From left to right:  $U_\infty = 0.045$  m/s, 0.090 m/s, 0.135 m/s (pump speeds 5 Hz, 10 Hz, 15 Hz). The colour contours show  $U_{diff}$ ; the contour lines represent  $Tu$  [%]. The size of the grey arrow heads is proportional to the value of the vertical velocity component  $W$ . The dashed red arrow visualizes the secondary flow in the sub-channel. ( $\alpha = 0.154$ ,  $g = 5$  mm,  $LE = 45^\circ$ )

gradient in vertical direction exists at  $U_\infty = 0.135$  m/s, with a difference of 6 percent points between  $z/h = 0$  and 0.9. The turbulence intensity remains between 1.5 and 2% in the top 2/3 of the channel depth, similar to the empty test section. An increase of  $Tu$  is observed in the bottom 1/3, with a local peak at  $y/W \approx 0.2$ ,  $z/h = 0.1$ – $0.2$ . This peak is somewhat puzzling, but might be related to the secondary flow in the sub-channel. This secondary flow is formed by a downward movement at the sub-channel walls, and a convergent upward movement in the centre-plane, as indicated by the dashed arrow in figure 4.6b at  $U_\infty = 0.135$  m/s. This motion might form a weak streamwise vortex, whose core is located at the turbulence peak. The highest vertical velocity of this secondary flow is around 3% of the plane mean.

For the lowest velocity  $U_\infty = 0.045$  m/s, the turbulence intensity increases to over 3%, with particularly high values in the centre-plane just below the water surface and above the bottom plate. These high values are caused by boundary layer separation with subsequent transition to turbulence at the entrance to the sub-channel due to the negative pressure gradient. Separation bubbles are observed on the bottom plate and below the free surface. Both separations are suppressed at velocities above  $U_\infty \approx 0.080$  m/s.

#### 4.3.4 Flow development along the streamwise direction

To estimate the flow quality throughout the streamwise extent of the sub-channel, LDV measurements in 5 cross-stream half-planes at  $x/L = 0.18, 0.33, 0.48, 0.63, 0.83$  were performed (the planes are 150 mm apart). The streamwise velocity in all planes of figure 4.7 is non-dimensionalized by the average velocity of the plane at model location, which makes velocity changes along streamwise direction visible. The bold red frame marks the plane at model location, which was discussed already in relation to figure 4.6b. The data show that the turbulence intensity remains between 1.5 and 2% throughout the sub-channel. Upstream of the model location, a horizontal velocity gradient is visible, with velocities close to the side wall being up to 6% lower than the average. This is a remnant of the flow expansion at the sub-channel entrance. This horizontal gradient vanishes at model location. Downstream of the model location, a vertical velocity gradient develops, with the flow in the bottom 1/3 of the sub-channel being up to 6% faster than the average. The top 2/3 of the flow field maintains a constant velocity (within  $\pm 2\%$ ) throughout the sub-channel extent.

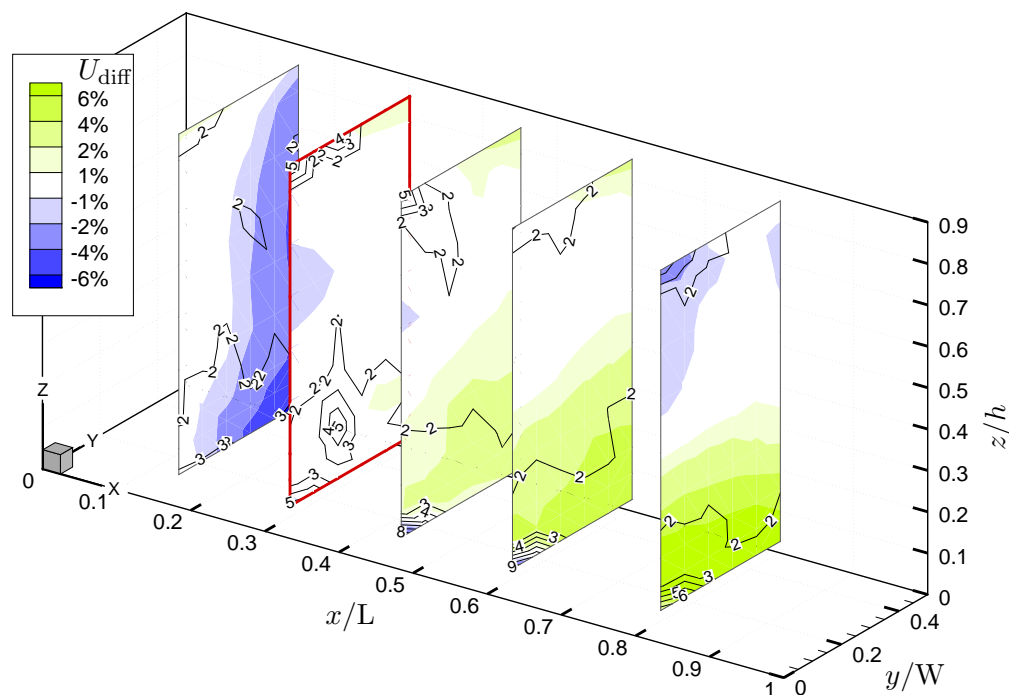


FIGURE 4.7: Streamwise velocity and turbulence contours in one half-plane of the sub-channel. The colour contours show  $U_{diff}$ ; the contour lines represent  $Tu$  [%]. The plane at model location is marked by the bold red frame. ( $U_\infty = 0.90$  m/s,  $\alpha = 0.154$ ,  $g = 5$  mm,  $LE = 45^\circ$ )

### 4.3.5 Dependence on screen porosity

The screen porosity  $\alpha$  was kept unchanged at a medium value of 0.154 during all cylinder experiments. This is why the flow quality at other porosities was not studied in detail. A comparison of the flow uniformity at model location for  $\alpha = 0.041$ , 0.154 and 0.39 at  $U_\infty = 0.090$  m/s is shown in figure 4.8. This data suggest that the flow quality does not change considerably for porosities above the used  $\alpha = 0.154$ . The lowest value of  $\alpha$ , on the other hand, leads to a deterioration of the flow uniformity inside the sub-channel, with large-scale flow separation below the water surface and on the bottom plate (figure 4.8a).

### 4.3.6 Side walls leading edges

It was found that the horizontal  $U$ -profiles could be slightly improved by tilting the side wall leading edges inwards. The stagnation points (actually lines) were observed not to lie on the tips of the leading edges, when these were oriented parallel to the flow direction. Due to the global inflow characteristics, they were located on the inside, approximately 20 mm downstream of the tips. When tilting the vertical leading edges



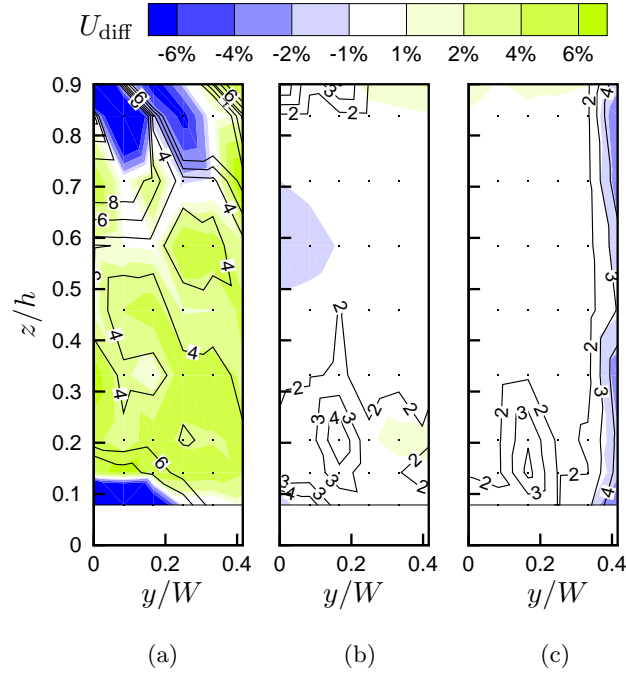


FIGURE 4.8: Flow uniformity at model location for three different screen porosities  $\alpha$ : (a) 0.041, (b) 0.154, (c) 0.39. The colour contours show  $U_{\text{diff}}$ ; the contour lines represent  $Tu$  [%]. The dots mark LDV sampling points. ( $U_{\infty} = 0.090$  m/s,  $g = 5$  mm,  $LE = 45^{\circ}$ )

inwards by  $45^{\circ}$ , the stagnation points were moved onto the leading edge tips. This also slightly improved the horizontal velocity profiles at the model location. Figure 4.9a shows two velocity profiles at the entrance to the sub-channel ( $x = -365$  mm). The profile with a leading edge tilt of  $45^{\circ}$  is considerably straighter, and possesses a less pronounced velocity deficit at the side wall. This improvement persists at the model location, as seen in figure 4.9b. Here, the variation along the span decreases below  $\pm 0.5\%$ .

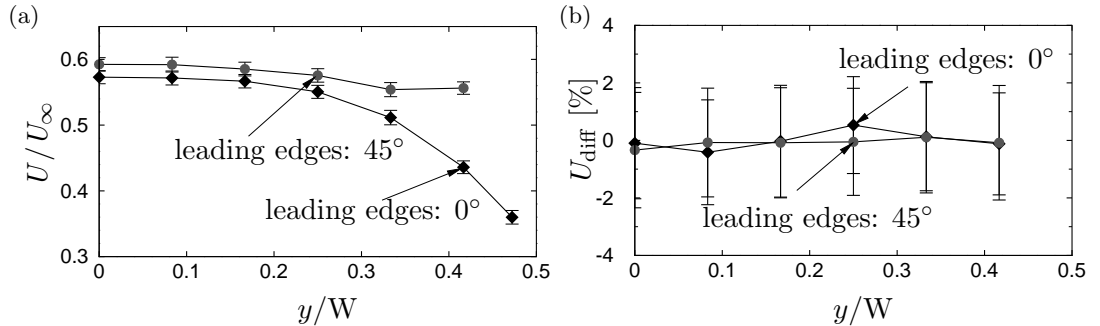


FIGURE 4.9: The effect of tilting the wall leading edges inwards by  $45^{\circ}$  on the uniformity of horizontal  $U_0$ -velocity profiles. (a) Velocity profiles at the entrance to the sub-channel; (b) at model location. Error bars are  $\pm \overline{u'}$ . ( $U_{\infty} = 0.09$  m/s,  $\alpha = 0.154$ ,  $g = 5$  mm)

## 4.4 Conclusions

The ‘sub-channel’ is essential for the present study, as it expands the Reynolds number range of the FLAIR water channel. The insert consists of a U-shaped acrylic structure with a perforated screen at its downstream end. The screen increases the pressure inside of this structure, leading to an uniform velocity reduction of the incoming flow. Experiments can be performed in the rear 2/3 of the structure, which possess a uniform streamwise velocity within  $\pm 2\%$  along the streamwise direction.

To maintain adequate flow quality inside the sub-channel several conditions must be met: The structure must be suspended above the main channel floor, leaving a gap of 5-10 mm. A rough estimate of the gap size is the displacement thickness of the main channel floor boundary layer. Very low screen porosities, below  $\alpha \approx 0.1$  should be avoided, as they lead to a strong deterioration of flow quality. The increased pressure gradient at low  $\alpha$  results in large-scale flow separation on the bottom plate and at the free surface at the sub-channel entrance. A porosity of 0.154 was used in all present experiments. This setting results in very good flow quality at  $U_\infty \geq 0.090$  m/s, and in acceptable quality for lower velocities. The leading edges of the side walls should be tilted inwards by  $45^\circ$  to improve the horizontal velocity profiles.

A velocity gradient along the vertical direction was observed, with the flow in the bottom 1/3 of the sub-channel being up to 6% faster than in the top 2/3. This might lead to non-uniform shedding patterns if long cylinder models are mounted vertically. Nevertheless, all models were studied in vertical orientation to achieve larger length-to-diameter ratios, and no substantial differences in flow behaviour were observed along the cylinder span. Quantitative measurements were performed in the top 2/3 of the water depth, where the flow has been shown to be more uniform.

## Declaration for Thesis Chapter 5

### Declaration by candidate

In the case of Chapter 5, the nature and extent of my contribution to the work was the following:

| Nature of contribution  | Extent of contribution (%) |
|---|----------------------------|
| Design & execution of experiments. Design & (partial) construction of experimental models. Data processing & presentation. Interpretation of results. | 80%                        |

The following co-authors contributed to the work. Co-authors who are students at Monash University must also indicate the extent of their contribution in percentage terms:

| Name                 | Nature of contribution  | Extent of contribution (%) for student co-authors only |
|----------------------|---|--|
| Prof. Mark Thompson  | Research guidance & interpretation of results. Revisions of manuscript and proof-reading. | -  |
| Anirudh Rao          | Help with execution of experiments. Interpretation of results. Proof-reading.             | 20%  |
| Prof. Kerry Hourigan | Research guidance & interpretation of results. Revisions of manuscript and proof-reading. | -  |
| Prof. John Sheridan  | Research guidance & interpretation of results. Revisions of manuscript and proof-reading. | -  |

Candidate's  
Signature

*ARadi*

Date

30.8.2013

### Declaration by co-authors

The undersigned hereby certify that:

- (1) the above declaration correctly reflects the nature and extent of the candidate's contribution to this work, and the nature of the contribution of each of the co-authors.
- (2) they meet the criteria for authorship in that they have participated in the conception, execution, or interpretation, of at least that part of the publication in their field of expertise;
- (3) they take public responsibility for their part of the publication, except for the responsible author who accepts overall responsibility for the publication;
- (4) there are no other authors of the publication according to these criteria;
- (5) potential conflicts of interest have been disclosed to (a) granting bodies, (b) the editor or publisher of journals or other publications, and (c) the head of the responsible academic unit; and
- (6) the original data are stored at the following location(s) and will be held for at least five years from the date indicated below:

Location(s)

*Monash university LARDS*

[Please note that the location(s) must be institutional in nature, and should be indicated here as a department, centre or institute, with specific campus identification where relevant.]

Signature 1

*[Signature]*

Date *30/AUG/13*

Signature 2

*Anirudh*

*30 Aug 2013*

Signature 3

*[Signature]*

*30/8/2013*

Signature 4

*[Signature]*

*30/08/2013*



## Chapter 5

# Rotating cylinder

This chapter is based on:

RADI, A., THOMPSON, M. C., RAO, A., HOURIGAN, K. & SHERIDAN, J. 2013b Experimental evidence of new three-dimensional modes in the wake of a rotating cylinder. *Journal of Fluid Mechanics* (accepted for publication on 24.08.2013)

### 5.1 Introduction

The rotating cylinder can be considered as a means of active flow control. The spinning motion can lead to vortex shedding suppression and to a (less studied) modification of three-dimensional transitions. The existence of three-dimensional modes, and their dependence on the control parameters  $Re$  and  $\alpha$ , are the focus of this chapter.

The present experiments are motivated by the numerical study of Rao *et al.* (2013) (see §2.3 for a detailed discussion), which predict the existence of several previously unobserved linearly unstable three-dimensional modes. While linear stability analysis suggests that some of these modes exist for relatively limited ranges of Reynolds numbers and rotation rates, this may not be true for fully developed nonlinear wakes. We explore the fully developed flow for Reynolds numbers  $175 \leq Re \leq 275$  and rotation rates  $0 \leq \alpha \leq 2.5$ . Using particle image velocimetry and digitally post-processed hydrogen bubble flow visualizations, we confirm the existence of the predicted modes for the first time experimentally and report on observations of the one-sided shedding process, known as the ‘second shedding’ (Stojković *et al.* 2003; Mittal & Kumar 2003; Kumar *et al.* 2011).

## 5.2 Setup validation

The experimental setup (see §3.2) was validated by comparing results of two experiments to published data. First, a flow visualization study was undertaken for the case of a non-spinning cylinder ( $\alpha = 0$ ) to estimate the critical Reynolds numbers and to measure the characteristics of the well known modes A and B (Williamson 1988; Barkley & Henderson 1996). Second, the process of vortex shedding suppression was compared to PIV data of Kumar *et al.* (2011).

### 5.2.1 Non-rotating cylinder

A two-dimensional von Kármán vortex street was observed for Reynolds numbers up to  $Re = 160$ . The vortices were shed under an angle of up to  $12^\circ$  with respect to the cylinder axis (oblique shedding), a value which varied with time and along the spanwise direction (figure 5.1a). This is not surprising, as only careful manipulation of the cylinder end conditions can assure parallel shedding (Williamson 1996b).

For higher Reynolds numbers, irregularities and deformations of the shed vortices appeared. At  $Re \approx 175$ , the wake developed a fully three-dimensional character, known as mode A (Williamson 1988). Stability analysis predicts the critical Reynolds number to be approximately 190 (Barkley & Henderson 1996); however, the transition is hysteretic and finite-amplitude perturbations can cause premature onset for Reynolds numbers down to approximately 180 (Henderson 1997). Visualization of this mode in our water channel with the technique employed turned out to be challenging, and the hydrogen bubble wire had to be placed in the wake, to provide the picture seen in figure 5.1b. The wavelength of the spanwise modulations in this image is  $\lambda_z/d \approx 3.4$ . The preferred wavelength from Floquet stability analysis is  $3.96d$ , although the mode is unstable over a reasonably wide wavelength band (Barkley & Henderson 1996).

For Reynolds numbers above 200, mode B developed gradually, and dominated the wake for  $Re > 270$ , in good agreement with the careful experiments of Williamson (1996b). Figure 5.1c shows a flow visualization at  $Re = 275$ . Streamwise vortices of mode B are clearly distinguishable. Numerical processing of a sequence of 1000 pictures, as described in §3.5, shows an average spanwise wavelength of  $\lambda_z/d \approx 0.96$ . Floquet analysis predicts the most unstable wavelength as  $0.822d$  (Barkley & Henderson 1996). The Strouhal number is  $St = 0.194$ , in good agreement with values found in the literature (e.g.  $St \approx 0.202$  in Norberg 1987).

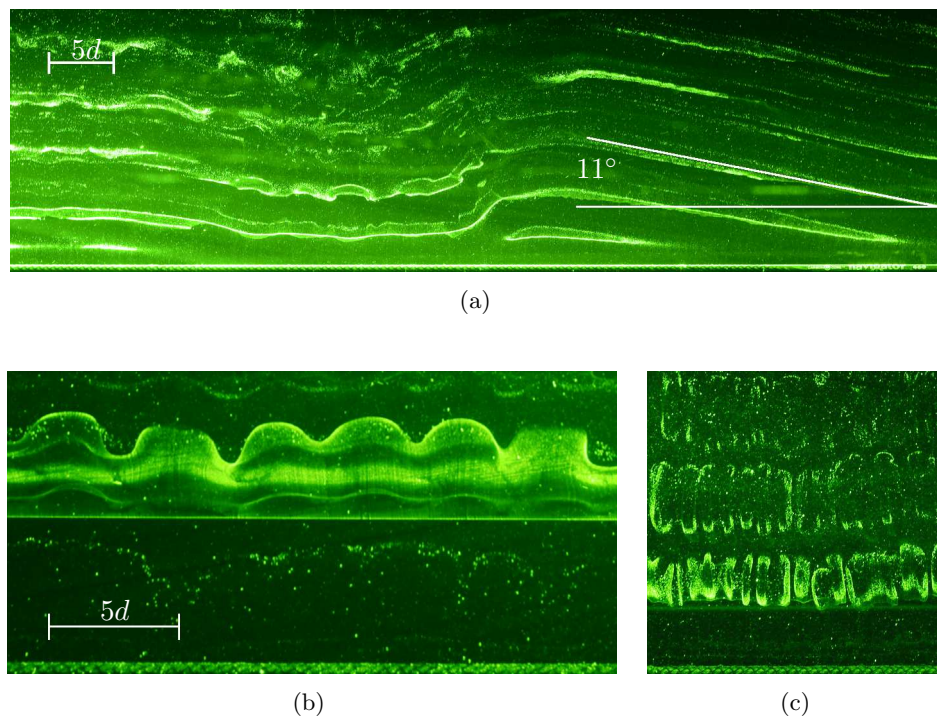


FIGURE 5.1: Hydrogen bubble flow visualizations of the non-rotating cylinder wake: (a) Oblique shedding on the right is observed simultaneously with a section of developing mode A in the left half of the picture at  $Re = 170$ . (b) Mode A at  $Re = 175$ , with a spanwise wavelength of  $\lambda_z/d \approx 3.4$ . The platinum wire is placed at  $6.5d$  downstream of the cylinder. (c) Mode B at  $Re = 275$ ; the average spanwise wavelength is  $\lambda_z/d \approx 0.96$ . The platinum wire is not visible in (a) and (c), being 5 cylinder diameters upstream of the cylinder. The scaling is the same for (b) and (c). The cylinder can be seen at the bottom edge of all pictures. The flow is from the bottom up.

### 5.2.2 Rotating cylinder

PIV data were recorded to validate the setup for the case of a rotating cylinder. Six rotation rates between  $\alpha = 0$  and  $\alpha = 2.0$  were chosen at  $Re = 200$ . For rotation rates above  $\alpha \approx 2$  and Reynolds numbers above 100, the von Kármán vortex street can be fully suppressed, resulting in a steady laminar double shear layer wake.

Kumar *et al.* (2011) demonstrated this phenomenon experimentally for Reynolds numbers  $Re = 200$ –400, and rotation rates  $0 < \alpha \leq 2.1$ . Their figure 6 shows the decay of vortex shedding at  $\alpha \approx 1.95$  for  $Re = 200$ . We repeated these experiments, and our results are shown in figure 5.2; the same flow behaviour was observed. The flow resembled the typical von Kármán vortex street for low values of  $\alpha$ . For increasing rotation rates, the double-row of vortices was deflected in cross-stream direction. At the same time, the shedding became weaker, as indicated by the decreased peak vorticity values. For  $\alpha = 1.85$ , the vortices were highly stretched, and the wake resembled a

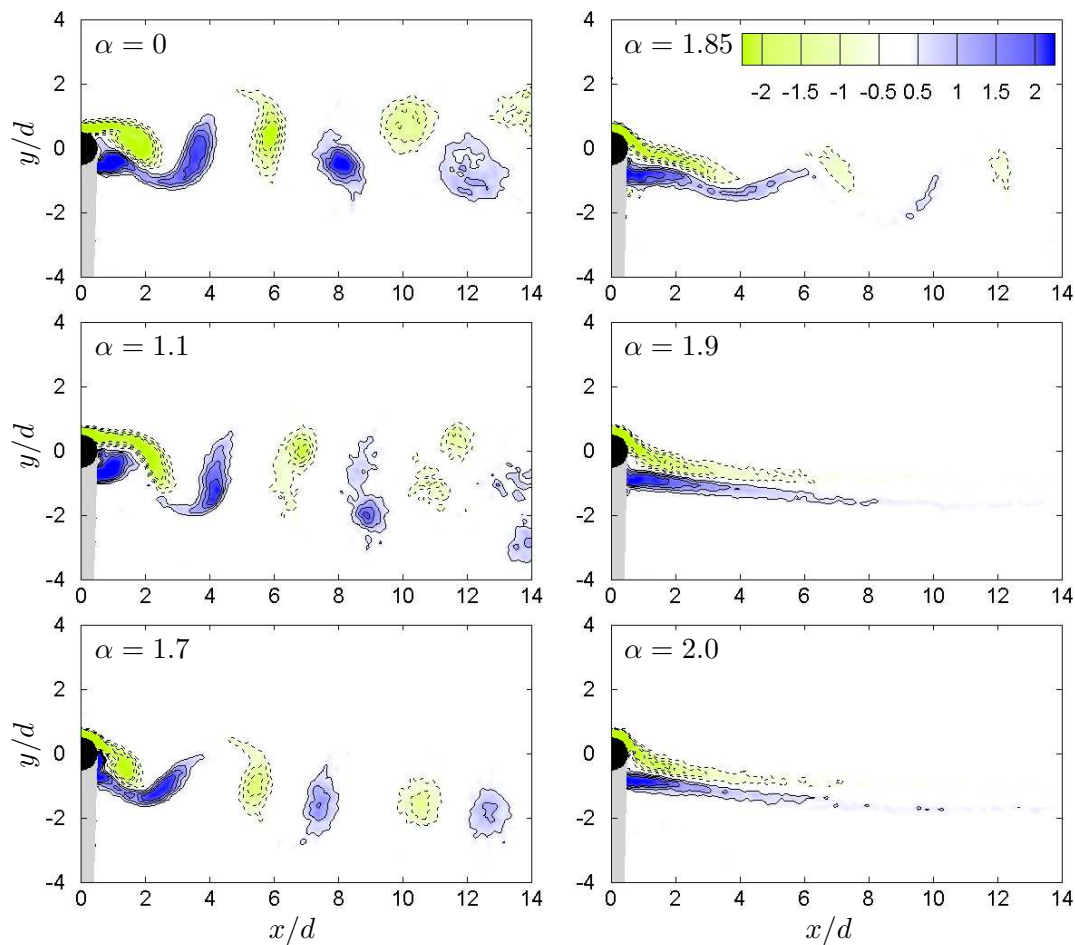


FIGURE 5.2: Instantaneous PIV vorticity fields in the  $x$ - $y$  plane at  $Re = 200$  for the marked clockwise rotation rates. Vorticity is non-dimensionalized as  $\omega_z d/U$ , with solid lines representing positive values. Vortex suppression is observed beyond  $\alpha \approx 1.9$ . This figure should be compared directly to figure 6 in Kumar *et al.* (2011). The grey areas mask spurious vectors in the obstructed region of the laser sheet.

snake-like pattern. For  $\alpha = 1.90$ , shedding ceased completely, and the steady wake consisted of the merger of the two separated shear layers. This wake showed some intermittent ‘flapping’, probably due to slight variations of freestream velocity. This rotation rate marks the critical value separating the shedding and non-shedding regimes. For all the higher rotation rates investigated at this Reynolds number,  $1.9 < \alpha \leq 2.10$ , the wake remained steady.

Compared with experiments by Kumar *et al.* (2011), the re-stabilization happened in our case at a slightly lower value of  $\alpha = 1.9$ . However, this is consistent with the linear stability analysis by Rao *et al.* (2013), and two-dimensional simulations by Mittal & Kumar (2003), which estimate the critical value to be  $\alpha = 1.91$ .



## 5.3 Results & discussion

The main experiments consisted of flow visualizations at  $Re = 250$  and  $Re = 275$ , with subsequent numerical analysis of the digital images, as described in §3.5. For rotation rates  $0 \leq \alpha < 2.5$ , all modes predicted by the linear stability analysis of Rao *et al.* (2013) were observed. In addition to the well known mode B for  $\alpha = 0$ , these were: the subharmonic mode C; mode D and its non-shedding version mode E; and for rotation rates above  $\alpha = 2.3$ , a short-wavelength mode F on the cylinder surface. The modes differ in their wavelengths, spatio-temporal symmetries and underlying base flows. Evidence will be presented of mode F being a travelling wave mode.

### 5.3.1 Mode C

Mode C is described for  $Re = 275$  and  $\alpha = 1.7$ . As seen in figure 2.16, this parameter combination lies in the centre of the region of the parameter space occupied by this linearly unstable mode. Here, the linear amplification rates can be expected to be highest, which should make the detection of this mode in experiments easier. Nonetheless, the visibility of this mode was very dependent on the correct positioning of the hydrogen bubble wire. Cross-stream movements of the wire of  $\pm 1$  mm made this mode invisible and created the impression of only slightly disturbed two-dimensional laminar shedding. Once the correct wire location was found, the mode could be visualised reliably for a wide range of rotation rates. However, this difficulty in detection is an indication that the saturated state of the mode does not lead to strong distortion of the otherwise two-dimensional nature of the wake, at least at this Reynolds number.

Figure 5.3a shows the strict periodicity of mode C along a span of  $70d$ . The flow structures will be described with the help of the close-up views in figure 5.3b. The photograph on the left is a flow visualization in the  $x$ - $z$  plane similar to 5.3a, whereas the right picture shows the wake cross-section in the  $x$ - $y$  plane. The later picture shows the first frame of a PIV double-exposure (inverse-colour), overlaid with  $\omega_z$ -vorticity contours calculated for this vector field. The non-dimensional contour levels range from  $-3$  to  $+2.5$  excluding 0, in steps of  $\pm 0.5$ , with solid lines denoting positive vorticity. The hydrogen bubble wire upstream of the cylinder was switched on during the recording, such that the bubble sheet cross-section can be seen as a dark streakline. The black speckles are PIV seeding particles. The two views in figure 5.3b were not recorded simultaneously, but represent the same stage of the shedding cycle. The approximate

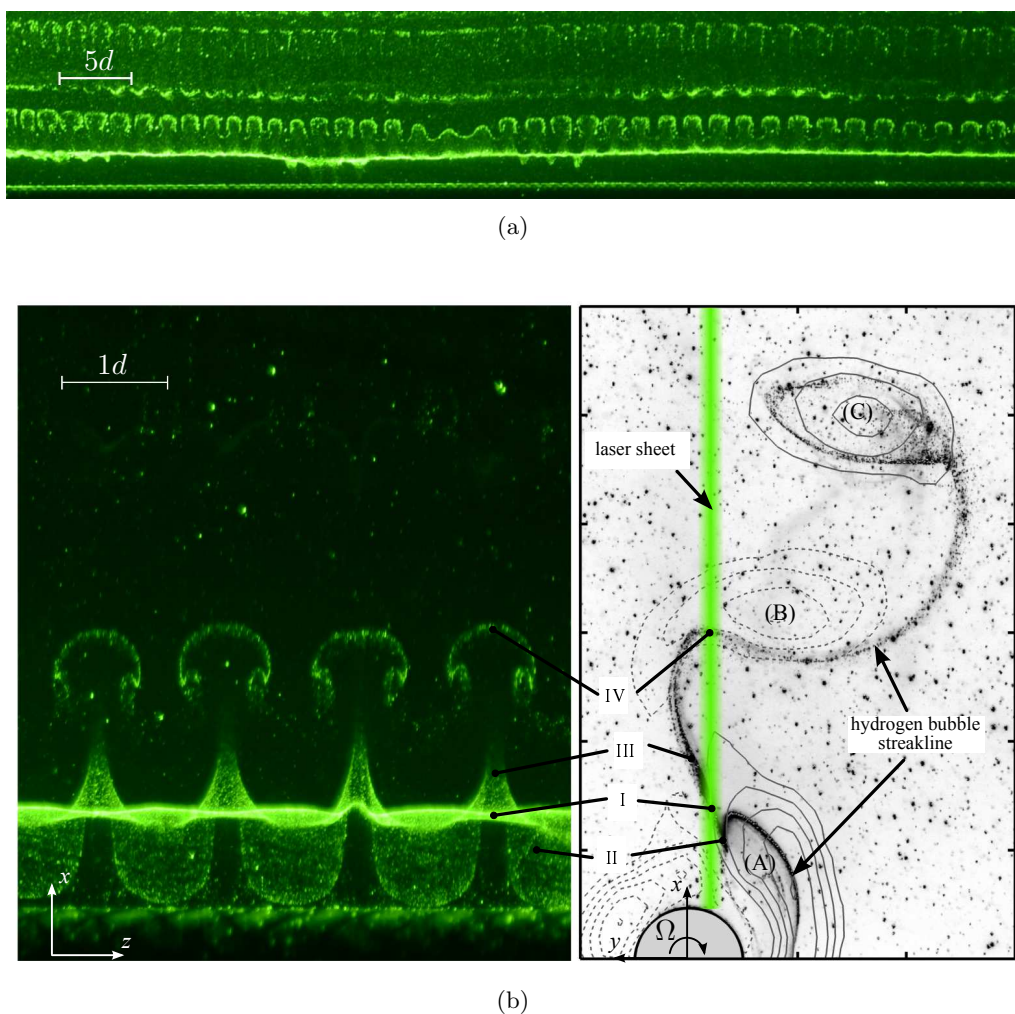


FIGURE 5.3: The subharmonic mode C at  $Re = 275$ . (a) Large-field view of the wake ( $70d \times 12d$ ), showing the strict spanwise periodicity at  $\alpha = 1.2$ . (b) Close-up view of the near wake at  $\alpha = 1.7$ : A row of streamwise double-vortices is shown in the flow visualization on the left, and the corresponding wake cross-section is seen on the right (both views are to scale). In the right picture, instantaneous vorticity contours are overlaid on the PIV snapshot. The hydrogen bubbles create the dark streakline. The flow is from the bottom to the top.

location of the laser sheet used for flow-visualization is marked in the right picture.

The flow visualization on the left can be interpreted the following way: The bubble sheet passes the rotating cylinder on the side facing away from the observer. The bubbles enter the near wake and cross the laser sheet at the location marked by I. The bubble sheet moves out of the plane of the paper when it is lit up as the bright wavy line. Approximately at this location the sheet splits up into a section which is moving upstream (marked as II) and which is being wrapped around the forming vortex core (A), and a section which is moving downstream (III). Already at this stage, the bubble sheet is deformed with a periodic spanwise modulation. The upstream-moving part

consists of a series of U-shapes, where the missing sections have been ‘folded out’, and move into downstream direction. These sections form the stems (III) leading to the mushroom shapes at IV. These shapes are typically created by a row of counter rotating double-vortices. The laser sheet cuts through these streamwise vortices at IV.

It is evident that sections III experience strong stretching between the forming vortex (A) and the downstream moving vortex (B), which leads to amplification of streamwise vorticity. Furthermore, the streakline shape in the right picture of figure 5.3b suggests that the bubble sheet entrains the near wake in the vicinity of an instantaneous saddle point (Délery 2001), close to marker I. This explains the splitting of the sheet into upstream and downstream moving sections. These observations lead to the conclusion that the mode C instability develops within  $1-2d$  downstream of the cylinder, and its streamwise double-vortices reside in the braid region and get amplified through stretching of this braid region between consecutive von Kármán vortices.

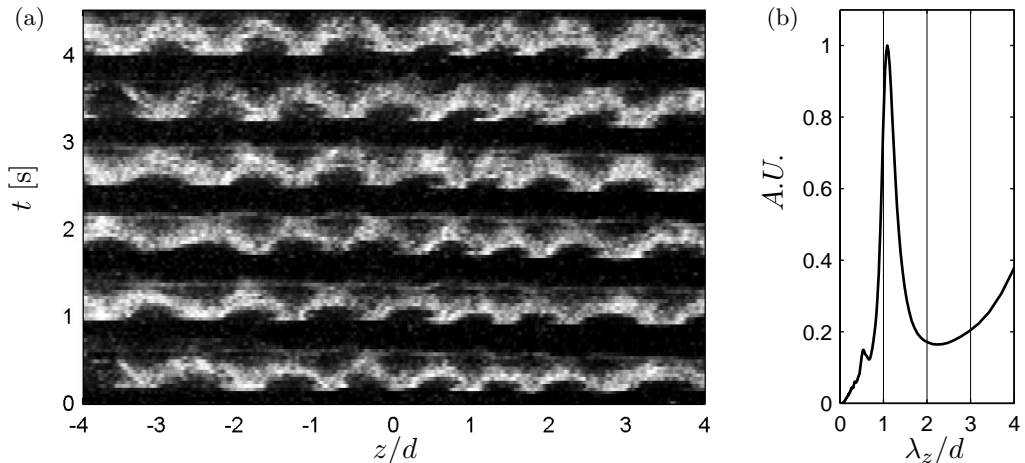


FIGURE 5.4: (a) Space-time diagram at  $x/d = 3$  and (b) time-averaged spanwise wavelength spectrum of mode C at  $Re = 275$  and  $\alpha = 1.7$ . The dominant spanwise wavelength is represented by the peak in the spectrum at  $\lambda_z/d \approx 1.1$ . The subharmonic nature of mode C is revealed in (a) by the interchange of peaks and valleys every shedding period.

To investigate the temporal development of mode C, space-time diagrams have been created using the technique described in § 3.5. Figure 5.4a shows a space-time diagram at  $Re = 275$  and  $\alpha = 1.7$ , created from pixel data at  $x/d = 3$ . At this location, the streamwise vortices are visible as mushroom shapes. The subharmonic nature of mode C can be inferred from the arrangement of these patterns, each of which is repeated every second shedding cycle. Equivalently, every ‘valley’ of the pattern is aligned with a ‘peak’ of the successive shedding cycle.

Figure 5.4b shows the spanwise wavelength spectrum, created by performing an FFT analysis of the space-time diagram. The peak shows the dominant spanwise wavelength of  $\lambda_z/d = 1.1$ . A small side peak can be seen at the first higher harmonic (half the wavelength). The spectral power rises again for larger wavelengths due to large-scale spanwise irregularities of the wake.

### 5.3.2 Co-existence of modes B and C

The wake of a stationary cylinder ( $\alpha = 0$ ) at  $Re = 275$  exhibits an (almost) pure mode B wake. A rotating cylinder at the same Reynolds number, but at  $\alpha = 1.7$ , leads to pure mode C, as shown in the previous section. It follows that a transition from one mode to the other has to take place somewhere between these two rotation rates. According to the neutral stability curves in figure 2.16, the following observations should be expected: Mode C is linearly unstable only above the critical rotation rate  $\alpha_{\text{crit}} \approx 1.5$ ; for smaller rotation rates, the wake should exhibit purely two-dimensional shedding; for rotation rates  $\alpha \lesssim 1.1$ , mode A becomes unstable, before finally changing to mode B close to  $\alpha = 0$ . The aim was to test whether this rather complex transition scenario really takes place in the experiment.

The same type of experiments as in the previous section (flow visualizations, with subsequent numerical analysis) were performed for  $0 \leq \alpha \leq 1.7$ , at  $Re = 275$ . In contrast to the scenario outlined above, mode C was found to dominate the wake for rotation rates far below  $\alpha_{\text{crit}} \approx 1.5$ . Its flow structures and subharmonic nature were observed at  $\alpha = 1.0$ . Unlike the linear prediction, the wake never lost its three-dimensionality, meaning that no purely two-dimensional shedding was observed. In addition, no traces of mode A could be found in flow visualizations for  $\alpha < 1$ .

Nevertheless, the absence of mode A cannot be claimed from these data alone. This mode is very difficult to visualise even under optimal conditions of a stationary cylinder, and might have been masked by the structures of modes B and C. On the other hand, it may have contributed to (or even caused) the increased randomness of the flow for  $\alpha < 1$  by its intrinsic broad-band nature (Henderson 1997). The existence, or possible contribution, of mode A was not explored further.

The spanwise wavelength of mode C was found to be dependent on the rotation rate. Figure 5.5a shows that in the linearly unstable region (to the right of the dashed vertical line), the wavelength was  $\lambda_z/d \approx 1.1$ , in good agreement with predictions

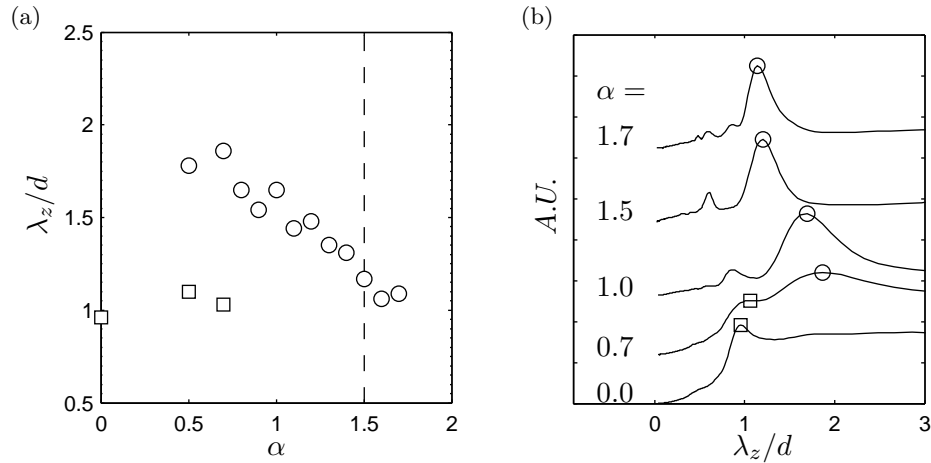


FIGURE 5.5: Co-existence of modes B and C at  $Re = 275$  is shown in terms of spanwise wavelengths. (a) Wavelength as function of rotation rate. Circular symbols depict mode C, square symbols are associated with mode B. To the right of the dashed vertical line, mode C is linearly unstable, according to Rao *et al.* (2013). (b) Wavelength spectra for chosen rotation rates show a gradual transition to mode C for increasing  $\alpha$ . The spectra are shifted with respect to each other in vertical direction for clarity. The spectra are based on measurements at  $x/d = 3 - 5$ , depending on  $\alpha$ .

by Rao *et al.* (2013). For rotation rates below  $\alpha_{\text{crit}} \approx 1.5$ , the wavelength of mode C increased steadily as  $\alpha$  was decreased, and almost doubled for  $\alpha = 0.5$  (round symbols).

For rotation rates below  $\alpha = 1.0$ , the flow became increasingly irregular. Neither the wavelength, nor the subharmonic nature of mode C could be clearly observed. The three-dimensional flow patterns were changing randomly with time and lacked spatial coherence. This leads us to conclude, that this marked the practical transition from mode C to B. This claim is supported by the growth of a second peak in the wavelength spectra at  $\lambda_z/d \approx 1$ , a wavelength associated with mode B. These peaks are represented by square symbols in figure 5.5a.

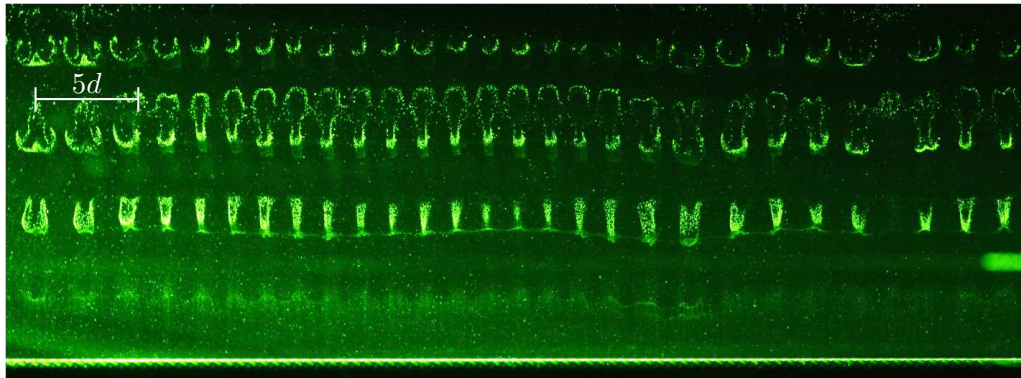
Some chosen wavelength spectra are shown in figure 5.5b. The identified peaks of mode B and C are marked by round and square symbols, consistent with figure 5.5a. The spectra can be interpreted as follows. Mode B exists in a spanwise incoherent flow ( $\alpha = 0.0$ ). Its peak is small, and hardly dominates the long-wavelength background noise, which is the plateau at  $\lambda_z/d > 1$ . Out of this noise, the peak of mode C rises, when  $\alpha$  is increased. For very small rotation rates, it is centred around a wavelength of two cylinder diameters, but shifts to lower wavelengths for higher  $\alpha$ , reaching its terminal value of  $\lambda_z/d \approx 1.1$  at  $\alpha = 1.5$ . Throughout this process, the peak becomes narrower and higher, soon dominating the background noise. This is caused by the flow becoming more coherent in the spanwise direction; the flow reaches a high degree of

regularity already at  $\alpha = 1.0$ .

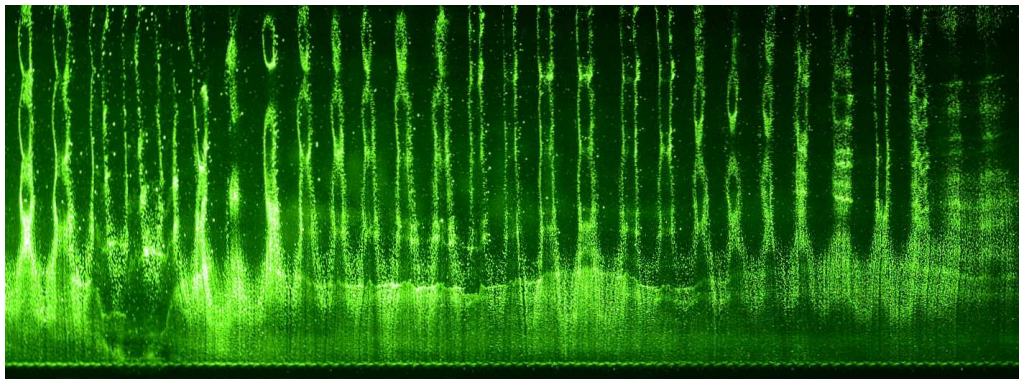
One should bear in mind that these data are extracted from flow visualizations, whose final appearance depend on the position of the hydrogen bubble wire and the laser sheet. In addition, the streamwise location in the pictures from which the wavelength spectra were created influenced, to some degree, the relative strengths of the two peaks representing modes B and C. In this sense, the data shown above should be treated as a rough sketch of the transition process between these two modes. A more robust experimental technique is needed to investigate this transitional region in more detail.

The observation of mode C below the critical rotation rate of  $\alpha_{\text{crit}} \approx 1.5$ , stands out as the greatest difference between linear stability analysis and experiment. An explanation for this unexpected behaviour might be the initial conditions in the experiments. Each point on the parameter map was approached from  $\alpha = 0$ , by quickly spinning up the cylinder from rest. This way, the initial condition at  $Re = 275$  was a fully developed mode B. Within a few seconds, the cylinder was spinning at its terminal rotation rate, and any new mode would have to grow on this base flow. This excludes a possible hysteresis effect of mode C, which may have been observed if the rotation rate was changed continuously. Instead, it is speculated that the presence of mode B triggers mode C, forcing it outside its predicted instability region to lower values of  $\alpha$ .

A similar relationship exists between modes A and B of a stationary cylinder. Mode A becomes linearly unstable through a sub-critical bifurcation at  $Re \approx 190$  (Henderson 1997). The critical Reynolds number for the onset of linear instability of mode B is  $Re \approx 260$ . This number is derived assuming a purely two-dimensional base flow. In spite of this, mode B has been experimentally and numerically observed by many researchers for Reynolds numbers below this critical value, some of them as low as  $Re = 220$  (Williamson 1988; Zhang *et al.* 1995; Thompson *et al.* 1996). Henderson (1997) and Barkley *et al.* (2000) explain this observation by a nonlinear interaction of these modes, in which mode A has a destabilizing effect on mode B, and mode B has a stabilizing effect on mode A, with a resulting mixed-mode state emerging from  $Re \approx 230$  on. Sheard *et al.* (2003a) extended this further, using a coupled Landau model, showing that in practice the transition from mode A to mode B occurs over the Reynolds number range  $230 \leq Re \leq 260$ . Remarkably, once the Reynolds number exceeds the critical value of  $Re \approx 260$ , this mixed-mode state gives way to what appears to be a much more ‘pure’ mode B wake.



(a)



(b)

FIGURE 5.6: Flow visualizations of (a) mode D and (b) mode E at  $Re = 250$ ,  $\alpha = 1.9$  and  $\alpha = 2.1$ , respectively. The flow is from bottom up.

A similar nonlinear interaction may be at play at the transition of mode B to C, with rotation rate  $\alpha$  as the control parameter. Confirmation of this conjecture, and the general influence of initial conditions on mode C, need further investigation.

### 5.3.3 Modes D & E

Once the rotation rate was increased above  $\alpha \approx 1.85$ , two new modes, termed here as modes D and E, developed in rapid succession on further increasing the rotation rate. As they have very similar characteristics, both modes will be discussed in this section. Note that the following experiments were performed at a slightly lower Reynolds number of  $Re = 250$ .

Linear stability analysis predicts mode D to exist for a narrow band of rotation rates, approximately  $1.85 < \alpha < 1.95$  (Rao *et al.* 2013). At these rotation rates, the cylinder wake is on the verge of undergoing transition from a shedding state to a laminar



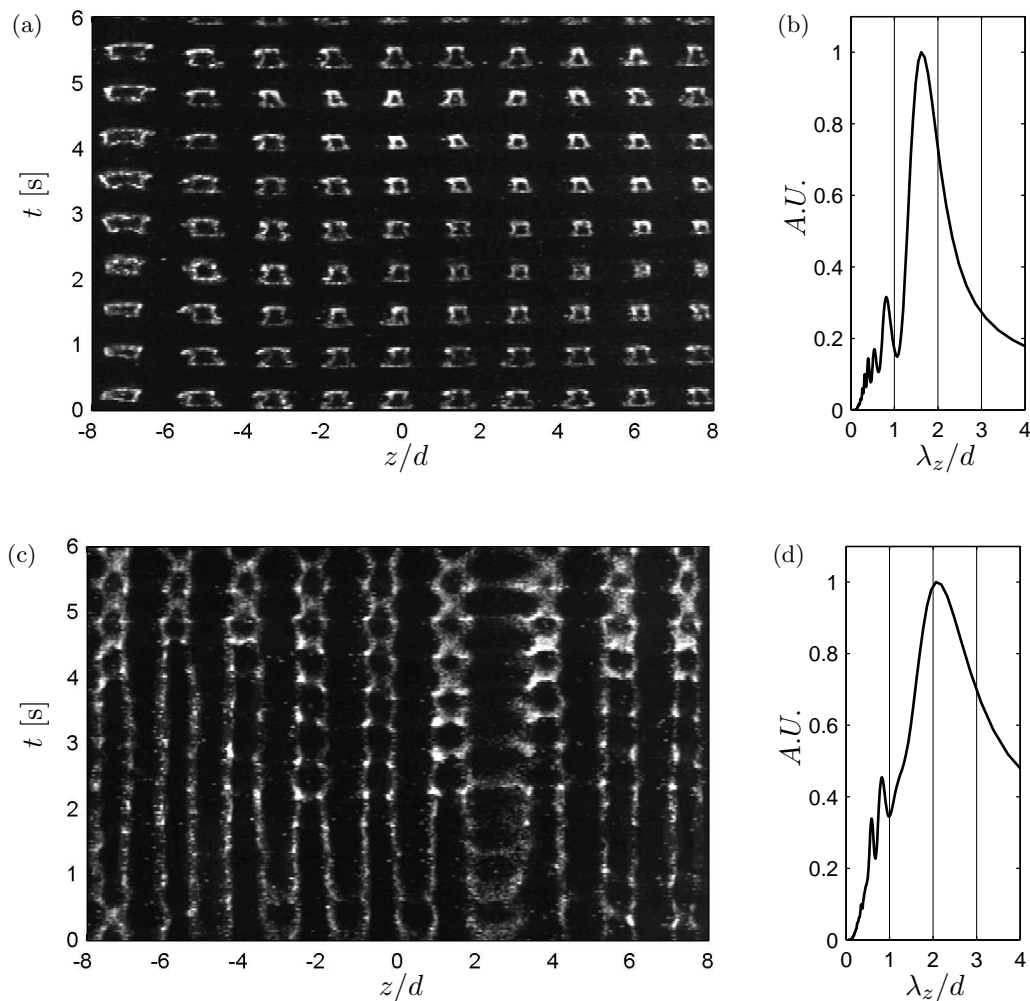


FIGURE 5.7: Space-time diagrams of (a) mode D at  $\alpha = 1.9$ ; and (c) mode E at  $\alpha = 2.1$  (both created at  $x/d = 9.2$ ). The time-averaged wavelengths are  $\lambda_z/d \approx 1.7$  and  $\lambda_z/d \approx 2.1$ , as seen in wavelength spectra (b) and (d), respectively.

steady double-shear layer wake. Mode D consists of uninterrupted streamwise vortices, which wind around the (now weakened) von Kármán vortices, resembling a serpentine pattern. Figure 5.6a shows a plan view of this wake at  $\alpha = 1.9$ . The hydrogen bubble sheet is wrapped around the streamwise vortices of mode D, and becomes illuminated when these cross the laser sheet. The streamwise distance of the illuminated sections in this image reflects the separation of the von Kármán vortices.

Figure 5.6b shows the wake at a slightly higher rotation rate of  $\alpha = 2.1$ , for which the two-dimensional von Kármán shedding no longer occurs. Superimposed on this steady wake, steady streamwise vortices can be seen, with a spanwise spacing similar to that of mode D. Due to the different base flow, this mode is referred to as mode E.



The temporal behaviour of both modes can be seen in the space-time diagrams of figure 5.7. Mode D is periodic in time with  $St = 0.206$  (figure 5.7a). Mode E is periodic in the spanwise direction, but steady in time, exhibiting only slight variations due to a small amount of unsteadiness of the wake. Particularly the diamond shaped cells connecting the vertical traces in figure 5.7c are formed by a remnant shedding oscillation of the double-shear layer. The reason for the changing linking between the longitudinal vortices at  $z/d = 1-4$  is not clear, but is probably caused by a slight flow disturbance. Yet, for both modes, the structures are stationary in the spanwise direction. In the case of mode D, von Kármán shedding is strictly periodic and parallel to the cylinder axis.

The spanwise wavelengths are  $\lambda_z/d = 1.7$  for mode D, and  $\lambda_z/d = 2.1$  for mode E, as can be seen in the wavelength spectra of figure 5.7b and d. It must be emphasized that these values are an average over the measured space and time domains. The space-time diagrams of figure 5.7 show only a small spanwise section of the collected data, and also for a particular time window. Particularly for mode D, the full data set shows a slow change in wavelength, which decreases from  $\lambda_z/d = 1.8$  to 1.6 over a time period of 45 s (68 shedding periods).

One concern regarding the use of qualitative flow visualization over extended streamwise domains, as in case of modes D and E, is the streakline effect with its spatially integrated view of the flow patterns. Combined with vortex stretching and the slow diffusion of the hydrogen bubbles as a passive scalar (Smits & Lim 2000, chapter 3.5), this effect can lead to a misinterpretation of the existence and strength of vorticity (this is shown impressively in Cimbala *et al.* 1988).

An estimate of the streakline effect for mode E is given in figure 5.8. Following Cimbala *et al.* (1988), the hydrogen bubble wire was placed at increasing distances downstream of the cylinder. The photographs show that the bubble sheet is deformed periodically along the span as far as  $x/d > 30$ , meaning that the streamwise vortices of mode E exist at least up to this distance. It can be concluded that the streakline effect plays a minor role in our visual data, and the photographs show a good estimate of the true location and strength of streamwise vorticity.

To support our flow visualizations and to confirm the spanwise periodicity of mode E, PIV data in the  $y-z$  plane at  $x/d = 3$  were recorded. For this plane orientation, the streamwise vortices ‘pierce’ the laser plane almost perpendicular and create a periodic

in-plane fluid motion. The vortices were strictly stationary, such that a time-average of 500 PIV snapshots (1 s apart) could be calculated. The insert on the lower right of figure 5.8 shows vorticity contours of this time-averaged vector field. Counter rotating vortex pairs can be clearly distinguished with a spanwise spacing of  $2.05d$ , confirming the flow visualizations and the space-time diagram.

Returning to the comparison of modes D and E, it has been mentioned that the transition between these modes is dominated by the gradual decay of the main vortex shedding. This makes it difficult to determine a precise critical rotation rate separating these two modes. Considering the similar wavelengths and spatio-temporal symmetries, we speculate that these modes result from the same physical mechanism, but grow on different but related base flows. As shown by PIV data in §5.2.2, shedding decayed for  $Re = 200$  and rotation rates beyond  $\alpha = 1.9$ . As the critical rotation rate of this process is only weakly dependent on Reynolds number, the wake can be expected to undergo transition back to steady flow at a rotation rate in the range  $1.9 < \alpha < 2$ , even for Reynolds numbers above 200. This would explain the striking similarity between modes D and E.

We wanted to confirm this process at  $Re = 275$ , and link the flow fields in the wake cross section ( $x$ - $y$  plane) to visual observations from a side perspective. Figure 5.9 shows instantaneous PIV vorticity fields in the  $x$ - $y$  plane, and flow visualizations in the  $x$ - $z$  plane. As expected, the PIV data confirm the shedding decay in the range  $1.9 < \alpha < 2.1$ . Flow visualizations of the shedding wake show mode D structures, periodic in the spanwise and streamwise directions (figure 5.9c). Once the wake becomes steady, the spanwise periodicity persists, as seen in figure 5.9d, whereas the structures now resemble streamwise vortices in a plane parallel to the  $x$ - $z$  plane (mode E). The approximate location of the laser sheet, which creates these flow visualizations, is indicated in the PIV vorticity fields as a dashed line. The cut through the serpentine wake at  $\alpha = 1.9$  creates the interrupted patterns seen in 5.9c, whereas the cut through the steady wake at  $\alpha = 2.1$  appears in figure 5.9d as steady streamwise structures.

The PIV data of figure 5.9 give clues on the physical mechanism behind these two modes. Up to  $x/d \approx 4$ , the wakes of both modes are practically identical, consisting of a steady double-shear layer. Only further downstream, the wake develops an oscillation for  $\alpha = 1.9$ . A close-up of the time-averaged near-wake for  $Re = 250$  and  $\alpha = 1.90$  is shown in figure 5.10. The two prominent features of this flow field are a single

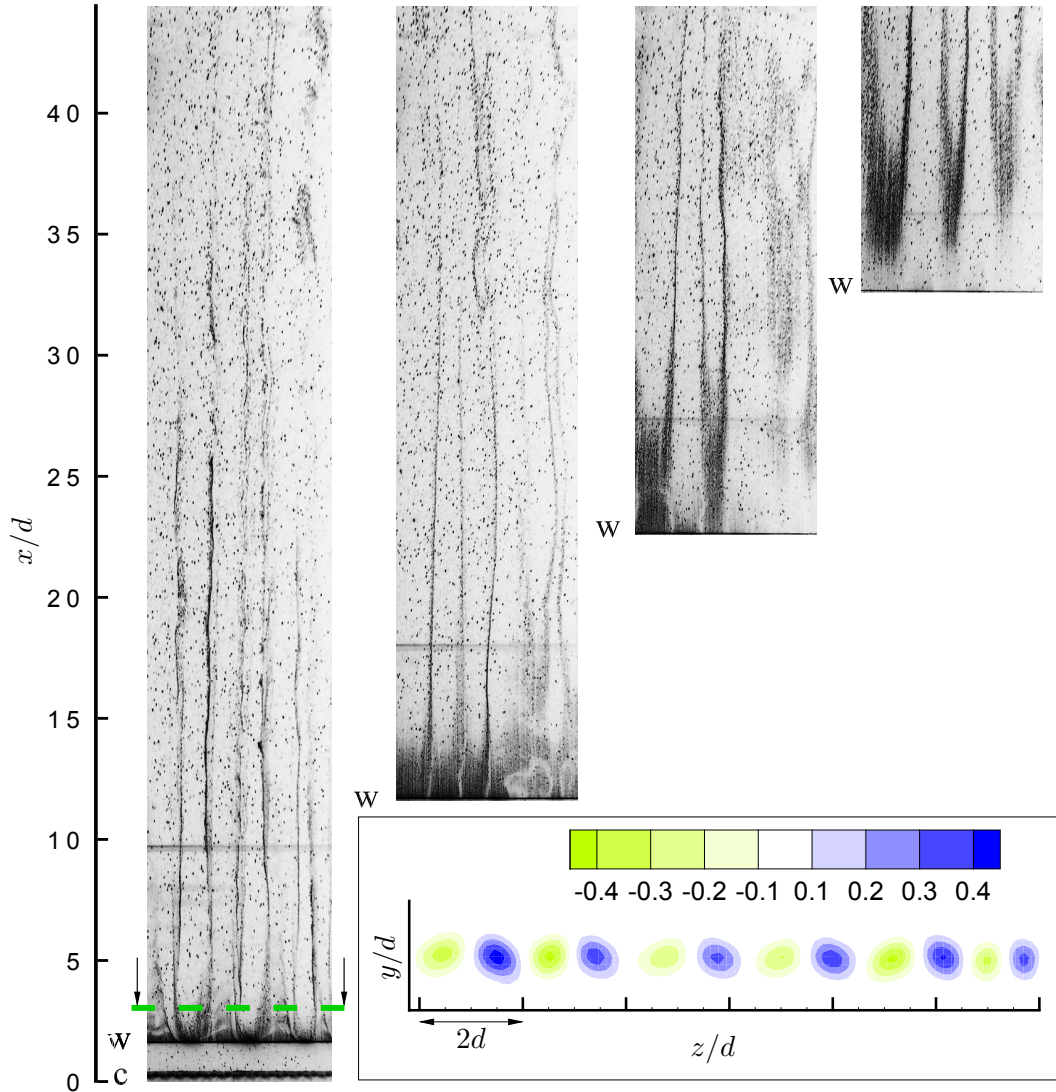


FIGURE 5.8: Inverse colour photographs of streakline patterns of mode E when the hydrogen bubble wire is placed at increasing distances downstream of the cylinder ( $Re = 250$ ,  $\alpha = 2.1$ ). The location of the cylinder is marked with 'c', all wire positions are marked with 'w'. The insert on the lower right shows non-dimensional streamwise vorticity obtained from time-averaged PIV data in the  $y$ - $z$  plane (the view is upstream; vorticity is non-dimensionalized as  $\omega_x d/U$ , with solid lines representing positive values). The PIV recording location is marked in the first photograph with a dashed line at  $x/d = 3$ .

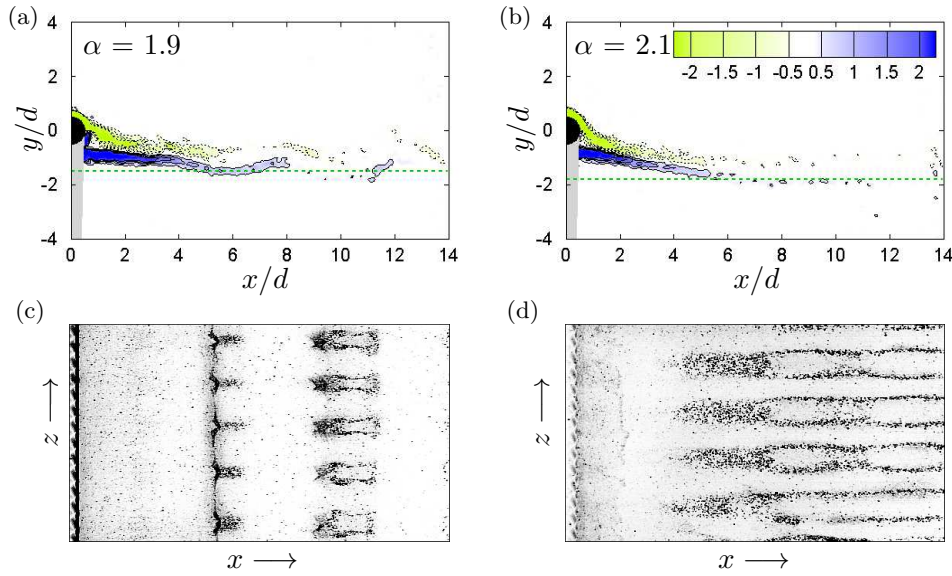


FIGURE 5.9: Comparing PIV and flow visualizations of modes D (a, c) and E (b, d) at  $Re = 250$ ,  $\alpha = 1.9$  and  $2.1$ , respectively. The PIV data show the instantaneous vorticity fields in the  $x$ - $y$  plane, and the flow visualizations are recorded from a side perspective in the  $x$ - $z$  plane. The horizontal dashed lines in (a) and (b) show approximate locations of the laser sheet used to illuminate the hydrogen bubbles. The images have the same scale, but were not taken simultaneously. The colour maps have been inverted to better show the flow structures. (The flow is from left to right; vorticity is non-dimensionalized as  $\omega_z d/U$ ).

closed recirculation region (rather a focal point), and a hyperbolic point at  $(x, y) = (1.52d, -0.66d)$ . The flow field of mode E at  $\alpha = 2.10$  is not shown, but displays the same characteristics, with the hyperbolic point moved slightly upstream, to  $(x, y) = (1.2d, -0.7d)$ .

The hyperbolic stagnation point is characterised by local acceleration of fluid and rapid stretching of vortices, resulting in amplification of vorticity perturbations. As shown by Kerr & Dold (1994) and Leblanc & Godefert (1999), hyperbolic instability can lead to formation of counter-rotating vortices ('ribs'), whose axes lie parallel to the direction of the diverging flow. This mechanism has been proposed by Williamson (1996b) and Leweke & Williamson (1998) as reason for mode B in the wake of a stationary cylinder, who argued that mode B scales on the smaller dimensions of the braid shear layer, which explains its comparable small wavelength of  $1d$  (for an alternative viewpoint on the nature of mode B, see Ryan *et al.* 2005). In case of mode D and E, the maximum streamwise vorticity occurs on the dividing streamline passing through the hyperbolic point, consistent with this hypothesis. Further discussion can be found in Rao *et al.* (2013).

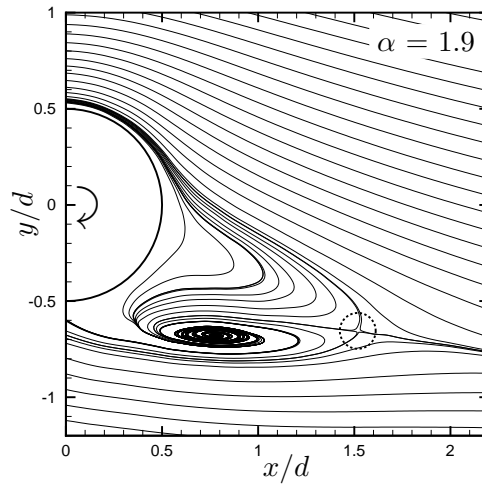


FIGURE 5.10: Time-averaged streamlines (PIV data) at  $Re = 250$  showing the location of the hyperbolic point (dashed circle) in the wake of the cylinder rotating at  $\alpha = 1.90$ . The approximate coordinates of this point are  $(x, y) = (1.5d, -0.7d)$ . The flow is from left to right.

### 5.3.4 Mode F

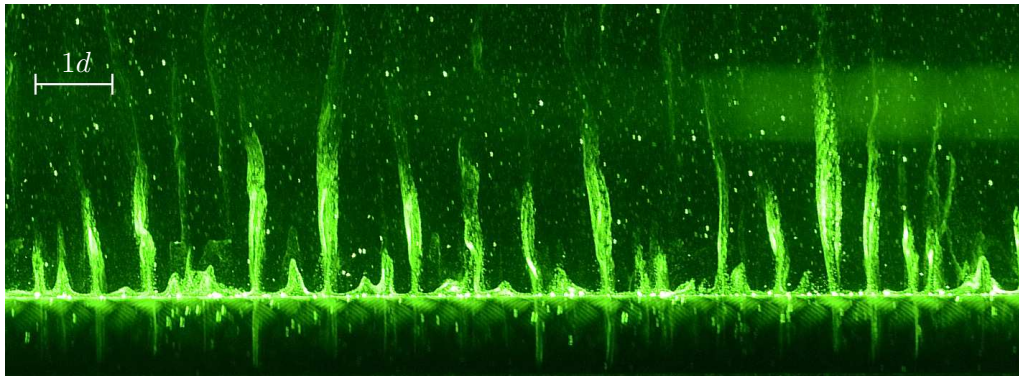


FIGURE 5.11: Flow visualization of mode F on the surface of the spinning cylinder, at  $Re = 275$  and  $\alpha = 2.3$ . The average spanwise wavelength is  $\lambda_z/d \approx 0.5$ . The flow is from bottom up. The sense of rotation is such that the cylinder surface seen by the observer is moving up.

The last instability investigated was the short-wavelength mode F, appearing at rotation rates above  $\alpha \approx 2.2$ , at  $Re = 275$ . Its flow structures formed on the cylinder surface, with an average spanwise spacing of  $\lambda_z/d \approx 0.5$ . These structures consisted of streamwise vortex filaments, partly wrapping around the cylinder and extending into the near wake, as seen in the flow visualization in figure 5.11. Considering the relatively high rotation rates and small length scales, a centrifugal instability seems to be the most likely explanation for this mode. Similar structures have been observed in the three-dimensional computations by Mittal (2004) at  $Re = 200$  and  $\alpha = 5$ , and were linked to the centrifugal instability mechanism.

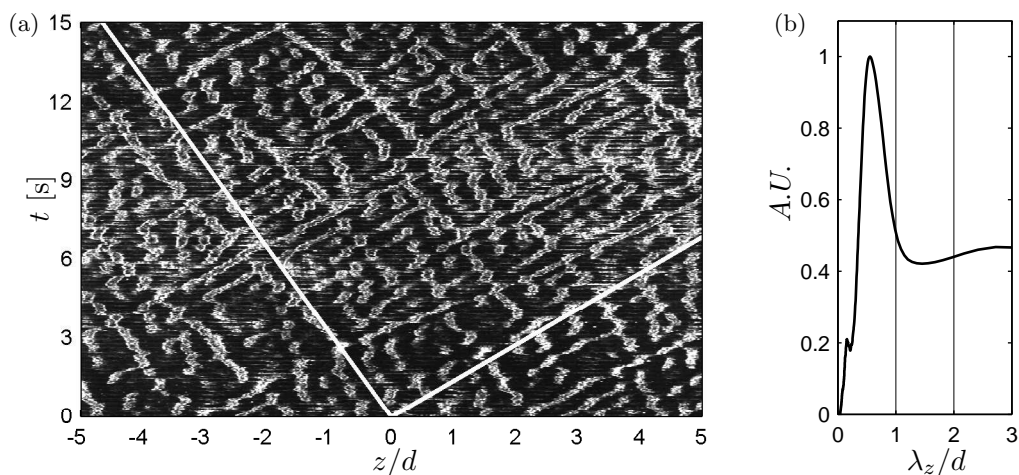


FIGURE 5.12: (a) Space-time diagram and (b) time-averaged wavelength spectrum of mode F at  $Re = 275$ ,  $\alpha = 2.3$ . White lines in (a) show principal directions of movement of mode F structures.

TABLE 5.1: Characteristics of spanwise movement of mode F.

|                          | $-z$ direction | $+z$ direction | abs. mean |
|--------------------------|----------------|----------------|-----------|
| phase velocity [ $d/s$ ] | -0.42          | +0.52          | 0.47      |
| frequency [Hz]           | 0.76           | 0.95           | 0.85      |
| $St_{3D}$                | 0.09           | 0.11           | 0.1       |

Unlike the previously discussed modes of this study, the streamwise vortices of mode F were not stationary, but wandered along the cylinder span. This can be seen in the space-time diagram of figure 5.12 (created at  $x/d = 1$ ), which shows consistent pattern of almost parallel inclined lines. These are oriented along the direction bottom left to top right, and are intersected by another group, orientated along bottom right to top left. A two-dimensional auto-correlation of the full space-time diagram (only a 15s segment is shown here) displays two correlation maxima in directions indicated by the two white lines. The inverse slopes of these lines are the average phase velocities  $\pm c_{ph}$  (in units of cylinder diameters per second) of mode F structures moving in positive and negative spanwise directions. Estimations of frequency ( $f = c_{ph}/\lambda_z$ ) and spanwise Strouhal number ( $St_{3D} = fd/U$ ) of this mode are shown in table 5.1. The three-dimensional Strouhal number is in good agreement with predictions by Rao *et al.* (2013) (0.11).

These results suggest that mode F is a travelling wave. Rao *et al.* (2013) reported a change in sign of streamwise vorticity within one perturbation field period. After a half period, the perturbation field was identical but of opposite sign. It was speculated



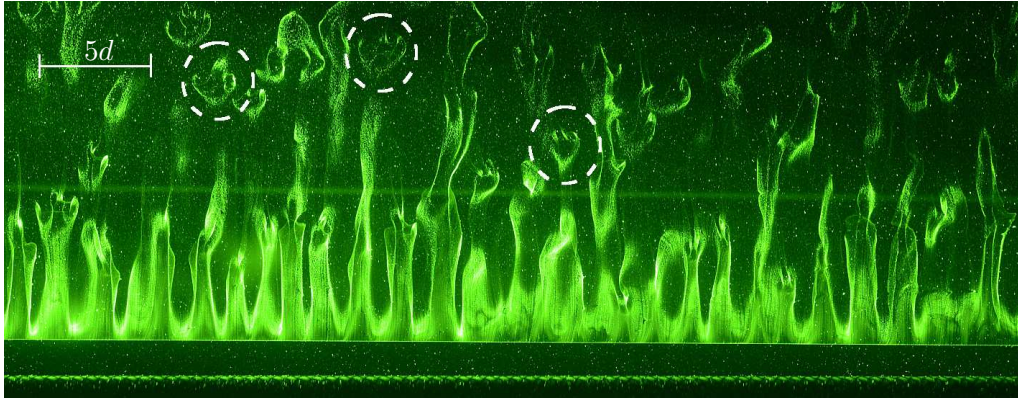


FIGURE 5.13: Flow visualization at  $Re = 275$ ,  $\alpha = 2.4$ , showing streamwise structures similar to mode E. Not visible in this picture –due to the chosen hydrogen bubble location– is mode F on the surface of the cylinder, similar to figure 5.11. Dashed circles mark ‘loop-like’ structures, which distinguish this flow regime from the pure mode E. The flow is from bottom up.

that mode F is subharmonic, although the present experimental results support the travelling wave explanation.

Furthermore, there are signs of coexistence and nonlinear interaction of modes E and F. This is evident from the parameter space in figure 2.16, which shows an overlap region of these two modes for  $Re > 290$  and  $\alpha \geq 2.2$ . Our experiments confirm the existence of structures similar to mode E in the far-wake, even at lower Reynolds numbers. Figure 5.13 shows the cylinder wake at  $Re = 275$  and  $\alpha = 2.4$  (for better clarity and contrast, the wire was positioned downstream of the cylinder). There is a striking visual similarity to mode E of figure 5.6b. The dominant spanwise wavelength at this rotation rate lies between 1.6 and 2 cylinder diameters, compared to  $\lambda_z/d \approx 2.1$  of the ‘pure’ mode E.

Despite the visual similarity, two characteristics distinguish this flow regime from mode E: First, the streamwise structures visible in figure 5.13 are moving in the spanwise direction. Numerical processing shows that the phase velocity is  $c_{ph} \approx \pm 0.5 d/s$ , similar to that of mode F. This is the first sign of a possible interaction between these two modes. The second difference is the appearance of ‘loop-like’ structures in the far wake, some of which are marked by dashed circles. This phenomenon has not been observed in the case of pure mode E. Preliminary experiments indicate that these structures are created in the vicinity of the cylinder, by ejection of large hairpin-vortices (in the order of  $2d$ ) into the near wake (figure 5.14). Nevertheless, the physics involved are not clear at this stage and should be investigated in future work.

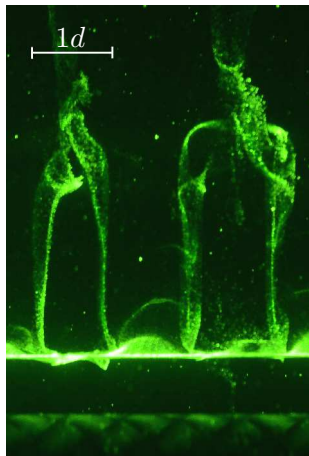


FIGURE 5.14: Ejection of two hairpin-vortices from the immediate near-wake of the rotating cylinder at  $Re = 275$ ,  $\alpha = 2.4$ . These vortices are likely to be the structures marked by dashed circles in figure 5.13. (The hydrogen bubble wire is placed downstream of the cylinder.)

### 5.3.5 Second shedding

Although outside the main scope of this study, a short note on the subject of second shedding, as reported by Stojković *et al.* (2003); Mittal & Kumar (2003); El Akoury *et al.* (2008); Kumar *et al.* (2011), will be added. It is remarkable that all evidence of this phenomenon in literature are either two-dimensional computations or experimental data (PIV and flow visualizations) of the wake cross section. Stunningly, some studies report the absence of this phenomenon altogether (Luo *et al.* 2010). To our best knowledge, no published data exist which show this process in three dimensions. Without such data, the question arises how strictly two-dimensional this process is in reality. In other words, it is not clear whether the one-sided vortex detaches simultaneously along the whole cylinder span, or whether it happens as a three-dimensional process.

Initially, we hoped to observe this phenomenon under conditions reported by other researchers. For example, Kumar *et al.* (2011) presented instantaneous PIV vorticity maps in the wake cross section at  $Re = 200$ ,  $\alpha = 4.45$ , which showed the detachment of a one-sided vortex from the rotating cylinder. For these conditions, we can not report anything comparable from our flow visualizations. The near wake was in a permanent chaotic state. In addition, a centrifugal instability (mode F) was present on the cylinder surface, adding to the disruption of the near wake. Nevertheless, large-scale vortical structures was ejected at random intervals into the wake, containing large amounts of vorticity.

The closest phenomenon resembling second shedding was observed only for a signif-



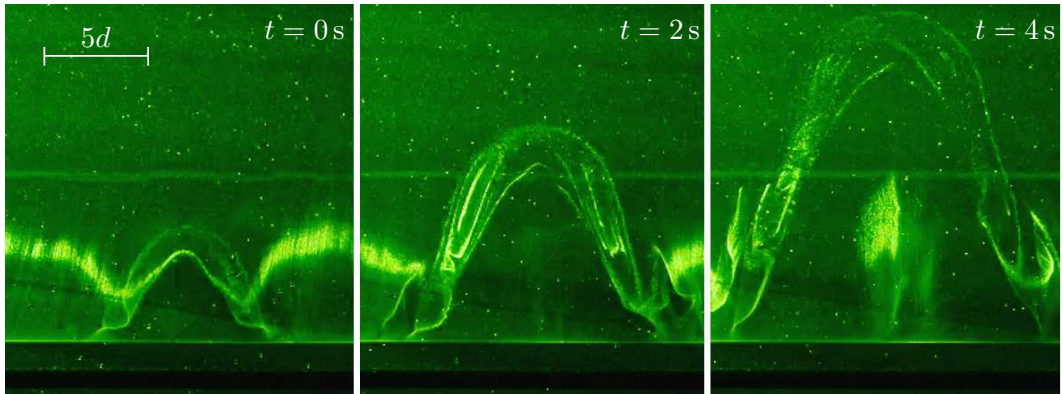


FIGURE 5.15: Flow visualization of one-sided shedding at  $Re = 100$ ,  $\alpha = 5.1$ . The detaching vortex forms a horse-shoe shaped vortex bend, which peels slowly off the cylinder. The rotating cylinder can be seen at the bottom edge; the hydrogen bubble wire is positioned downstream of it. The flow is from bottom up.

icantly reduced Reynolds number. This had two effects: the wake became more stable; and the centrifugal instability was suppressed due to the lower rotation rates. In this ‘clean’ wake, we made the observation of a single-sided vortex detachment at  $Re = 100$  and  $\alpha = 5.1$ . Against expectations, this process was very localized, initiating from random ‘detachment points’ along the cylinder span in an unpredictable fashion.

Figure 5.15 shows three video snapshots cropped around one of these points. The overall wake is initially steady. The first picture shows the start of detachment, as the vortex passes the hydrogen bubble wire. The vortex wraps the bubble sheet into a horse-shoe shaped tube. As this peeling process continues, the base of the ‘horse-shoe’ structure widens, its two end points moving apart in the spanwise direction. In most cases, the process stops only when one of these base points reaches the base point of a neighbouring vortex bend.

No further data were collected on this phenomenon, and at this point it can only be speculated on the reasons for the described behaviour. Is the observed three-dimensionality due to end effects of the finite cylinder, the imperfections of the experimental setup (free-stream turbulence and unavoidable (but small) cylinder vibrations), or is this process inherently three-dimensional? Previously published observations in the cross-sectional plane might be the result of an opportune positioning of the recording plane. A cut parallel, and close to the symmetry plane of one of these vortex bends, would appear in planar PIV vector fields as a single spanwise vortex moving downstream.

On the other hand, PIV recordings by Kumar *et al.* (2011) confirm one-sided shedding at  $Re = 200$ , a Reynolds number at which no coherent shedding was visually perceivable in our experiments. One explanation for this might be the interaction of centrifugal instability and second shedding. One-sided shedding may be present in our flow, but visually masked by the flow disruptions caused by centrifugal instability. The previously mentioned ejection of large-scale vortical structures at this Reynolds number might in fact consist of actual vortex bends, disrupted and deformed by the interaction with mode F. For now, these claims are of a speculative nature and further thorough investigation is needed to address these issues.

## 5.4 Summary

The results presented in this chapter are the first to show experimentally a new set of three-dimensional instability modes in the wake of rotating cylinders. These match the modes first found in the linear stability analysis of Rao *et al.* (2013).

The subharmonic mode C was observed for rotation rates  $1.0 \leq \alpha \leq 1.85$ . Its nominal spanwise wavelength was  $\lambda_z/d \approx 1.1$  at  $\alpha = 1.7$ , but increased significantly with decreasing rotation rate. This mode has similar characteristics to the subharmonic mode C, observed in the wakes of a torus (Sheard *et al.* 2003b), and of a cylinder disturbed by a thin wire (Zhang *et al.* 1995; Yildirim *et al.* 2013b). Furthermore, a complex interaction with mode B took place for  $\alpha \leq 1.0$ . This nonlinear interaction could not be predicted by linear stability analysis.

Two modes with a wavelength of  $\lambda_z/d \approx 2$  appeared in close succession at  $Re = 250$ . For rotation rates above  $\alpha = 1.85$ , mode D consisted of continuous streamwise vortices in a shedding wake. Mode E was observed at a slightly higher rotation rate of  $\alpha = 2.1$ . It appears that this mode is a continuation of mode D, but on a henceforth steady wake. This is supported by the observation of a smooth transition between these two modes, as the wake changes gradually from a shedding to a steady state. Both modes are attributed to an hyperbolic instability of the mean wake.

The fourth mode, mode F, was observed on the cylinder surface for  $Re = 275$  and rotation rates above  $\alpha \approx 2.2$ . It consisted of ring-like vortices at an average spanwise spacing of  $\lambda_z/d \approx 0.5$ . Similar structures with a spanwise wavelength of one cylinder diameter were observed in three-dimensional computations by Mittal (2004) for  $\alpha = 5$ . It is speculated that this mode is the result of centrifugal instability. However, in

TABLE 5.2: Summary of the main characteristics of the newly observed three-dimensional modes C – F. A comparison is made between numerical results (num.) of Rao *et al.* (2013) and experimental measurements (exp.) of this publication. (\* ‘period’ refers to the period  $T$  of the two-dimensional periodic base flow. In case of mode F, the reference is made to the spanwise movement of the three-dimensional structures, expressed as Strouhal number  $St_{3D}$ .)

| mode<br>data  | C          |      | D          |           | E          |      | F               |      |
|---------------|------------|------|------------|-----------|------------|------|-----------------|------|
|               | num.       | exp. | num.       | exp.      | num.       | exp. | num.            | exp. |
| $\lambda_z/d$ | 1          | 1.1  | 2          | 1.6 – 1.8 | 2          | 2.1  | 0.45            | 0.5  |
| period        | $2T$       | $2T$ | $1T$       | $1T$      | N\A        |      | 0.11*           | 0.1* |
| movement      | stationary |      | stationary |           | stationary |      | travelling wave |      |

our experiments, the three-dimensional structures moved along the span, resembling a travelling wave of  $St_{3D} \approx 0.1$ . In addition, while mode F was fully developed on the cylinder surface, streamwise structures similar to mode E were observed in the wake for rotation rates  $\alpha \geq 2.3$ . There is indication of a nonlinear interaction between these two modes, which needs further investigation.

One-sided shedding (second shedding/mode II) was visualised for  $Re = 100$ ,  $\alpha = 5.1$ . Unlike the current assumption of a two-dimensional vortex parallel to the cylinder axis, the observed shedding created localized horse-shoe shaped vortex structures peeling off the cylinder. The detachment was initiated at randomly distributed ‘detachment points’ along the span, giving this process a fully three-dimensional character.

Overall, the presented experimental results largely confirm the linear stability analysis of Rao *et al.* (2013). The predicted modes C – F have been observed experimentally, with a good agreement in terms of spanwise wavelengths and spatio-temporal symmetries.

The largest discrepancy concerns the observation of mode C at rotation rates significantly below its linearly unstable range. A possible cause might be the fully developed mode B as an initial triggering condition in the experiment. This does not seem to play a role for  $\alpha > 1.0$ , but leads to a complex interaction of these two modes for  $\alpha \leq 1.0$ , which should be investigated in future work.

A side-to-side comparison of the main characteristics of the newly observed modes is presented in table 5.2.



## Declaration for Thesis Chapter 6

### Declaration by candidate

In the case of Chapter 6, the nature and extent of my contribution to the work was the following:

| Nature of contribution  | Extent of contribution (%) |
|---|----------------------------|
| Design & execution of experiments. Design & (partial) construction of experimental models. Data processing & presentation. Interpretation of results. | 80%                        |

The following co-authors contributed to the work. Co-authors who are students at Monash University must also indicate the extent of their contribution in percentage terms:

| Name                 | Nature of contribution  | Extent of contribution (%) for student co-authors only |
|----------------------|---|--|
| Prof. Mark Thompson  | Manuscript formulation. Research guidance & interpretation of results. Proof-reading.     | -  |
| Prof. John Sheridan  | Research guidance & interpretation of results. Revisions of manuscript and proof-reading. | -  |
| Prof. Kerry Hourigan | Research guidance & interpretation of results. Revisions of manuscript and proof-reading. | -  |

Candidate's  
Signature

*ARadi* Date 30.8.2013

### Declaration by co-authors

The undersigned hereby certify that:

- (1) the above declaration correctly reflects the nature and extent of the candidate's contribution to this work, and the nature of the contribution of each of the co-authors;
- (2) they meet the criteria for authorship in that they have participated in the conception, execution, or interpretation, of at least that part of the publication in their field of expertise;
- (3) they take public responsibility for their part of the publication, except for the responsible author who accepts overall responsibility for the publication;
- (4) there are no other authors of the publication according to these criteria;
- (5) potential conflicts of interest have been disclosed to (a) granting bodies, (b) the editor or publisher of journals or other publications, and (c) the head of the responsible academic unit; and
- (6) the original data are stored at the following location(s) and will be held for at least five years from the date indicated below:

Location(s)

*Monash University CARDS*

[Please note that the location(s) must be institutional in nature, and should be indicated here as a department, centre or institute, with specific campus identification where relevant.]

Signature 1

*[Signature]* Date 30/08/2013

Signature 2

*[Signature]* 30/08/2013

Signature 3

*[Signature]* 30/08/2013



## Chapter 6

# Elliptical cylinders: $St-Re$ relationship

The second main study of this thesis deals with the flow about elliptical and stationary circular cylinders, and the normal flat plate. All models are thought of as members of a continuous spectrum of bodies, differing only by their cross-sectional aspect ratio  $Ar$ . The modifications of the wake, as  $Ar$  is varied, are investigated in detail in the next two chapters. The present chapter discusses changes to the Strouhal–Reynolds number relationship ( $St-Re$  curves) as a function of the aspect ratio  $Ar$  in the range  $100 < Re < 300$  and the associated three-dimensional transitions. These findings lead to an hypothesis, which will be tested in chapter 7 in the form of a detailed PIV study. This chapter is based on:

RADI, A., THOMPSON, M. C., SHERIDAN, J. & HOURIGAN, K. 2013c  
From the circular cylinder to the flat plate wake: the variation of Strouhal number with Reynolds number for elliptical cylinders. *Physics of Fluids* (submitted for publication)

### 6.1 $St-Re$ curves

#### 6.1.1 Introduction

For the circular cylinder, the Strouhal numbers lie on a curve which has been established by many experimental (e.g., see Williamson 1996b, and references therein) and numerical (e.g., Henderson 1997) studies. For this model, the  $St-Re$  curve reflects the major flow regimes and transitions of the wake in the form of possibly hysteretic discontinuities and slope changes (Williamson 1996c).

We attempt to use this ‘imprint’ of a cylinder’s transition behaviour as a first guide in the search for wake transitions of the elliptical cylinders. We seek to obtain the  $St-Re$  curves by means of hot film velocimetry, identify associated flow transitions and

their potential causes, and compare the transition scenarios of the elliptical cylinders to the two limiting cases of a flat plate and a stationary circular cylinder. The hot film findings will be supported by hydrogen bubble flow visualizations, which will confirm the transition between the two-dimensional laminar wake to three-dimensional flow, and will provide an estimate of spanwise wavelengths.

This chapter will show that whilst modified versions of the mode A and B transitions of a circular cylinder wake occur at aspect ratios above  $Ar \approx 0.4$ , at lower aspect ratios some major differences occur. In particular, for  $Ar \lesssim 0.4$ , the wake appears to re-laminarize after it has already undergone three-dimensional transition. The possible cause for this surprising observation will be explored in a short case study at the end of this chapter, which will lay the foundation for the major investigation presented in chapter 7.

### 6.1.2 Method

A hot film probe, placed at  $(x, y) \approx (10d, -1.5d)$ , was used to record the velocity fluctuations. The chosen  $y$ -location assured larger velocity oscillation amplitudes compared to the symmetry plane (Fage & Johansen 1927); the streamwise distance from the cylinder was kept large to prevent an interaction of the hot film probe with the cylinder's near wake and unintended triggering of three-dimensional modes. The analogue signal was low-pass filtered at 10 Hz and sampled at 20 Hz. For each Reynolds number, a velocity time series of 20 min was recorded (equivalent to 440–1600 main shedding cycles). The Reynolds numbers were increased stepwise from 100 to 300; then the series was reversed, to capture any hysteretic effects in the flow. The water temperature was measured throughout the experiments, to correct for changes in viscosity. The freestream velocity was recorded simultaneously by LDV upstream of the model. The full experimental setup is described in §3.3.

To obtain the shedding frequency, a windowed FFT was performed on the velocity time series, with a window width of 512 points (25.3 s), and 50% overlap. The spectra of all windows were averaged, and the highest spectral peak was defined as the von Kármán shedding frequency. The width of the frequency peak in the power spectrum contains useful information on the transition process (Williamson 1996b). This *spectral bandwidth*  $\Delta f^*$  is defined as the difference between the frequencies where the spectral level is 3 dB below the peak value (Prasad & Williamson 1997). As it depends on the

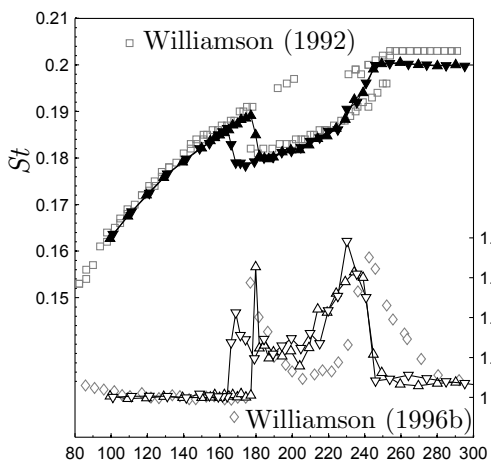


window width (see appendix B), only relative values will be given.  $\Delta f^*$  is normalized with the averaged spectral bandwidth of the circular cylinder in the laminar regime ( $Re < 177$  in our experiments).

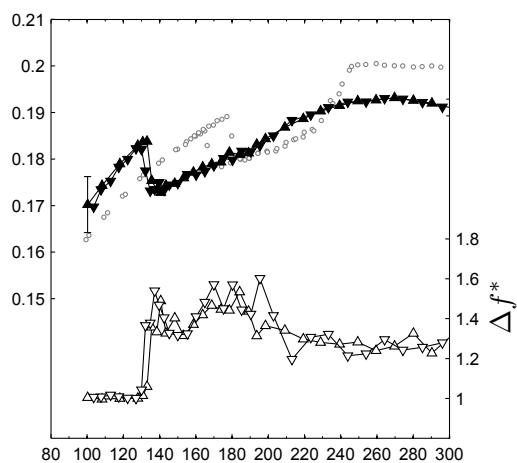
To make all three-dimensional transitions associated with the different cylinder types more comparable, the following terminology will be used for the three-dimensional modes: (1) ‘Mode L’ refers to a long-wavelength instability appearing at lower Reynolds numbers. This is equivalent to mode A for the circular cylinder; (2) ‘Mode S’ refers to a short-wavelength instability (similarly equivalent to mode B) at higher  $Re$ . Their critical Reynolds numbers are  $Re_{c_1}$  and  $Re_{c_2}$ ;  $\lambda_L$ ,  $\lambda_S$  are the wavelengths of each mode. The spanwise wavelength of the modes was estimated from flow visualization pictures. Note that for larger aspect ratios, the identified modes are effectively equivalent to variants of modes A and B; however for lower aspect ratios, and especially the flat plate, they do not necessarily correspond to the circular cylinder modes.

### 6.1.3 Results

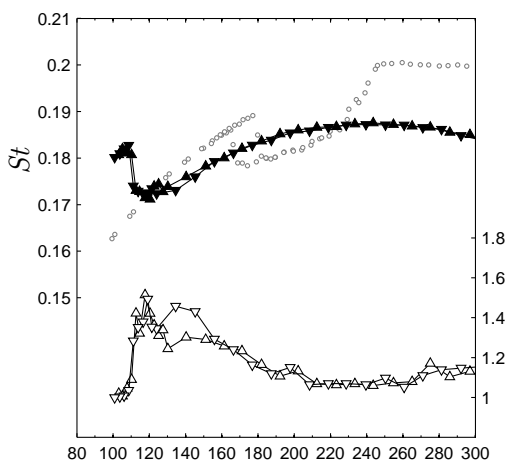
The validation of the experimental setup is presented in figure 6.1a, which shows the  $St-Re$  curve for the circular cylinder. The initial section of the curve is known to begin outside of the measured Reynolds number range at  $Re_{c_0} \approx 47$ , when the steady wake starts shedding spanwise vortices of alternate sign (see §2.1.1). The Strouhal numbers increase monotonically, until a hysteretic discontinuity takes place at  $Re_{c_1} = 160-190$  (depending on the experimental conditions, Williamson 1996c). The discontinuity is reproduced accurately in our experiment at  $Re = 177$ , with a pronounced hysteresis. This sudden drop is caused by the appearance of the first three-dimensional mode (mode A) with a spanwise wavelength  $\lambda_L = 3-4$ , combined with large-scale vortex dislocations, which evolve spontaneously and intermittently along the span. These dislocations lead to low-frequency irregularities of the measured velocity signal and to a broadening of the spectral bandwidth (Braza *et al.* 2001). For Reynolds numbers above 220, perturbation energy is gradually transferred to the second three-dimensional mode (mode B) with  $\lambda_S \approx 1$ , which dominates the wake completely at  $Re = 260$ . See figure 5.1 in the previous chapter for a flow-visualization of these modes. During this gradual transition, the  $St-Re$  curve experiences a steep increase, followed by a plateau. The curve plateaus in our experiments at  $Re > 250$  with a dimensionless shedding frequency of  $St \approx 0.20$ .



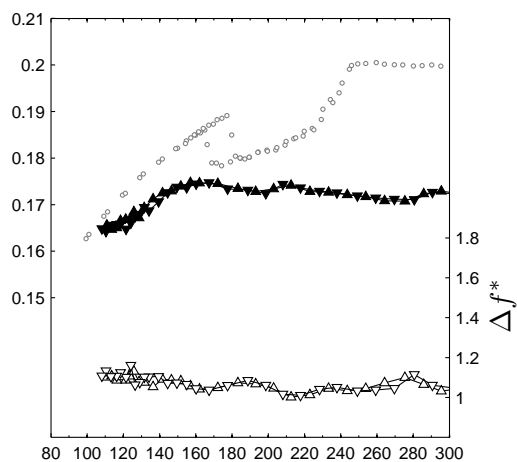
(a)  $Ar = 1.00$



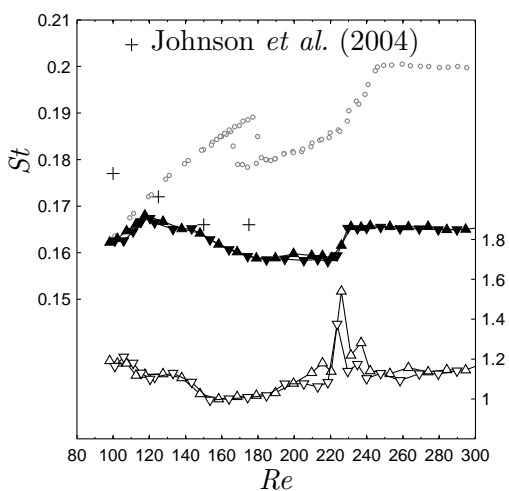
(b)  $Ar = 0.72$



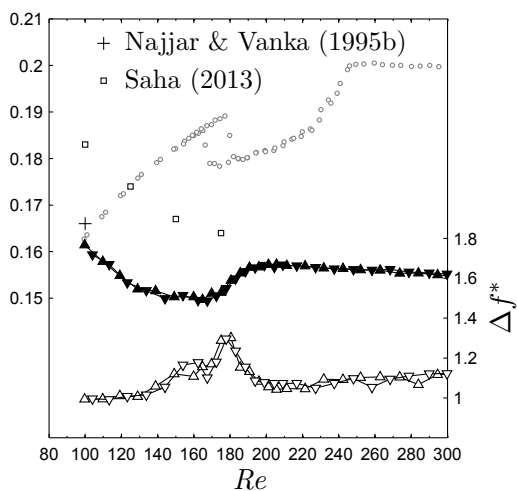
(c)  $Ar = 0.64$



(d)  $Ar = 0.39$



(e)  $Ar = 0.26$



(f)  $Ar = 0$

The spectral bandwidth  $\Delta f^*$  reflects the appearance of the three-dimensional modes by exhibiting two maxima: A first sharp peak at  $Re \approx 180$  caused by mode A, and a broader peak centred at  $Re = 230$ , as a result of gradual transition to mode B. These observations are consistent with previous experimental studies (Williamson 1996c).

Figure 6.1b shows the  $St-Re$  curve and the spectral bandwidths of the  $Ar = 0.72$  cylinder. The step drop in Strouhal number is the most prominent feature of this curve. The following changes compared to the circular cylinder can be observed: (1) The discontinuity is shifted to a lower critical Reynolds number  $Re_{c_1} = 135$ . (2) The steep increase of Strouhal numbers, associated with the circular cylinder wake mode B, is not present. (3) The  $St-Re$  curve plateaus at a lower value of  $St \approx 0.19$ .

The discontinuity at  $Re_{c_1} = 135$  is a reliable indicator of a transition from a laminar two-dimensional shedding to a three-dimensional flow. Analogous to the circular cylinder, this process is accompanied by a sudden increase in spectral bandwidth. Flow visualizations show a spanwise modulation of the wake with a wavelength of  $\lambda_L = 3.6-4.0$  (figure 6.2a). The appearance of mode S is not obvious from the  $St-Re$  curve, but can be inferred from a wide peak in the spectral bandwidth at  $160 < Re < 190$ . Flow visualizations indeed show a short-wavelength mode with  $\lambda_S \approx 1.2$  for Reynolds numbers above this range (figure 6.2b).

The wide second peak in the spectral bandwidth might be an indication of a competing process between modes L and S, similar to the overlap region of modes A and B of the circular cylinder. Although this process is not reflected in the Strouhal number variation, overall the curve for the  $Ar = 0.72$  cylinder appears to be just a modified version of the circular cylinder's curve. The same observation holds for the  $Ar = 0.64$  cylinder (figure 6.1c). Only for smaller aspect ratios below  $Ar = 0.39$  are major changes observed, which are indicative of new physical processes.

These changes will be highlighted with results for the  $Ar = 0.26$  cylinder, whose  $St-Re$  curve is shown in figure 6.1e. This curve differs fundamentally from the circular cylinder. Firstly, it must be emphasized that the Strouhal number drop at  $Re \approx$

---

FIGURE 6.1 (*facing page*):  $St-Re$  curves and spectral bandwidths of the elliptical cylinders. The curve of the circular cylinder ( $Ar = 1.00$ ) is reproduced in each plot for easier comparison (grey circular symbols). The Reynolds number was increased (triangles up), and then decreased (triangles down) to capture hysteresis effects. The  $Ar = 0.72$  cylinder curve shows error estimates of  $St$  for  $Re = 100$  and  $300$ . The data by Williamson (1996b) are rescaled and normalized. The results by Saha (2013) are for an  $Ar = 0.125$  normal plate.

---

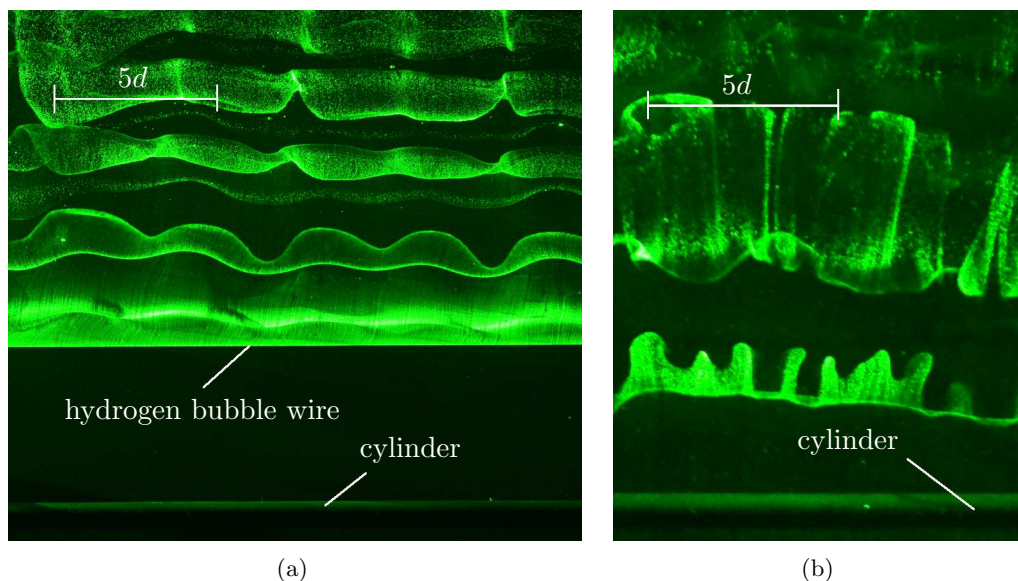


FIGURE 6.2: (a) Mode L in the wake of the  $Ar = 0.72$  cylinder at  $Re = 150$ . The spanwise wavelength in this photograph is  $\lambda_L \approx 3.6$  (b) Mode S at  $Re = 200$  with a spanwise wavelength  $\lambda_S \approx 1.2$ . The cylinder can be seen at the bottom. The hydrogen bubble wire is placed downstream of the cylinder in (a), and upstream in (b). Flow is from bottom to top.

120 is *not* the discontinuity marking the transition to three-dimensional flow. This transition takes place outside of the measured range at  $Re < 100$ , with the flow being already fully three-dimensional with a mode L structure at the lowest Reynolds numbers investigated, as will be shown in figure 6.3a. Accordingly, the spectral bandwidths are large in the range  $100 < Re < 150$ , and the hot film signals show low-frequency irregularities, reminiscent of mode A and vortex dislocations known to occur from the circular cylinder.

In addition to the strongly decreased critical Reynolds number  $Re_{c1}$ , two more unique properties are noticed: (1) A step increase of the Strouhal numbers at  $Re \approx 225$ , accompanied by a peak in the spectral bandwidth. (2) A gradual decrease of Strouhal numbers over the range  $120 < Re < 180$ , paired with the lowest spectral bandwidths measured for this cylinder type for  $150 < Re < 190$ .

The step increase of the Strouhal numbers at  $Re \approx 225$  can be reliably attributed to the appearance of the three-dimensional mode S. At this Reynolds number, this short-wavelength mode is fully developed with a wavelength of  $\lambda_S = 1.2d$ , as estimated from flow visualizations. It appears intermittently already at  $Re = 200$ , which explains the increased spectral bandwidths (figure 6.3b).

For  $Re < 150$ , flow visualizations show the long-wavelength mode L with  $\lambda_L \approx$

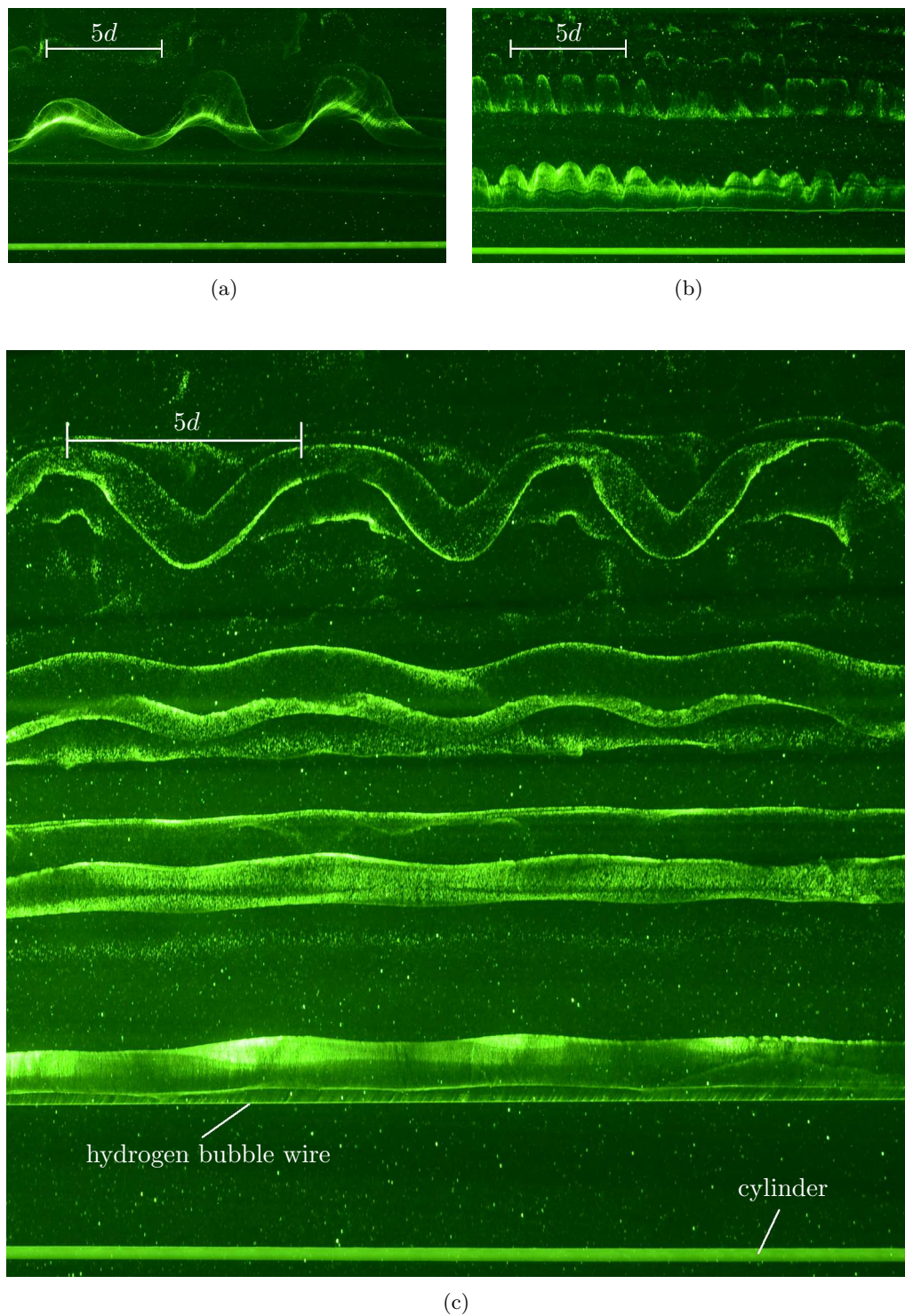


FIGURE 6.3: Flow visualizations of the  $Ar = 0.26$  cylinder wake. (a)  $Re = 100$ : mode L with  $\lambda_L \approx 6d$ ; (b)  $Re = 200$ : mode S with  $\lambda_S \approx 1.4d$ . (c)  $Re = 160$ : re-laminarized wake. The flow is from bottom to top.

$5d$  (figure 6.3a). This mode strongly deforms the von Kármán vortices from their inception. The presence of a three-dimensional mode is the most likely reason for the differences between the Strouhal numbers obtained from two-dimensional computations by Johnson *et al.* (2004) and the experiment, particularly for  $Re < 120$  (figure 6.1e). The discrepancy decreases as the Reynolds number approaches 150. Surprisingly, the near wake in the experiment becomes two-dimensional again in the range  $150 < Re < 190$ , devoid of three-dimensional modes or vortex dislocations! This can be seen in figure 6.3c. The figure shows that the von Kármán vortex cores are shed initially parallel to the cylinder axis, with only minor spanwise modulation. This stands in stark contrast to figure 6.3a at  $Re = 100$ , which shows a strong three-dimensional deformation. Yet, the minor spanwise modulation in figure 6.3c is amplified strongly as the vortex cores are advected downstream, which is indicative of a high strain region for distances  $x/d \gtrsim 10$ .

The described condition will be referred to as the ‘re-laminarized’ regime, because it is characterized by a strictly periodic hot film signal and narrow spectral bandwidths, similar to the laminar shedding regime of the circular cylinder at  $Re \lesssim 190$  (No reference is made by this term to the distinction between laminar and turbulent flows!). A comparison of velocity time traces in figure 6.4 exemplifies this trend: The velocity signal (a), prior to re-laminarization, shows gradual amplitude modulations, which are characteristic of vortex dislocations. Once mode S appears, the velocity signal (c) exhibits high frequency bursts. The velocity trace (b) is strictly periodic with a constant amplitude, which defines the re-laminarized regime.

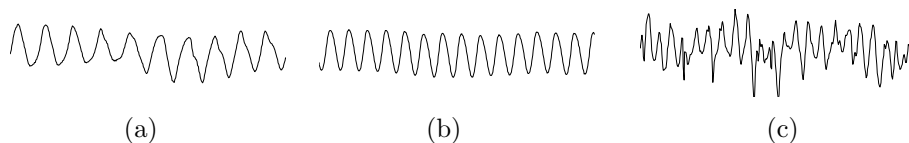


FIGURE 6.4: Velocity time traces of the  $Ar = 0.26$  cylinder wake at (a)  $Re = 107$ ; (b)  $Re = 165$ ; (c)  $Re = 240$ . The re-laminarized regime (b) exhibits strictly periodic shedding.

Apart from the  $Ar = 0.26$  cylinder, this newly found regime was observed in a weaker form in the  $Ar = 0.39$  wake for  $200 < Re < 250$ , although its  $St-Re$  curve does not show such a pronounced decrease of Strouhal number (figure 6.1d).

The flat plate curve resembles the  $Ar = 0.26$  case, with the transitions shifted to lower Reynolds and Strouhal numbers (figure 6.1f), tempting the interpretation of its features in the same way. The steep increase of  $St$  values between  $Re = 170$  and 200 is



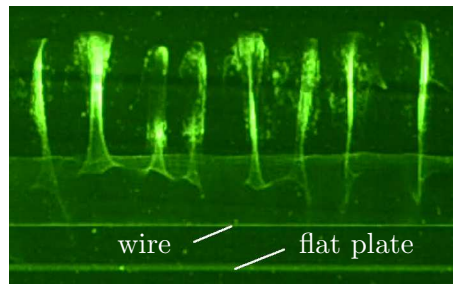


FIGURE 6.5: Flat plate mode S at  $Re = 200$ . The spanwise wavelength is  $\lambda_S \approx 1.8d$ . Flow is from bottom to top.

indeed caused by a short-wavelength mode S, which is fully developed at  $Re > 200$  with a wavelength  $\lambda_S \approx 1.2 - 1.8$ . This is in accordance with reports of a short-wavelength mode for  $Re > 200$  (Najjar & Vanka 1995a; Najjar & Balachandar 1998). This mode is shown in figure 6.5.

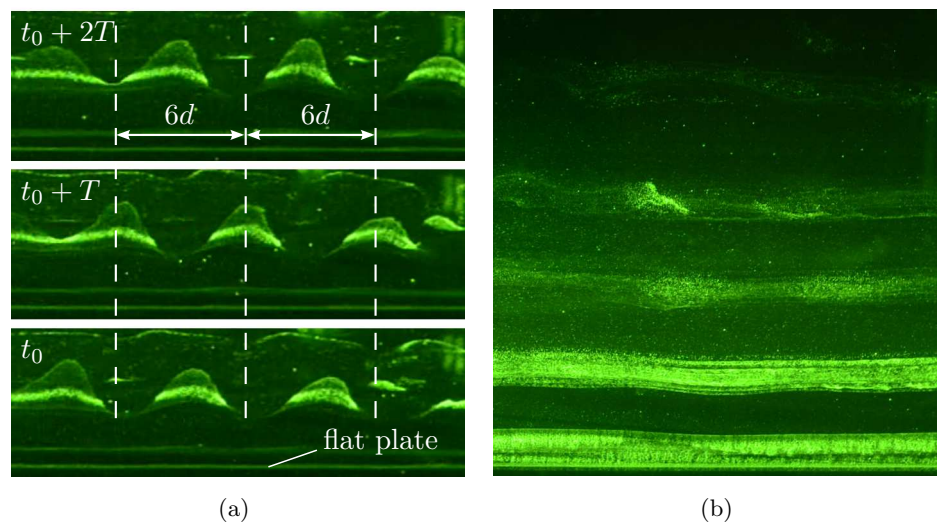


FIGURE 6.6: (a) Mode L in the wake of the flat plate at  $Re = 150$ . The spanwise pattern repeats every second shedding cycle. (b) The same wake with a slightly differently positioned hydrogen bubble wire. The wire is placed  $2.8d$  upstream of the model in both pictures. Flow is from bottom to top.

Nevertheless, the flat plate wake differs from the previous cases by a surprising property: Its mode L is subharmonic, as can be seen in figure 6.6a at  $Re = 150$ . Spanwise modulations of  $\lambda_L \approx 6d$  form immediately downstream of the model. The structures shift by a half-wavelength in spanwise direction every shedding cycle  $T$ , such that the same pattern is repeated every  $2T$ . Yet, the vortex cores are shed strictly parallel to the cylinder axis, without a three-dimensional modulation, as can be seen

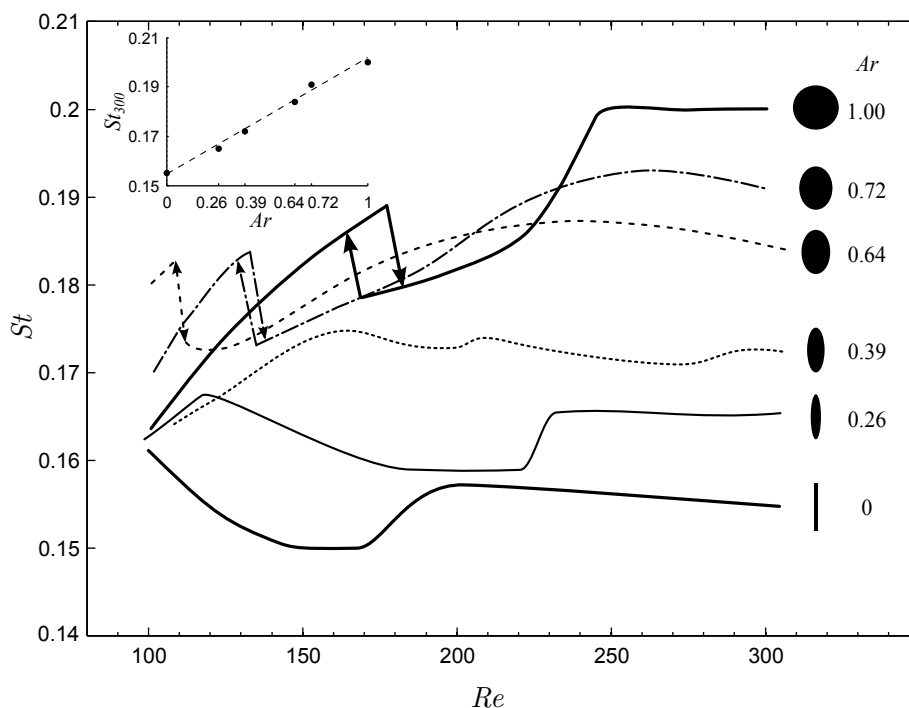


FIGURE 6.7: Schematic  $St-Re$  curves of all investigated models. The insert on the top left shows Strouhal number values sampled at  $Re = 300$ , representing the region in which the curves plateau.

in figure 6.6b. The wavelength and the subharmonic nature of this mode match the predictions by Thompson *et al.* (2006), who state a critical Reynolds number  $Re_{c_1} = 105-110$ . An additional long-wavelength mode with  $\lambda_z \approx 2d$ , as described in the same publication, has not been observed in our experiment yet.

A unified comparison of all investigated models is made in figure 6.7, in which the data points have been replaced by hand-drawn curves to emphasize the trends. Four characteristics can be identified, which describe the main changes as the aspect ratio decreases from 1 to 0:

- First, the critical Reynolds number marking the transition to three-dimensionality reduces. The accompanying discontinuity is captured for  $Ar = 1.00, 0.72$  and  $0.64$ ; it is assumed to exist at  $Re < 100$  for  $Ar = 0.39$  and  $0.26$ , as the flow is already three-dimensional at  $Re = 100$ . The discontinuity is hysteretic for  $Ar = 1.00$  and  $0.72$ , only (marked by arrows). It is not clear if/how the flow undergoes three-dimensional transition in the case of the flat plate.
- Second, all curves flatten for  $Re > 250$ , with the Strouhal number of this plateau



decreasing for smaller aspect ratios. The Strouhal numbers  $St_{300}$  (sampled at  $Re = 300$ ) show a linear relationship with aspect ratio, as can be seen in the top left insert of figure 6.7.

- Third, the steep increase of Strouhal numbers marking the appearance of mode S (mode B equivalent), vanishes for  $Ar = 0.72, 0.64$  and  $0.39$ , but reappears again for  $Ar = 0.26$  and the flat plate. In all cases, a short-wavelength mode with a spanwise wavelength  $\lambda_S = 1-2$  was observed.
- Fourth, a gradual decrease of Strouhal numbers, associated with the phenomenon of wake re-laminarization, is observed for  $Ar \leq 0.39$ . This regime is associated with highly periodic shedding, at least in the near wake.

In conclusion, as the aspect ratio of an elliptical cylinder is varied between  $0 \leq Ar \leq 1$ , bridging the geometries of a circular cylinder and a flat plate, a range of different modifications of the  $St-Re$  curves can be observed. Some of these modifications can be explained in terms of variations of known circular cylinder transitions (e.g., the impact of modes L and S), in line with changes to the two-dimensional base flow, whilst the origin of others are less predictable and demand further research. Perhaps the most prominent of these being the re-laminarized wake for  $Ar \leq 0.39$ . The main experimental observations are summarized in table 6.1.

TABLE 6.1: Overview of all investigated models. Missing data were linearly interpolated from Jackson (1987). (H) denotes hysteretic transitions.

| $Ar$ | $Re_{c_0}$        | $Re_{c_1}$ | $Re_{c_2}$ | $\lambda_L$       | $\lambda_S$        | $St_{300}$ | re-lam. |
|------|-------------------|------------|------------|-------------------|--------------------|------------|---------|
| 1.00 | 45.4 <sup>1</sup> | 177 (H)    | 220–260    | 3.96 <sup>2</sup> | 0.822 <sup>2</sup> | 0.20       | No      |
| 0.72 | 40.1 <sup>1</sup> | 135 (H)    | 160–190    | 3.7–4.0           | 1.3                | 0.191      | No      |
| 0.64 | 38.2 <sup>1</sup> | 110        | 140–160    | 4–6               | 1.2–1.4            | 0.184      | No      |
| 0.39 | 34.2 <sup>1</sup> | < 100      | 220        | 4–6               | 1.1–1.2            | 0.172      | Weak    |
| 0.26 | 32.0 <sup>1</sup> | < 100      | 220–230    | 5–6               | 1.2–1.4            | 0.165      | Yes     |
| 0    | 27.8 <sup>1</sup> | ?          | 180–200    | 6                 | 1.2–1.8            | 0.155      | Yes     |

<sup>1</sup> Jackson (1987)

<sup>2</sup> Henderson & Barkley (1996)

## 6.2 Spectral energy of the primary frequency

In addition to the characteristics of the velocity signal, the  $St-Re$  relationship and flow visualizations, one more quantity was extracted from the hot film data presented in §6.1. The temporal variation of the energy content of the shedding frequency was

computed by measuring the spectral energy of a finite frequency band of width  $2\Delta f$ , centred around the primary von Kármán frequency ( $\Delta f = 0.05$  Hz). This was done for each window of the windowed FFT and for each Reynolds number. Figure 6.8 shows the resulting diagrams for all cylinder models. Each vertical stripe of tiles represents a 20 min time series. As the windowed FFT was performed with 25.3 s wide windows and 50% overlap, each tile represents 12.7 s in the time domain. The stripe width is determined by the Reynolds number increment during the experiments. The energy content of the tiles is represented by its grey tone. A vertical sequence of dark tiles means strong and coherent shedding, while a rapid and random change of grey tones is caused by incoherent velocity fluctuations, typically the result of vortex dislocations. The  $St-Re$  curves from figure 6.1 are overlaid for easier comparison.

The diagram of the circular cylinder in figure 6.8a clearly shows its three flow regimes. To the left of  $Re \approx 180$ , the tiles pattern is uninterrupted and dark, meaning very periodic shedding with the fluctuation energy concentrated in the primary frequency. This is characteristic for the laminar shedding regime. Once mode A develops in the transition regime, the tiles pattern becomes random, meaning that the primary shedding is less energetic and interrupted. Both observations, leakage of energy out of the primary frequency peak and temporal randomness, are a direct result of vortex dislocations (Braza *et al.* 2001). Interestingly, once mode B is fully developed at  $Re > 250$ , the shedding becomes more regular with a higher spectral energy content. This implies the absence of vortex dislocations for  $Re > 250$ , which explains the henceforth increased Strouhal numbers. The transitions between these three flow regimes correlate with changes in the overlaid  $St-Re$  curve.

Figures 6.8b and 6.8c show the decrease of the critical Reynolds number of the onset of three-dimensionality for decreasing aspect ratios. In both cases, the uniformly dark regions are shifted to the left, coinciding with the discontinuity in the corresponding  $St-Re$  curves. The transition is followed by a more random shedding, reminiscent of the transition region of the  $Ar = 1.00$  cylinder. Yet, none of the elliptical cylinders recover the spectral energy at higher Reynolds numbers, as in the case of the circular cylinder at  $Re > 250$ . Although short wavelength modes are present in all cases at higher Reynolds numbers, they do not lead to the same flow coherence as mode B did. The diagrams suggest that vortex dislocations persist until the highest Reynolds number studied for all elliptical cylinders, with the exception of the re-laminarized regimes.

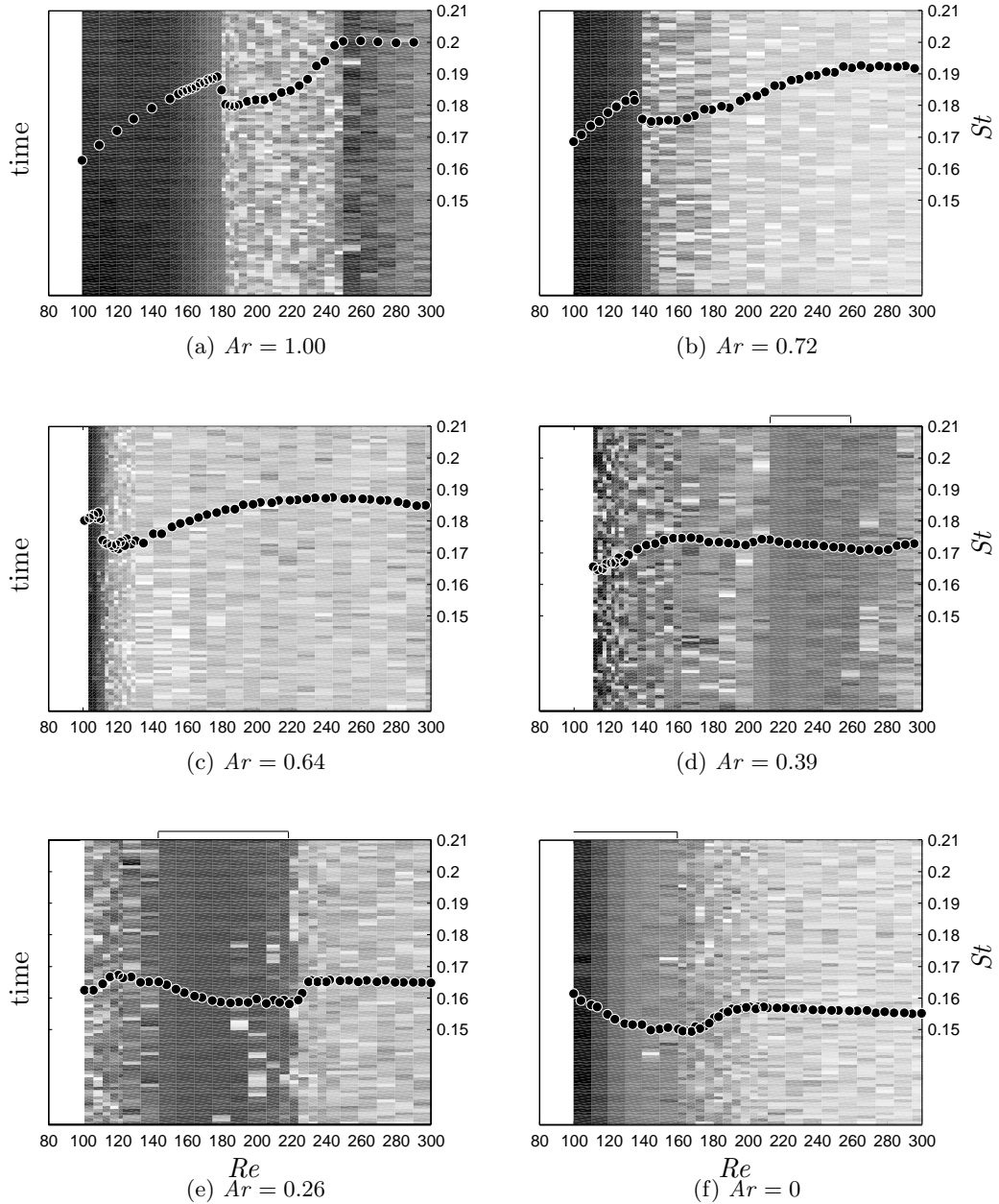


FIGURE 6.8: Energy content of the von Kármán frequency band as a function of Reynolds number and time. The laminar shedding regimes are visible as regions of uniform dark grey. The presence of three-dimensional modes and vortex dislocations leads to randomly interrupted patterns. The re-laminarized regimes are visible as the darker segments for  $Ar = 0.39, 0.26, 0$ , and are marked by the horizontal brackets. The  $St-Re$  curves are overlaid for easier comparison.

The re-laminarized regimes become apparent for the  $Ar = 0.26$  cylinder and the flat plate as uniform and continuous tile mosaics. Although not reflected in the  $St-Re$  curve, a particularly smooth region is observed for  $Ar = 0.39$  in the range  $210 \leq Re \leq 260$ . These data confirm that the wake begins to laminarize already at  $Ar = 0.39$ . The approximate extent of this regime is marked by the horizontal brackets in figure 6.8d–f.

The region of re-laminarization exhibits the same trend as  $Re_{c_0}$  (the onset of three-dimensionality), by moving to lower Reynolds numbers for smaller  $Ar$ . Uniformly grey bands of regular shedding are observed at  $Re \geq 210$  for  $Ar = 0.39$ , they develop at  $Re \geq 150$  for  $Ar = 0.26$ , and exist already at  $Re = 100$  for  $Ar = 0$ . In case of the flat plate, it can be speculated that this region merges with the initial laminar shedding regime, which is assumed to prevail at  $Re < 100$ .

### 6.3 Low frequency oscillation in the wake of the $Ar = 0.26$ cylinder: a case study

The previous section showed that there are profound changes to the primary shedding during the re-laminarized regime. Primarily, the spectral energy of the von Kármán frequency increases and the shedding becomes more uniform in time. Before the potential cause of this phenomenon is studied in detail in chapter 7, it shall be shown that the re-laminarized regime is linked to the appearance of a second (low) frequency in the wake. This will be done as a case study for the  $Ar = 0.26$  cylinder at  $Re = 150$ .

#### 6.3.1 Comparison to Johnson *et al.* (2004)

Johnson *et al.* (2004) analysed numerically the vortex structures in the wake of 2D elliptical cylinders for  $75 < Re < 175$ . The power spectrum analysis of the  $v$  velocity component along the horizontal centreline showed the presence of secondary and tertiary frequencies in the far region of the wake. As the Reynolds number was increased and/or the aspect ratio was decreased, the lower frequencies in the far wake became more dominant and their inception point occurred closer to the elliptical cylinder. Consistent with the discussion on the secondary vortex street in §2.1.2, it was suggested that this low frequency unsteadiness does not need to be due to vortex interaction, but rather, can result from the presence of a two-dimensional instability of the mean wake.

Figure 6.9 shows the downstream development of spectral energy for the three most dominant frequencies of the velocity spectrum for  $Ar = 0.25$  and  $Re = 150$ . It can

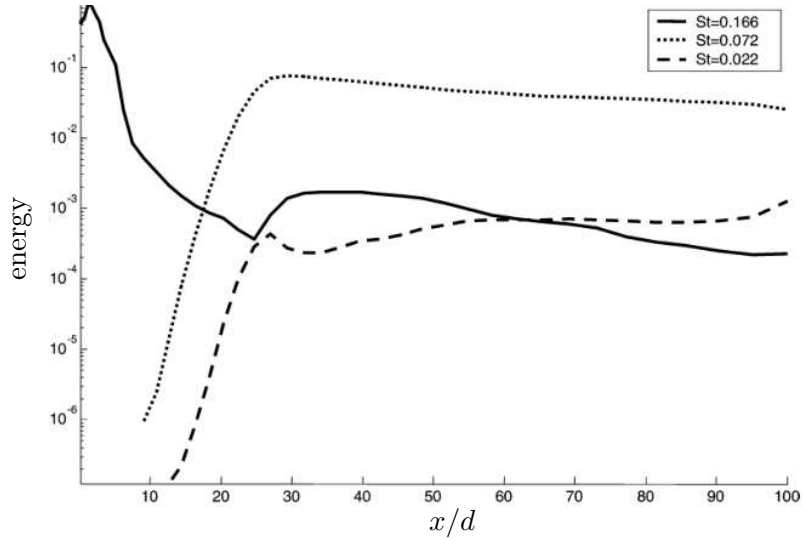


FIGURE 6.9: Downstream development of selected frequency energy for  $Ar = 0.25$  at  $Re = 150$  (numerical results from Johnson *et al.* 2004, reproduced with permission from Elsevier).

be seen that the primary shedding frequency at  $St = 0.166$  loses energy rapidly, while a lower frequency oscillation, at  $St = 0.072$ , gains energy and dominates the wake for  $x/d > 30$ . Already at  $x/d \approx 15$ , both oscillations have equal energy.

A reproduction of this numerical experiment in the water channel is shown in figure 6.10. The velocity oscillations were measured with a hot film probe at several downstream locations. The recording length per point was 1 hour (equivalent to almost 2500 shedding periods). In contrast to the numerical setup, the probe was positioned outside the centre plane, at  $y/d \approx 1$ , and the velocity data consist of both, the  $u$  and  $v$  velocity components. Nevertheless, the same qualitative behaviour can be observed: The primary shedding frequency at  $St = 0.17$  loses energy quickly, and is replaced by a much lower secondary shedding frequency at  $St = 0.08$ . Both oscillations have equal energy content at  $x/d \approx 14$ , in agreement with the numerical results. In contrast to the two-dimensional simulations, the secondary shedding frequency decays fast with downstream distance, and is undetectable already at  $x/d = 40 - 50$ .

The insert in the top right of figure 6.10 contrasts the spectral energy distribution at  $x = 6d$  to that at  $x = 16d$ . At  $x = 6d$ , the oscillation energy is concentrated in the von Kármán shedding frequency  $f_K$  and its first higher harmonic  $2f_K$ . These two frequencies are replaced by a broader peak at  $f_{sec}$ , representing the secondary shedding.

The third frequency of  $St = 0.022$ , as seen in figure 6.9, was not observed in the experiment. The frequency bands below  $St = 0.03$  consisted mainly of uniform noise and were filtered out by a high-pass filter during post-processing.

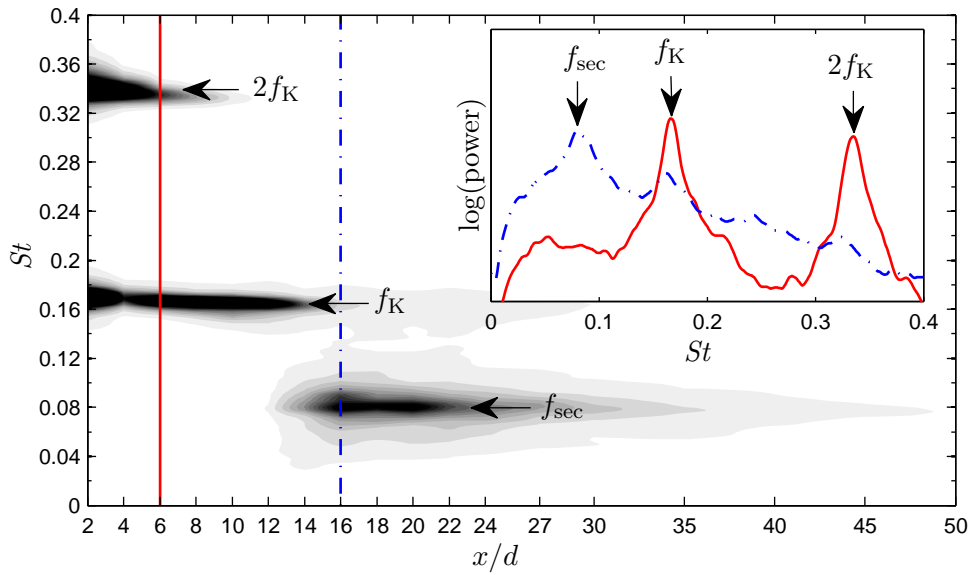


FIGURE 6.10: Downstream development of the velocity frequency spectrum in the wake of the  $Ar = 0.26$  cylinder at  $Re = 150$ . The main von Kármán shedding frequency  $f_K$  at  $St = 0.17$  decays rapidly and is replaced by a lower frequency  $f_{sec}$  at  $St = 0.08 - 0.09$ . The insert in the top right shows a comparison of power density spectra at  $x/d = 6$  and  $16$ . The  $x$ -axis labels are placed at the streamwise locations of the sampling points.

Figure 6.10 confirms the numerical results for this cylinder type and shows the presence of a secondary shedding frequency in the wake of the  $Ar = 0.26$  during the re-laminarization regime. Johnson *et al.* (2004) explained the appearance of this low frequency by the formation of the secondary vortex street (see §2.1.2). We conclude that there is a possible link between the re-laminarized regime and the secondary vortex street.

### 6.3.2 Instantaneous flow field

The question arises how the decay of the primary, and the rise of the secondary, shedding frequencies are reflected in the flow field downstream of the  $Ar = 0.26$  cylinder. For this purpose, PIV data were recorded in the  $x-y$  plane. Figure 6.11a shows the instantaneous streamwise velocity contour map at  $Re = 150$ . Two observations can be made: First, downstream of the initial recirculation region in the immediate near wake (region *I*), an unusual low-velocity region exists in the range  $4 < x/d < 12$  (region *II*). The extent of this region is shown by overlaying the  $0.2U/U_\infty$  contour line of the time-averaged flow field<sup>1</sup> onto the instantaneous flow field (white line in figure 6.11a). Within the closed contour of region *II*, the streamwise velocity decreases to 5.5% of  $U_\infty$ . It will be

<sup>1</sup>The time-averaged flow field was created from 1000 PIV snapshots, 1 sec apart.

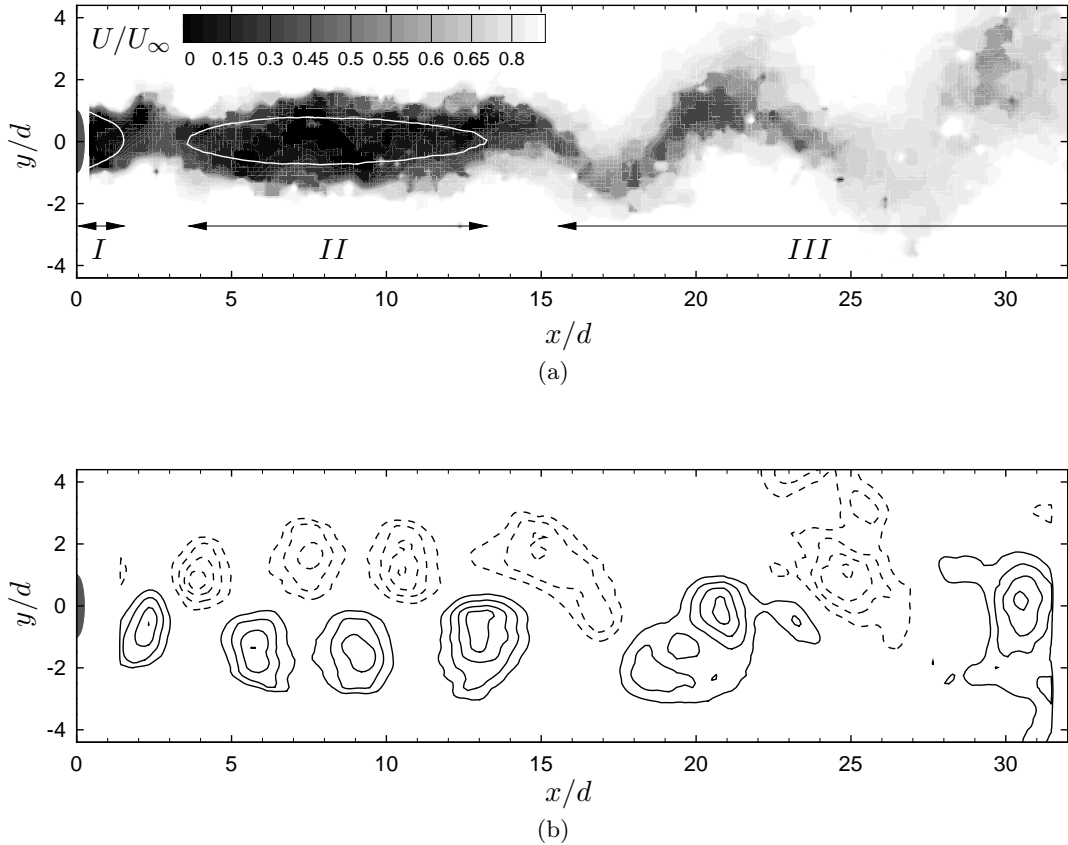


FIGURE 6.11:  $Ar = 0.26$  cylinder wake at  $Re = 150$ . (a) The grey colour map shows the instantaneous streamwise velocity; the white line is the  $0.2U/U_\infty$  contour of the time-averaged flow field. (b)  $\Gamma_2$  contours showing the instantaneous vortex cores. (The contour levels are  $\pm 0.4$ ,  $\pm 2/\pi$ ,  $\pm 0.8$  and  $\pm 0.9$ , with dashed lines denoting negative values.). The cylinder is shown at the left edge; the flow is from left to right.

shown in §7.1 that this velocity deficit is an intrinsic property of the elliptical cylinder wakes during the re-laminarized regime. The second observation is a long-wavelength oscillation of the entire wake at  $x/d > 14$  (region *III*). This oscillation bears remarkable resemblance to the secondary wake described in §2.1.2.

To locate the vortex cores in the flow field of figure 6.11a, the  $\Gamma_2$  vortex identification functions was computed from the PIV data. This Galilean invariant function identifies the boundary of a vortex on the basis of the velocity field. These boundaries are defined by the value  $\Gamma_2 = \pm 2/\pi$ ; details can be found in Graftieaux *et al.* (2001). We concluded that this function shows the vortices much clearer than the vorticity field, particularly at advanced stages of wake development (for  $x/d > 10$ ).

Figure 6.11b shows contours of  $\Gamma_2$ . The primary von Kármán vortex street is observed until  $x/d \approx 15$ . The vortices detach from the cylinder and arrange themselves

into a staggered double-row, travelling downstream. For  $x/d > 15$ , these vortices rearrange into larger structures, and the streamwise spacing between them more than doubles.

It can be concluded, that the formation of the large vortical structures at  $x/d > 15$  causes the wavy oscillation of the wake seen in figure 6.11a. Furthermore, the rearrangement of the primary von Kármán shedding into these large vortices – accompanied by a significant increase of the streamwise wavelength – explains the secondary frequency in the velocity signal ( $St = 0.080$  in figure 6.10).

The circular cylinder wake develops the secondary vortex street at downstream distances in the order of  $x/d = 100$ . Our case study shows for the first time experimentally that equivalent structures can be observed at much smaller streamwise distances ( $x/d < 30$ ), if an elliptical cylinder is used. Furthermore, these PIV data are additional evidence for a link between the re-laminarized regime and the secondary vortex street. It has been demonstrated that a rearrangement of the primary von Kármán street into large-scale structures, resembling the secondary vortex street, takes place during the re-laminarized regime of the  $Ar = 0.26$  cylinder wake. Nevertheless, the discussed data are only an instantaneous snapshot of the flow field, and a systematic study of all available models at various Reynolds numbers is needed to elucidate the connection with the phenomenon of wake re-laminarization. This study will be presented in the next chapter.

## 6.4 Chapter summary

This chapter described the first study of the largely unexplored elliptical cylinder flows, focusing on the Strouhal-Reynolds number relationship. The shape of the  $St-Re$  curves provides a wealth of information on the cylinder wake transitions, three-dimensional modes and base-flow changes. An in-depth analysis of the collected hot film velocity data, supported by flow visualizations and preliminary PIV data, leads to the following conclusions:

- The Reynolds number of the transition to three-dimensionality decreases for smaller aspect ratios.
- The Strouhal number variations degrade for  $Re > 250$ , reaching a plateau whose Strouhal number decreases linearly with aspect ratio.



- All cylinder types possess a long wavelength mode L, and a shorter wavelength mode S (modes A and B equivalents). Mode L is subharmonic in case of the flat plate. The Strouhal number discontinuity marking the appearance of mode S vanishes for  $Ar = 0.72$ ,  $0.64$  and  $0.39$ , but reappears again for  $Ar = 0.26$  and the flat plate.
- A gradual decrease of Strouhal numbers, associated with the phenomenon of ‘wake re-laminarization’, is observed for  $Ar \leq 0.39$ . This regime is associated with highly periodic shedding, at least in the near wake, and the absence of vortex dislocations.
- The re-laminarized regime is shifted to lower Reynolds numbers for decreasing aspect ratios.
- A secondary (low) frequency in the velocity signal and the formation of large-scale vortical structures, resembling the secondary von Kármán vortex street, are observed during the re-laminarized regime.

The last item on this list is the basis for the following hypothesis, which will be tested in the next chapter:

---

The re-laminarized wake regime is caused by the secondary von Kármán vortex street, whose inception point shifts upstream for decreasing aspect ratios.

---



## Chapter 7

# Elliptical cylinders: Secondary wake

The previous chapter showed that, as the aspect ratio of an elliptical cylinder is varied between  $0 \leq Ar \leq 1$ , certain modifications of the  $St-Re$  curve cannot be explained in terms of known circular cylinder transitions (e.g., the appearance of modes A and B). The most interesting and puzzling observation is the re-laminarization of the wake for  $Ar \leq 0.39$ . This flow regime is defined by a particularly regular primary shedding, similar to the laminar shedding regime of the circular cylinder at  $Re \lesssim 180$ , and a possible suppression of a previously developed three-dimensional mode. This new regime appears at lower Reynolds numbers for decreasing aspect ratios  $Ar$ . Finally, a hypothesis was put forward, stating that the wake re-laminarization is caused by the formation of the secondary von Kármán vortex street.

This chapter aims to support this hypothesis by showing the following:

1. The conditions for the breakdown of the *primary* von Kármán vortex street are fulfilled during wake re-laminarization.
2. Downstream of this breakdown, a long wavelength / low frequency *secondary* vortex street develops.

This chapter discusses PIV data at  $Re = 100, 150, 200, 250$ . The wake of each cylinder type was sampled 672 times at  $f_s = 1$  Hz in the  $x-y$  plane. The interrogation window size was  $32 \times 32$  pixels, with a 50% overlap. The freestream velocity was measured with LDV 15*d* upstream of the cylinder. A schematic of the experimental setup is shown in figure 7.1. The suction tubes (see §3.3) were removed for optical access of the PIV camera from below the tunnel.

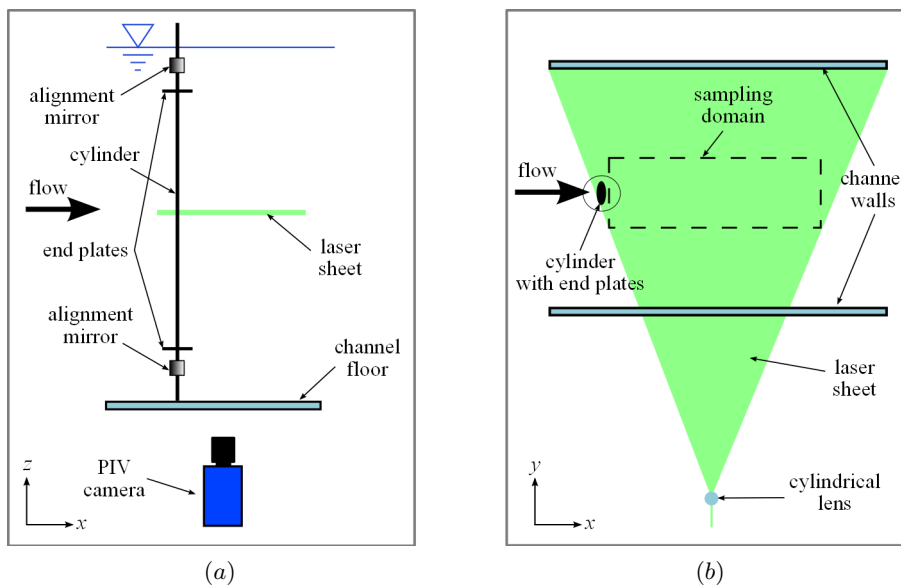


FIGURE 7.1: Experimental setup for the PIV data collection. (a) View from the side; (b) view from above.

It was realized only during post-processing that the PIV sampling rate  $f_s$  coincided with the shedding frequency of the flat plate at  $Re = 250$ . This led to an inferior convergence of the time-averaged flow field, which is seen as a waviness in the wake centreline velocity profile (figure 7.2). In addition, the POD analysis failed for this case, as most of the snapshots were not linearly independent. However, all other cases were sampled satisfactorily.

## 7.1 Wake centreline velocity profiles

First, the time averaged flow fields will be discussed. For easier comparison, only the streamwise velocity profiles along the wake centreline are presented, which were created by selecting the lowest velocity value of the  $U(y)$  velocity at each streamwise location.

Figure 7.2 shows a comparison of all profiles. For all  $Re$ , the circular cylinder profiles show the typical velocity deficit in the immediate near wake, caused by the recirculation bubble. The velocity recovers to about 80% of  $U_\infty$  within the first 5 cylinder diameters. A comparison is made to Williamson & Prasad (1993) at  $Re = 150$ , which shows that the velocity recovery is slightly lower in our experiment. This might be caused by oblique shedding, as the suction tubes were removed. At  $Re = 250$ , a shallow trough in the velocity profile is visible, centred at  $x/d \approx 25$ . This trough exists at  $x/d \approx 50-60$  for  $Re = 150$ , and is thought to be caused by the formation of the secondary wake (Williamson & Prasad 1993; Kumar & Mittal 2012).

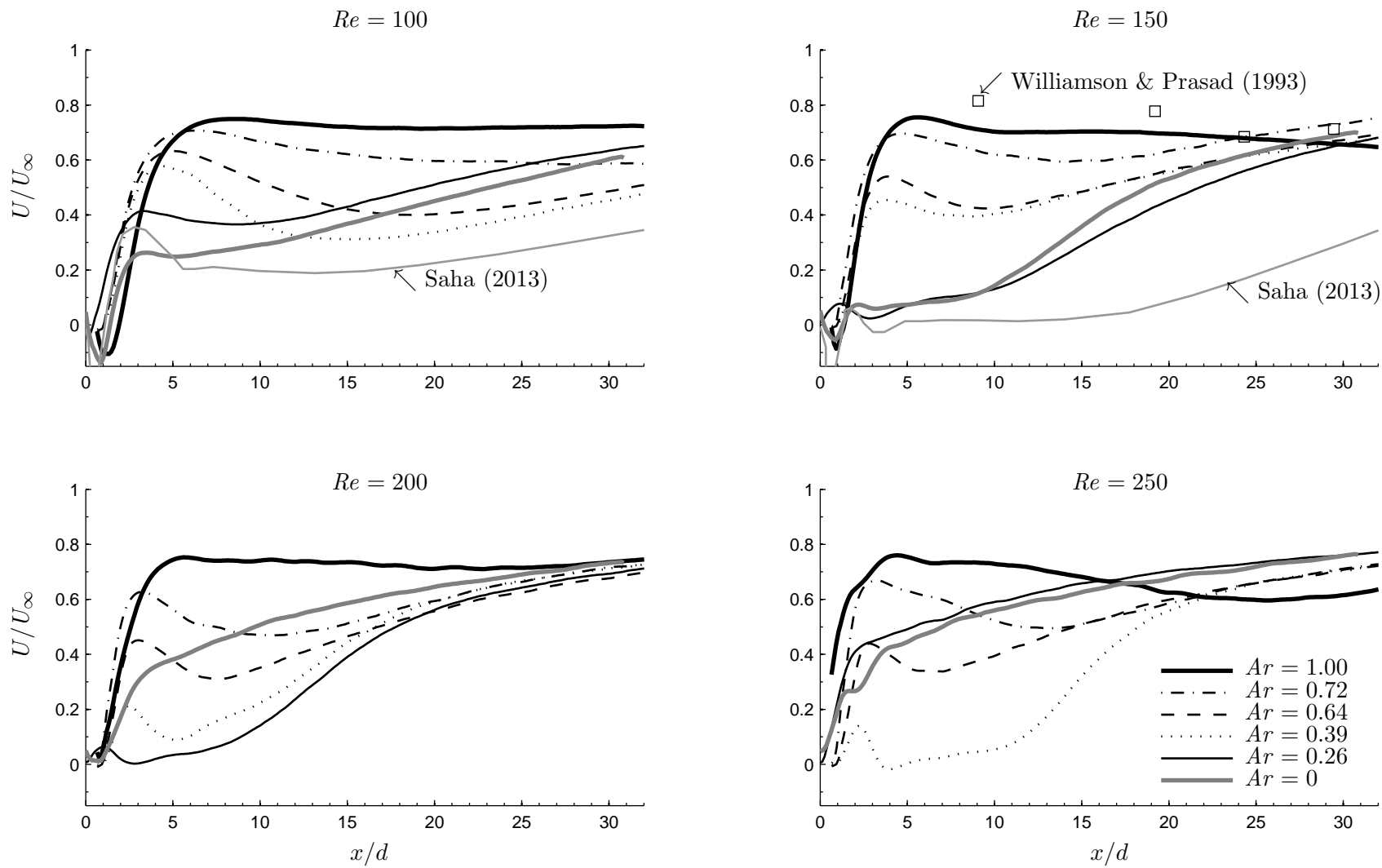


FIGURE 7.2: Time-averaged streamwise velocity profiles along the wake centreline. The data by Saha (2013) are from 2D simulations of an  $Ar = 0.125$  flat plate; the data by Williamson & Prasad (1993) are from circular cylinder experiments.

As the aspect ratio is decreased / Reynolds number is increased, this trough deepens and shifts upstream. This is a continuous process for  $Ar = 1.00$ – $0.64$ . For  $Ar = 0.39$ – $0$  a new behaviour is observed: the trough develops into a deep wake deficit, spanning the range  $x/d \approx 3$ – $12$ . This happens at lower Reynolds numbers for lower  $Ar$ : the  $Ar = 0.26$  cylinder and the flat plate exhibit this wake deficit at  $Re = 150$ . The Reynolds number has to be increased to  $200$ – $250$  for the  $Ar = 0.39$  cylinder to exhibit this effect. Interestingly, once a certain  $Re$  is exceeded, the velocity profile develops a steep velocity recovery within the first 5 cylinder diameters again (see  $Ar = 0.39$  and  $0.26$  at  $Re = 250$ ).

At this point, it is instructive to divide the centreline velocity profiles into 3 groups: *Type I* profiles, for Reynolds numbers prior to the development of the extreme wake deficit; *type II* profiles exhibiting the deficit; and *type III* profiles, at Reynolds numbers above the wake deficit regime. The three profile types are sketched in figure 7.3.

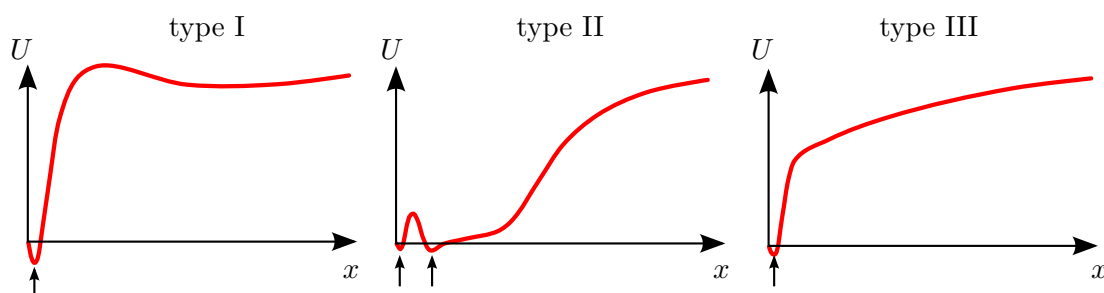


FIGURE 7.3: Schematic representation of three types of centreline velocity profiles for increasing  $Re$ . Type II was observed for  $Ar \leq 0.39$  during the re-laminarization regime. The arrows mark reverse-flow regions.

For type II profiles, streamwise velocities in the wake deficit region lie between 5% and 20% of freestream. For  $Ar = 0.26$  at  $Re = 200$ , and for  $Ar = 0.39$  at  $Re = 250$ , even a small reverse flow region exists at  $x/d \approx 3$ . This is the first experimental confirmation of the secondary recirculation bubble, as reported by Saha (2013) (see figure 2.15 on page 28). This bubble is located at the upstream end of the wake deficit. The numerically obtained velocity profiles by Saha (2013) are overlaid on our experimental data in figure 7.2 for comparison. The reverse-flow region is clearly visible at  $x/d = 4 - 5$  in these data. The wake deficit region is longer in simulations than in the experiment, likely due to stronger vortices in the 2D simulation compared to the 3D physical flow.

To quantify the profile shape changes in the  $Ar$ – $Re$  parameter space, an ‘integrated

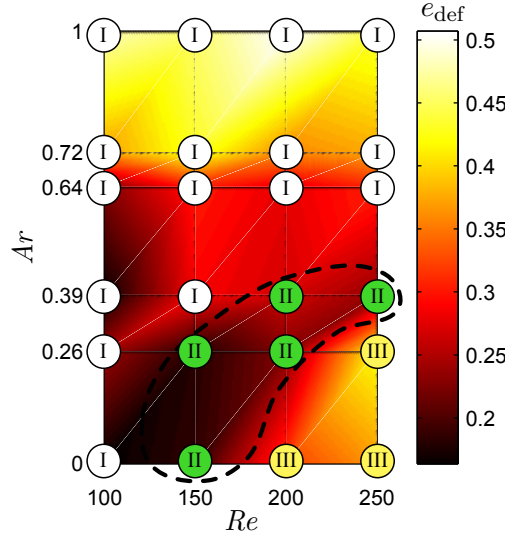


FIGURE 7.4:  $Re$ – $Ar$  parameter space showing the integrated kinetic energy deficit ratio  $e_{\text{def}}$ . The profile type is shown in the circles. The dashed line marks the parameter space of wake re-laminarization.

kinetic energy deficit ratio will be defined as:

$$e_{\text{def}} = \int_{1d}^{30d} \left( \frac{U(x)}{U_{\infty}} \right)^2 dx.$$

The value of  $e_{\text{def}}$  is rather insensitive to the integration limits, which were chosen to cover the wake deficit and most of the recovery region.

This parameter is shown in figure 7.4 as an interpolated colour map. The profile type is overlaid for each  $Ar$ – $Re$  combination. The  $e_{\text{def}}$  values tend to decrease from high to low  $Ar$ , with type II profiles having some of the lowest values. The  $Ar = 0$  profile at  $Re = 100$  lies between types I and II, as it has a very low value of  $e_{\text{def}}$ , while having a wake deficit velocity above 20% of  $U_{\infty}$ .

The parameter space for which wake re-laminarization was observed in chapter 6, is marked by the black dashed contour in figure 7.4. It is apparent that all type II profiles fall into this region. For higher Reynolds numbers, these profiles change to type III profiles.

We can conclude that the wake re-laminarization regime is characterized by type II velocity profiles, exhibiting a strong velocity deficit. The velocity deficit disappears for higher Reynolds numbers, and type III profiles are established. For  $Ar \geq 0.64$ , only type I profiles exist in the studied Reynolds number range.

## 7.2 Vortex street geometry

Chapter 2.1.2 discussed the geometrical parameters of the vortex street, which are associated with its breakdown. Several studies (Taneda 1959; Durgin & Karlsson 1971; Tsuboi & Oshima 1985; Karasudani & Funakoshi 1994) observed that the von Kármán vortex street was likely to decay into a steady double shear layer when its *vortex spacing ratio*  $h/a$  exceeded the critical range 0.3–0.5 (with  $h$  being the distance between the vortex rows, and  $a$  being the spacing of the vortices in each row). Durgin & Karlsson (1971) presented a derivation of the theoretical value  $h/a = 0.365$ , whereas Karasudani & Funakoshi (1994) report an experimentally obtained value 0.4–0.5. Once the double shear layer was formed, the secondary vortex street of larger dimensions was very likely to appear downstream of the breakdown location.

Naturally, the value of  $h/a$  increases in downstream direction, as the vortex row separation  $h$  increases, but the streamwise distance of the vortices does not change considerably. The following study examines the streamwise development of the vortex street geometry of elliptical cylinders and assesses the applicability of the  $h/a$  criterion in predicting an earlier vortex street breakdown as the condition for the development of the secondary vortex street for  $Ar < 1$ .

### 7.2.1 Method

The  $\Gamma_2$  vortex identification function was computed from PIV vector fields (Graftieaux *et al.* 2001). In each vector field, the vortex boundaries were identified based on the condition  $\Gamma_2 = \pm 2/\pi$ ; vortices with contours clipped at the frame edges and vortices with an area below a minimum threshold were ignored. The vortex core centres were computed from an area integral within each boundary, weighted by the vorticity distribution within these boundaries. Figure 7.5a shows the identified vortex boundaries as bold lines; positive and negative core centres are marked by plus and circle symbols, respectively. The vorticity colour maps are plotted within each vortex boundary; positive vorticity is blue, negative is green.

To track the development of the geometry parameters in downstream direction,  $h$ ,  $a$  and  $h/a$  were calculated for each identified vortex. This was done by measuring the streamwise ( $\Delta x$ ) and cross-stream ( $\Delta y$ ) distances to the next vortex of opposite sign within a properly sized bounding box. The geometric parameters were then:  $h = \Delta y$  and  $a = 2\Delta x$ . The direct connection lines of length  $\sqrt{\Delta x^2 + \Delta y^2}$  between all identified



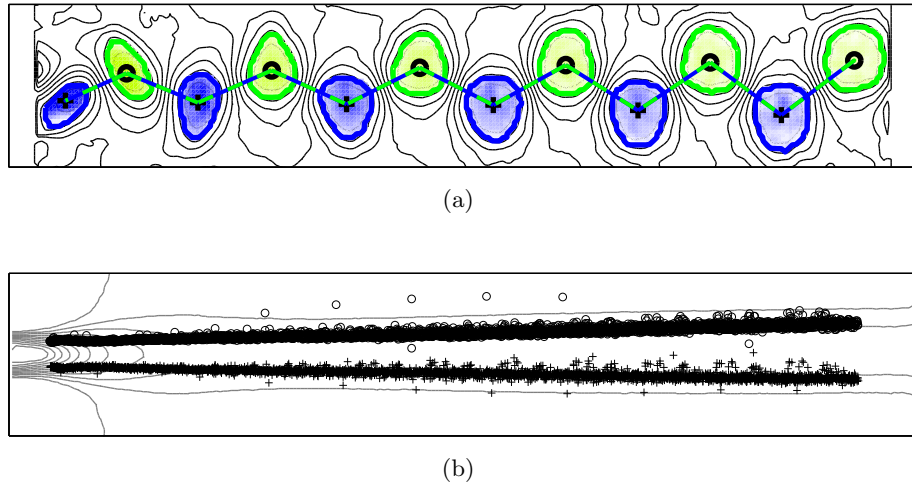


FIGURE 7.5: Geometric analysis of the circular cylinder wake: (a) sample PIV frame showing identified vortex core boundaries in bold blue (positive) and green (negative) lines. (b) Locations of the vortex core centres at  $Re = 100$  (identified from 672 vector fields), overlaid on the time-averaged streamwise velocity contours (grey lines).

vortices are shown as the green-blue dashed lines in figure 7.5a.

The time-averaged vortex core trajectories were approximated by averaging all vortex locations. Figure 7.5b shows that, in case of the circular cylinder at  $Re = 100$ , the vortex locations collapse onto two narrow paths. By binning these data along the streamwise direction into bins of width  $1d$ , local averages of  $h$ ,  $a$ ,  $h/a$ , and their spread (standard deviation) were calculated. Typically, over 100 vortices were combined in each bin; this number decreased significantly when the secondary vortex street appeared. This is why data only up to  $x/d = 15$  will be plotted for  $Ar = 0.26$ .

## 7.2.2 Results

Figure 7.6 shows the streamwise development of the geometry parameters of the circular cylinder at  $Re = 100$ , 150 and 250. It can be seen in the left column that the two vortex paths diverge in cross-stream direction after an initial parallel section. The trajectories are in good agreement with data by Karasudani & Funakoshi (1994) (dashed bold lines). During the laminar shedding regime at  $Re = 100$  and 150, the spread of the core loci in cross-stream direction is small, but increases after the transition to three-dimensionality at  $Re = 250$ , as can be seen by the error bars (showing two standard deviations of the spread in each bin).

The streamwise separation between vortices of each row reaches a constant value  $a/d = 4-5$  for  $x/d > 8$ , after an initial rapid increase (figure 7.6, middle column). It

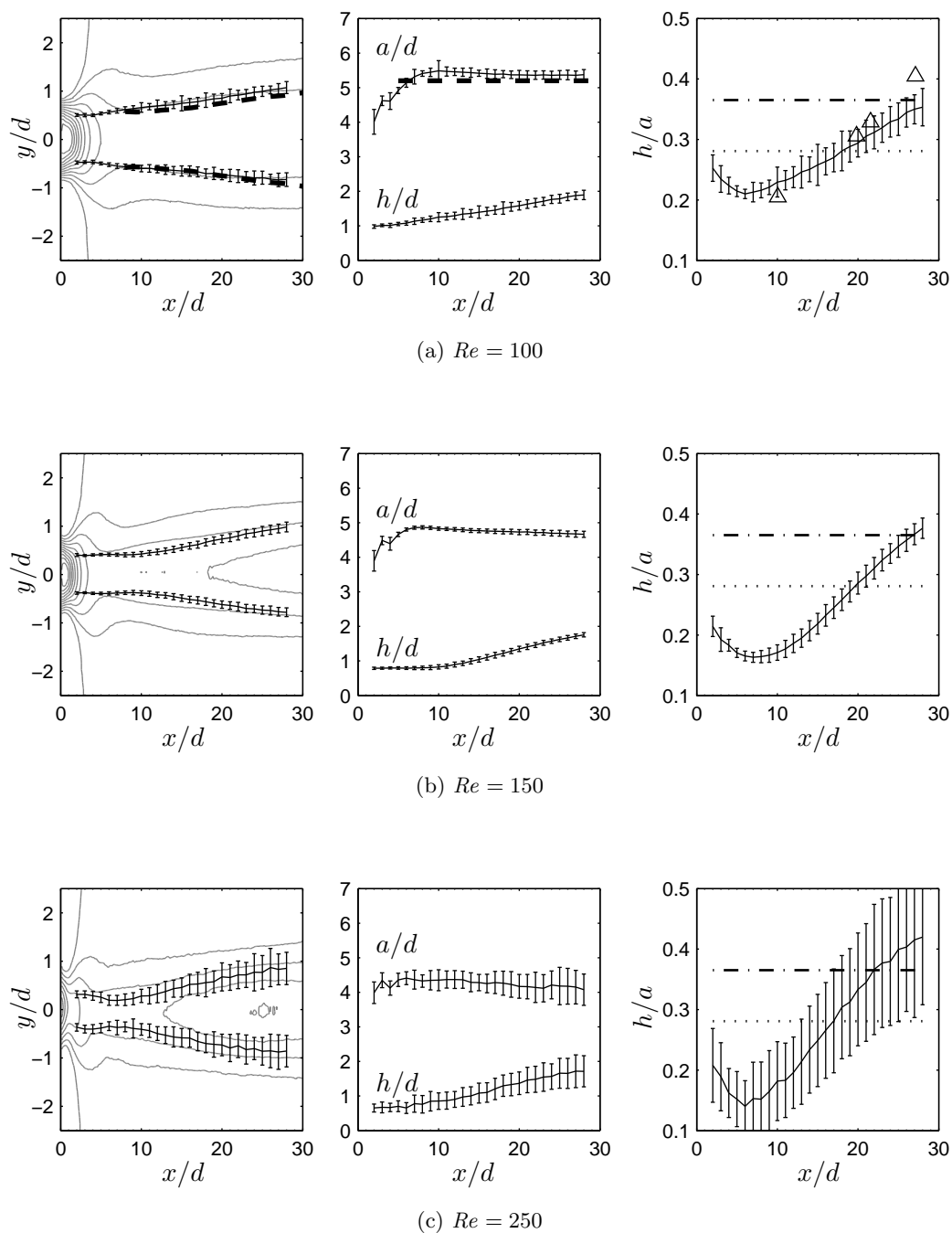


FIGURE 7.6: Vortex street geometry of the circular cylinder wake. The left column shows the vortex cores trajectories (black lines with error bars) overlaid on the time-averaged streamwise velocity contours (grey). The middle and the right columns show the streamwise development of streamwise core spacing  $a$ , lateral spacing  $h$  and their ratio  $h/a$ . The dashed-dotted line in the right column is the critical value  $h/a = 0.365$ ; the dotted line is the von Kármán ratio  $h/a = 0.281$ . The bold dashed lines and the triangles in (a) show data from Karasudani & Funakoshi (1994).

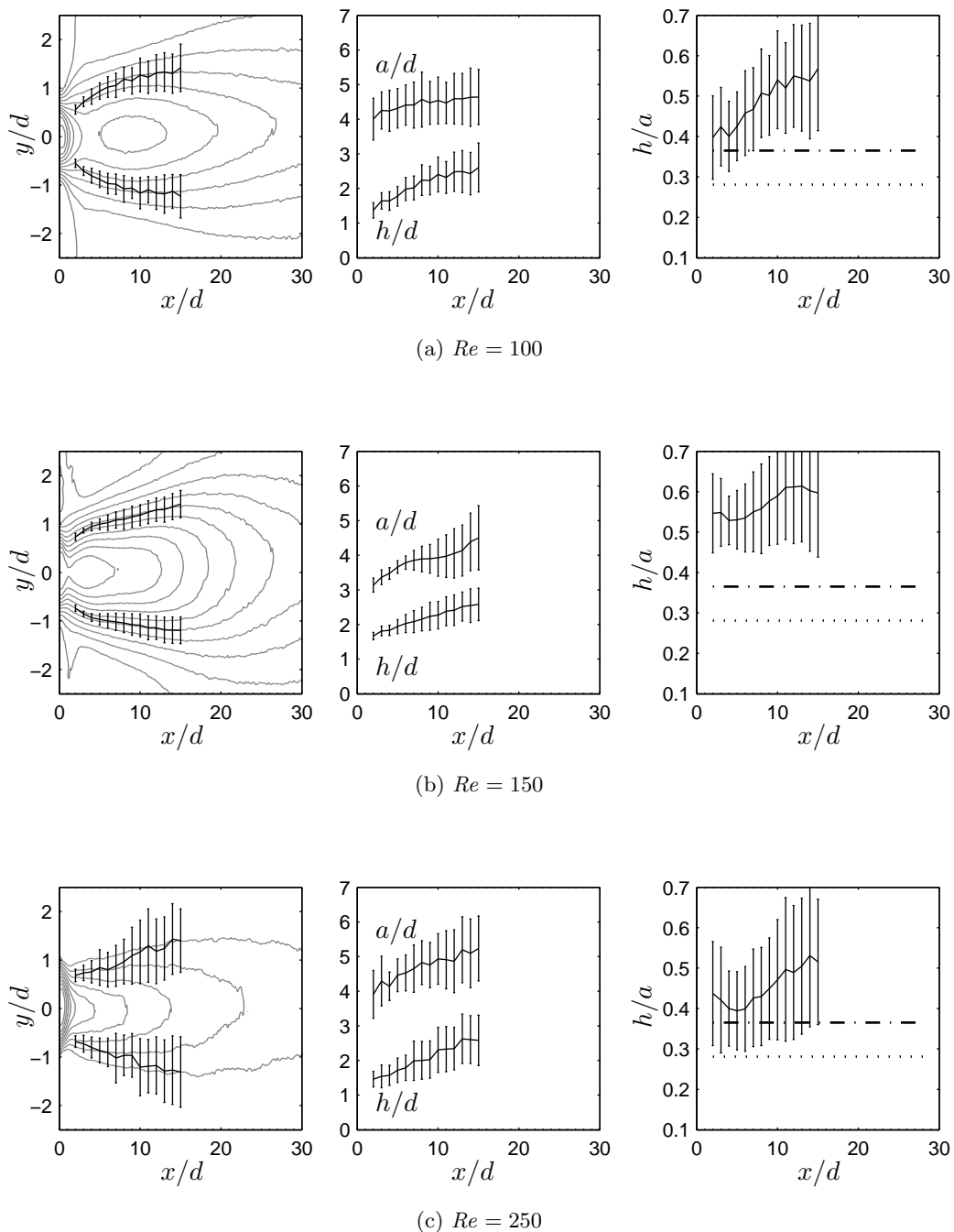


FIGURE 7.7: Vortex street geometry of the  $Ar = 0.26$  cylinder wake. Compare to figure 7.6; note the different scale in the right column. The wake is re-laminarized at  $Re = 150$ .

is the simultaneous growth of the cross-stream vortex separation  $h$  which leads to an increase of the parameter  $h/a$  in streamwise direction (right column).  $h/a = 0.365$  is reached at  $x/d \approx 30$  at  $Re = 100$  and  $200$ . This point shifts upstream to  $x/d = 20$ – $25$  for  $Re = 250$ . As no data was recorded downstream of  $x/d = 32$ , the consequences of exceeding the critical value are not clear. For comparison with elliptical cylinders, it should be noted that  $h/a$  stays largely below the critical range  $0.3$ – $0.5$ .

As a side note, the von Kármán ratio of the idealized vortex street  $h/a = 0.281$  exists only in a very limited streamwise extent, at  $x/d \approx 18$ . The cross-stream separation of the vortex rows in the real vortex street increases considerably in streamwise direction.

Figure 7.7 shows the wake geometry of the  $Ar = 0.26$  cylinder. The left column reveals a wider wake compared to the circular cylinder at all three Reynolds numbers, and the absence of the initial parallel section of the two vortex rows. The cross-stream distance between the vortex rows  $h$  within the first 5 diameters downstream of the cylinder is almost twice as large compared to the circular cylinder ( $h/d = 1.4$ – $1.8$  for  $Ar = 0.26$ , compared to  $0.6$ – $1.0$  for  $Ar = 1.00$ ; middle column). The vortex spacing ratio is above the critical value  $0.365$  throughout the sampled domain at all three Reynolds numbers (right column). This ratio is particularly high ( $> 0.5$ ) at  $Re = 150$ , which is in the re-laminarized regime of this cylinder type. Comparing the graphs of the middle column, it is apparent that the high value of  $h/a$  at this Reynolds number is primarily caused by a decrease of  $a$ . At  $Re = 150$ , the vortices are formed at an initial streamwise spacing of just 3 cylinder diameters, whereas this distance is above  $4d$  at  $Re = 100$  and  $250$ .

### 7.2.3 Conclusions

The vortex spacing ratio  $h/a$  increases consistently for decreasing aspect ratios  $Ar$  (figure 7.8). Yet, the data do not show a clear enough trend to allow the use of  $h/a$  as a criterion for the identification of the re-laminarized flow regime. For  $Ar = 0.26$ , this ratio is equal, or above the critical value  $0.365$ , independently of the flow regime. Nevertheless, it can be concluded that the re-laminarized regime is characterized by a particularly high vortex spacing ratio ( $h/a > 0.5$ ), which is caused by a decreased streamwise separation of newly formed vortices.

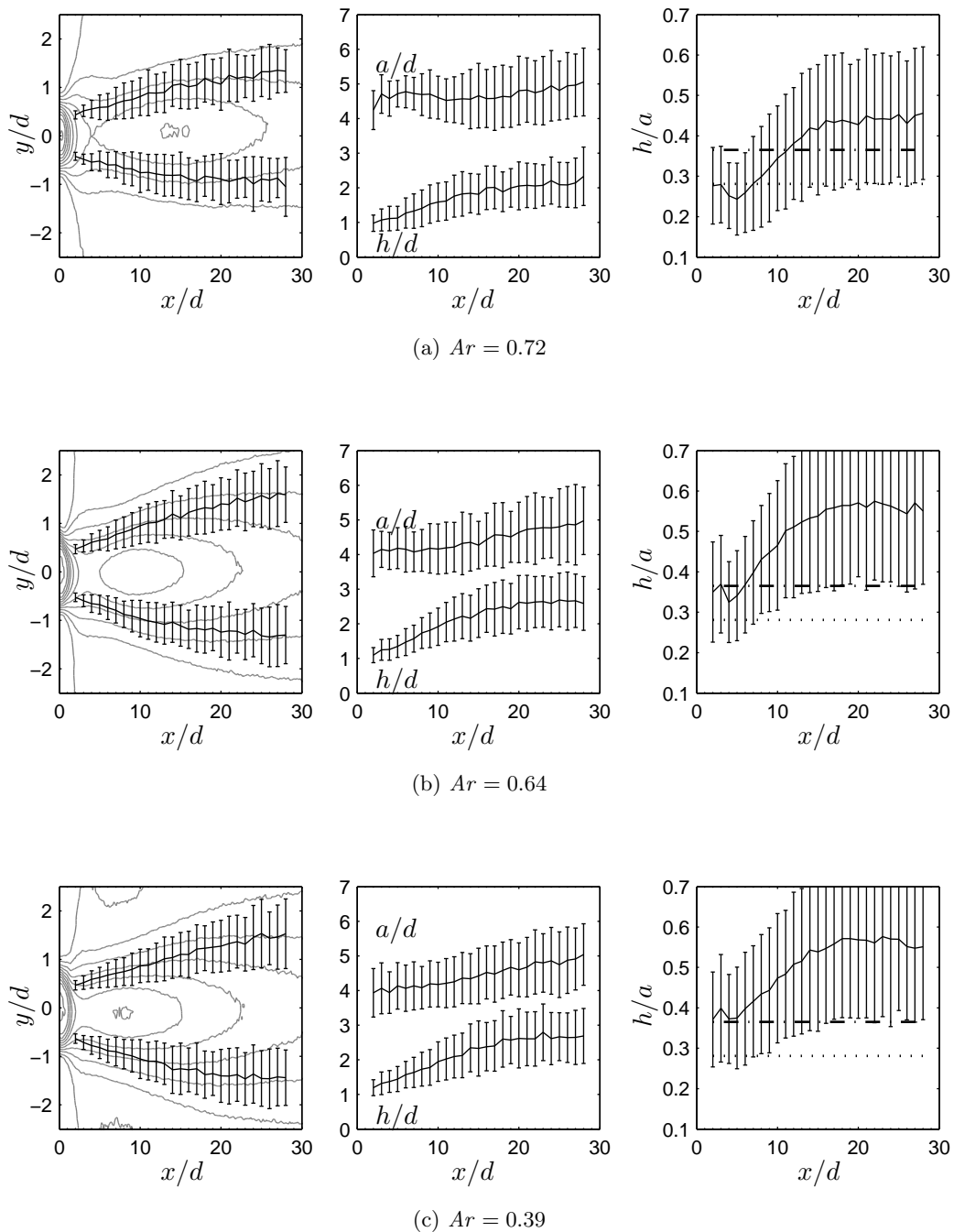


FIGURE 7.8: Dependence of the vortex street geometry on the aspect ratio  $Ar$  at  $Re = 150$ . The vortex spacing ratio  $h/a$  is observed to increase consistently with decreasing aspect ratio.

## 7.3 Proper orthogonal decomposition of velocity fields

Direct evidence of the secondary vortex street will be presented in form of a proper orthogonal decomposition (POD) of PIV vector fields (see §3.5.2 for the mathematical background). First, the accuracy of the decomposition will be evaluated for the  $Ar = 1.00$  cylinder at  $Re = 100$ . Then, selected cases will be presented, showing the appearance of the second wake during the re-laminarization regime. Flow fields of modes 0–5 for all  $Ar$ – $Re$  combinations can be found in appendix C.

As the POD was performed on velocity fields<sup>1</sup>, the modes are ordered according to their kinetic energy. All modes will be presented as  $\omega_z$ -vorticity contours, which have been computed by taking the curl of the modes' velocity fields. Positive vorticity is marked in blue, negative vorticity is coloured light green. The contour levels are arbitrary, but of the same order of magnitude for all modes, as the mode flow fields are orthonormal. The kinetic energy content of each mode is expressed by its eigenvalue  $\lambda$ . For plotting, these energies are normalized by the sum of all modes excluding mode 0 (the time-averaged flow field), which is equal to the fraction of the fluctuating energy content of the flow.

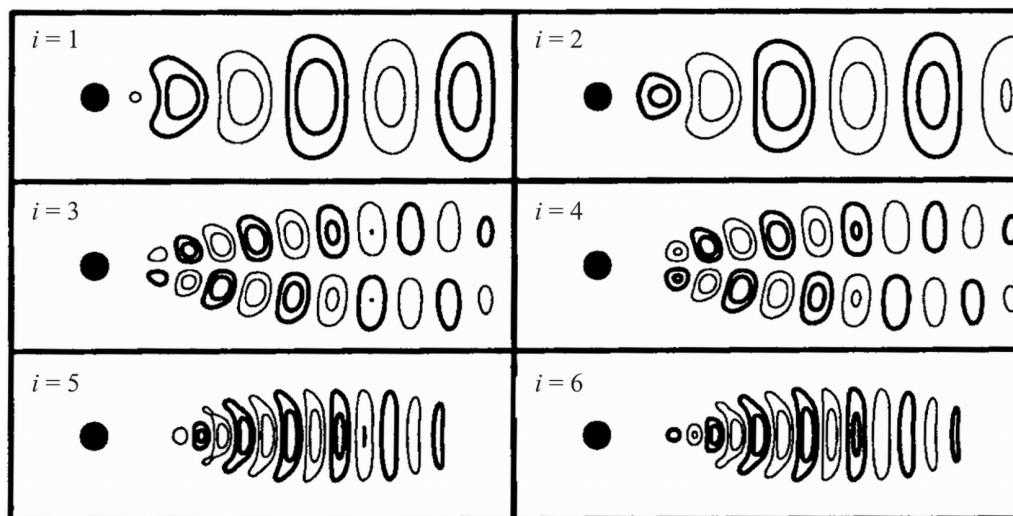
### 7.3.1 Circular cylinder

The circular cylinder wake is known to exhibit strictly periodic laminar shedding at  $Re = 100$ . The POD modes form pairs, due to the closeness of the vortex street to a travelling wave (Ma *et al.* 2000). As the harmonic oscillation of the wake contains most of the fluctuating kinetic energy, the two most energetic POD modes can be expected to represent the von Kármán vortex shedding, followed by higher harmonics of this motion. In figure 7.9, the streamfunctions  $\Psi$  ( $d\Psi = -v dx + u dy$ ) of the experimentally obtained modes are compared to numerical results by Noack *et al.* (2003). Naturally, the (2D) simulation has a lower noise level than the experiment, and reproduces the higher harmonics much cleaner. Still, the match of modes 1 & 2 is very good, and the mode shapes of the higher harmonics are recognizable in the experimental data. In both cases, the paired modes have the same flow pattern, shifted in streamwise direction by a quarter wavelength.

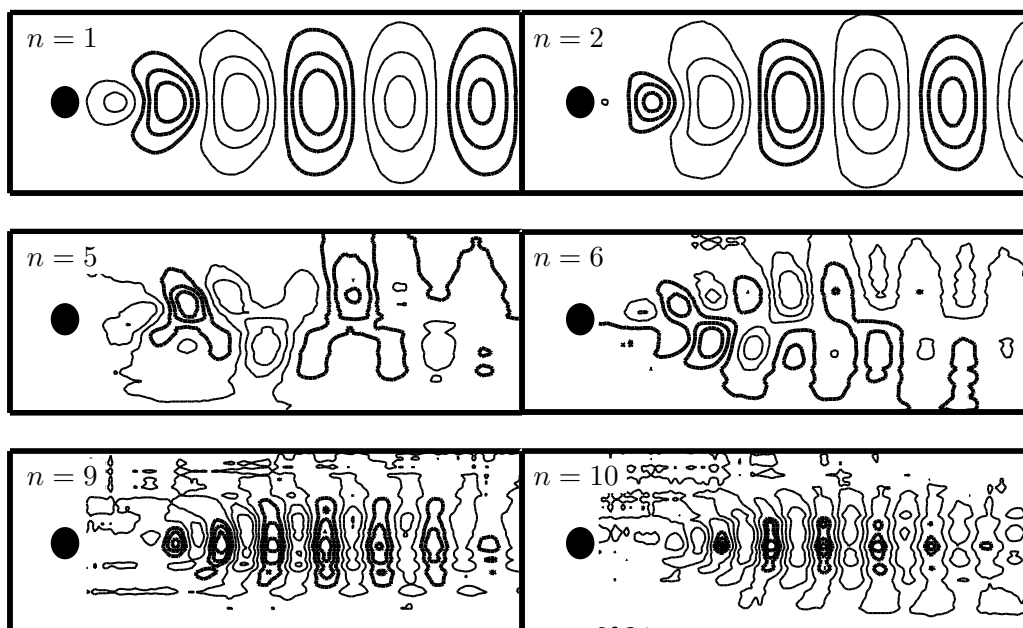
The energy distribution of the first 15 modes is shown in figure 7.10. The first

---

<sup>1</sup>According to Kostas *et al.* (2005), for low-Reynolds number flows with dominant periodic motion, no significant differences exist between a decomposition based on velocity fields and a decomposition based on vorticity fields. This is not the case for turbulent flows.



(a)



(b)

FIGURE 7.9: Circular cylinder POD modes at  $Re = 100$ . (a) Numerical results by Noack *et al.* (2003). (b) Selected modes from the present experiments. The flow field is visualized by iso-contour lines of the streamfunction. Positive (negative) values are indicated by thick (thin) lines. The cylinder is represented by the solid circle. ((a) is reproduced with permission from Noack *et al.* 2003)

two modes contain over 98% of all fluctuating kinetic energy in the 2D simulations by Deane *et al.* (1991), and similarly by Noack *et al.* (2003). In the experiment, modes 1 & 2 combine over 80% of energy, and a drastic drop for the next 2 modes is observed. The ‘energy cascade’ is not as steep, and the mode pairs are not as discretely defined as in the simulations. The match is good up to mode 6, after which the energy is spread rather equally over the higher modes. This is probably due to the fact that the real flow is not perfectly periodic, creating a limited number of higher harmonics.

It should also be noted that not all mode numbers in figure 7.9b match the numerical modes in 7.9a. Considering the flat energy cascade of higher modes in the experiment, it is possible that modes are ‘pushed up’ along this cascade by energetic flow irregularities or intermittent events. In particular, the omitted modes 3 & 4 have a strong cross-stream velocity component, which might be the result of ‘wake flapping’. At higher Reynolds numbers, vortex dislocations can create specific mode shapes that reside relatively high in the eigenvalue spectrum (Zhao & Ling 2003).

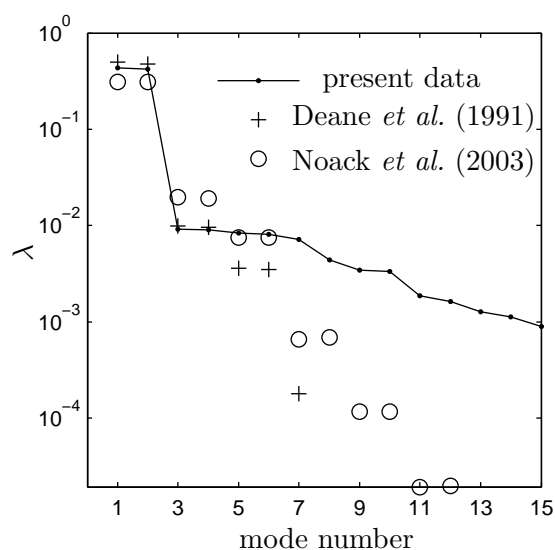


FIGURE 7.10: Eigenvalues of the 15 most energetic POD modes of the circular cylinder wake at  $Re = 100$ .

The energy distributions of the first 4 modes at  $Re = 100$ , 150, 200 and 250 are compared in figure 7.11. The first two Reynolds numbers lie in the laminar shedding regime, thus, no significant changes of the modes’ shape or order are observed, while the fluctuating energy remains concentrated in the first two modes. This changes in the transitional regime at  $Re = 200$ , when mode A develops, and irregularities in the form of vortex dislocations disrupt the periodic shedding. This leads to a broader distribution of fluctuating energy across the modes, decreasing the energy content of



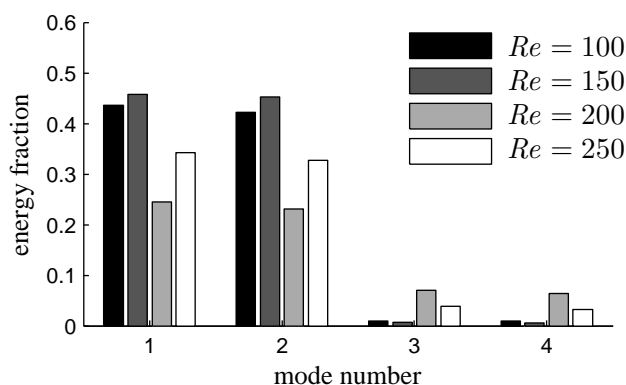


FIGURE 7.11: Comparison of the energy distribution of modes 1–4 of the circular cylinder wake at various Reynolds numbers. Modes 1 and 2 contribute most to the von Kármán shedding motion.

the first two modes to just over 20% each (which is still a high value). Consistent with the discussion in §6.2, the von Kármán shedding becomes more regular again for  $Re \geq 250$  (see also Williamson 1996c), which leads to increased energy content of modes 1 and 2 at  $Re = 250$ .

### 7.3.2 $Ar = 0.72$ and $Ar = 0.64$ cylinders

The energy distribution among the first four modes of the  $Ar = 0.72$  and  $0.64$  cylinders is shown in figure 7.12. Similar to the circular cylinder, modes 1 and 2 contain at least 70% of the fluctuating energy at  $Re = 100$ . This value is almost halved for  $Re \geq 150$ , when the first three-dimensional mode develops. The energy recovery of modes 1 and 2 at  $Re = 250$  is much weaker than in the circular cylinder case, and is observed only for  $Ar = 0.72$ .

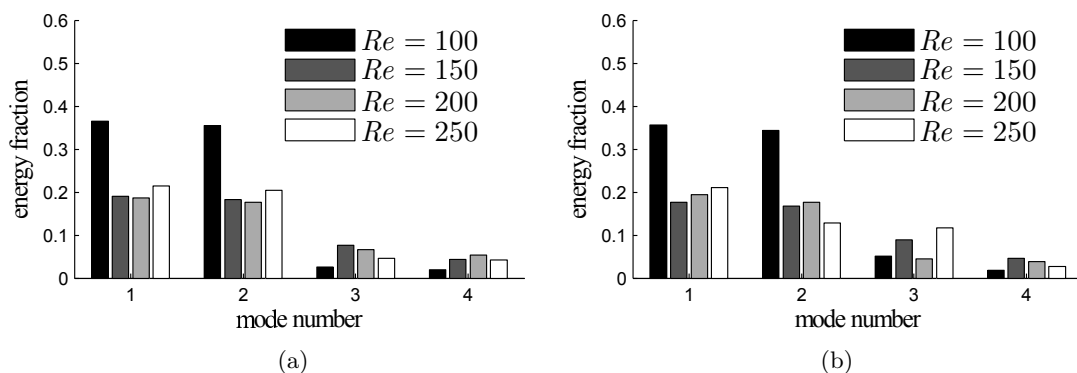


FIGURE 7.12: Comparison of the energy distribution of modes 1–4 between the  $Ar = 0.72$  (a) and  $Ar = 0.64$  (b) cylinder wakes.

The most prominent changes of the flow field, as the aspect ratio is decreased to  $Ar = 0.64$ , are exemplified in figure 7.13. Compared to the circular cylinder at  $Re = 100$  (figure 7.13a), the streamwise extent of the von Kármán wake is decreased (figure 7.13b). It can be speculated that the von Kármán vortices are disrupted and ‘smeared out’ into two parallel rows of opposite vorticity. This assumption is supported by the appearance of a mode representing a double shear layer, which becomes strongest downstream of the decaying main vortices ( $x/d = 15$ – $30$ ). This mode type is observed up to  $Re = 200$  for  $Ar = 0.72$  and  $0.64$ . It should be noted that the streamwise extent of the highest vorticity of this mode coincides with the ‘trough’ in the wake velocity profile, discussed previously (figure 7.2).

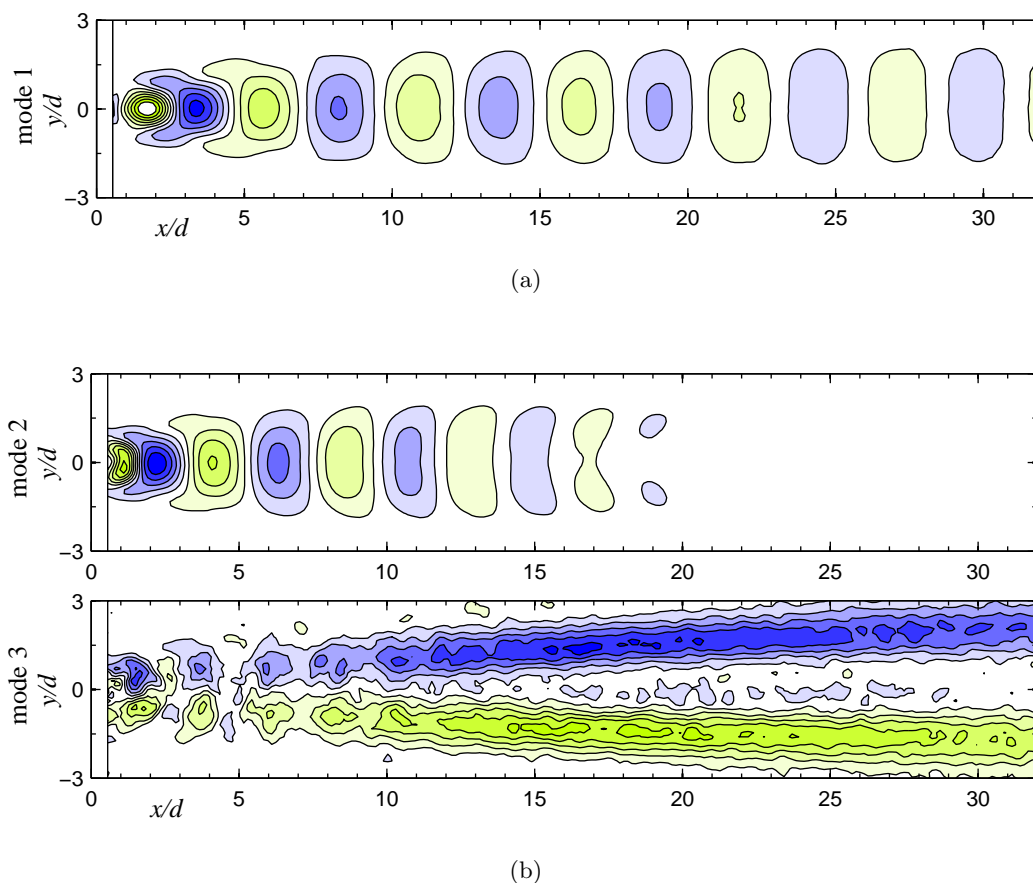


FIGURE 7.13: (a) Mode 1 of the circular cylinder wake at  $Re = 100$ . (b) Modes 2 and 3 of the  $Ar = 0.64$  cylinder wake at  $Re = 100$  show that the streamwise extent of the von Kármán vortex street decreases, which tends to be replaced by a double shear layer. Note that the energy content of mode 2 is seven times higher than of mode 3.

### 7.3.3 $Ar = 0.39$ cylinder

The first evidence of the secondary wake is observed in the sampling domain for  $Ar = 0.39$  at  $Re = 250$  (in a weak form already at  $Re = 200$ ). The second wake appears in form of a mode pair (modes 3 & 4). The streamwise wavelength of these modes is approximately 2.1 times larger than of the von Kármán modes 1 & 2. Assuming equal convection velocity, this would result in approximately half the shedding frequency compared to the primary frequency. A similarly low frequency  $f_{\text{sec}} \approx f_{\text{K}}/2$  was already observed in the  $Ar = 0.26$  wake (see §6.3)<sup>2</sup>.

Figure 7.14 shows the flow fields of modes 0, 1 and 3. Mode 1 (and similarly mode 2) bear little resemblance to the previously discussed von Kármán vortex street modes. The mode structure is defined now by two rows of vortices offset from the wake centreline. The replacement of the regular von Kármán – type wake by a double-row of vortices is known from the flat plate flow at  $Re < 100$  (Thompson *et al.* 2006). The current results show that this process sets in already at  $Ar = 0.39$  for  $Re = 200$ –250.

Mode 3, which represents the secondary wake, is equivalent in structure to the regular von Kármán vortex street. The vorticity peaks are centred on the wake centreline, but at double the streamwise distance. When comparing this mode to mode 2 of the circular cylinder in figure 7.13a, we see that in both cases the main structures develop from a reversed ‘C’-shape into oval shapes with increasing streamwise distance from the cylinder.

In case of the secondary wake, the main structures originate from a region 5–10 cylinder diameters downstream of the model. This is the vorticity-free region enclosed by vortices of mode 1 and the strong time-averaged vorticity seen in mode 0. It is concluded that strong vortices traverse this region and retard fluid between them. This leads to the velocity deficit discussed in connection with type II velocity profiles in §7.1. This velocity deficit is outlined by the  $0.2U/U_{\infty}$  contour in the mode 0 flow field (bold black line).

Finally, the bar graph in figure 7.14 shows that modes 1 & 2 and modes 3 & 4 have comparable energies, each containing approximately 10% of the overall fluctuating energy. This confirms that two vortex streets of similar strength are present in the flow: a short wavelength street represented by modes 1 & 2, and a long wavelength street

<sup>2</sup>Unfortunately, the PIV sampling rate (1 Hz) was not sufficient to resolve the frequencies of modes 1–4. The hot film measurements of chapter 6 suggest:  $f_{\text{K}} = 1.33$  Hz and  $f_{\text{sec}} \approx 0.66$  Hz (assuming  $f_{\text{sec}} = f_{\text{K}}/2$ ).

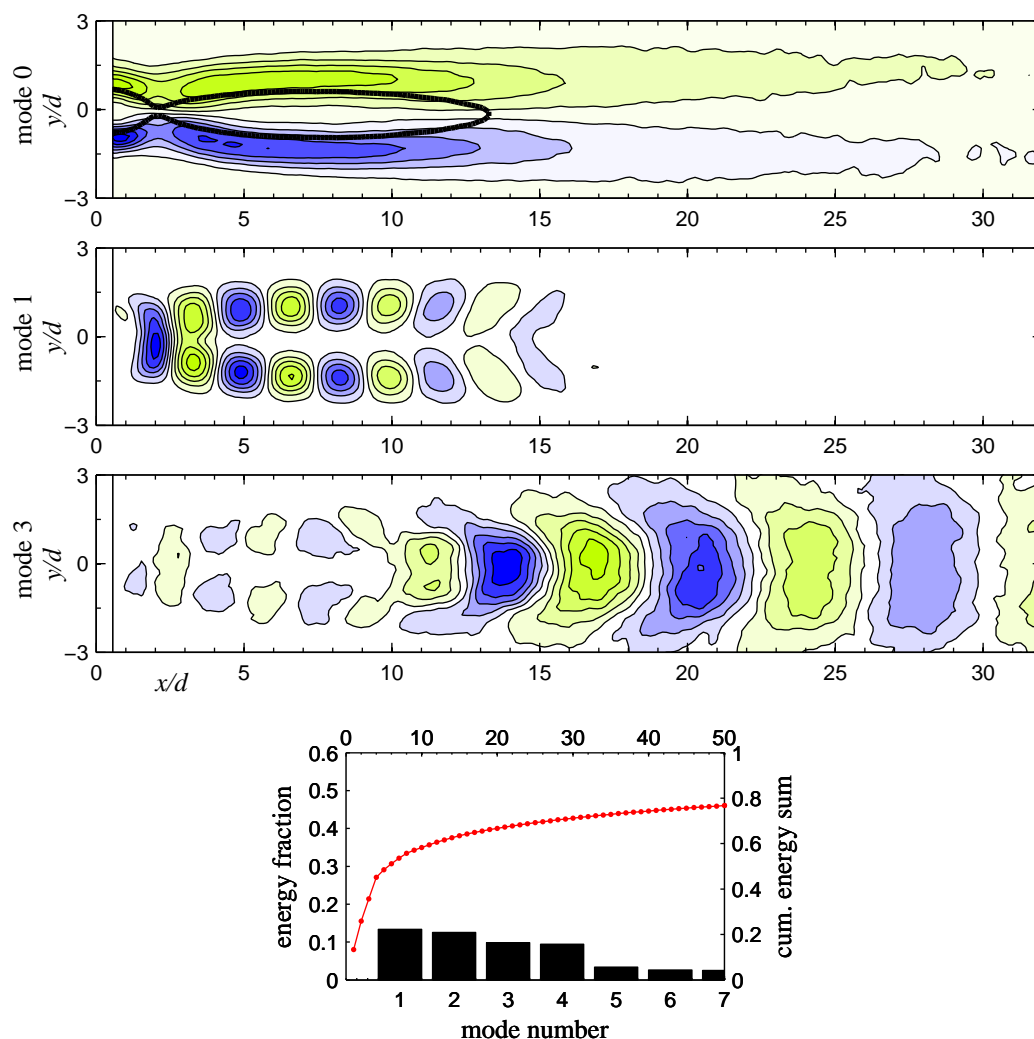


FIGURE 7.14: POD modes of the  $Ar = 0.39$  cylinder wake at  $Re = 250$ . Modes 1 & 2 represent the primary von Kármán street; modes 3 & 4 can be attributed to the secondary vortex street. The bold black line in mode 0 is the  $0.2U/U_\infty$  contour of the time-averaged flow field. The graph at the bottom shows the energy distribution of the first 7 modes (black bars; left ordinate axis), and the energy convergence of the first 50 modes (red markers; right ordinate axis).

formed by modes 3 & 4.

### 7.3.4 Flat plate

The  $Ar = 0.26$  cylinder and the flat plate show similar wake behaviour: For low Reynolds numbers, a weak double-row of vortices develops already at  $Re = 100$ , which tends to collapse into a double shear layer at increasing downstream distance, similar to the discussion of figure 7.13. Modes representing the secondary vortex street are observed for  $Re = 150$  and  $200$  in case of  $Ar = 0.26$ , and for  $Re = 150$  for the flat plate. The full data set can be found in the appendix C.

Figure 7.15 shows modes of the flat plate wake at  $Re = 150$ , when the second vortex street is present. Modes 1 & 2 and 4 & 5 represent the primary and the secondary vortex streets, respectively. Similar modes were already observed in the  $Ar = 0.39$  wake at  $Re = 250$ . The main difference (besides a shortened primary wake) is the appearance of a double shear layer mode 3. The effect of this mode can be deduced from the time history of its projection coefficient  $a^{(3)}(t)$ , shown in the right half of figure 7.15. Most of the time,  $a^{(3)}(t)$  is small, meaning that this mode is weak. Yet, larger bursts are observed at 35 and 65 main shedding periods. These bursts are of positive sign ( $a^{(3)}(t_k) > 0$ ) and coincide with periods of reduced amplitudes of  $a^{(1)}(t)$  and  $a^{(4)}(t)$ . Superimposing mode 3 with mode 0, leads to a reduction of vorticity strength of the primary wake. The conclusion is that mode 3 represents a random collapse of the primary (and secondary) vortex street, which is ‘smeared out’ into a double-shear layer. Although  $Re = 150$  belongs to the re-laminarized regime, this data show that the vortex street still can collapse intermittently. This was already observed in the hot film data presented in chapter 6.2 (see figure 6.8f on page 101).

The shedding frequency of the flat plate at the discussed Reynolds number lies above the PIV Nyquist frequency, which means that the time history of  $a^{(1)}(t)$  is aliased. Hot film data show that the flat plate sheds with  $f_K = 0.566$  Hz at  $Re = 150^3$ . Nevertheless, the PIV sampling frequency was sufficient to resolve the secondary shedding frequency, which is  $f_{sec} = 0.32 - 0.37$  Hz. The ratio of Strouhal numbers is  $St_K/St_{sec} = 0.56 - 0.65$ , close to 1:2.

Finally, the reconstruction process for a PIV snapshot, which exhibits a well developed secondary wake, is presented in figure 7.16. The reconstruction of the  $k$ 'th PIV frame using  $n$  modes has been computed as

$$\omega_z(\vec{x}, t_k) = \sum_n \sqrt{\lambda^{(n)}} a^{(n)}(t_k) \phi^{(n)}(\vec{x}, t_k),$$

with  $\lambda$  being the eigenvalue and  $a$  the projection coefficient from equation 3.3 (Sirovich 1987; Kostas *et al.* 2005). The multiplication with  $\sqrt{\lambda^{(n)}}$  is due to the normalization of  $a$  and  $\phi$ .

---

<sup>3</sup>The Fourier transform of  $a^{(1)}(t)$  shows a peak at 0.43 Hz, which matches the folding frequency of  $f_K$  about the Nyquist frequency.

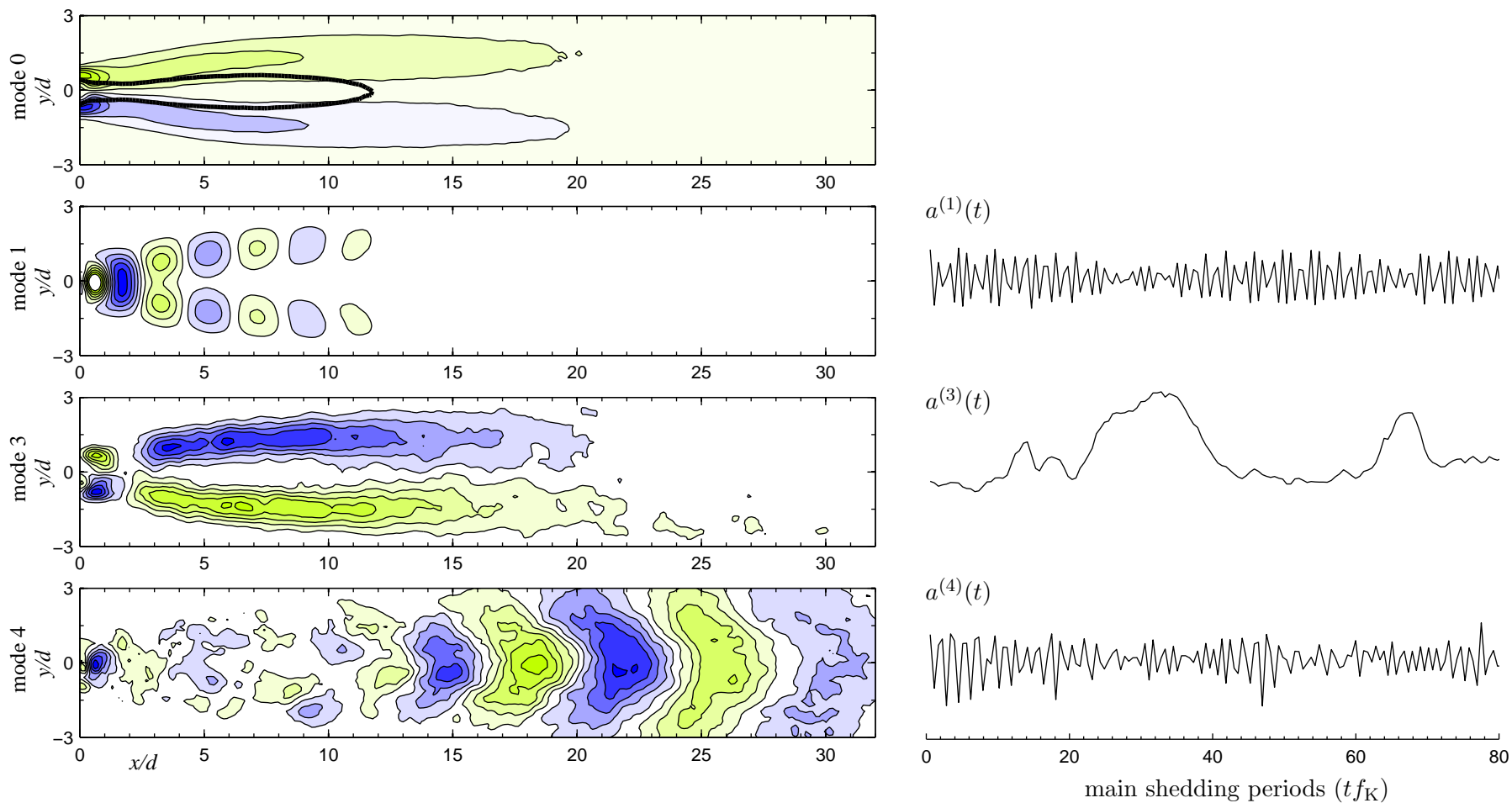


FIGURE 7.15: POD modes of the flat plate wake at  $Re = 150$  (left), and the time evolution of the projection coefficients  $a^{(n)}(t)$  for modes 1, 3 and 4 (right). Note that mode 1 is aliased. The bold black line in mode 0 is the  $0.2U/U_\infty$  contour of the time-averaged flow field.

Figure 7.16a is the superposition of the time-averaged flow (mode 0) and modes 1 & 2, which reconstructs largely the primary vortex street. The combination of the shear layer mode 3 and modes 4 & 5 recreates the second wake, and is shown in figure 7.16b. Note that the vorticity levels are one order of magnitude smaller in (b). The superposition of modes 0–5 in figure 7.16c shows the transition from the primary to the secondary vortex street. Compared to the ‘raw’ PIV frame in figure 7.16d, the POD reconstruction has a lower noise level and shows the coherent structures of the two vortex streets more clearly. Modes 1–5 contain 39% of the fluctuating kinetic energy of the flow field.

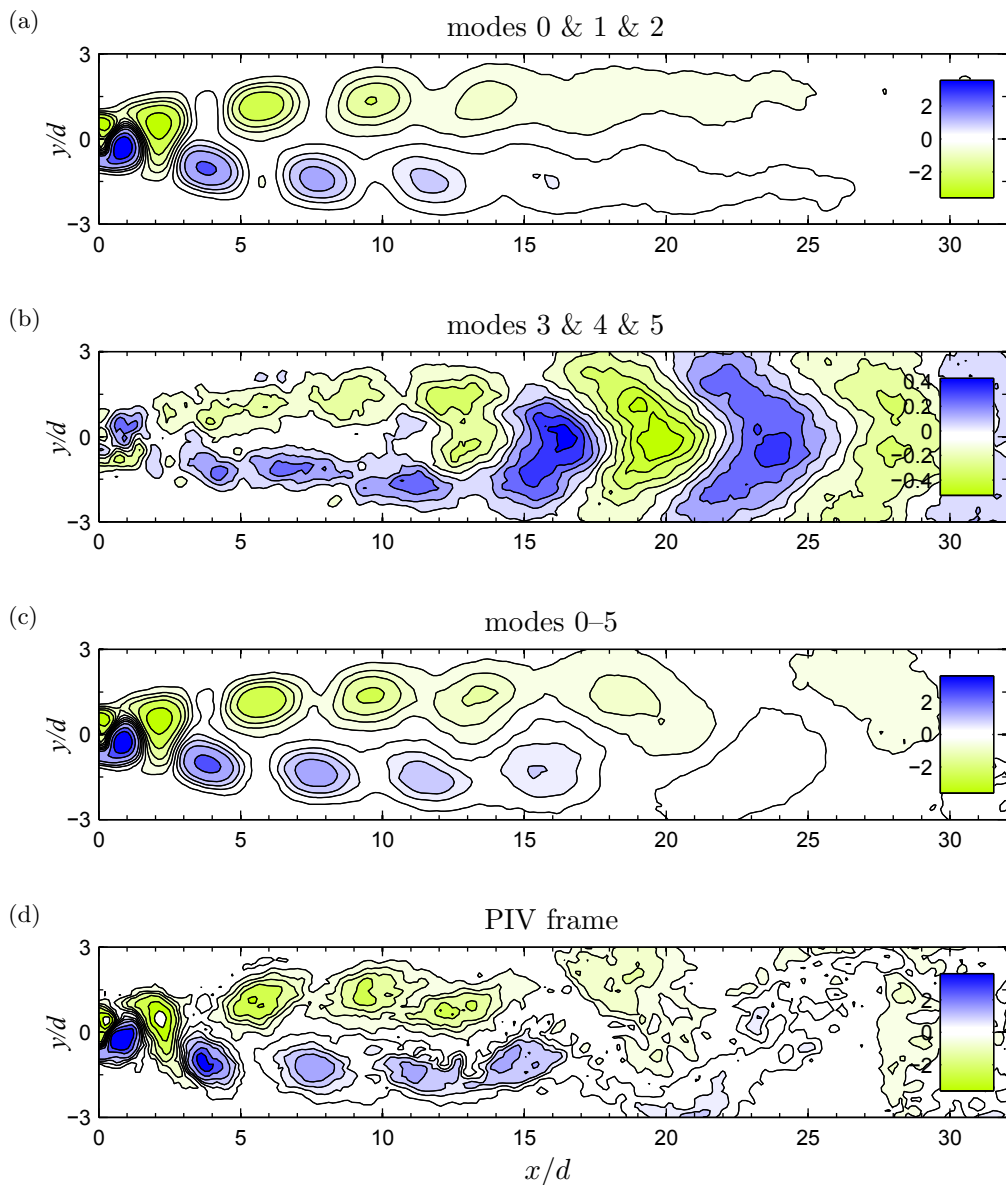


FIGURE 7.16: Reconstruction of the flat plate wake at  $Re = 150$  using the first 5 modes. Spanwise vorticity contours are non-dimensionalized as  $\omega_z d / U_\infty$ .

### 7.3.5 Discussion

Numerous reports exist on the streamwise vortex distance in the primary ( $a_K$ ) and secondary ( $a_{\text{sec}}$ ) vortex streets of the circular cylinder (e.g. Taneda 1959; Karasudani & Funakoshi 1994), and the flat plate (e.g. Taneda 1959; Najjar & Vanka 1995b). Depending on Reynolds number, the ratio  $a_{\text{sec}}/a_K$  lies between 2 and 3, although Taneda (1959) reported ratios up to 10 for turbulent wakes. These parameters are compared to the elliptical cylinder wakes in table 7.1. In the present experiments,  $a_K$  and  $a_{\text{sec}}$  were determined by autocorrelation of the wake centreline vorticity profiles<sup>4</sup> of the POD modes representing the two wake types. As the vortex distance  $a$  grows rapidly in the wake formation region  $x/d < 5$ , only the domain  $5 < x/d < 30$  was used for the autocorrelation. The presented values have an uncertainty of  $\pm 4\%$ , based on the vector field resolution.

TABLE 7.1: Average streamwise vortex distance in the primary ( $a_K$ ) and secondary ( $a_{\text{sec}}$ ) vortex streets for  $5 < x/d < 30$ .

| $Ar$ | $Re$ | $a_K$ [ $d$ ]             | $a_{\text{sec}}$ [ $d$ ] | $a_{\text{sec}}/a_K$ |
|------|------|---------------------------|--------------------------|----------------------|
| 1.00 | 100  | 5.3 (5.2 <sup>1</sup> )   | (12 <sup>1</sup> )       | (2.3 <sup>1</sup> )  |
| 0.39 | 250  | 3.3                       | 6.9                      | 2.1                  |
| 0.26 | 150  | 3.6                       | 8.8                      | 2.5                  |
| 0.26 | 200  | 3.8                       | 7.3                      | 1.9                  |
| 0    | 150  | 3.8 (5.25 <sup>2</sup> )  | 7.7                      | 2.6                  |
| 0    | 100  | 4.2 ( $\approx 4^{3,4}$ ) | N\A                      | N\A                  |

<sup>1</sup> Karasudani & Funakoshi (1994)

<sup>2</sup> Fage & Johansen (1927)

<sup>3</sup> Najjar & Vanka (1995b)

<sup>4</sup> Saha (2007)

Table 7.1 shows that  $a_K$  and  $a_{\text{sec}}$  depend on the Reynolds number and the aspect ratio  $Ar$ . At  $Re = 100$ ,  $a_K$  decreased from  $5.3d$  to  $4.2d$ , when comparing the circular cylinder and the flat plate. The values of  $a$  are in good agreement with literature, with the exception of Fage & Johansen (1927). The exceptionally high value of  $a_K = 5.25$  appears questionable, as one can expect a lower value of  $a$  at  $Re = 150$  than the confirmed  $\approx 4d$  at  $Re = 100$ .

In cases in which the second vortex street could be observed, the ratio of the vortex spacing  $a_{\text{sec}}/a_K$  was on average 2.2. This value suggests a pairing mechanism between the vortices of the primary vortex street, although this mechanism has been

<sup>4</sup>The results did not change when autocorrelating velocity profiles.



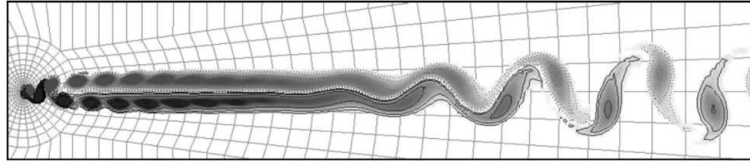


FIGURE 7.17: Transition from primary to secondary vortex street in case of the  $Ar = 0.25$  elliptic cylinder at  $Re = 125$  (Reproduced with permission from Johnson *et al.* 2004).

dismissed in literature for the circular cylinder (Durgin & Karlsson 1971; Karasudani & Funakoshi 1994). The extended 'calm region' between the decayed primary and the forming secondary wakes at  $Ar = 1$  is likely to promote an independent development of the secondary vortex street. The present experiments have shown that such a spatial separation does not exist for elliptical cylinders of low aspect ratios. This supports the idea of a direct relationship between the streamwise wavelengths of these two streets.

Related to this thought is the observation of a wake deficit in the time-averaged wake centreline velocity profile (type II profiles). In this region, the streamwise velocity exhibits strong gradients in cross-stream direction, which are known to lead to high linear amplification rates of disturbances (Schlichting & Gersten 2000). The selective amplification of disturbances in the velocity deficit region is a possible explanation for the formation of the secondary wake. Kumar & Mittal (2012) report convectively unstable modes in the 'trough' region of the circular cylinder wake at  $x/d \approx 46$  and  $Re = 150$  (compare figure 16 in Kumar & Mittal 2012). It has been shown in the present work that this trough is shifted upstream for decreasing  $Ar$ , and deepens rather suddenly for  $Ar \leq 0.39$ . It is plausible that the linear instability mechanism, as described by Kumar & Mittal (2012), creates the secondary wake in case of elliptical cylinders. Yet, the streamwise extent of the transition region from the primary to secondary wake shortens as  $Ar$  is decreased (Johnson *et al.* 2004). The merging of the von Kármán vortices into a steady double shear layer, as known from the circular cylinder wake or elliptical cylinders at moderate Reynolds numbers (see figure 7.17), is replaced by a sudden transition in form of a rapid stretching and amalgamation of the primary vortices into structures of the secondary street (compare figure 7.16c). The intermediate region between the wakes (called the 'middle wake' in Williamson & Prasad 1993) shrinks to a minimum. As a conclusion, the close proximity of both vortex streets makes a close relationship, such as forcing of preferred wavelengths in the secondary street, very likely. The interaction of the two streets for  $Ar < 1$  remains a subject of future studies.

## 7.4 Chapter summary

This chapter established the following properties of the elliptic cylinders wakes:

1. The ‘trough’ in the time-averaged streamwise velocity profile along the wake centreline, which is known from the circular cylinder wake (Williamson & Prasad 1993; Kumar & Mittal 2012), moves upstream and deepens for smaller  $Ar$  and higher  $Re$ . Below a critical aspect ratio of  $Ar \approx 0.39$ , the trough deepens into a pronounced wake deficit, where velocities decrease to 5–20% of the freestream. A small secondary recirculation bubble is observed in some cases.
2. The vortex spacing ratio  $h/a$  increases for smaller aspect ratios. For  $Ar = 0.26$ , it reaches a maximum during the re-laminarized regime. During this regime, the streamwise separation of the vortices decreases from over 4 to approximately 3 cylinder diameters for  $x < 5d$ .
3. Proper orthogonal decomposition of the elliptic cylinder wakes shows that the von Kármán wake shortens as the aspect ratio  $Ar$  is decreased. The von Kármán vortex street is replaced by two rows of vortices offset from the wake centreline during the re-laminarization regime. The three-dimensional wake resembles the von Kármán type again for higher Reynolds numbers. Within re-laminarization, modes representing a von Kármán type wake of double the wavelength are observed downstream of the primary vortex street. The transition between the wake types is rather abrupt; no extended double shear layer, as in the circular cylinder wake, was observed within the sampling domain  $x/d < 32$ . The wavelength ratio of secondary to primary vortex street is approximately 2 : 1 for all cases.

# Chapter 8

## Conclusions

### 8.1 Rotating cylinder

The first part of this study investigated the effect of constant angular rotation on the three-dimensionality of the circular cylinder wake. A new set of 3D modes has been demonstrated for the first time experimentally in such flows. Different spatio-temporal symmetries and wavelengths point to different physical mechanisms responsible for these modes.

The  $2T$ -periodic (subharmonic) mode C is observed for rotation rates  $1.0 \leq \alpha \leq 1.85$  at  $Re = 275$ . Its nominal spanwise wavelength is  $\lambda_z/d \approx 1.1$  at  $\alpha = 1.7$ , but increases significantly with decreasing rotation rate. This mode has characteristics similar to the subharmonic mode C, observed in the wakes of a torus (Sheard *et al.* 2004), and of a cylinder disturbed by a thin wire (Zhang *et al.* 1995; Yildirim *et al.* 2013b). In particular, when extrapolating the wavelength values for decreasing rotation rates,  $\lambda_z \approx 2d$  is obtained for  $\alpha = 0$ , which matches the wavelength reported by Yildirim *et al.* (2013b).

Mode C consists of streamwise vortex pairs, which experience strong amplification through stretching in the braid region between consecutive von Kármán vortices. The amplification process in the strained braid region is similar to the circular cylinder's mode A (Thompson *et al.* 2001). Yet, the instability mechanism of this mode is not understood at the present.

A complex interaction of this mode with mode B takes place for  $\alpha < 1.0$ . This nonlinear interaction is not predictable by linear stability analysis (Rao *et al.* 2013). The use of flow-visualization alone was not sufficient to understand this mixed state; more sophisticated methods (e.g. , hot film cross-correlation along the cylinder span or time-resolved PIV) should be employed in future studies.

The largest discrepancy between experiment and linear stability analysis concerns the observation of mode C at rotation rates significantly below its linearly unstable range. A possible cause might be the fully developed mode B as an initial triggering condition in the experiment or the presence of the hydrogen-bubble wire upstream of the cylinder.

It has been shown that shedding activity can be suppressed for  $\alpha > 2$ . During this transition, two modes with a wavelength of  $\lambda_z/d \approx 2$  develop in close succession. For  $\alpha > 1.85$ , mode D consists of continuous streamwise vortices in a weakly shedding wake. Once shedding ceases, the 3D mode retains its structure and wavelength. This mode E can be considered as a continuation of mode D, but on a henceforth steady wake. Both modes are attributed to an hyperbolic instability of the mean wake. The time-averaged velocity fields of the shedding and non-shedding wakes possess a hyperbolic stagnation point just downstream of the recirculation zone.

The last observed mode, mode F, consists of short-wavelength structures in the cylinder's wall-bounded shear layer. With a spanwise wavelength of  $\lambda_z/d \approx 0.5$ , it is presumably a manifestation of centrifugal instability. Similar structures were observed by Mittal (2004) for  $Re = 200$  and  $\alpha = 5$ . Unlike the previously discussed modes, mode F is a travelling wave with a spanwise frequency of  $St_{3D} \approx 0.1$ . There is indication of a nonlinear interaction between modes F and E for  $\alpha \geq 2.3$  that needs further investigation.

One-sided shedding (second shedding mode) was visualised for  $Re = 100$ ,  $\alpha = 5.1$ . Unlike the current assumption of a two-dimensional vortex parallel to the cylinder axis, the observed shedding created localized horse-shoe shaped vortex structures peeling off the cylinder. The detachment was initiated at randomly distributed 'detachment points' along the span, giving this process a fully three-dimensional character.

## 8.2 Elliptical cylinders

The role of 'flatness' of the cylinder cross-section, quantified as the aspect ratio  $Ar$ , was studied in the second part of the project. As the aspect ratio is varied between  $0 \leq Ar \leq 1$ , bridging the geometries of a flat plate and a circular cylinder, a range of different modifications of the wake is observed. For aspect ratios above  $Ar \approx 0.4$ , the transition scenario is similar to that of the circular cylinder wake: A long-wavelength mode L appears for Reynolds numbers above 100, before a short-wavelength mode S

develops for Reynolds numbers approaching 200. Both modes are considered as modified versions of the mode A and B transitions, having a spanwise wavelength of  $4-6d$  and  $1-4d$ , respectively. Yet, the critical Reynolds number for the onset of mode L decreases for decreasing  $Ar$ , and the typical increase of Strouhal numbers caused by the appearance of mode B is missing. Mode S develops gradually, without leaving a clear imprint on the  $St-Re$  curve.

For  $Ar \leq 0.39$ , modes L and S appear in the same sequence, but the wake develops a new feature: for a limited Reynolds number range, vortex shedding becomes highly periodic, devoid of wake irregularities, and previously developed three-dimensionality is largely suppressed. Due to the resemblance of the wake characteristics of this new flow state to the laminar regime of the circular cylinder at  $Re \lesssim 180$ , we termed it the ‘re-laminarized’ regime.

In this regime, the primary shedding Strouhal numbers decrease significantly, and a secondary low frequency of  $f_{\text{sec}} \approx 2f_K$  appears in the wake. A change of the two-dimensional base flow is observed in form of an extended wake velocity deficit containing a second minor reverse flow region. The former von Kármán wake structure gives way to two rows of vortices, offset from the wake centreline. This primary vortex street rearranges rather abruptly into the secondary vortex street of much larger dimensions. The ratio of secondary to primary wake wavelength is 2–2.6.

Whilst the existence of a secondary vortex street is known from the far-wake of the circular cylinder (at  $x/d > 100$ ), our results show for the first time experimentally that the onset moves upstream for decreasing  $Ar$  (confirming the simulations by Johnson *et al.* 2004). It appears that for  $Ar \lesssim 0.4$ , the secondary wake has moved so far upstream that it starts interacting with the primary wake. The main effect of this interaction is the stabilisation of the primary shedding process, which leads to strictly periodic hot film velocity traces and an increase of spectral power of the primary shedding.

Wake re-laminarization described in this thesis is a first-time observation, which requires further studies. In particular, the reason for increased periodicity of the primary shedding and the exact mechanism leading to the suppression of 3D modes during this regime are not clear.

In conclusion, the elliptical cylinder study highlights similarities and differences between the circular cylinder and the flat plate wakes. The long and short wavelength modes reappear consistently with a wavelength of  $4-6d$  and  $1-1.4d$ , respectively, for

all aspect ratios. The flat plate wake shows a rather sudden change of behaviour compared to the elliptic cylinders, as its mode L is subharmonic. Nevertheless, our experiments show that it develops on a highly periodic two-dimensional wake, which is a consequence of the re-laminarized regime. This explains the common assumption of a 2D laminar flow until the appearance of the ‘first’ 3D mode at  $Re \approx 200$  (Saha 2007). The present experiments support the scenario of Thompson *et al.* (2006) of a 3D transition at  $Re = 105$ – $110$ .

## 8.3 Recommended future work

### 8.3.1 Rotating cylinder

- The instability mechanism of the subharmonic mode C remains unknown, although this mode has gained recent attention in the research community (Pralits *et al.* 2013; Yildirim *et al.* 2013a,b).
- The observation of mode C below rotation rates of its instability region is a puzzling observation. The assumption, that the existence of mode B as the initial condition triggers an early appearance of mode C, needs confirmation.
- The nonlinear interaction of modes C and B for rotation rates  $0 < \alpha < 1$  requires further investigation with appropriate experimental techniques.
- ‘Second shedding’ needs to be studied quantitatively for  $Re = 100$  and  $\alpha = 5$ , when the wake is devoid of 3D modes. When increasing the rotation rate, the impact of 3D modes on this one-sided shedding should be clarified.

### 8.3.2 Elliptical cylinders

The newly observed re-laminarized regime needs further studies. The following are suggested:

- The extended wake deficit of the time-averaged flow field leads to high velocity gradients in cross-stream direction. A linear stability analysis of the  $U(y)$  velocity profiles in this region could provide further insight into the mechanism responsible for the secondary vortex street. Can the low shedding frequency  $f_{sec}$  be predicted? Is the observed second wake a convective instability, as has been shown by Kumar & Mittal (2012) for the circular cylinder?

- Is the increased periodicity of the primary vortex shedding due to suppression of vortex dislocations caused by the secondary street?
- For the circular cylinder and elliptical cylinders in simulations, a transition region between the two vortex streets is observed, consisting of a steady double shear layer. This ‘calm region’ (Durgin & Karlsson 1971) was not observed in the elliptical cylinder wakes; the transition between the two wakes was rather abrupt. Considering that the flow reported here is in a fully developed nonlinear state, transient experiments (accelerating the cylinders from rest) might show a developed double shear layer, which is ‘overridden’ by an upstream shifting secondary wake, until a final, converged state is reached.

---



# Appendix A

## Uncertainty analysis

### A.1 Estimation of error

The experimental uncertainty estimates are based on techniques described in Coleman & Steele (1995), which deal specifically with error analysis of wind tunnel data.

For each variable it is assumed that the *total error*  $\delta$  is the sum of the *bias error*  $\beta$  and the *precision error*  $\theta$ . For  $N$  readings, the bias error is the difference between the *mean value* of the readings  $\mu$  and the true value of that variable. Unlike the precision error  $\theta$ , it cannot be determined statistically.

The precision errors  $\theta$  will have different values for each measurement, and are due to limitations on repeatability of the measurement system and facility, and environmental effects. When repeated measurements are made for fixed conditions, precision errors are observed as “scatter” of the data.

As the the true values of the measured quantities are rarely known,  $\beta$  and  $\theta$  need to be estimated. The estimate of  $\beta$  is called *bias limit*  $B$ , the estimate of  $\theta$  is the *precision limit*  $P$ . These estimates are made at a certain *confidence level* – usually 95% –, meaning that the true value of the quantity expected will lie within  $\pm B$  ( $\pm P$ ) interval about the mean 95 times out of 100.

The desired experimental result is often a combination of several variables, and is defined by the *data reduction equation*  $r$ . Each variable has bias and precision errors, all of which contribute to the total error of the result (*error propagation*). How much the error of the  $i$ th variable  $X_i$  contributes to the error of the result  $r$ , is described by its *sensitivity coefficient*  $\theta_i$ :

$$\theta_i = \frac{\partial r}{\partial X_i} \tag{A.1}$$

For a given distribution of  $N \rightarrow \infty$  values, its spread is measured by the *variance*

---

$\sigma^2$ . In reality the variance is not known exactly, but estimates of the variances can be used to describe the bias and precision errors.  $b_i$ ,  $b_{ik}$  are the estimates of variances and covariances of the bias errors, and  $S_i$ ,  $S_{ik}$  are the estimates of the precision errors. To obtain the bias and precision limits at a specific confidence level, these values are multiplied by a *coverage factor*. Under the assumption of a normal distribution of error, the  $t$  value from the *Student t distribution* can be used, which is  $t = 2$  for  $N \geq 10$  measurements, and 95% confidence level. Then, the uncertainty of the result  $U_r$  can be determined with the *uncertainty propagation equation*:

$$U_r^2 = \sum_{i=1}^J \theta_i^2 B_i^2 + 2 \sum_{i=1}^{J-1} \sum_{k=i+1}^J \theta_i \theta_k B_{ik} + \sum_{i=1}^J \theta_i^2 P_i^2 + 2 \sum_{i=1}^{J-1} \sum_{k=i+1}^J \theta_i \theta_k P_{ik} \quad (\text{A.2})$$

where  $B_i = t b_i$ ,  $B_{ik} = t^2 b_{ik}$ ,  $P_i = t S_i$ ,  $P_{ik} = t^2 S_{ik}$  and  $t = 2$  for  $N \geq 10$ .  $B_i$ ,  $P_i$  are the bias and precision limits in each variable,  $P_{ik}$ ,  $B_{ik}$  are the correlated bias and precision limits.  $S_i$  is the standard deviation of a sample of  $N$  readings of the  $i$ th variable.

In case a variable is measured  $M$  times at the same experimental set point, the *multiple tests* method can be used, which results in a smaller precision limit:

$$P_i = \frac{t S_i}{\sqrt{M}} \quad (\text{A.3})$$

This equation will be applied to the LDV measurement of the freestream velocity, because otherwise the natural noise of the LDV at low flow velocities inflates the uncertainty of the results  $U_r$  to unrealistically high values.

### A.1.1 Reynolds number uncertainty

The uncertainties will be calculated for the  $Ar = 0.72$  cylinder model (as it has the largest spread in the diameter measurement), and for a rotation rate of  $\alpha = 2$ . All reference values are listed in table A.1. The results of this base case are assumed to represent the maximum uncertainty for all used models.

The data reduction equation for the Reynolds number is:

$$Re = Re(U, d, \nu) = \frac{dU}{\nu} \quad (\text{A.4})$$

The total uncertainty  $U_{Re}$  is calculated using equation A.2, in which no correlation between variables will be assumed (the second and fourth terms are zero)<sup>1</sup>:

$$U_{Re} = \pm \sqrt{B_{Re}^2 + P_{Re}^2} \quad (\text{A.5})$$

---

<sup>1</sup>This is permissible, as the variables were measured with different instruments.

---

TABLE A.1: Reference values for the uncertainty calculation.

| definition             | symbol   | ref. value               |
|------------------------|----------|--------------------------|
| Reynolds number        | $Re$     | 200                      |
| Strouhal number        | $St$     | 0.183                    |
| non-dim. rotation rate | $\alpha$ | 2                        |
| cylinder diameter      | $d$      | 5.78 mm                  |
| freestream velocity    | $U$      | 33.8 mm/s                |
| kinematic viscosity    | $\nu$    | 1.004 mm <sup>2</sup> /s |
| shedding frequency     | $f$      | 1.036 Hz                 |
| rotation rate          | $\Omega$ | 23.71 rad                |

TABLE A.2: Bias limits for error analysis of Reynolds number  $Re$ , Strouhal number  $St$  and rotation rate  $\alpha$ .

| Bias Limit | Magnitude                | Percentage     | Estimation                  |
|------------|--------------------------|----------------|-----------------------------|
| $B_d$      | 0.001 mm                 | 0.02% $d$      | 1/2 instrument resolution   |
| $B_U$      | 0.1 mm/s                 | 0.29% $U$      | LDV last significant digit  |
| $B_\nu$    | 0.001 mm <sup>2</sup> /s | 0.10% $\nu$    | 1/2 temperature resolution  |
| $B_f$      | 0.02 Hz                  | 1.92% $f$      | 1/2 PSD spectral resolution |
| $B_\Omega$ | 0.008 rad/s              | 0.03% $\Omega$ | 1/2 instrument resolution   |

Using equation A.2, the bias and precision limits of the Reynolds number are:

$$B_{Re}^2 = \sum_{i=1}^J \theta_i^2 B_i^2 = \theta_U^2 B_U^2 + \theta_d^2 B_d^2 + \theta_\nu^2 B_\nu^2$$

$$P_{Re}^2 = \sum_{i=1}^J \theta_i^2 P_i^2 = \theta_U^2 P_U^2 + \theta_d^2 P_d^2$$

The bias limits of all variables are given in table A.2; the precision limits are summarized in table A.3. The precision limit  $P_{Re}$  is estimated with the *single test* method, meaning that the ‘test’ (calculation of  $Re$ ) is performed only once, even if the measurements of one or more variables are made from many samples.

The precision limit of the freestream velocity measurement was calculated using the multiple tests method (equation A.3). 11 velocity measurements of 5 min each were recorded with the LDV in the empty test section. Each time series  $m$  was averaged to obtain  $\bar{U}_m$ . The standard deviation of all 11 averages was  $S_U$ . With  $M - 1 = 10$  degrees of freedom, the Student t value is 2.228 at 95% confidence limit. The precision limit of the LDV velocity measurement becomes

$$P_U = \frac{2.228 S_U}{\sqrt{M}},$$

which value is shown in table A.3.

TABLE A.3: Precision limits for error analysis of Reynolds number  $Re$ , Strouhal number  $St$  and rotation rate  $\alpha$ .

| variable   | magnitude | of ref value | estimation            |
|------------|-----------|--------------|-----------------------|
| $P_d$      | 0.09 mm   | 1.56%        | 2 standard deviations |
| $P_U$      | 0.05 mm/s | 0.14%        | multiple tests method |
| $P_\Omega$ | 0.082 rad | 0.34%        | 2 standard deviations |

TABLE A.4: Uncertainty estimates of the Reynolds number

|       | $\theta_i B_i$ | % $B_{Re}^2$ | $\theta_i P_i$ | % $P_{Re}^2$ | $B_{Re}$ | % $U_{Re}^2$ | $P_{Re}$ | % $U_{Re}^2$ | $U_{Re}$    | % $Re$       |
|-------|----------------|--------------|----------------|--------------|----------|--------------|----------|--------------|-------------|--------------|
| $d$   | 0.03           | 0.3%         | 3.11           | 99.2%        | 0.61     | 3.7%         | 3.13     | 96.3%        | <b>3.19</b> | <b>1.59%</b> |
| $U$   | 0.58           | 89.0%        | 0.29           | 0.8%         |          |              |          |              |             |              |
| $\nu$ | -0.20          | 10.7%        | –              | –            |          |              |          |              |             |              |

The sensitivity coefficients  $\theta_i$  of the Reynolds number measurement are:

$$\theta_U = \frac{\partial Re}{\partial U} = \frac{d}{\nu} = 5.8 \text{ s/mm}$$

$$\theta_d = \frac{\partial Re}{\partial d} = \frac{U}{\nu} = 34.6 \text{ mm}^{-1}$$

$$\theta_\nu = \frac{\partial Re}{\partial \nu} = \frac{dU}{\nu^2} = -199.2 \text{ s/mm}^2$$

The results of the uncertainty analysis are shown in table A.4. The measured Reynolds number is:

$$Re = 200 \pm 3.19 (\pm 1.59\%)$$

Table A.4 shows that the precision limit  $P_{Re}$  contributes 96.3% to overall uncertainty  $U_{Re}$ ; the bias limit is negligible with only 3.7%.  $P_{Re}$  is dominated by the random error of the diameter measurement  $P_d$  (resulting from the non-uniformity of the cylinder model).

### A.1.2 Strouhal number uncertainty

The data reduction equation for the Strouhal number is:

$$St = St(f, U, d) = \frac{fd}{U} \quad (\text{A.6})$$

with the shedding frequency  $f$ ;  $d$  and  $U$  defined as previously. This leads to the following sensitivity coefficients:

$$\theta_U = \frac{\partial St}{\partial U} = \frac{fd}{U^2} = -0.005 \text{ s/mm}$$

$$\theta_d = \frac{\partial St}{\partial d} = \frac{f}{U} = 0.030 \text{ mm}^{-1}$$

$$\theta_f = \frac{\partial St}{\partial f} = \frac{d}{U} = 0.166 \text{ Hz}^{-1}$$

---

TABLE A.5: Uncertainty estimates of the Strouhal number.

|     | $\theta_i B_i$ | $\% B_{St}^2$ | $\theta_i P_i$ | $\% P_{St}^2$ | $B_{St}$ | $\% U_{St}^2$ | $P_{St}$ | $\% U_{St}^2$ | $U_{St}$      | $\% St$      |
|-----|----------------|---------------|----------------|---------------|----------|---------------|----------|---------------|---------------|--------------|
| $d$ | 0.00003        | 0.1%          | 0.0027         | 99.2%         | 0.0033   | 55.3%         | 0.003    | 44.7%         | <b>0.0045</b> | <b>2.26%</b> |
| $U$ | -0.0005        | 2.2%          | -0.0003        | 0.8%          |          |               |          |               |               |              |
| $f$ | 0.0033         | 97.7%         | –              | –             |          |               |          |               |               |              |

Using the bias and precision limits from tables A.2 and A.3, the Strouhal number uncertainty is:

$$St = 0.183 \pm 0.0045 (\pm 2.26\%)$$

### A.1.3 Non-dimensional rotation rate uncertainty

The data reduction equation for the non-dimensional rotation rate is:

$$\alpha = \alpha(\Omega, U, d) = \frac{d\Omega}{2U} \quad (\text{A.7})$$

with the cylinder rotation rate  $\Omega$ ;  $d$  and  $U$  defined as previously. The sensitivity coefficients  $\theta_i$  are:

$$\theta_U = \frac{\partial \alpha}{\partial U} = \frac{d\Omega}{2U^2} = -0.1 \text{ s/mm}$$

$$\theta_d = \frac{\partial \alpha}{\partial d} = \frac{\Omega}{2U} = 0.35 \text{ mm}^{-1}$$

$$\theta_\Omega = \frac{\partial \alpha}{\partial \Omega} = \frac{d}{2U} = 0.083 \text{ Hz}^{-1}$$

Using the bias and precision limits from tables A.2 and A.3, the rotation rate uncertainty is:

$$\alpha = 2 \pm 0.011 (\pm 0.53\%)$$

TABLE A.6: Uncertainty estimates of the non-dimensional rotation rate (based on the rotating cylinder dimensions).

|          | $\theta_i B_i$ | $\% B_\alpha^2$ | $\theta_i P_i$ | $\% P_\alpha^2$ | $B_\alpha$ | $\% U_\alpha^2$ | $P_\alpha$ | $\% U_\alpha^2$ | $U_\alpha$   | $\% \alpha$  |
|----------|----------------|-----------------|----------------|-----------------|------------|-----------------|------------|-----------------|--------------|--------------|
| $d$      | 0.0003         | 0.3%            | 0.005          | 29.8%           | 0.006      | 30.5%           | 0.009      | 69.5%           | <b>0.011</b> | <b>0.53%</b> |
| $U$      | -0.006         | 98.4%           | -0.003         | 10.8%           |            |                 |            |                 |              |              |
| $\Omega$ | 0.0007         | 1.3%            | 0.007          | 59.4%           |            |                 |            |                 |              |              |



## Appendix B

# FFT code testing

The Strouhal numbers of the elliptical cylinders in chapter 6 were calculated by performing a windowed FFT on the discrete hot film time series. The spectra of all windows were averaged, and the highest peak of the averaged frequency domain was attributed to the von Kármán shedding frequency  $f_K$ . The choice of the window width  $N_W$  determined the spectral resolution of the frequency domain. A short study was undertaken to determine a suitable window width for identification of  $f_K$ .

The raw data consisted of hot film time series of 12,000 data points each at three different Reynolds numbers, sampled at  $f_s = 40$  Hz. 5 window widths were chosen: 256, 512, 1024, 2048 and 4096 data points, which translate to windows of 6.4, 12.8, 25.6, 51.2 and 102.4 s. These windows contain 3.7–59 shedding periods at  $Re = 109$ , 3.8–62 shedding periods at  $Re = 111$  and 7.3–116 shedding periods at  $Re = 205$ . A Hanning function was applied to each window. A non-windowed FFT was also performed for comparison (in this case, a Hanning function function was applied to the full time series).

Figure B.1 shows power spectra of the  $Ar = 0.64$  elliptic cylinder. The frequency domain is cropped around the shedding frequency peak. The averaged spectra of the five window widths are shifted vertically with respect to each other for clarity. The non-windowed FFT is plotted with a dashed line. The identified von Kármán shedding frequencies are marked by black triangles.

It can be seen in figures B.1a and B.1c that the frequency peak narrows for larger window widths. The peak width (defined as the difference between the limiting frequencies where the peak power decreases by half) is roughly halved for each doubling of the window size. The identified peak frequency value is insensitive to changes of  $N_W$ . Furthermore, the location of the peak of the non-windowed transform of the whole data

---

set does not differ considerably from the windowed transforms (the differences remain below 1%). This shows that the vortex shedding at  $Re = 109$  and  $205$  is highly periodic at a fixed frequency.

$Re = 111$  on the other hand, lies in the transition regime of the  $Ar = 0.64$  cylinder (figure B.1b). At this Reynolds number, the wake has just undergone transition to three-dimensionality, which is accompanied by wake irregularities, such as vortex dislocations. These flow irregularities widen the frequency peak, which now becomes strongly dependent on the used window size  $N_W$ . For window sizes of 256–2048 points, the spectrum plot shows a single broad peak. For larger window sizes, and for the non-windowed transform, side-peaks are resolved, which make the identification of  $f_K$  ambiguous. The conclusion is, that a widening of the FFT window does not necessarily lead to a convergence of the peak location to a unique frequency value in the transitional wake regime. For the present experiments,  $N_W = 512$  was considered as a good compromise, which avoided the ambiguousness of multiple frequency peaks, while providing an acceptable spectral resolution. This resulted in a temporal window width of 12.8 s, equivalent to approximately 7 shedding cycles at  $Re = 100$ .



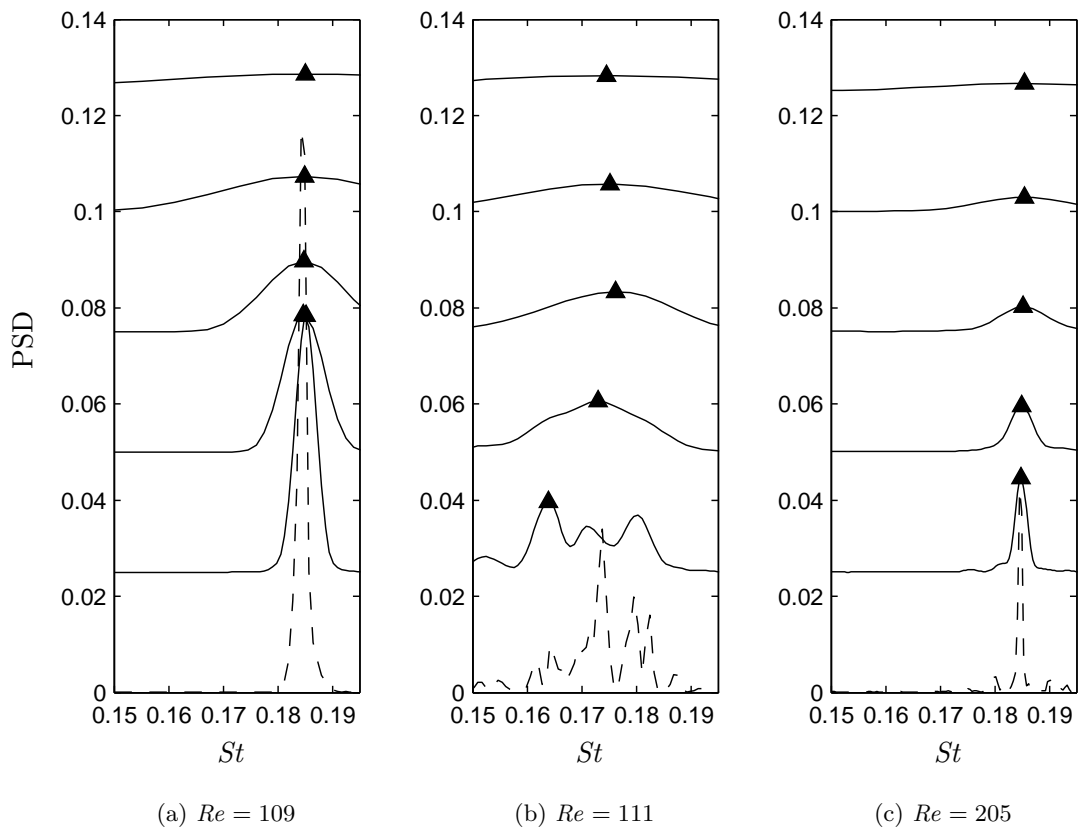


FIGURE B.1: Power spectral densities (PSD) of a hot film time series computed with a windowed FFT of various window sizes  $N_W$ ; from top to bottom:  $N_W = 256, 512, 1024, 2048$  and  $4096$  points. The non-windowed transform of the whole data set is plotted with the dashed line. The identified frequency peaks are marked by the black triangles. The spectra are shifted vertically with respect to each other for clarity.

---

## Appendix C

# POD modes of elliptical cylinders at $Re = 100, 150, 200$ & $250$

Flow fields of POD modes 0–5 of all investigated elliptical cylinder types are included in this appendix. All modes will be presented as  $\omega_z$ -vorticity contours, which have been computed by taking the curl of the modes' velocity fields. Positive vorticity is marked in blue, negative vorticity is coloured light green. The contour levels are arbitrary, but of the same order of magnitude for all modes, as the mode flow fields are orthonormal. The flow is from left to right.

The kinetic energy content of each mode is expressed by its eigenvalue  $\lambda$ . The eigenvalues of modes 0–5 are plotted as black bars in the graphs below the mode flow fields. The energies are normalized by the sum of all modes excluding mode 0 (the time-averaged flow field), which is equal to the fraction of the fluctuating energy content of the flow. The cumulative energy sum of the first 50 modes is shown in the same graph as the red symbols.

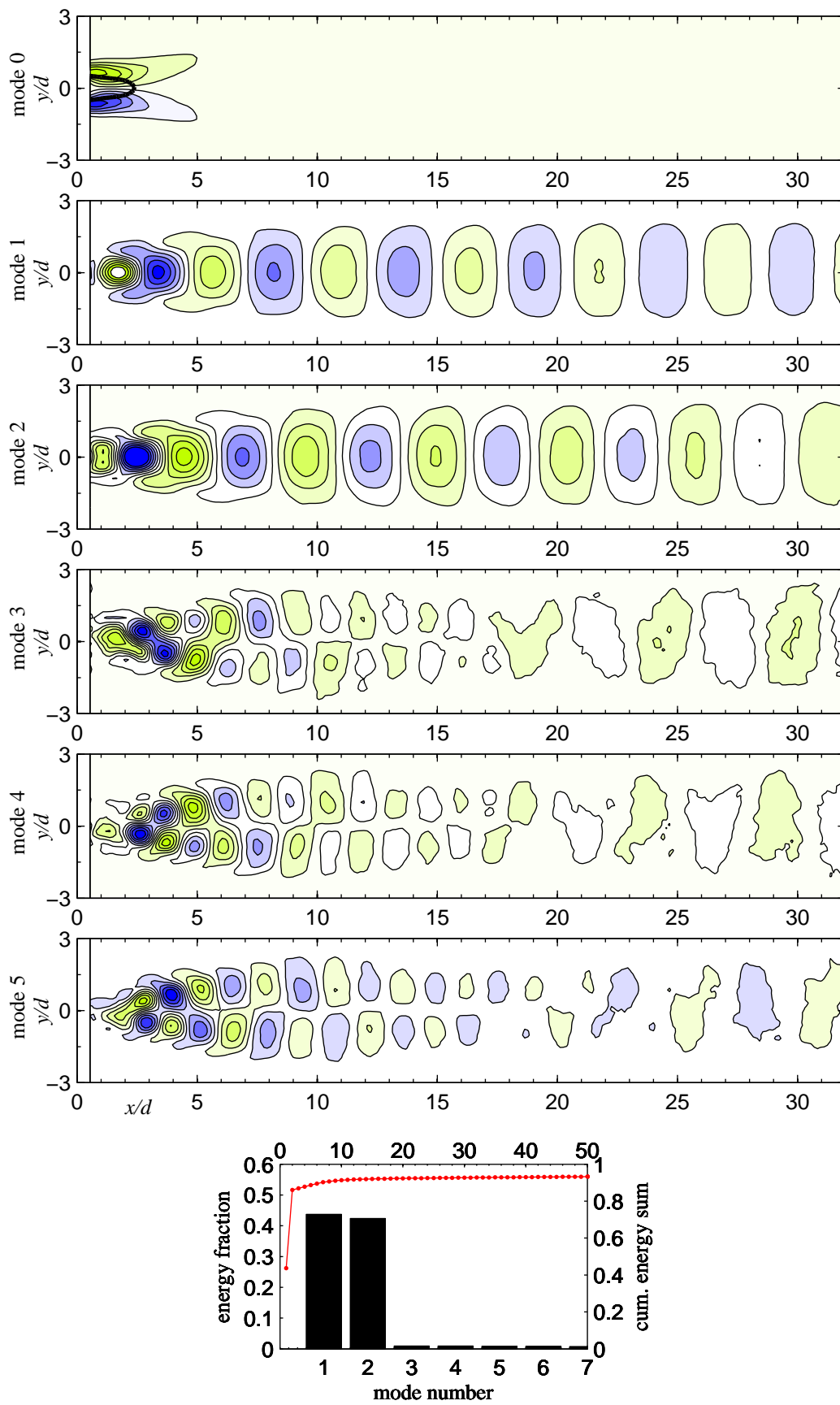


FIGURE C.1:  $Ar = 1.00$ ,  $Re = 100$

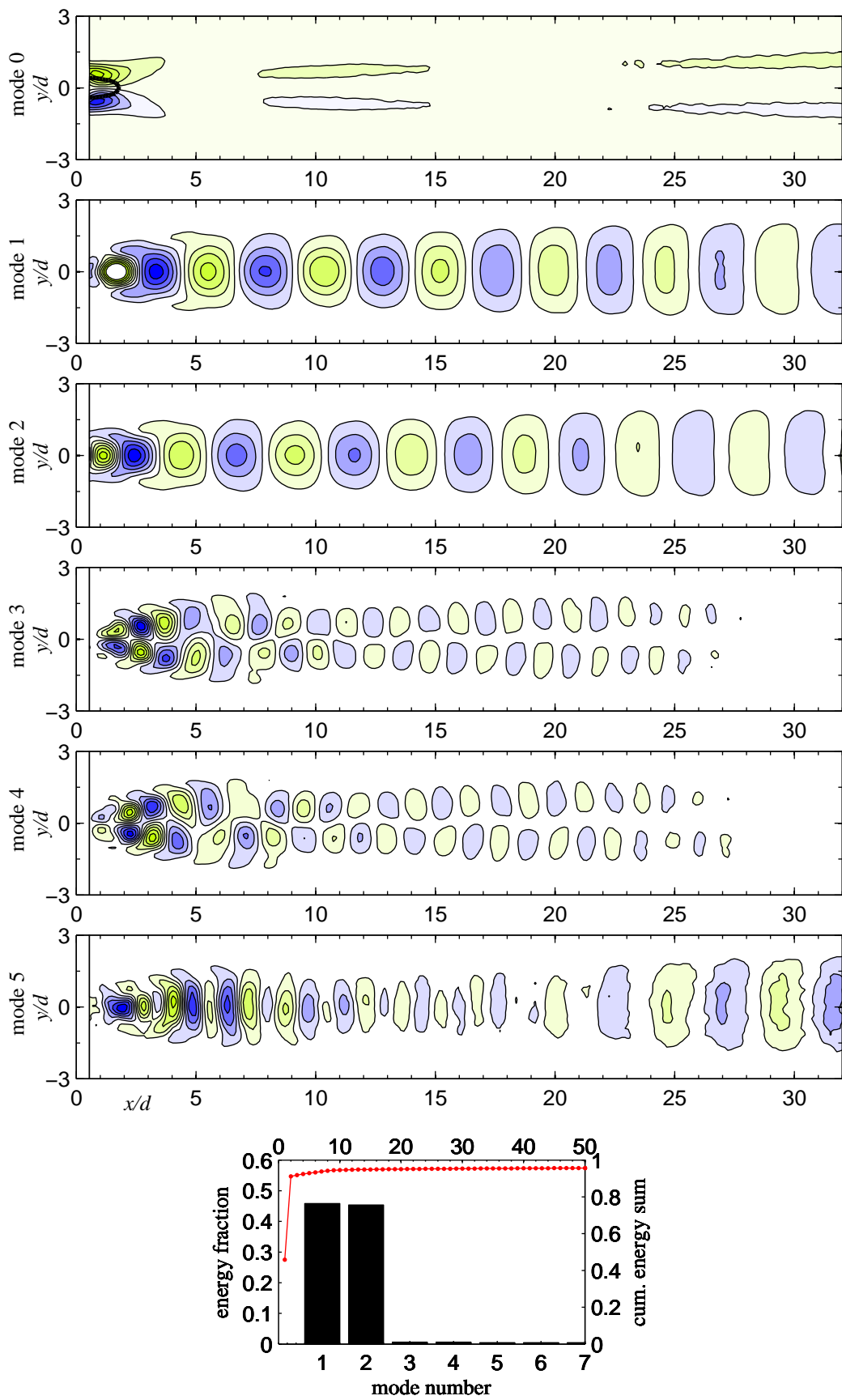


FIGURE C.2:  $Ar = 1.00$ ,  $Re = 150$

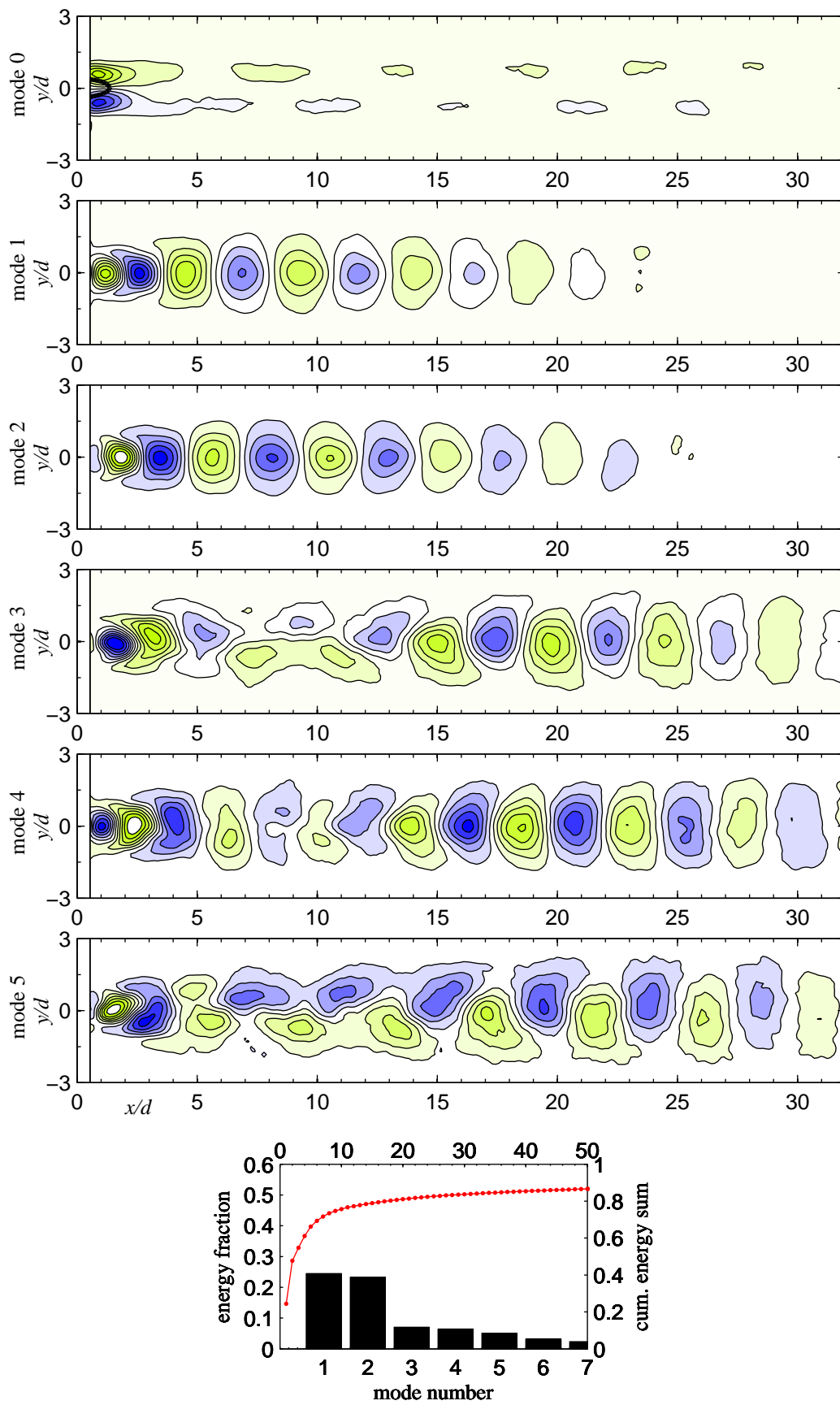


FIGURE C.3:  $Ar = 1.00$ ,  $Re = 200$

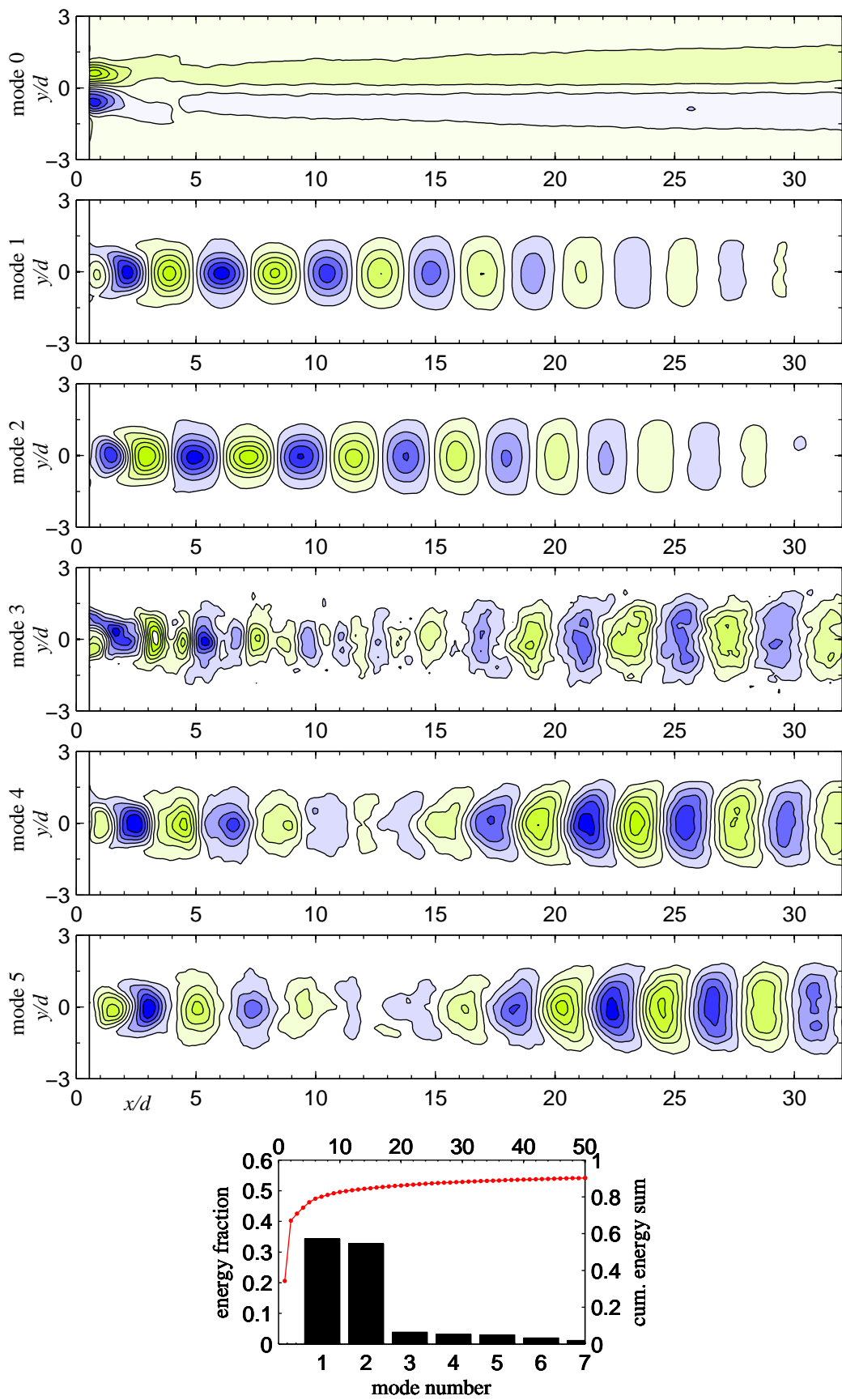


FIGURE C.4:  $Ar = 1.00$ ,  $Re = 250$

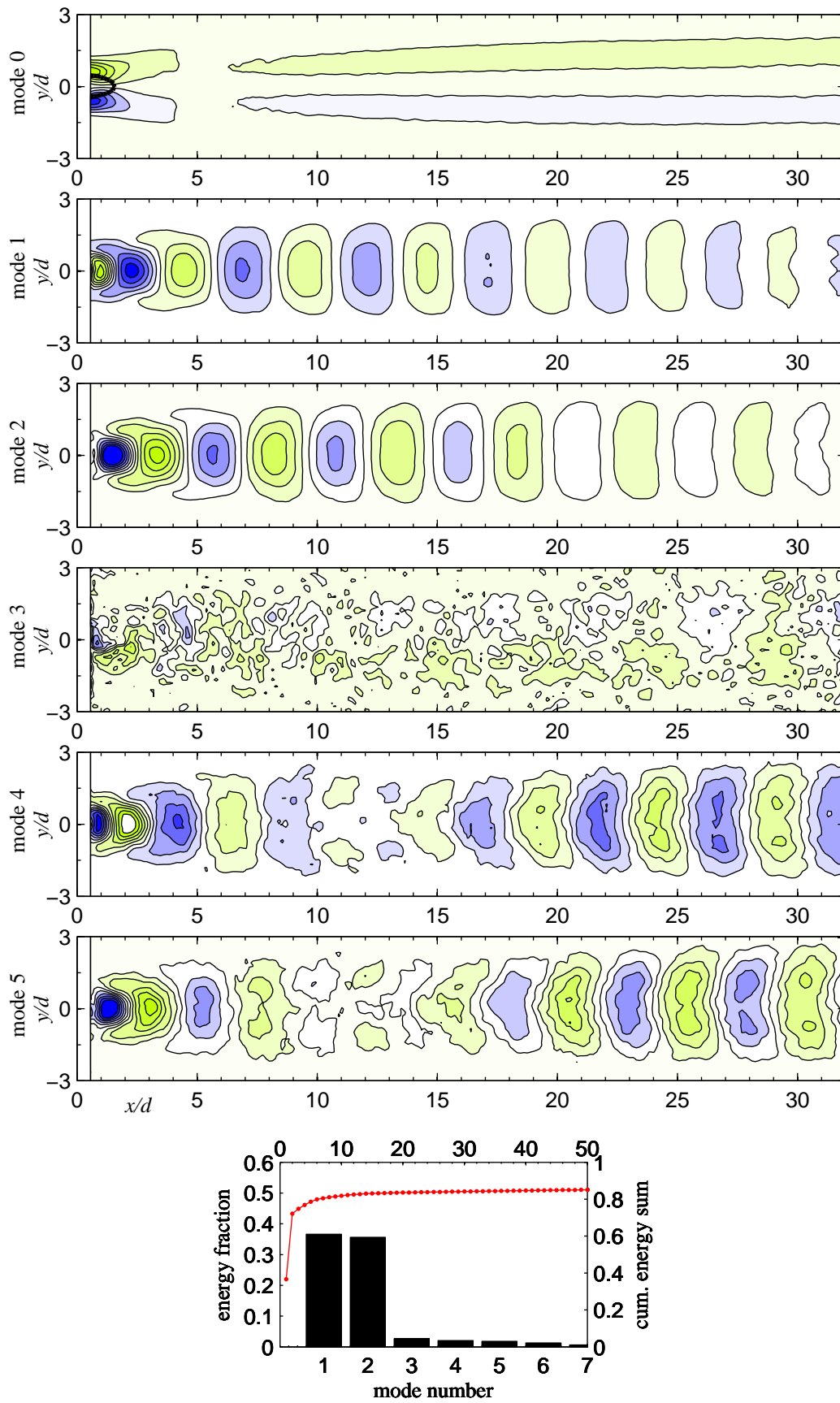


FIGURE C.5:  $Ar = 0.72$ ,  $Re = 100$



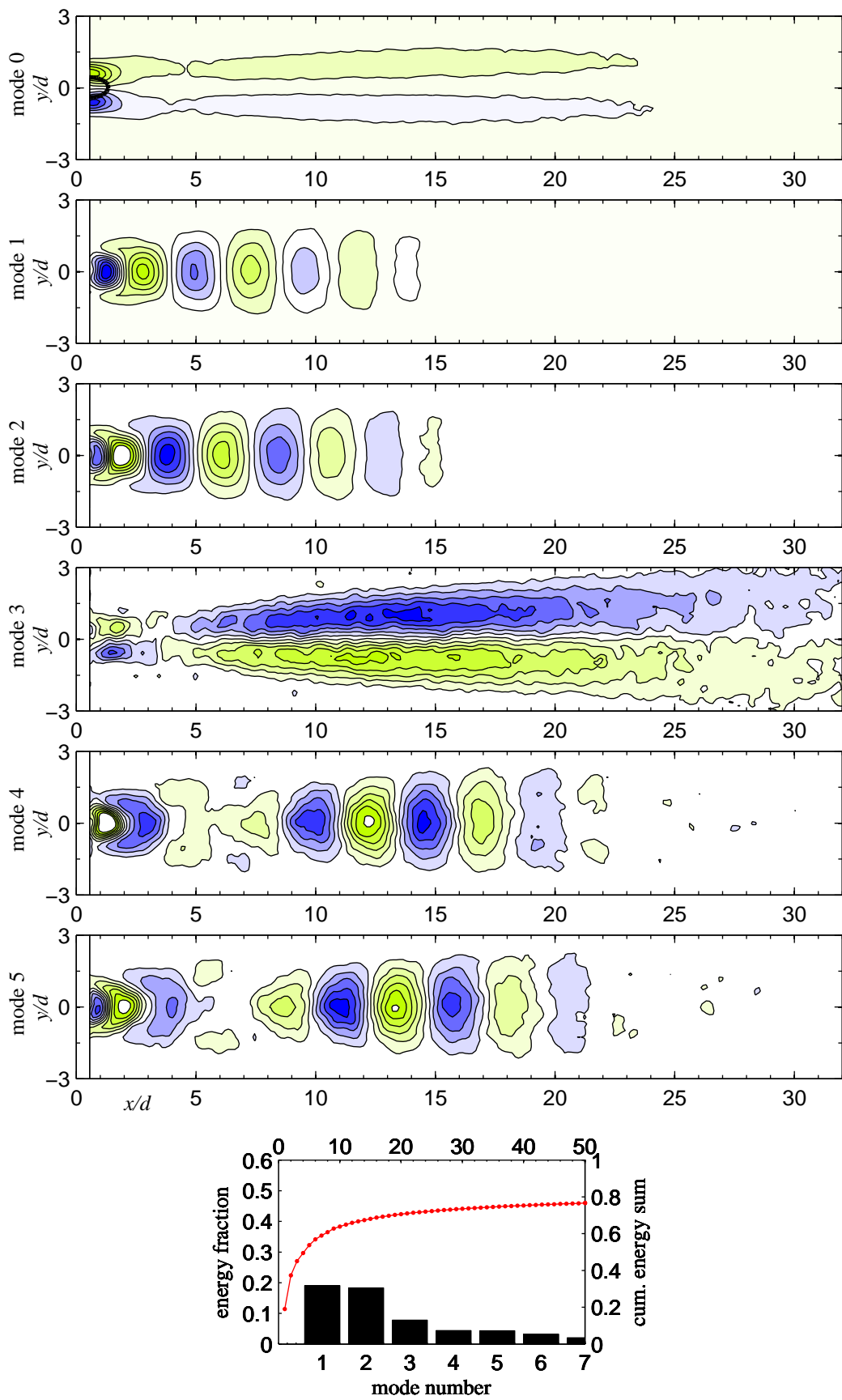


FIGURE C.6:  $Ar = 0.72$ ,  $Re = 150$

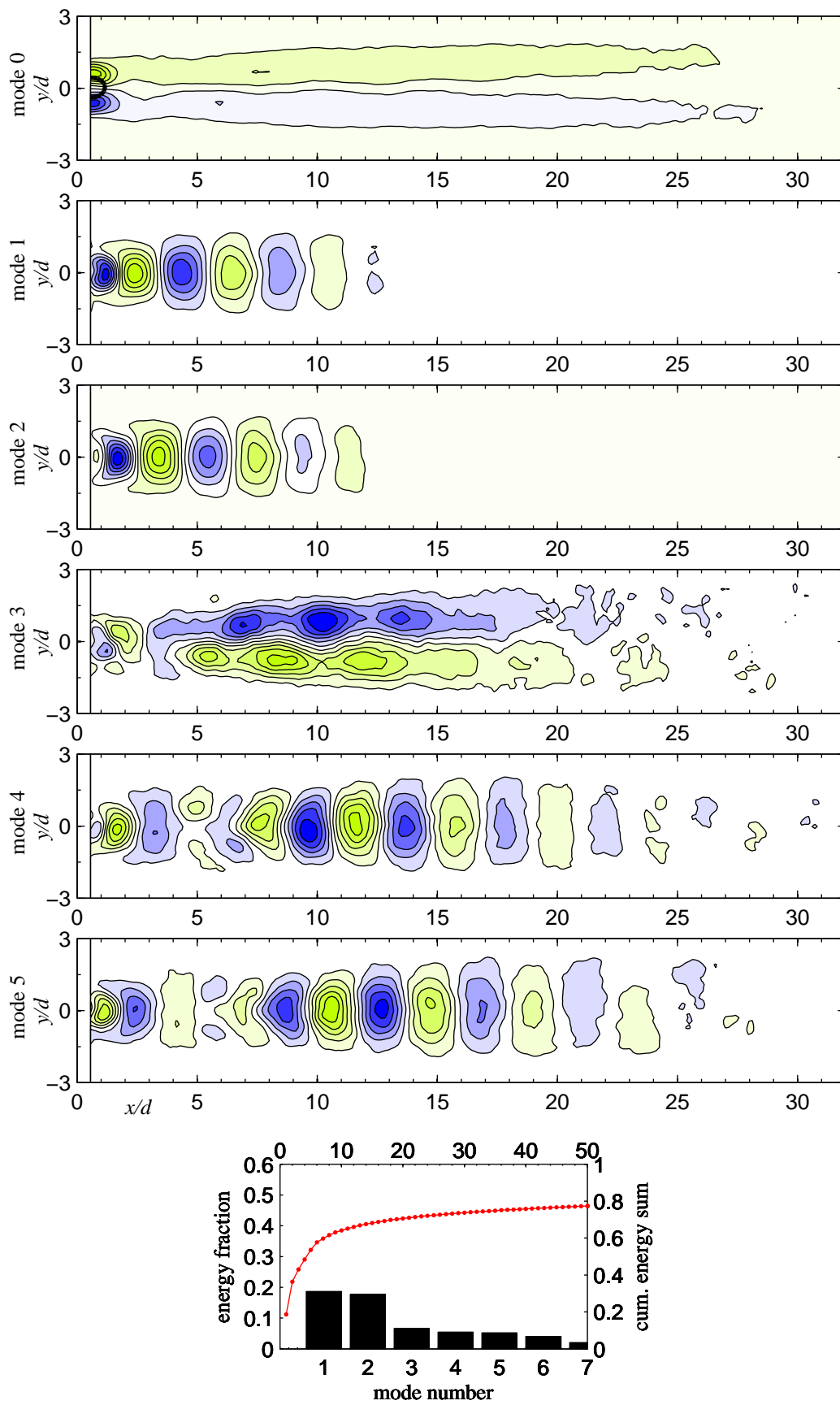


FIGURE C.7:  $Ar = 0.72$ ,  $Re = 200$

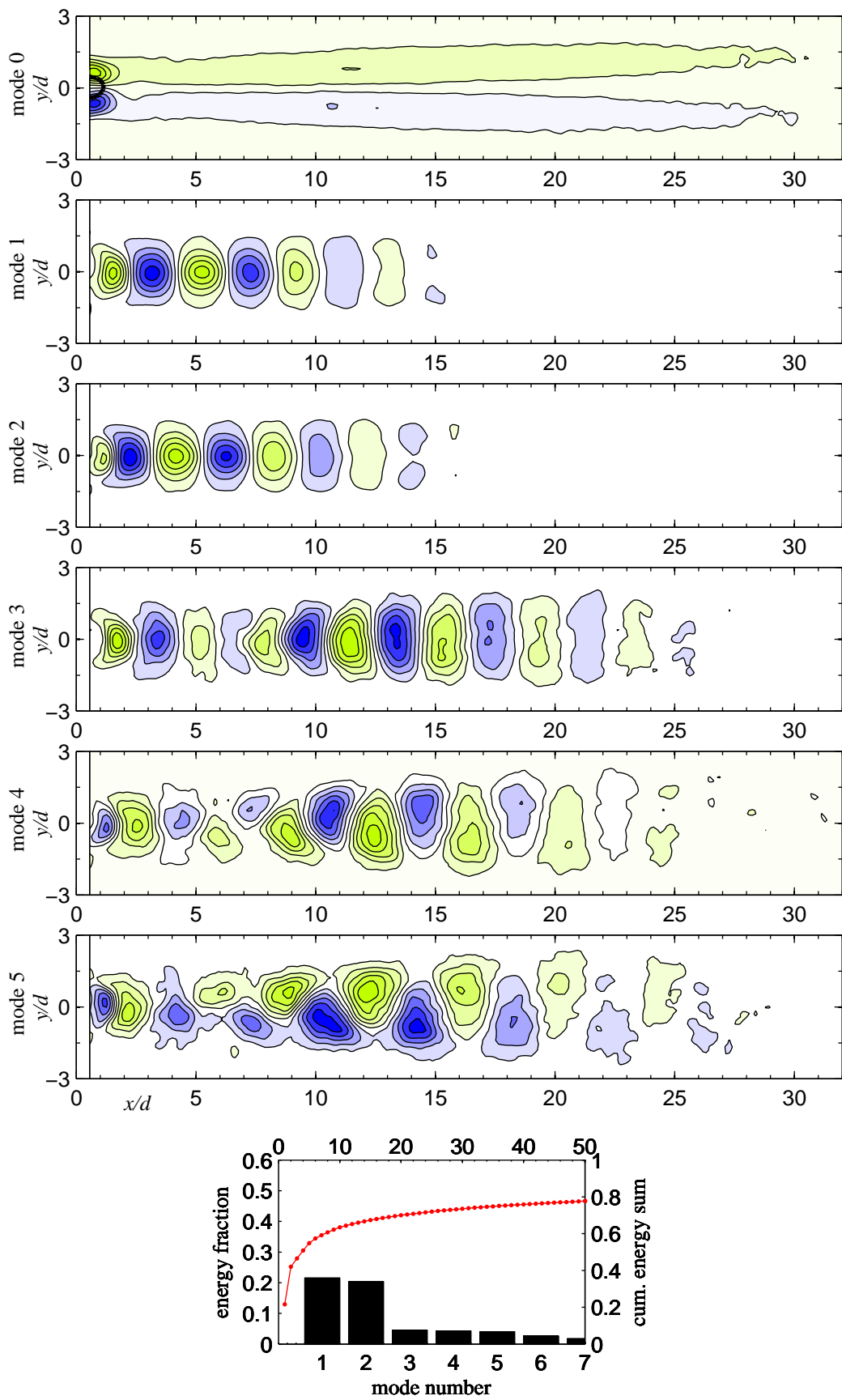


FIGURE C.8:  $Ar = 0.72$ ,  $Re = 250$

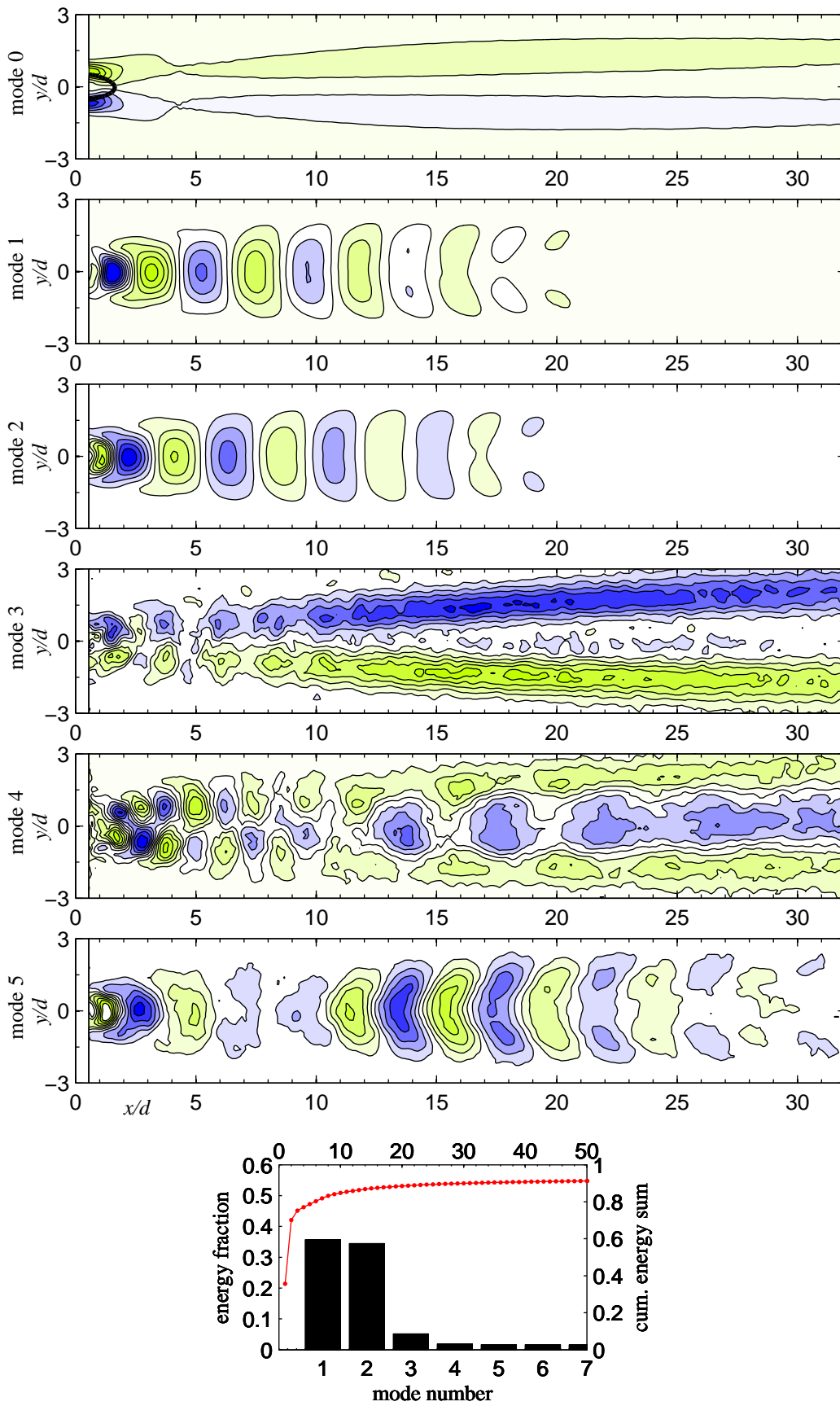


FIGURE C.9:  $Ar = 0.64$ ,  $Re = 100$

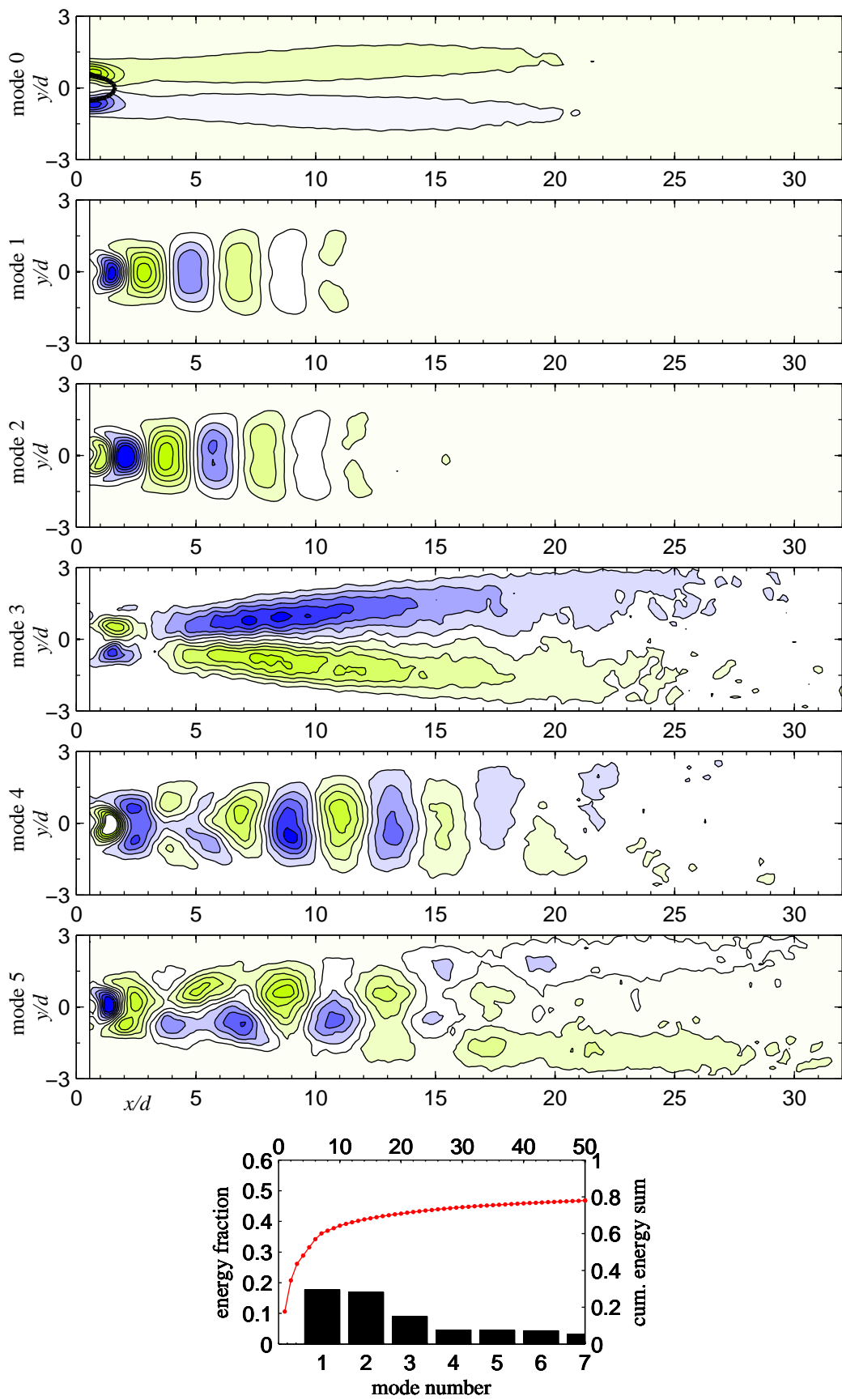


FIGURE C.10:  $Ar = 0.64$ ,  $Re = 150$

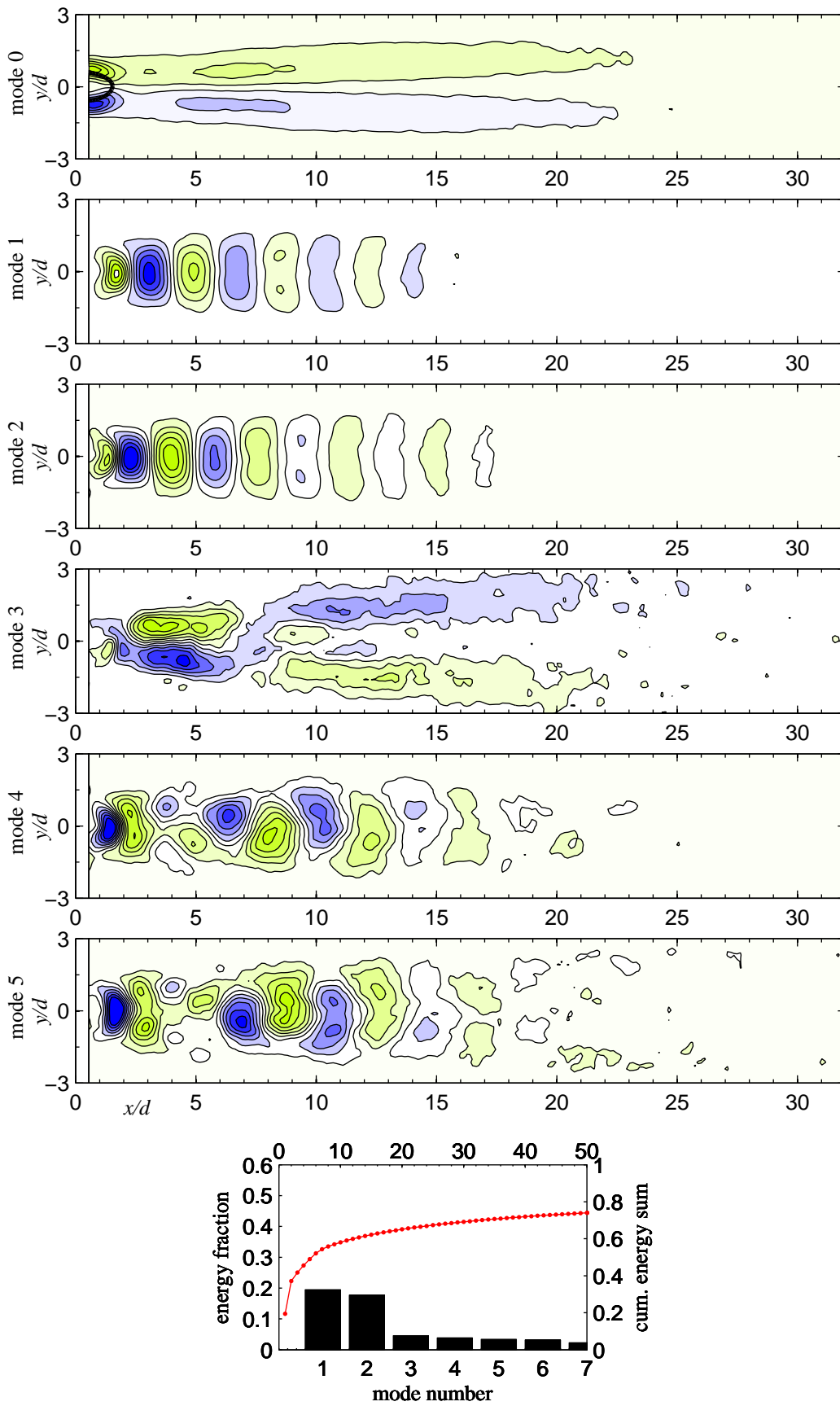


FIGURE C.11:  $Ar = 0.64$ ,  $Re = 200$

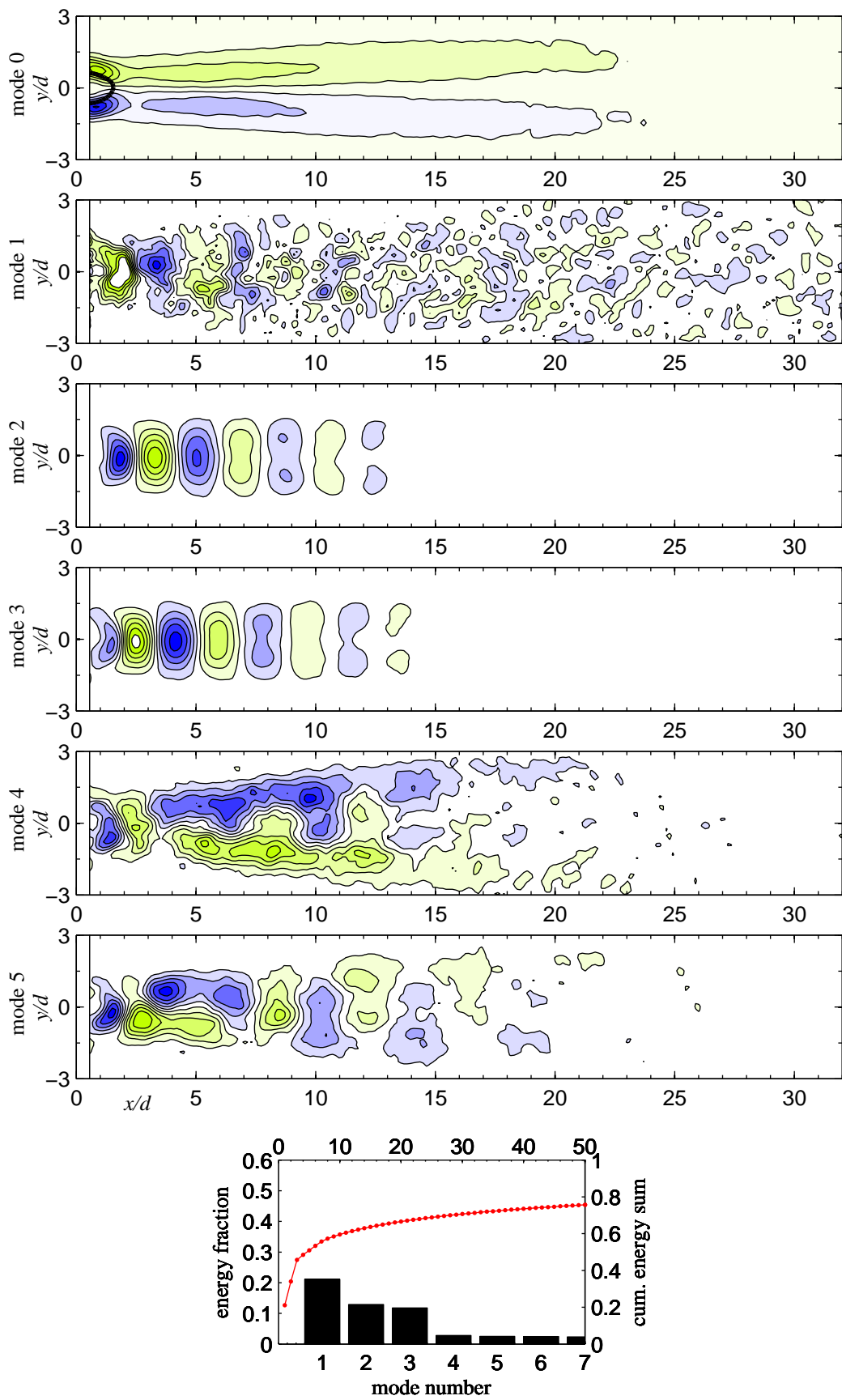


FIGURE C.12:  $Ar = 0.64$ ,  $Re = 250$

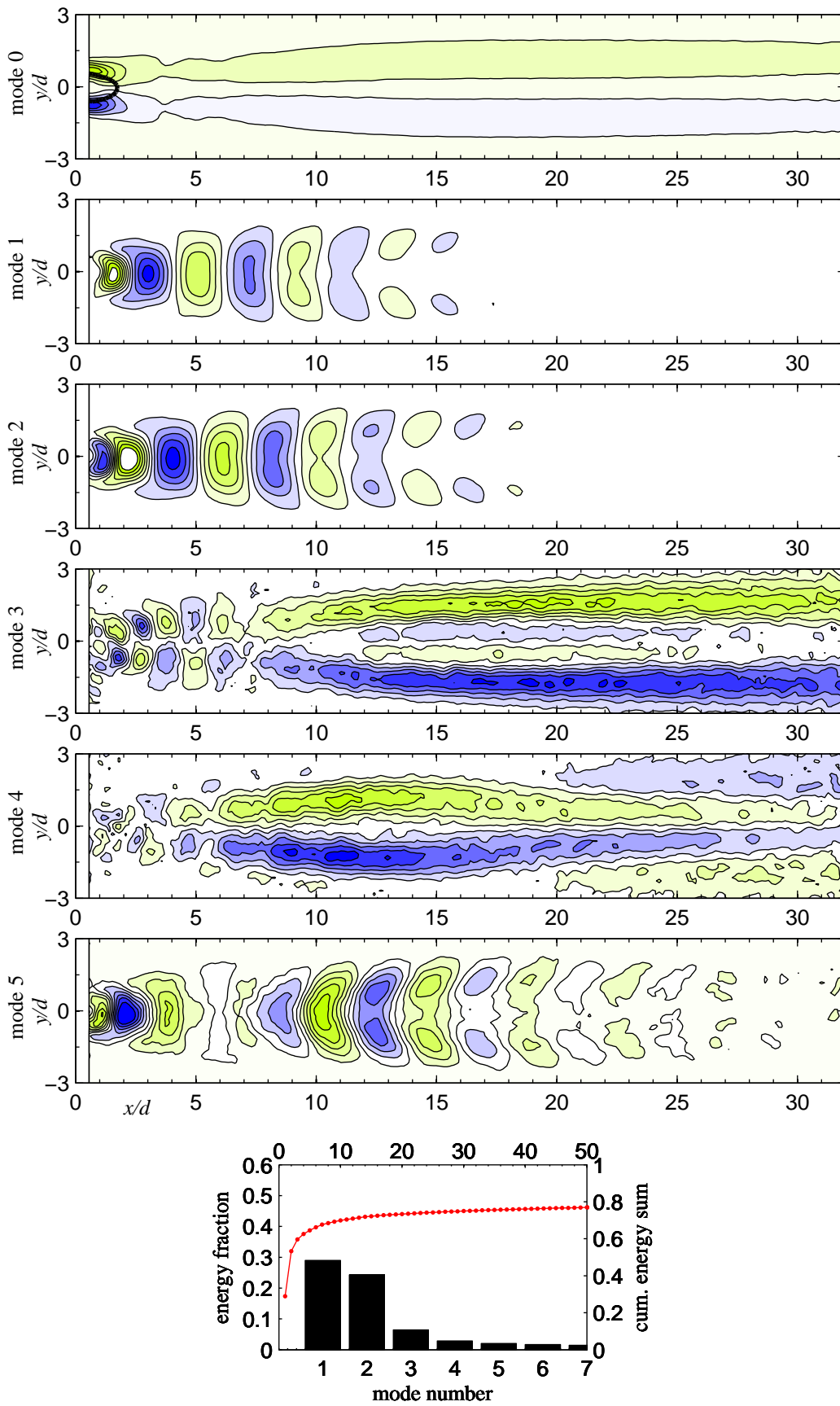


FIGURE C.13:  $Ar = 0.39$ ,  $Re = 100$



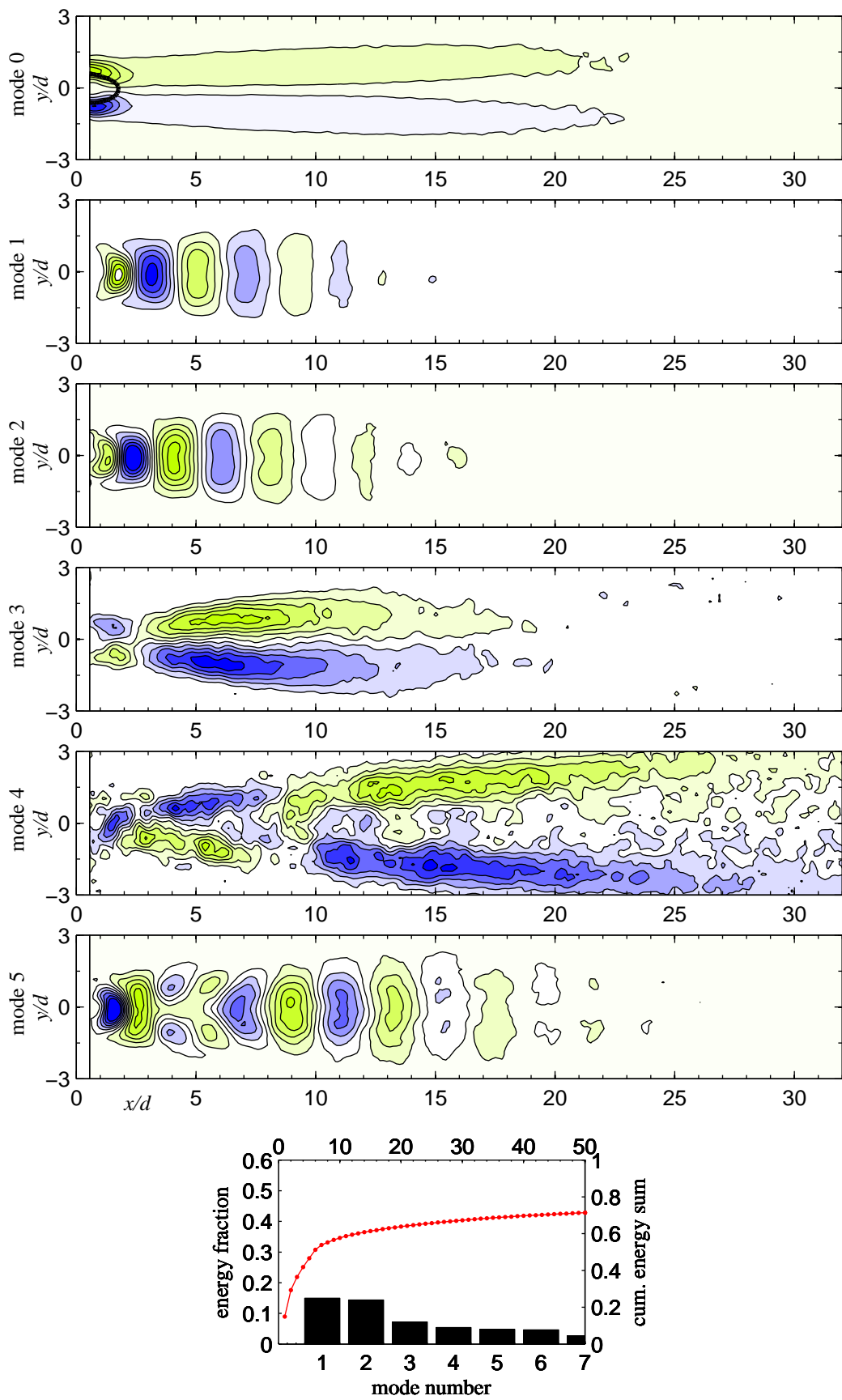


FIGURE C.14:  $Ar = 0.39$ ,  $Re = 150$

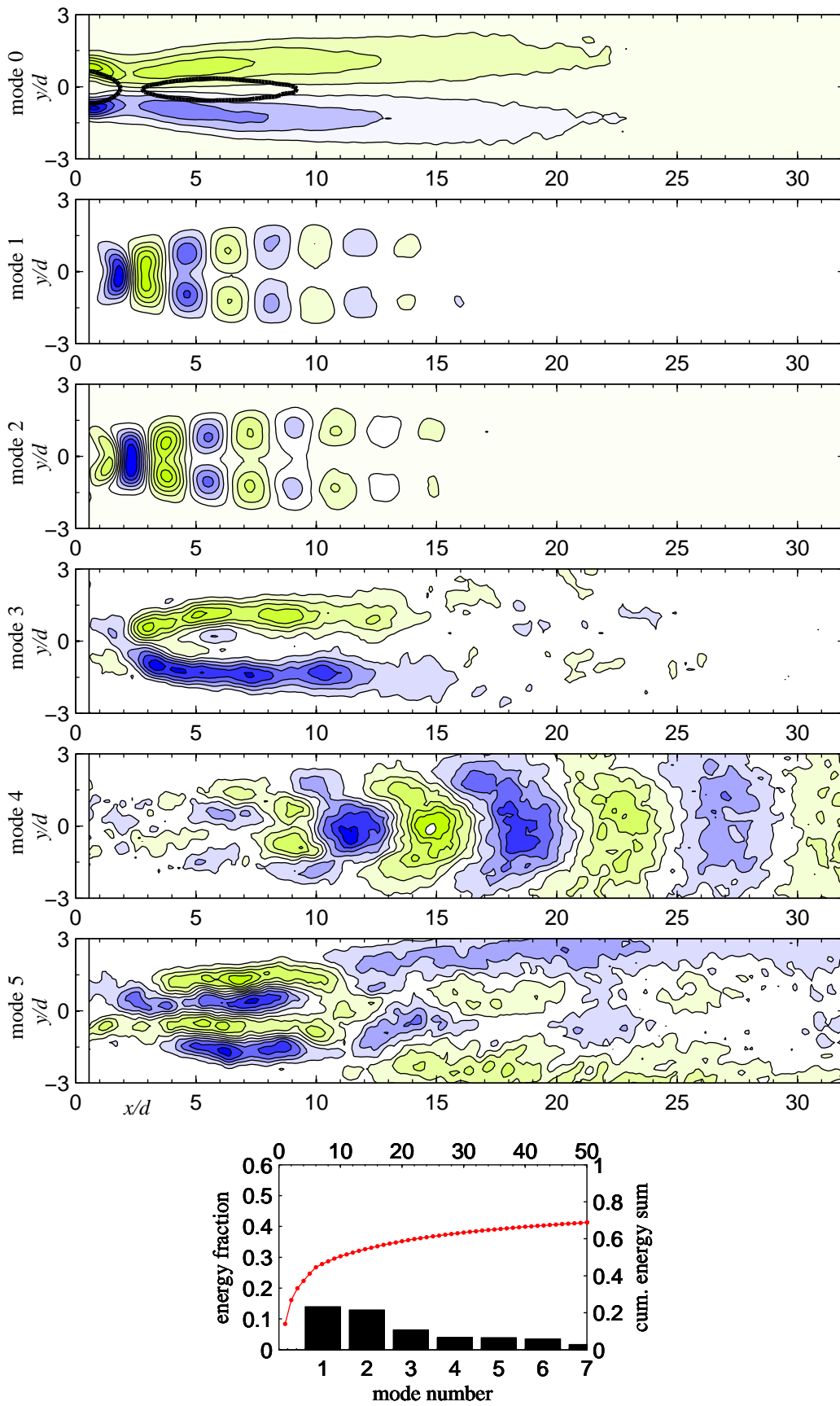


FIGURE C.15:  $Ar = 0.39$ ,  $Re = 200$

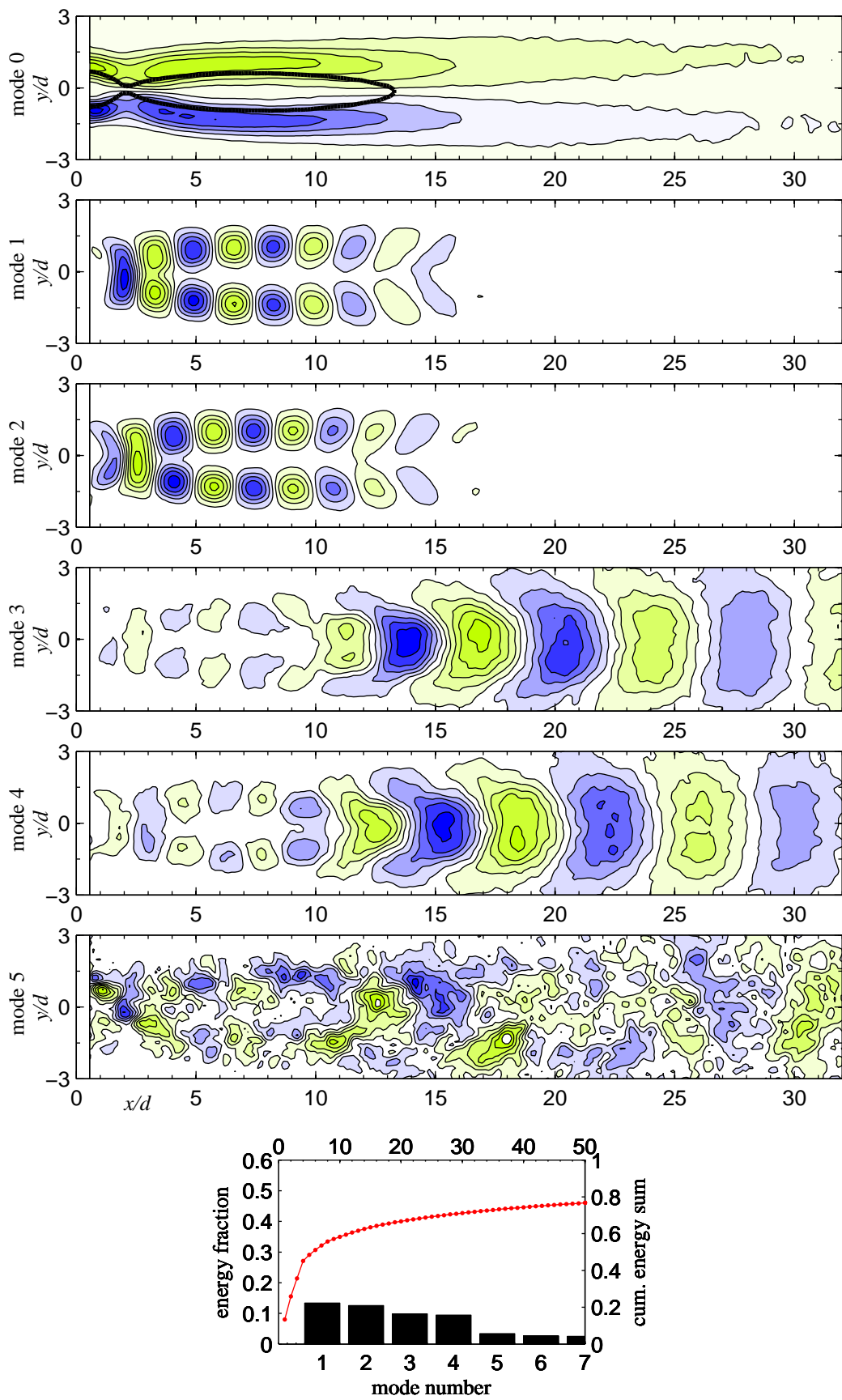


FIGURE C.16:  $Ar = 0.39$ ,  $Re = 250$

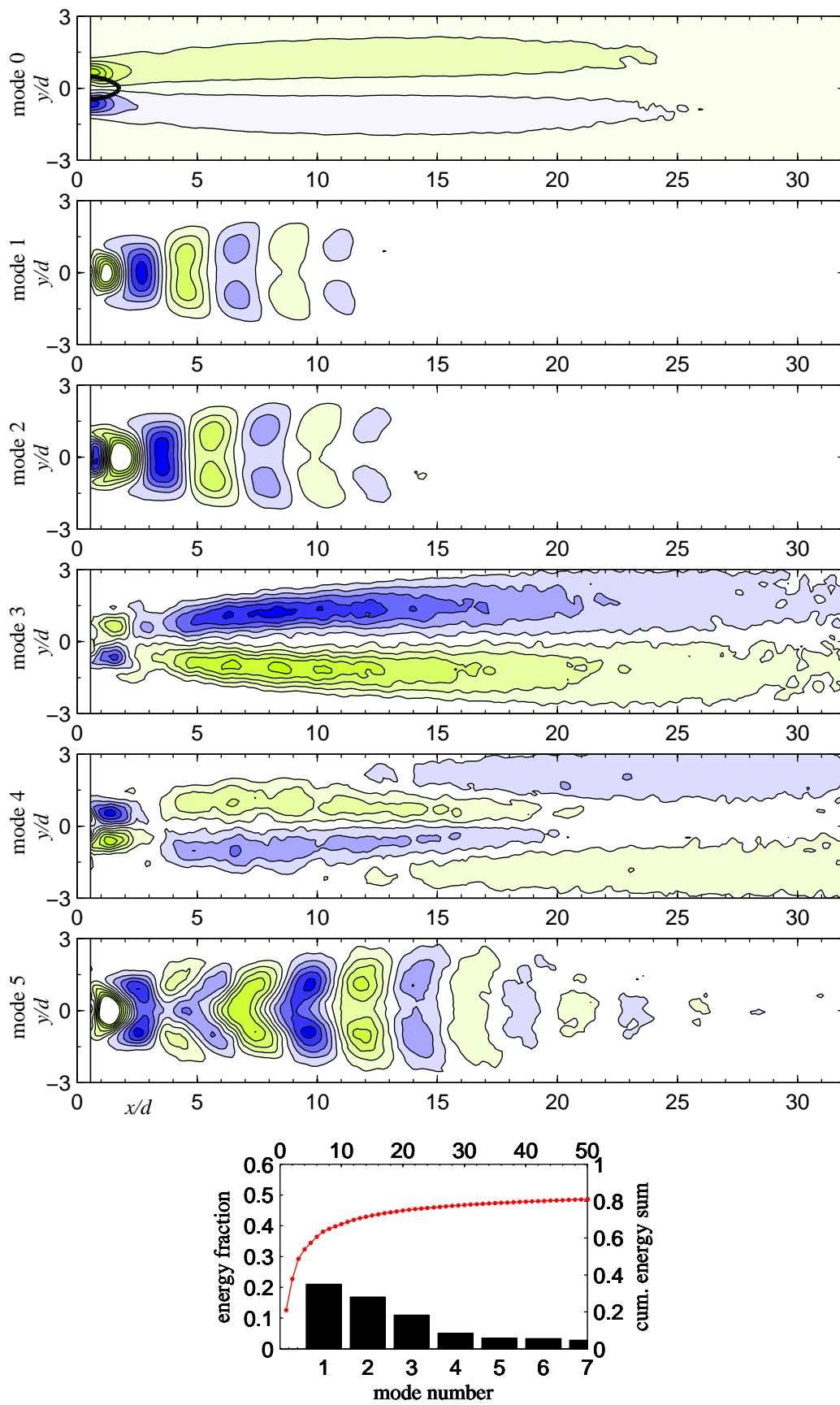


FIGURE C.17:  $Ar = 0.26$ ,  $Re = 100$

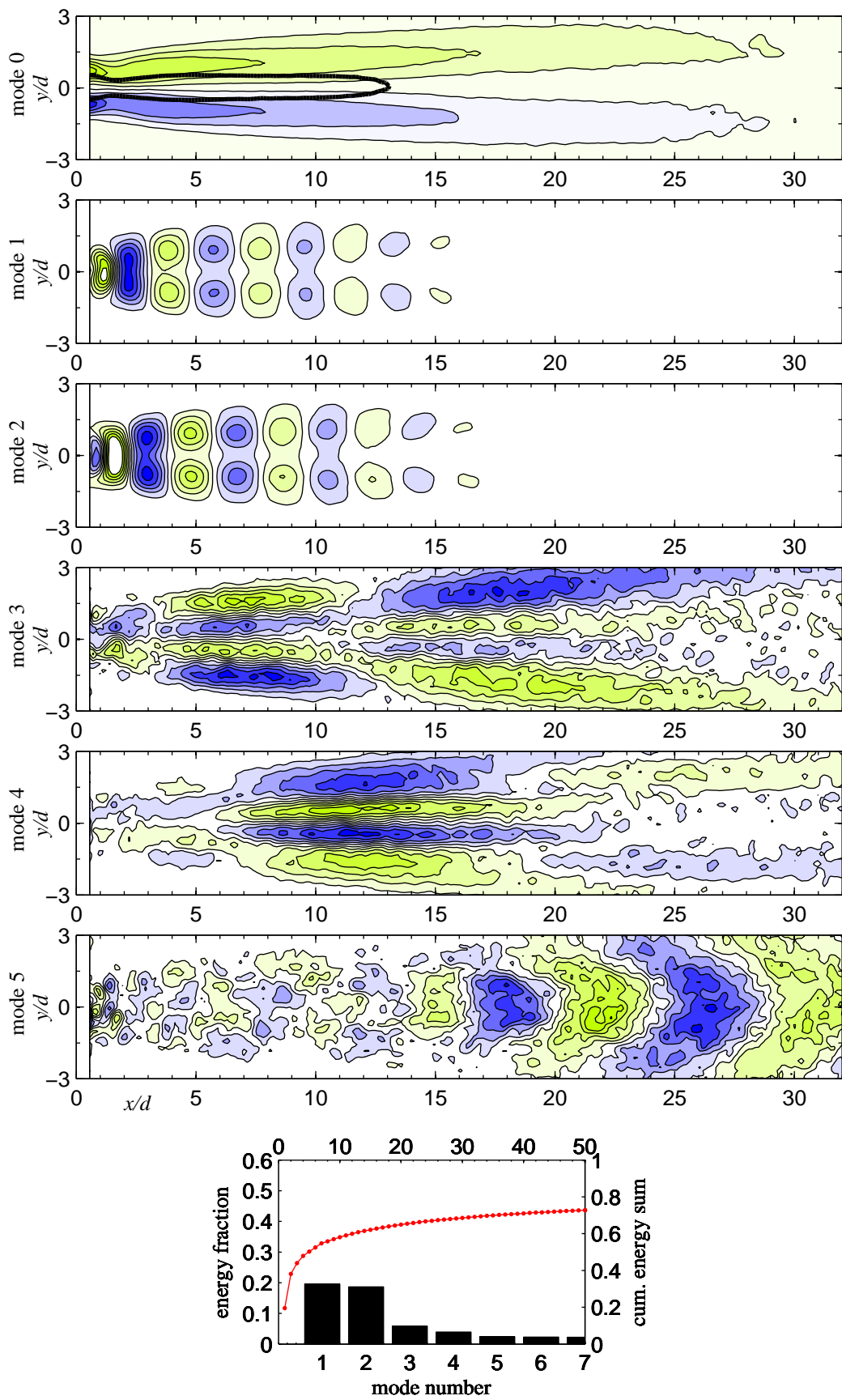


FIGURE C.18:  $Ar = 0.26$ ,  $Re = 150$

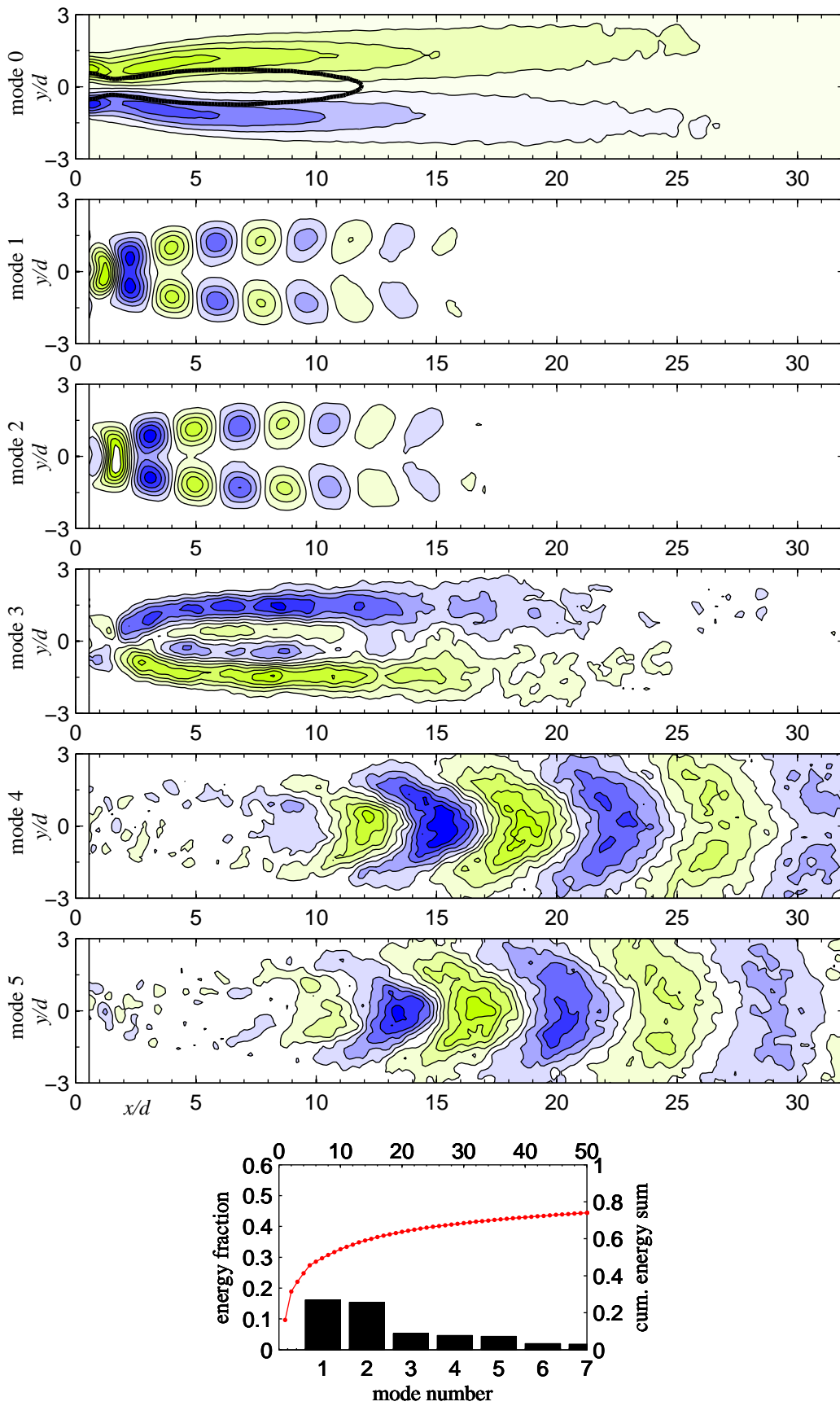


FIGURE C.19:  $Ar = 0.26$ ,  $Re = 200$



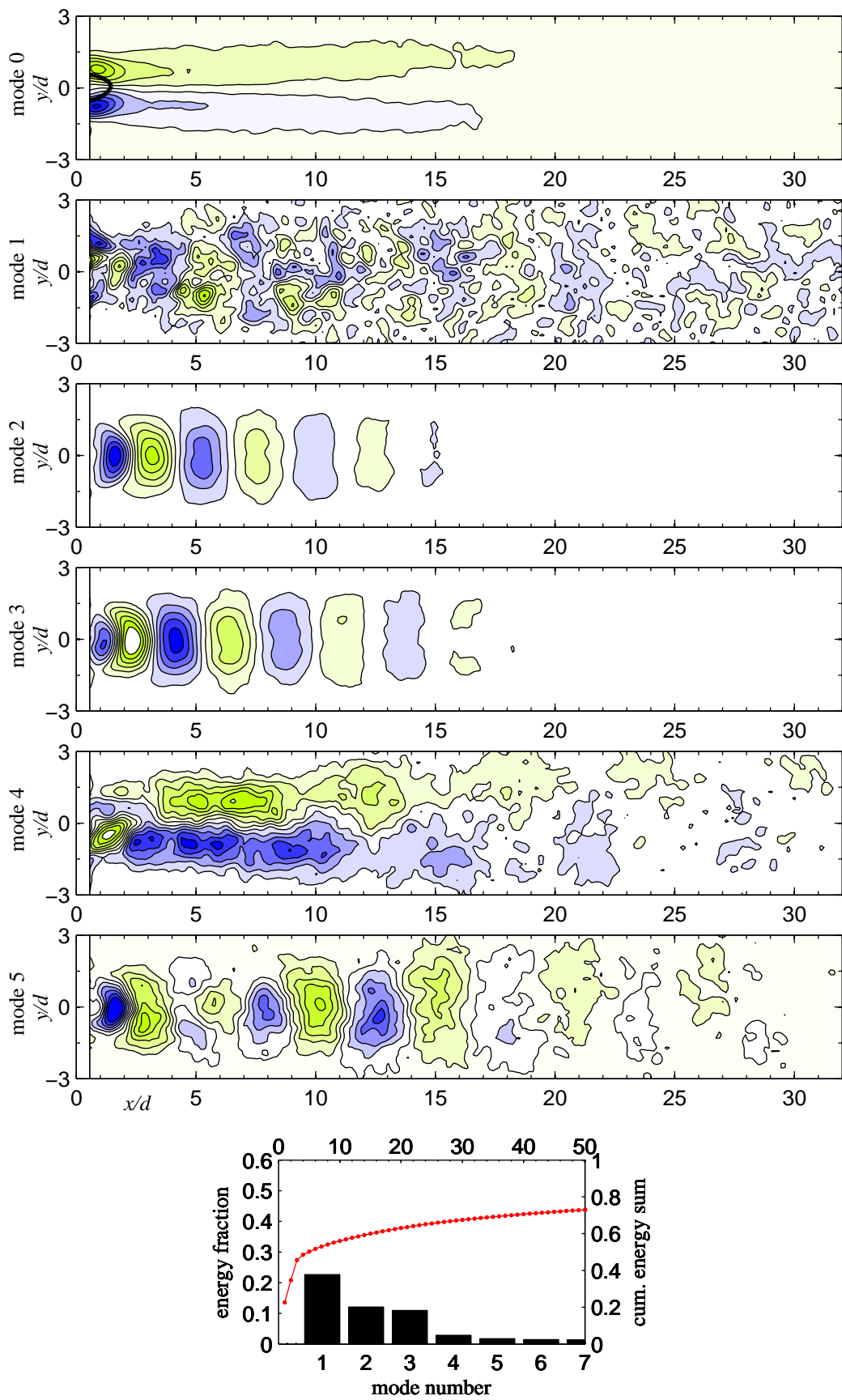


FIGURE C.20:  $Ar = 0.26$ ,  $Re = 250$

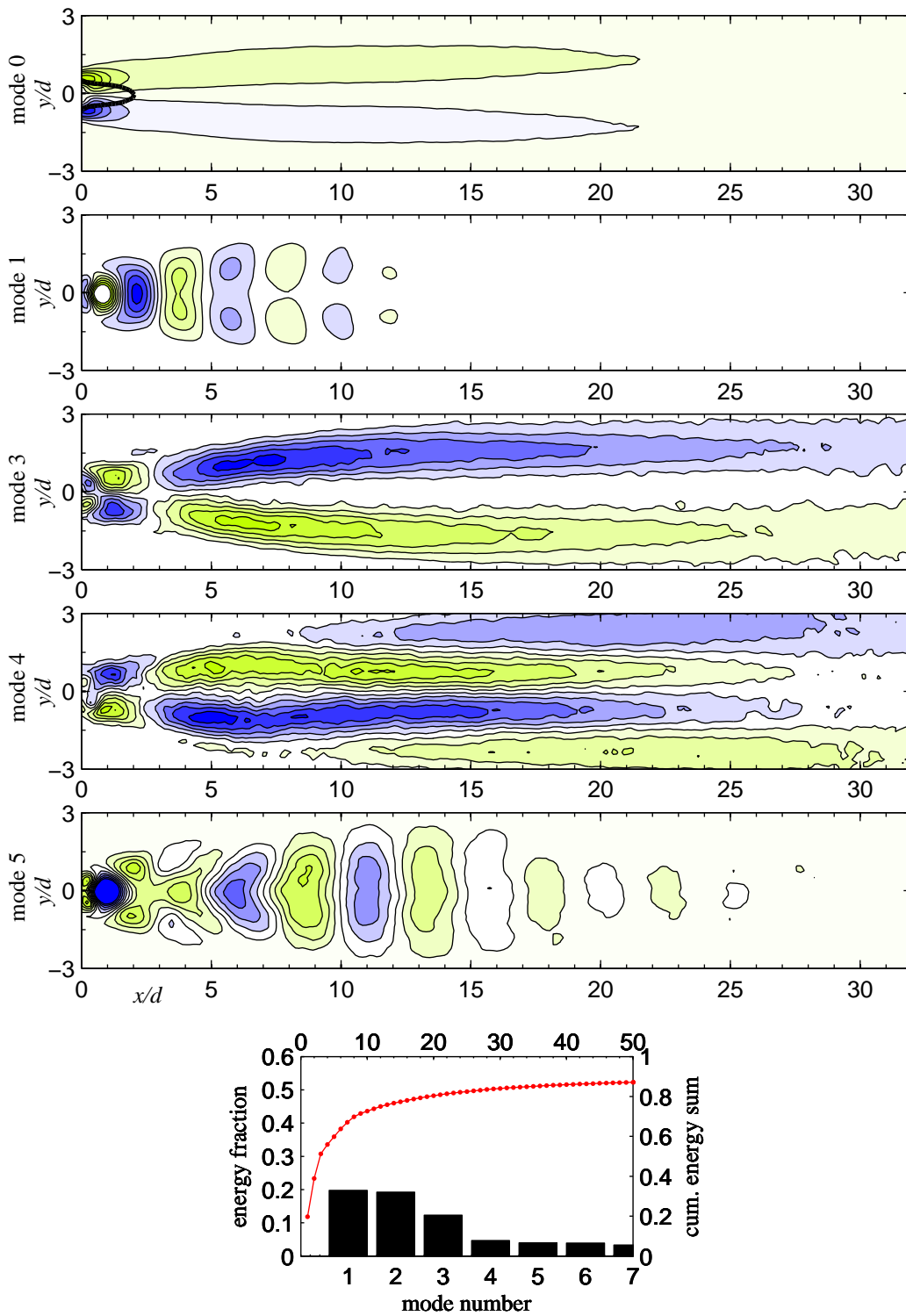


FIGURE C.21:  $Ar = 0$ ,  $Re = 100$



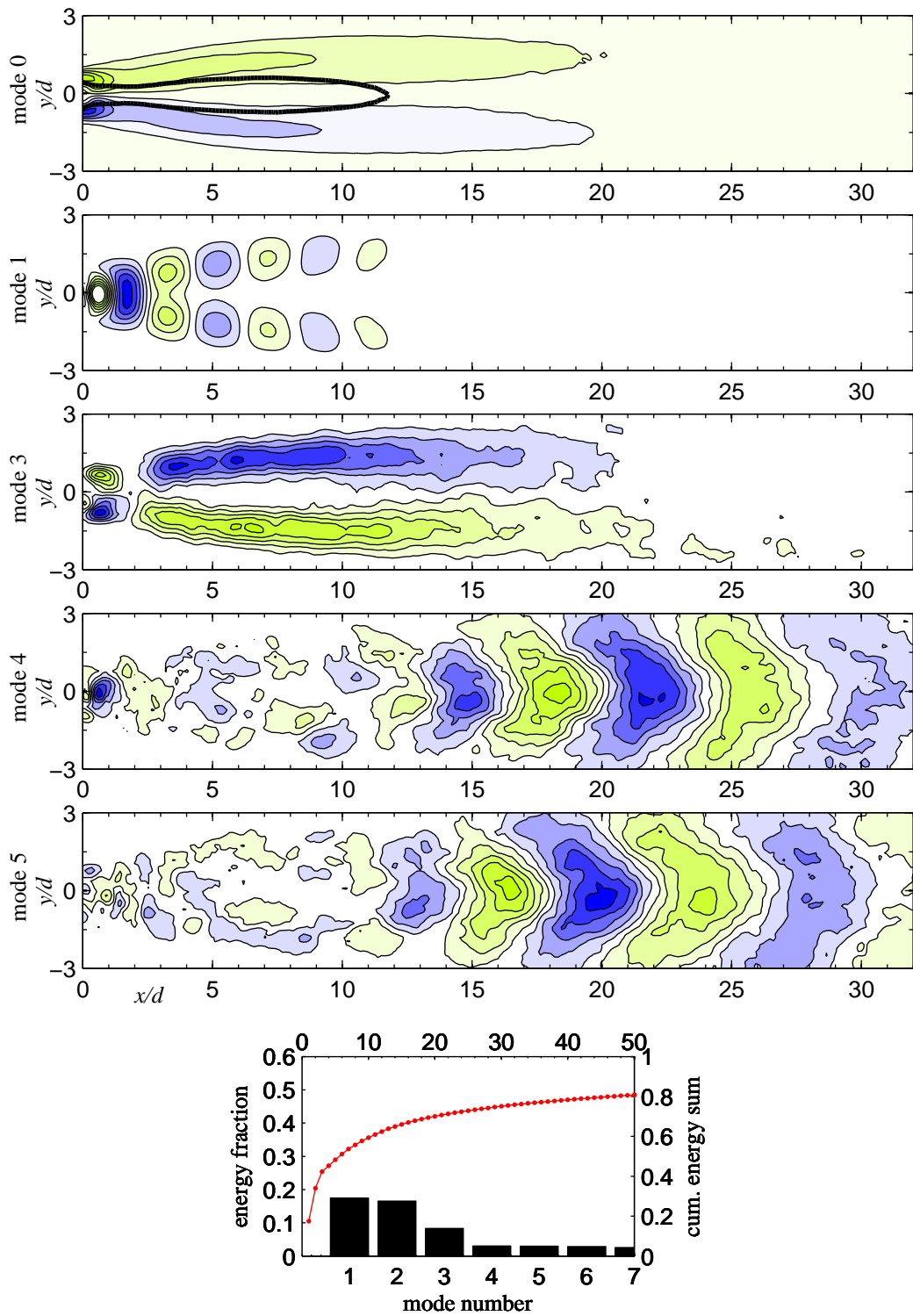


FIGURE C.22:  $Ar = 0$ ,  $Re = 150$

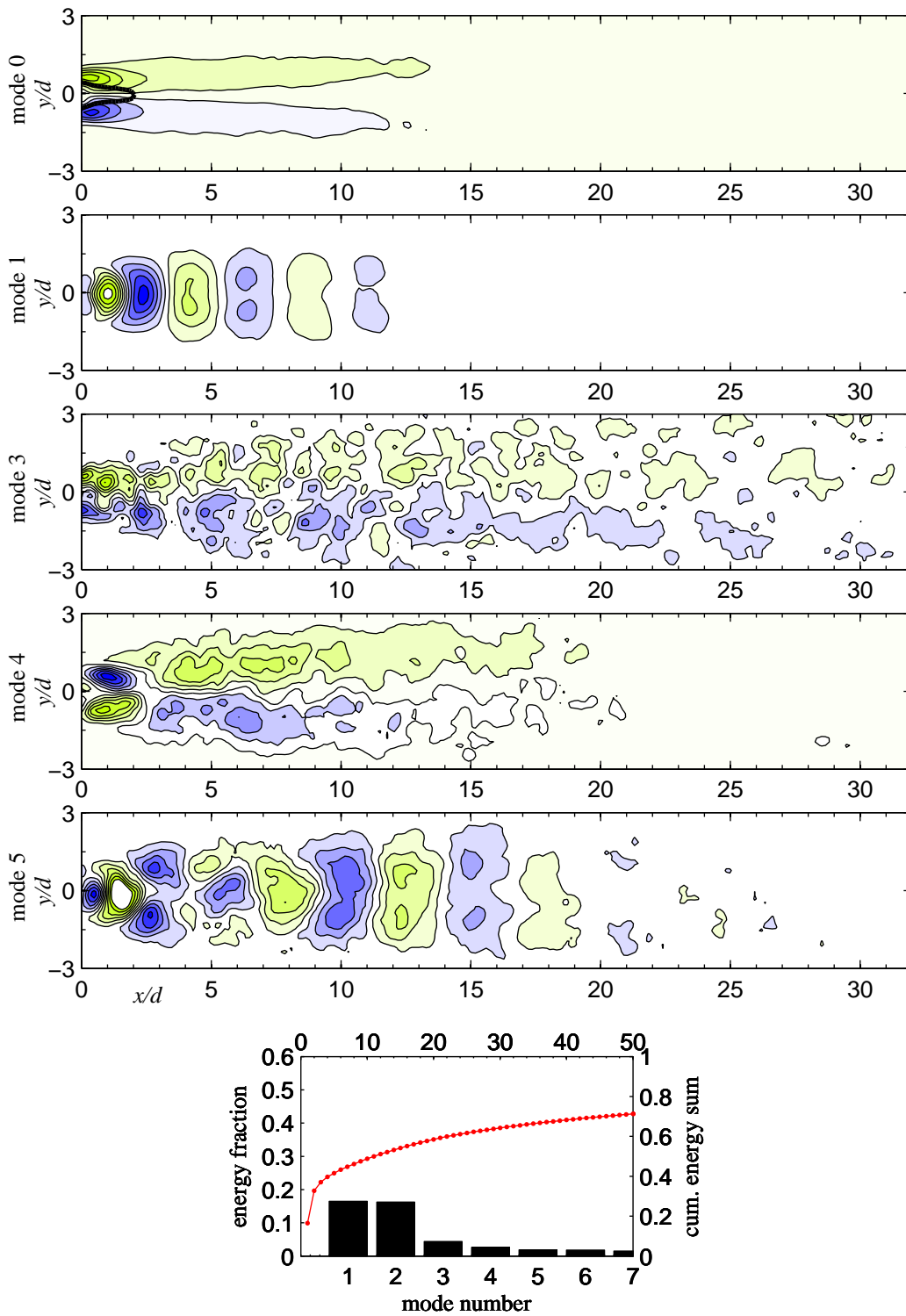


FIGURE C.23:  $Ar = 0$ ,  $Re = 200$

# Bibliography

- ADRIAN, R. J. 1991 Particle-imaging techniques for experimental fluid mechanics. *Annual review of fluid mechanics* **23**, 261–304.
- ADRIAN, R. J. & WESTERWEEL, J. 2010 *Particle Image Velocimetry*. Cambridge University Press.
- AFGAN, I., BENHAMADOUCHE, S., HAN, X., SAGAUT, P. & LAURENCE, D. 2013 Flow over a flat plate with uniform inlet and incident coherent gusts. *Journal of Fluid Mechanics* **720**, 457–485.
- ALBAREDE, P. & MONKEWITZ, P. A. 1992 A model for the formation of oblique shedding and “chevron” patterns in cylinder wakes. *Physics of Fluids A: Fluid Dynamics* **4** (4), 744–756.
- ALEKSYUK, A. I., SHKADOVA, V. P. & SHKADOV, V. Y. 2012 Formation, evolution, and decay of a vortex street in the wake of a streamlined body. *Moscow University Mechanics Bulletin* **67** (3), 53–61.
- BARKLEY, D. 2005 Confined three-dimensional stability analysis of the cylinder wake. *Physical Review E* **71** (1).
- BARKLEY, D. & HENDERSON, R. D. 1996 Three-dimensional Floquet stability analysis of the wake of a circular cylinder. *Journal of Fluid Mechanics* **322**, 215–241.
- BARKLEY, D., TUCKERMAN, L. & GOLUBITSKY, M. 2000 Bifurcation theory for three-dimensional flow in the wake of a circular cylinder. *Physical Review E* **61** (5), 5247–5252.
- BECHERT, D. W., HOPPE, G., VAN DER HOEVEN, J. G. & MAKRIS, R. 1992 The Berlin oil channel for drag reduction research. *Experiments in Fluids* **12** (4-5), 251–260.
- BEHARA, S. & MITTAL, S. 2010 Wake transition in flow past a circular cylinder. *Physics of Fluids* **22** (11), 114104–11.
- BEHR, M., HASTREITER, D., MITTAL, S. & TEZDUYAR, T. 1995 Incompressible flow past a circular cylinder: dependence of the computed flow field on the location of

- 
- the lateral boundaries. *Computer Methods in Applied Mechanics and Engineering* **123** (1), 309–316.
- BÉNARD, H. 1908 Formation de centres de giration à l’arrière d’un obstacle en mouvement. *C. R. Acad. Sci. Paris* **147**.
- BLACKBURN, H. M. & LOPEZ, J. M. 2003 On three-dimensional quasiperiodic Floquet instabilities of two-dimensional bluff body wakes. *Physics of Fluids* **15**, L57.
- BLACKBURN, H. M. & SHEARD, G. J. 2010 On quasiperiodic and subharmonic Floquet wake instabilities. *Physics of Fluids* **22** (3), 031701–4.
- BRAZA, M., FAGHANI, D. & PERSILLON, H. 2001 Successive stages and the role of natural vortex dislocations in three-dimensional wake transition. *Journal of Fluid Mechanics* **439**, 1–41.
- BRUUN, H. H. 1995 *Hot-wire Anemometry - Principles and Signal Analysis*. Oxford University Press.
- CASTRO, I. P. 1971 Wake characteristics of two-dimensional perforated plates normal to an air-stream. *Journal of Fluid Mechanics* **46** (3), 599–609.
- CHOI, H., JEON, W.-P. & KIM, J. 2008 Control of flow over a bluff body. *Annual Review of Fluid Mechanics* **40** (1), 113–139.
- CIMBALA, J. M., NAGIB, H. M. & ROSHKO, A. 1988 Large structure in the far wakes of two-dimensional bluff bodies. *Journal of Fluid Mechanics* **190**, 265–298.
- COLEMAN, H. W. & STEELE, W. G. 1995 Engineering application of experimental uncertainty analysis. *AIAA Journal* **33** (10), 1888–1896.
- CROW, S. C. 1970 Stability theory for a pair of trailing vortices. *AIAA Journal* **8** (12), 2172–2179.
- DEANE, A. E., KEVREKIDIS, I. G., KARNIADAKIS, G. E. & ORSZAG, S. A. 1991 Low-dimensional models for complex geometry flows: Application to grooved channels and circular cylinders. *Physics of Fluids A: Fluid Dynamics* **3** (10), 2337–2354.
- DÉLERY, J. M. 2001 Robert Legendre and Henri Werlé: Toward the elucidation of three-dimensional separation. *Annual Review of Fluid Mechanics* **33** (1), 129–154.
- DURGIN, W. W. & KARLSSON, S. K. F. 1971 On the phenomenon of vortex street breakdown. *Journal of Fluid Mechanics* **48** (03), 507–527.
- DUSEK, J., LE GAL, P. & FRAUNIE, D. 1994 A numerical and theoretical study of the first Hopf bifurcation in a cylinder wake. *Journal of Fluid Mechanics* **264**, 59–80.

- 
- EISENLOHR, H. & ECKELMANN, H. 1989 Vortex splitting and its consequences in the vortex street wake of cylinders at low reynolds number. *Physics of Fluids A: Fluid Dynamics* **1** (2), 189–192.
- EL AKOURY, R., BRAZA, M., PERRIN, R., HARRAN, G. & HOARAU, Y. 2008 The three-dimensional transition in the flow around a rotating cylinder. *Journal of Fluid Mechanics* **607**, 1–11.
- FAGE, A. & JOHANSEN, F. C. 1927 On the flow of air behind an inclined flat plate of infinite span. *Proceedings of the Royal Society of London. Series A, Containing Papers of a Mathematical and Physical Character* **116** (773), 170–197.
- FOURAS, A. & SORIA, J. 1998 Accuracy of out-of-plane vorticity measurements derived from in-plane velocity field data. *Experiments in Fluids* **25** (5-6), 409–430.
- GERICH, D. & ECKELMANN, H. 1982 Influence of end plates and free ends on the shedding frequency of circular cylinders. *Journal of Fluid Mechanics* **122**, 109–121.
- GRAFTIEAUX, L., MICHARD, M. & GROSJEAN, N. 2001 Combining PIV, POD and vortex identification algorithms for the study of unsteady turbulent swirling flows. *Measurement Science and Technology* **12** (9), 1422.
- HAMMACHE, M. & GHARIB, M. 1991 An experimental study of the parallel and oblique vortex shedding from circular cylinders. *Journal of Fluid Mechanics* **232**, 567–590.
- HAN, X., SAGAUT, P., LUCOR, D. & AFGAN, I. 2012 Stochastic response of the laminar flow past a flat plate under uncertain inflow conditions. *International Journal of Computational Fluid Dynamics* **26** (2), 101–117.
- HENDERSON, R. D. 1997 Nonlinear dynamics and pattern formation in turbulent wake transition. *Journal of Fluid Mechanics* **352** (1), 65–112.
- HENDERSON, R. D. & BARKLEY, D. 1996 Secondary instability in the wake of a circular cylinder. *Physics of Fluids* **8** (6), 1683–1685.
- HUCHO, W.-H. & SOVRAN, G. 1993 Aerodynamics of road vehicles. *Annual Review of Fluid Mechanics* **25** (1), 485–537.
- INOUE, O. & YAMAZAKI, T. 1999 Secondary vortex streets in two-dimensional cylinder wakes. *Fluid Dynamics Research* **25** (1), 1–18.
- JACKSON, C. P. 1987 A finite-element study of the onset of vortex shedding in flow past variously shaped bodies. *Journal of Fluid Mechanics* **182**, 23–45.
- JOHNSON, S. A., THOMPSON, M. C. & HOURIGAN, K. 2004 Predicted low frequency structures in the wake of elliptical cylinders. *European Journal of Mechanics - B/Fluids* **23** (1), 229–239.

- 
- KARASUDANI, T. & FUNAKOSHI, M. 1994 Evolution of a vortex street in the far wake of a cylinder. *Fluid Dynamics Research* **14** (6), 331–352.
- KÁRMÁN, T. V. 1911 Über den Mechanismus des Widerstandes, den ein bewegter Körper in einer Flüssigkeit erfährt. *Göttinger Nachrichten* pp. 509–511.
- KERR, O. S. & DOLD, J. W. 1994 Periodic steady vortices in a stagnation-point flow. *Journal of Fluid Mechanics* **276** (-1), 307–325.
- KERSWELL, R. R. 2002 Elliptical instability. *Annual Review of Fluid Mechanics* **34**, 83–113.
- KHALEDI, H., ANDERSSON, H. I., BARRI, M. & PETTERSEN, B. 2012 Flow past a normal flat plate undergoing inline oscillations. *Physics of Fluids* **24** (9), 093603.
- KOSTAS, J., SORIA, J. & CHONG, M. S. 2005 A comparison between snapshot POD analysis of PIV velocity and vorticity data. *Experiments in Fluids* **38** (2), 146–160.
- KUMAR, B. & MITTAL, S. 2006 Effect of blockage on critical parameters for flow past a circular cylinder. *International Journal for Numerical Methods in Fluids* **50** (8), 987–1001.
- KUMAR, B. & MITTAL, S. 2012 On the origin of the secondary vortex street. *Journal of Fluid Mechanics* **711**, 641–666.
- KUMAR, S., CANTU, C. & GONZALEZ, B. 2011 Flow past a rotating cylinder at low and high rotation rates. *Journal of Fluids Engineering* **133** (4).
- LANDMAN, M. J. & SAFFMAN, P. G. 1987 The three-dimensional instability of strained vortices in a viscous fluid. *Physics of Fluids* **30** (8), 2339–2342.
- LE GAL, P., NADIM, A. & THOMPSON, M. 2001 Hysteresis in the forced Stuart-Landau equation: Application to vortex shedding from an oscillating cylinder. *Journal of Fluids and Structures* **15**, 445–457.
- LEBLANC, S. & GODEFERD, F. S. 1999 An illustration of the link between ribs and hyperbolic instability. *Physics of Fluids* **11** (2), 497–499.
- LEE, T. & BUDWIG, R. 1991 A study of the effect of aspect ratio on vortex shedding behind circular cylinders. *Physics of Fluids A: Fluid Dynamics* **3** (2), 309–315.
- LEWEKE, T. & WILLIAMSON, C. H. K. 1998 Three-dimensional instabilities in wake transition. *European Journal of Mechanics B/Fluids* **17**, 571–586.
- LISOSKI, D. 1993 Nominally two-dimensional flow about a normal flat plate. Ph.D. thesis, California Institute of Technology.

- 
- LUO, S. C., CHEW, Y. T. & DUONG, T. T. L. 2010 PIV investigation of flow past a rotating circular cylinder. *Fourth International Conference on Experimental Mechanics* pp. 752219–752219, 10.1117/12.851460.
- MA, X., KARAMANOS, G. S. & KARNIADAKIS, G. E. 2000 Dynamics and low-dimensionality of a turbulent near wake. *Journal of Fluid Mechanics* **410**, 29–65.
- MAGNUS, G. 1853 Über die Abweichung der Geschosse, und: Über eine abfallende Erscheinung bei rotierenden Körpern. *Annalen der Physik* **164** (1), 1–29.
- MEUNIER, P. & LEWEKE, T. 2005 Elliptic instability of a co-rotating vortex pair. *Journal of Fluid Mechanics* **533**, 125–160.
- MILLER, G. D. & WILLIAMSON, C. H. K. 1994 Control of three-dimensional phase dynamics in a cylinder wake. *Experiments in Fluids* **18** (1), 26–35.
- MING-HSUN WU, C.-Y. W., RUEY-HOR YEN, M.-C. W. & WANG, A.-B. 2004 Experimental and numerical study of the separation angle for flow around a circular cylinder at low Reynolds number. *Journal of Fluid Mechanics* **515**, 233–260.
- MITTAL, R. & BALACHANDAR, S. 1995 Effect of three-dimensionality on the lift and drag of nominally two-dimensional cylinders. *Physics of Fluids* **7**, 1841.
- MITTAL, S. 2001 Flow past rotating cylinders: Effect of eccentricity. *Journal of Applied Mechanics* **68** (4), 543–552.
- MITTAL, S. 2004 Three-dimensional instabilities in flow past a rotating cylinder. *Journal of Applied Mechanics* **71** (1), 89–96.
- MITTAL, S. & KUMAR, B. 2003 Flow past a rotating cylinder. *Journal of Fluid Mechanics* **476**, 303–334.
- MODI, V. J. 1997 Moving surface boundary-layer control: a review. *Journal of Fluids and Structures* **11** (6), 627–663.
- MODI, V. J. & DIKSHIT, A. K. 1975 Near-wakes of elliptic cylinders in subcritical flow. *AIAA Journal* **13** (4), 490–497.
- MODI, V. J. & WILAND, E. 1970 Unsteady aerodynamics of stationary elliptic cylinders in subcritical flow. *AIAA Journal* **8** (10), 1814–1821.
- MONKEWITZ, P. A. 1988 The absolute and convective nature of instability in two-dimensional wakes at low Reynolds numbers. *Physics of Fluids* **31**, 999.
- MORTON, B. R. 1984 The generation and decay of vorticity. *Geophysical & Astrophysical Fluid Dynamics* **28** (3-4), 277–308.

- 
- NAJJAR, F. M. & BALACHANDAR, S. 1998 Low-frequency unsteadiness in the wake of a normal flat plate. *Journal of Fluid Mechanics* **370**, 101–147.
- NAJJAR, F. M. & VANKA, S. P. 1995a Effects of intrinsic three-dimensionality on the drag characteristics of a normal flat plate. *Physics of Fluids* **7**, 2516.
- NAJJAR, F. M. & VANKA, S. P. 1995b Simulations of the unsteady separated flow past a normal flat plate. *International Journal for Numerical Methods in Fluids* **21** (7), 525–547.
- NARASIMHAMURTHY, V. D. & ANDERSSON, H. I. 2009 Numerical simulation of the turbulent wake behind a normal flat plate. *International Journal of Heat and Fluid Flow* **30** (6), 1037–1043.
- NAZARINIA, M. 2010 Flow around oscillating circular cylinders. Ph.D. thesis, Monash University.
- NOACK, B. R., AFANASIEV, K., MORZYNSKI, M., TADMOR, G. & THIELE, F. 2003 A hierarchy of low-dimensional models for the transient and post-transient cylinder wake. *Journal of Fluid Mechanics* **497**, 335–363.
- NORBERG, C. 1987 Effects of reynolds number and a low-intensity freestream turbulence on the flow around a circular cylinder. Ph.D. thesis, Chalmers University of Technology.
- NORBERG, C. 1994 An experimental investigation of the flow around a circular cylinder: influence of aspect ratio. *Journal of Fluid Mechanics* **258**, 287–316.
- OTA, T., NISHIYAMA, H. & TAOKA, Y. 1987 Flow around an elliptic cylinder in the critical Reynolds number regime. *Journal of Fluids Engineering* **109** (2), 149–155.
- PANTON, R. L. 2006 *Incompressible flow*, 3rd edn. John Wiley & Sons.
- PERRY, A. E., CHONG, M. S. & LIM, T. T. 1982 The vortex-shedding process behind two-dimensional bluff bodies. *Journal of Fluid Mechanics* **116**, 77–90.
- PERRY, A. E. & FAIRLIE, B. D. 1974 Critical points in flow patterns. *Advances in geophysics* **18B**.
- PONCET, P. 2002 Vanishing of mode B in the wake behind a rotationally oscillating circular cylinder. *Physics of Fluids* **14** (6), 2021–2023.
- PRALITS, J. O., BRANDT, L. & GIANNETTI, F. 2010 Instability and sensitivity of the flow around a rotating circular cylinder. *Journal of Fluid Mechanics* **650**, 513.
- PRALITS, J. O., GIANNETTI, F. & BRANDT, L. 2013 Three-dimensional instability of the flow around a rotating circular cylinder. *Journal of Fluid Mechanics* **730**, 5–18.



- 
- PRASAD, A. & WILLIAMSON, C. H. K. 1997 Three-dimensional effects in turbulent bluff-body wakes. *Journal of Fluid Mechanics* **343**, 235–265.
- QU, L., NORBERG, C., DAVIDSON, L., PENG, S.-H. & WANG, F. 2013 Quantitative numerical analysis of flow past a circular cylinder at Reynolds number between 50 and 200. *Journal of Fluids and Structures* **39**, 347–370.
- RADI, A., LO JACONO, D. & SHERIDAN, J. 2013a A device to achieve low Reynolds numbers in an open-surface water channel. *Experiments in Fluids* (submitted for publication).
- RADI, A., THOMPSON, M. C., RAO, A., HOURIGAN, K. & SHERIDAN, J. 2013b Experimental evidence of new three-dimensional modes in the wake of a rotating cylinder. *Journal of Fluid Mechanics* (accepted for publication on 24.08.2013).
- RADI, A., THOMPSON, M. C., SHERIDAN, J. & HOURIGAN, K. 2013c From the circular cylinder to the flat plate wake: the variation of Strouhal number with Reynolds number for elliptical cylinders. *Physics of Fluids* (submitted for publication).
- RAFFEL, M., WILLERT, C. E. & WERELEY, S. T. KOMPENHANS, J. 2007 *Particle Image Velocimetry: A Practical Guide*. Springer.
- RAO, A., LEONTINI, J., THOMPSON, M. C. & HOURIGAN, K. 2013 Three-dimensionality in the wake of a rotating cylinder in a uniform flow. *Journal of Fluid Mechanics* **717**, 1–29.
- ROSHKO, A. 1954 On the drag and shedding frequency of two-dimensional bluff bodies. *National Aeronautics and Space Administration Washington D C* .
- ROSHKO, A. 1993 Perspectives on bluff body aerodynamics. *Journal of Wind Engineering and Industrial Aerodynamics* **49** (1-3), 79–100.
- RYAN, K., THOMPSON, M. C. & HOURIGAN, K. 2005 Three-dimensional transition in the wake of elongated bluff bodies. *Journal of Fluid Mechanics* **538**, 1–29.
- SAFFMAN, P. & SCHATZMAN, J. 1982 Stability of a vortex street of finite vortices. *Journal of Fluid Mechanics* **117**, 171–185.
- SAHA, A. K. 2007 Far-wake characteristics of two-dimensional flow past a normal flat plate. *Physics of Fluids* **19**, 128110.
- SAHA, A. K. 2013 Direct numerical simulation of two-dimensional flow past a normal flat plate. *Journal of Engineering Mechanics* (accepted for publication) .
- SCHLICHTING, H. & GERSTEN, K. 2000 *Boundary-layer theory*. Springer.

- 
- SHEARD, G. J., THOMPSON, M. C. & HOURIGAN, K. 2003a A coupled Landau model describing the Strouhal-Reynolds number profile of the three-dimensional wake of a circular cylinder. *Physics of Fluids* **15** (9), L68–L71.
- SHEARD, G. J., THOMPSON, M. C. & HOURIGAN, K. 2003b From spheres to circular cylinders: the stability and flow structures of bluff ring wakes. *Journal of Fluid Mechanics* **492**, 147–180.
- SHEARD, G. J., THOMPSON, M. C. & HOURIGAN, K. 2004 From spheres to circular cylinders: non-axisymmetric transitions in the flow past rings. *Journal of Fluid Mechanics* **506** (1), 45–78.
- SHEARD, G. J., THOMPSON, M. C. & HOURIGAN, K. 2005 Subharmonic mechanism of the mode C instability. *Physics of Fluids* **17** (11), 111702–4.
- SHERRY, M. 2012 An experimental investigation of wind turbine wake evolution and flow over complex terrain. Ph.D. thesis, Monash University.
- SHINTANI, K., UMEMURA, A. & TAKANO, A. 1983 Low-Reynolds-number flow past an elliptic cylinder. *Journal of Fluid Mechanics* **136** (1), 277–289.
- SIROVICH, L. 1987 Turbulence and the dynamics of coherent structures. I-Coherent structures. II-Symmetries and transformations. III-Dynamics and scaling. *Quarterly of applied mathematics* **45** (11), 561571.
- SMITS, A. J. & LIM, T. T. 2000 *Flow visualization: techniques and examples*, 1st edn. Imperial College Press London, UK.
- STOJKOVIĆ, D., SCHÖN, P., BREUER, M. & DURST, F. 2003 On the new vortex shedding mode past a rotating circular cylinder. *Physics of Fluids* **15**, 1257–1260.
- STROUHAL, V. 1878 Über eine besondere Art der Tonerregung. *Annalen der Physik* **241** (10), 216–251.
- STRYKOWSKI, P. J. & SREENIVASAN, K. R. 1990 On the formation and suppression of vortex shedding at low Reynolds numbers. *Journal of Fluid Mechanics* **218**, 71–107.
- TAFTI, D. K. & VANKA, S. P. 1991 A numerical study of flow separation and reattachment on a blunt plate. *Physics of Fluids A: Fluid Dynamics* **3**, 1749.
- TANEDA, S. 1959 Downstream development of the wakes behind cylinders. *Journal of the Physical Society of Japan* **14**, 843.
- THOMPSON, M. C., HOURIGAN, K., RYAN, K. & SHEARD, G. J. 2006 Wake transition of two-dimensional cylinders and axisymmetric bluff bodies. *Journal of Fluids and Structures* **22** (6-7), 793–806.

- 
- THOMPSON, M. C., HOURIGAN, K. & SHERIDAN, J. 1996 Three-dimensional instabilities in the wake of a circular cylinder. *Experimental Thermal and Fluid Science* **12** (2), 190–196.
- THOMPSON, M. C., LEWEKE, T. & WILLIAMSON, C. H. K. 2001 The physical mechanism of transition in bluff body wakes. *Journal of Fluids and Structures* **15** (3-4), 607–616.
- TROPEA, C., YARIN, A. L. & FOSS, J. F. 2007 *Springer handbook of experimental fluid mechanics*, , vol. 1. Springer.
- TSUBOI, K. & OSHIMA, Y. 1985 Numerical study of two-dimensional vortex street. *Proc. Computational Fluid Dynamics, Tokyo* pp. 230–237.
- VAN DYKE, M. 1982 *An Album of Fluid Motion*. The Parabolic Press.
- VOROBIEFF, P. & ECKE, R. 1999 Cylinder wakes in flowing soap films. *Physical Review E* **60**, 2953–2956.
- VOROBIEFF, P., GEORGIEV, D. & INGBER, M. S. 2002 Onset of the second wake: Dependence on the Reynolds number. *Physics of Fluids* **14** (7), L53–L56.
- WANG, J., BIRCH, J., & DICKINSON, M. 2004 Unsteady forces and flows in low reynolds number hovering flight: two-dimensional computations v.s. robotic wing experiments. *Journal of Experimental Biology* **207**, 449–460.
- WILLERT, C. E., MUNSON, M. & GHARIB, M. 2010 Real-time Particle Image Velocimetry for closed-loop flow control applications. In *5th Int. Symp. on Applications of Laser Techniques to Fluid Mechanics*.
- WILLIAMSON, C. H. K. 1988 The existence of two stages in the transition to three-dimensionality of a cylinder wake. *Physics of Fluids* **31** (11), 3165–3168.
- WILLIAMSON, C. H. K. 1989 Oblique and parallel modes of vortex shedding in the wake of a circular cylinder at low Reynolds numbers. *Journal of Fluid Mechanics* **206**, 579–627.
- WILLIAMSON, C. H. K. 1992 The natural and forced formation of spot-like ‘vortex dislocations in the transition of a wake. *Journal of Fluid Mechanics* **243**, 393–441.
- WILLIAMSON, C. H. K. 1996a Mode A secondary instability in wake transition. *Physics of Fluids* **8** (6), 1680–1682.
- WILLIAMSON, C. H. K. 1996b Three-dimensional wake transition. *Journal of Fluid Mechanics* **328**, 345–407.

- 
- WILLIAMSON, C. H. K. 1996c Vortex dynamics in the cylinder wake. *Annual Review of Fluid Mechanics* **28** (1), 477–539.
- WILLIAMSON, C. H. K. & PRASAD, A. 1993 A new mechanism for oblique wave resonance in the far wake. *Journal of Fluid Mechanics* **256**, 269–313.
- WU, J., SHERIDAN, J., WELSH, M. C. & HOURIGAN, K. 1996 Three-dimensional vortex structures in a cylinder wake. *Journal of Fluid Mechanics* **312**, 201–222.
- YANG, D., NARASIMHAMURTHY, V. D., PETTERSEN, B. & ANDERSSON, H. I. 2012 Three-dimensional wake transition behind an inclined flat plate. *Physics of Fluids* **24** (9), 094107–17.
- YILDIRIM, I., RINDT, C. & STEENHOVEN, A. 2010 Vortex dynamics in a wire-disturbed cylinder wake. *Physics of Fluids* **22**, 094101.
- YILDIRIM, I., RINDT, C. C. M. & VAN STEENHOVEN, A. A. 2013a Energy contents and vortex dynamics in mode-C transition of wired-cylinder wake. *Physics of Fluids* **25** (5), 054103–18.
- YILDIRIM, I., RINDT, C. C. M. & VAN STEENHOVEN, A. A. 2013b Mode C flow transition behind a circular cylinder with a near-wake wire disturbance. *Journal of Fluid Mechanics* **727**, 30–55.
- ZHANG, H.-Q., FEY, U., NOACK, B. R., KÖNIG, M. & ECKELMANN, H. 1995 On the transition of the cylinder wake. *Physics of Fluids* **7** (4), 779–794.
- ZHAO, H. & LING, G. 2003 Low-dimensional dynamical systems for a wake-type shear flow with vortex dislocations. *Fluid Dynamics Research* **33** (3), 299–312.